

University of St Andrews



Full metadata for this thesis is available in
St Andrews Research Repository
at:

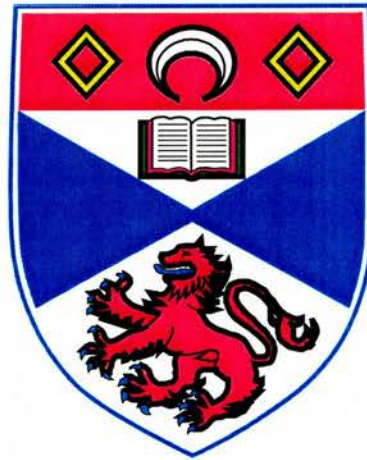
<http://research-repository.st-andrews.ac.uk/>

This thesis is protected by original copyright

Ultrafast Dynamics in Semiconductor Optical Amplifiers

Thesis submitted to the University of St Andrews
in application for the degree of Doctor of Philosophy

Julia Gabrielle Fenn



1st April 2003



Declarations

I, Julia Gabrielle Fenn, hereby certify that this thesis, which is approximately 60,000 words in length, has been written by me, that it is the record of work carried out by me and that it has not been submitted in any previous application for a higher degree.

26th May 2003
Date

I was admitted as a research student in November, 1998 and as a candidate for the degree of Doctor of Philosophy in 1999; the higher study for which this is a record was carried out in the University of St. Andrews between 1999 and 2003.

26th May 2003
Date

I hereby certify that the candidate has fulfilled the conditions of the Resolution and Regulations appropriate for the degree of Doctor of Philosophy in the University of St. Andrews and that the candidate is qualified to submit this thesis in application for that degree.

26/5/03

Date

Signature of supervisor

Unrestricted

In submitting this thesis to the University of St. Andrews I understand that I am giving permission for it to be made available for use in accordance with the regulations of the University Library for the time being in force, subject to any copyright vested in the work not being affected thereby. I also understand that the title and abstract will be published, and that a copy of the work may be made and supplied to any bona fide library or research worker.

26th May 2003
Date

*'Face it. Curiosity
will not cause us to die -
only lack of it will.
Never to want to see
the other side of the hill
or that improbable country
where living is an idyll
(although a probable hell)
would kill us all.
Only the curious
have if they live a tale
worth telling at all.'*

*'Jeff had gone through the long tunnel of a PhD...
and his curiosity continued as alive as ever'*

Alistair Reid

Abstract

This thesis presents an investigation of gain dynamics in a semiconductor optical amplifier (SOA). The motivation behind the work was the demand for ultrafast digital signal processing for datacomms applications and the potential of SOA-based interferometric switches as key components in future all-optical networks. Using an SOA, interferometric switching was achieved with ultrafast low energy pulses (~ 150 fJ, 700 fs) at $1.5 \mu\text{m}$.

The study focused on a 1 mm long SOA, with AR-coated, angled-facets. Its active region was a superlattice composed of InGaAs strained barriers/unstrained wells, giving gain in both TE and TM modes. The gain over wavelengths from 1510 to 1610 nm was investigated using amplified spontaneous emission spectra and optically-induced changes in junction voltage.

Both continuous-wave light and 700 fs pulses, from an 80 MHz Optical Parametric Oscillator, were used to measure the small signal gain and saturation characteristics of the device. The difference in output powers at 3 dB gain saturation was quantified for both cases, and calculations were used to demonstrate that ultrafast processes, such as carrier heating and spectral hole burning, dominate the saturation for such ultrashort pulses (< 10 ps).

Two and three beam pump-probe experiments were used to time-resolve gain and phase changes respectively, as a function of electrical bias and optical pulse energy at different wavelengths. Transmission measurements revealed strong ultrafast gain dynamics ($\tau \sim 1.2$ ps), in addition to slow gain recovery. Phase measurements were used to explore and optimise the switching window in the Terahertz Optical Asymmetric Demultiplexer (TOAD) configuration. In addition, wavelength shifts ($\Delta\lambda \pm 1$ nm), attributed to pump-induced refractive index changes, were observed in probe pulse spectra. Phenomenological, rate-equation-based models were developed to clarify the device behaviour with co- and counter-propagating pulses. The consequences of measured amplitude gain and refractive index dynamics for interferometric switching applications are discussed.

Contents

1	Background	1
1.1	Introduction	1
1.2	Optical processing and applications of SOAs	2
1.2.1	Trends in optical communications	2
1.2.2	Types of optical switch	4
1.2.3	SOA-based switches	8
1.2.4	Challenges in the optimisation of SOA-based switches	14
1.3	Introduction to propagation in optical media	17
1.3.1	The wave equation	18
1.3.2	Complex refractive index	18
1.3.3	Polarisation and susceptibilities	19
1.3.4	Linear propagation	20
1.3.5	Nonlinear effects	22
1.4	Summary	24
	Bibliography for Chapter 1	26
2	Optical properties of semiconductor devices	30
2.1	Introduction	30
2.2	SOA device design	30
2.3	Semiconductor basics	32
2.3.1	Interband transitions	33
2.3.2	Fermi distributions and bulk density of states	34
2.4	Semiconductor devices	36
2.4.1	The p-n junction	36

2.4.2	Heterostructures	37
2.5	The band structure of a III-V semiconductor	40
2.6	Quantum wells	41
2.6.1	Energy levels in a quantum confined system	42
2.6.2	QW density of states	43
2.6.3	Superlattices	44
2.7	Optical transitions	45
2.7.1	Polarisation and QW selection rules	46
2.7.2	Absorption and gain	47
2.8	Strained materials	50
2.9	Optical nonlinearities in semiconductors	53
2.9.1	Nonlinear gain	53
2.9.2	Index nonlinearities	59
2.9.3	Link between gain and index effects	61
2.9.4	Spatially dependent effects	62
2.10	Summary	63
	Bibliography for Chapter 2	65
3	Optical sources: principles and operation	70
3.1	Introduction	70
3.2	Overview of optical sources	70
3.3	Optical Parametric Oscillators	71
3.3.1	The principle of the OPO	71
3.3.2	Phase matching and wavelength tuning	72
3.3.3	Optical properties of the OPO crystal	74
3.3.4	Dispersion compensation	77
3.3.5	Synchronously pumped singly resonant OPO	79
3.3.6	Summary of methods for wavelength tuning	82
3.4	The pump laser system	83
3.4.1	Optical pumping of the OPO	83
3.4.2	The CW pump laser	84

3.4.3	The Titanium:Sapphire pulsed laser	85
3.5	Diagnostics	86
3.5.1	Spectrum measurements	86
3.5.2	Autocorrelation for temporal measurements	87
3.5.3	Monitoring program	92
3.6	Summary	97
	Bibliography for Chapter 3	98
4	Device characterisation	99
4.1	Introduction	99
4.2	Description of SOA structure	99
4.3	Mounting of the device	101
4.4	Coupling efficiencies	102
4.5	Amplified Spontaneous Emission	105
4.5.1	ASE from an SOA	105
4.5.2	Experimental set-up for ASE measurements	105
4.5.3	ASE results	105
4.6	CW transmission measurements	108
4.6.1	Amplification of CW source	108
4.6.2	Experimental set-up for transmission measurements	109
4.6.3	CW transmission results	109
4.7	Photo-induced voltage	115
4.7.1	Three regimes: absorption, transmission and gain	115
4.7.2	Experimental set-up for voltage measurements	116
4.7.3	Photo-induced voltage with pulses	117
4.7.4	Photo-induced voltage with CW light	123
4.8	Oscillations in the spectra	125
4.9	Summary	128
	Bibliography for Chapter 4	130
5	Modelling the SOA dynamics	132
5.1	Introduction	132

5.2	Different approaches: what is the model for?	132
5.3	A tale of two versions	135
5.4	Introducing the rate equations	136
5.4.1	The basic set of rate equations	136
5.4.2	Implementing the rate equation model	138
5.5	Results from solving the rate equations	139
5.5.1	Interband recombination	139
5.5.2	A quasi-equilibrium regime	139
5.6	Definition of the sliced propagation equations	142
5.6.1	The simplest equations - interband transitions only	142
5.6.2	Implementing the iterative calculations	143
5.6.3	Including ultrafast dynamics	143
5.7	Defining the input parameters	147
5.7.1	Time constants	147
5.7.2	Unsaturated gain as a function of current	148
5.7.3	Gain saturation as a function of the optical field	149
5.8	Results from sliced propagation calculations	150
5.8.1	Pump-induced gain changes	150
5.8.2	Co-propagating probe dynamics	154
5.8.3	Counter-propagating probe dynamics	156
5.8.4	Interference signal	157
5.9	Summary	163
	Bibliography for Chapter 5	165
6	Single pulse propagation	167
6.1	Introduction	167
6.2	Single pulse propagation	167
6.2.1	From the linear regime to gain saturation	167
6.2.2	Pulse shaping under different conditions	169
6.3	Input/output power experiments	171
6.4	Results of gain measurements	172

6.4.1	Small signal gain	172
6.4.2	Pulsed gain saturation	174
6.4.3	Comparison of saturation due to pulses and CW light	180
6.4.4	Calculations of saturation as a function of pulse duration	181
6.5	Pulse profile experiments	185
6.6	Results of spectral measurements	187
6.6.1	Under linear conditions	187
6.6.2	Under nonlinear conditions	187
6.6.3	Analysis of spectral changes	191
6.7	Summary	193
	Bibliography for Chapter 6	196
7	Pump-probe transmission experiments	199
7.1	Introduction	199
7.2	Choice of experimental technique	199
7.3	Two beam pump-probe experiments	201
7.3.1	The principle	201
7.3.2	Operating conditions	202
7.3.3	Experimental configurations	202
7.3.4	Data acquisition and processing	204
7.4	Transmission change results and analysis	207
7.4.1	Co-propagation results	207
7.4.2	Counter-propagation results	220
7.5	Summary	226
	Bibliography for Chapter 7	228
8	Phase changes and refractive index dynamics	230
8.1	Introduction	230
8.2	Three beam pump-probe experiments	230
8.2.1	Experimental configuration	230
8.2.2	Difference frequency lock-in detection	232
8.2.3	Interferometric experiments	233

8.3	Interferometric results and analysis	235
8.3.1	Dynamics as function of pump delay	235
8.3.2	Interference strength as a function of pump pulse energy	237
8.3.3	The effect of changing the bias	238
8.3.4	Different operating wavelengths	241
8.3.5	Switching window	243
8.3.6	Amplitude gain to refractive index coupling	250
8.4	Dynamic spectral shifts	251
8.4.1	Measurement of probe spectra	251
8.4.2	Results of spectral measurements during pump-probe	252
8.5	Summary	253
	Bibliography for Chapter 8	256
9	Summary and Conclusions	258
9.1	Overall Summary	258
9.2	Discussion and conclusions	259
	Bibliography for Chapter 9	265
10	Appendix	267
	Bibliography for Chapter 10	273

Chapter 1

Background

1.1 Introduction

On ultra short timescales, the dynamics in a semiconductor subsequent to optical excitation are complex, involving many different nonlinear processes. There are numerous mechanisms, some only identified in recent years, by which changes in the number of carriers (electrons and holes) and their energy distribution may occur. An understanding of these processes is necessary to account for the behaviour of semiconductor optical amplifiers (SOAs) on ultra short timescales. The carrier dynamics are manifested by ultrafast changes in gain and refractive index; parameters which can be investigated experimentally. This thesis is focused on measuring and analysing these gain and refractive index dynamics in a particular SOA structure.

In order to be able to view the results in the context of the wide international interest in SOAs it is helpful first to consider a range of the possible applications of this device. This chapter begins with a review of applications of SOAs, applications which are dependent on the semiconductor optical properties of the device.

Also in this chapter the general theory of propagation in optical media is reviewed. The basic concepts and terminology being relevant to both the more detailed theory of optical properties of semiconductors, introduced in Chapter 2, and to the operation and monitoring of the pulse sources, described in Chapter 3.

1.2 Optical processing and applications of SOAs

1.2.1 Trends in optical communications

Optical transmission of information is now commonplace. Almost all long distance terrestrial telecommunications traffic in the UK is carried by optical fibre networks, as is trans-Atlantic traffic, and optical interconnects are extensively used in Local Area Networks. Such systems can handle very high bandwidths, beyond the capacity of electronic networks. However, the high hopes of widespread use of all-optical signal processing have not yet been realised; signals continue to be converted from the optical to the electrical domain to effect, for example, regeneration. Consequently, it is the speed of optoelectronic conversion and electronic processing at the end of fibre links that are the prime capacity limitations of today's systems.

Electronic devices continue to be used since their production is economically viable and they are continually being made more efficient and faster. However the rate of operation an electrical system is limited to approximately 100 Gbit/s, due to noise problems (at such high data rates, the requirement for low values of noise necessary for timing accuracy being compounded by the difficulty of achieving sufficient heat extraction). In addition, by comparison to electrical, optical signals are inherently immune to magnetic fields, propagate at high speeds and within a potentially huge bandwidth. This optical bandwidth derives from the parallelism offered by light in space, polarisation and optical wavelength. So far, the use of wavelength division multiplexing (WDM), the sending of signals at different wavelengths down the same link simultaneously, has enabled network providers to meet the transmission rates required. It is proposed that time division multiplexing (TDM) at high line rates be used to enable more of the total capacity of optical networks to be exploited [1]. Optical signal processing has the potential to be conducted at the very high rates that will be required for TDM and moreover using less bulky, less complex devices [2]. However by comparison to electricity, light is less readily guided and this means that optical systems have a tendency to be more energy demanding.

A key technological challenge is to produce high speed switches which have minimal losses and low overall power consumption; achievements to date mean that further

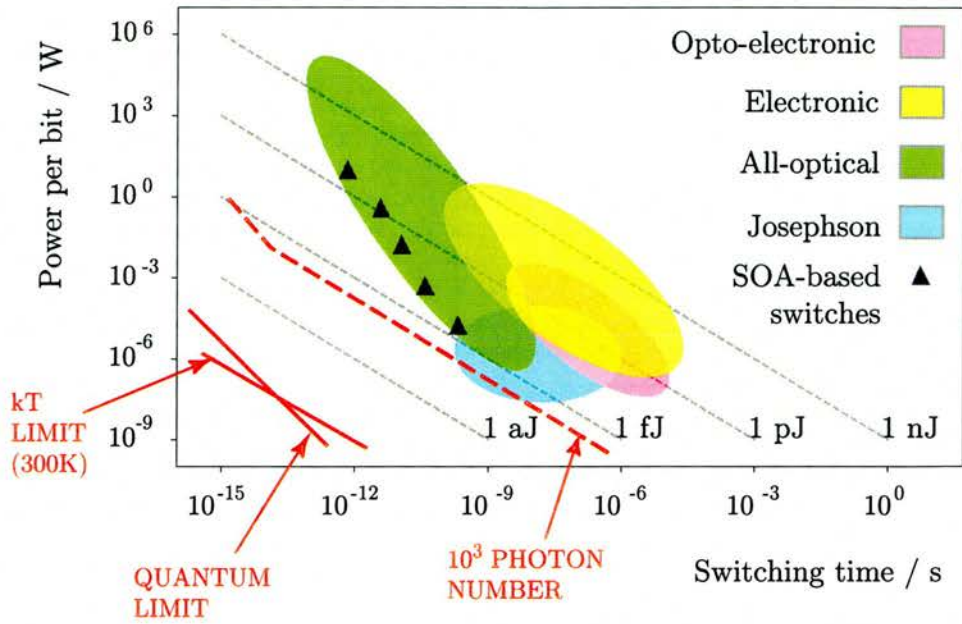


Figure 1.1: Schematic of power per bit versus delay time incurred in switching for various switch types including opto-electronic, electronic, all-optical and Josephson (following from [3], and references therein supplemented by recent results from the literature)

improvements in this regard mean approaching physical limits. Figure 1.1 indicates schematically the current status of all-optical switching technology with respect to these parameters, and includes three other general categories of switch: electronic, opto-electronic, and Josephson, for comparison.

Recently there has been considerable progress in the development of optical signal processing devices using semiconductors. Semiconductor devices possess characteristics important for optical processing applications, namely sufficiently large nonlinear material responses to excitation in the bandwidths used for telecommunications and, under certain conditions, fast recovery. This thesis focuses on one type of device that exploits these nonlinearities, the Semiconductor Optical Amplifier (SOA) (alternatively known as a Semiconductor Laser Amplifier or Travelling Wave Amplifier). With respect to other competing technologies, SOA-based switches are promising, generally lying towards the high-speed, low-power side of the region covered by all-optical switches, as indicated in figure 1.1.

Type	Switching rate	Strengths	Weaknesses
Opto-mechanical (traditional)	> ms	optical performance	bulky, scalability reliability, speed
MEMS	ms or less	size, scalability low crosstalk	cost, reliability
Thermo-optical (traditional)	>ms	integration	power consumption, scalability, speed
Bubble/gel-based	< 10 ms	modular scalability	reliability, insertion loss
Acousto-optic	< ms	size, speed	optical performance
Liquid crystal (traditional)	ms	reliability	scalability, temperature dependent
Liquid crystal in polymer	100 μ s	reliability	scalability, temperature dependent
Electro-optic (dielectric)	ns	speed, reliability	loss, scalability polarisation dependent
Fibre-based	<ns	speed, loss compensation	latency, scalability power consumption
EAM-based	<ns	speed	scalability
SOA-based	<ns	speed, loss compensation	noise, scalability
Ferro-magnetic (Faraday)	fs	speed	scalability reliability not proven

Table 1.1: Characteristics of optical switching technologies

1.2.2 Types of optical switch

A host of options

The literature documents a plethora of approaches to achieving optical switching. The main categories are opto-mechanical including micro electro-mechanical systems (MEMS), thermo-optical including gel/oil based ‘bubble’ switches, liquid crystal including liquid-crystal-in-polymer, electro-optical (using materials such as Lithium Niobate), magneto-optic and schemes employing acousto-optic modulators (AOMs), semiconductor optical amplifiers (SOAs), electro absorption modulators (EAMs) and optical fibres or fibre amplifiers.

Table 1.1 summarises some of the factors critical in determining which of these technologies may be adopted in real world systems (extracted from the literature, see for example [1] and [3], and references therein). It is likely that different schemes will fulfil different functions in future networks. Consider the following examples of

applications:

- Packet switching: at the nodes of optical networks, which requires the handling of high numbers of ports/channels with switching times on the order of nanoseconds.
- Multiplexing: to add or drop specific wavelengths from WDM and TDM signals, with switching times sub-ms but generally for small numbers of ports.
- Protection switching: to restore optical paths in the event of failure of a link, with switch reliability, as opposed to speed, being key (at least currently, since other processes in the protection schemes are likely to take longer than the switching)
- Signal monitoring: to ease network management, which would need to be wavelength selective and with low requirements on optical power (since it would be using small fraction of signal in each channel).

For example, traditional opto-mechanical switches, that deflect optical signals with moveable mirrors, faced the drawback of limited lifetime. However the sub-category of semiconductor-fabricated MEMS have shown improved reliability in testing and can be scaled to handle multiple ports whilst retaining small device size. Given the characteristics of low insertion loss and minimal cross-talk of MEMS, they are an appealing solution for most applications that do not demand sub-millisecond switching times and where wavelength selectivity is not required. For protection switching, where wavelength sensitivity is necessary, other schemes operating on the millisecond time scale such as magneto-optic or liquid crystal based switches may be implemented.

However the options for ultrafast switching are more limited. In particular a host of interferometric switching topologies can be used at bit rates of the order of 100 Gbit/s, especially for simple, repetitive operations such as demultiplexing. Whilst the jury is still out, SOAs, with their potential to be operated at high rates and using low optical energies, are a very promising devices for the nonlinear elements in these configurations.

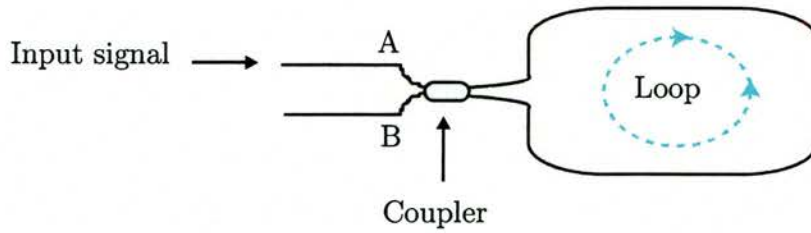


Figure 1.2: Schematic of the Nonlinear Optical Loop Mirror (NOLM) switching configuration based on a fibre loop

Configurations for interferometric switching

Fifteen years ago the nonlinear optical loop mirror (NOLM) was proposed as an interferometric optical switch. It boasted a simpler construction than earlier optical switches, was robust and importantly it did not require interferometric alignment [4]. The NOLM configuration is essentially a Sagnac interferometer composed of a coupler spliced into a fibre loop, as shown in figure 1.2. Under linear conditions the loop acts as a mirror: the signal input at A is split, the co- and counter-clockwise propagating components follow identical paths, though in opposite directions, and recombine constructively at the coupler, emerging again at A. However when the input intensity is sufficient and the splitting ratio unequal, the co- and counter-clockwise fields propagate differently. Consequently the interferometric conditions at the coupler are modified and, if the phase difference between the fields is a multiple of π , the signal emerges at the other port, B.

In order to obtain good modulation, with a high contrast ratio between the on and off states, the splitting ratio in the NOLM has to be close to 50:50. However this must be balanced against the fact that to achieve switching with a smaller intensity difference between co- and counter-clockwise components a longer length of fibre in the loop or higher input energies are necessary.

The concept of the NOLM was extended to the nonlinear amplifying loop mirror (NALM), in which a length of fiber amplifier was spliced into the loop asymmetrically [5]. This permits more efficient exploitation of the fibre nonlinearities, with lower optical powers (signal ~ 1 mW but also amplifier pump of 10 mW [5]). However it was the idea of using the loop geometry with a semiconductor device as the nonlinear element that enabled optical energy requirements for interferometric switches to be

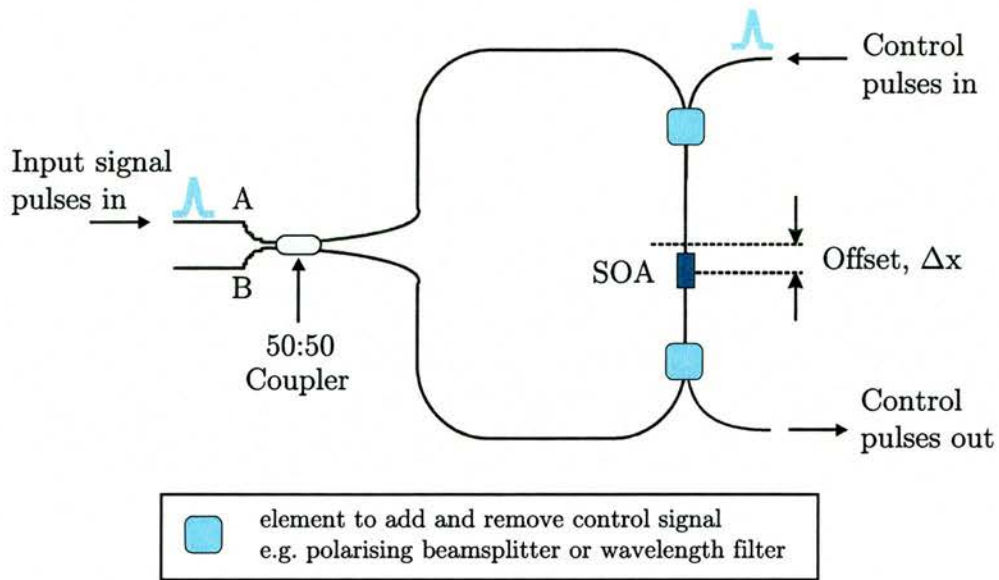


Figure 1.3: Schematic of the Terahertz Optical Asymmetric Demultiplexer (TOAD) switching configuration using an SOA in a fibre loop

dropped further. For example, with a loop containing both a semiconductor amplifier and attenuator (a non-reciprocal pair) switching was demonstrated with the relatively lower power requirement of hundreds of microwatts [6]. Note that in this configuration the switching is based on phase changes due to the direction of propagation of the two signal components, through the nonlinear elements, being different.

Ten years ago, the terahertz optical asymmetric demultiplexer (TOAD) configuration was demonstrated [7]. The TOAD comprises an SOA, as the nonlinear element, offset from the centre of an optical loop mirror, hence the alternative name SLALOM (from Semiconductor Laser Amplifier in a Loop Mirror). In this case, the switching concept relies on a difference in the arrival time at the nonlinear element of the two signal components, with respect to the arrival of a control signal. Figure 1.3 shows a schematic of the TOAD configuration. Note that it retains the attractive feature of the paths of the two components of the signal being intrinsically matched. Moreover, since the length of the loop is irrelevant to the operation of the switch beyond the need to accommodate the asymmetric positioning of the semiconductor device, it was for the first time possible to conceive of a low-power, all-optical switch integrated on a single substrate [8].

1.2.3 SOA-based switches

Comparison nonlinear elements for interferometric switching

Whilst each of the interferometric configurations proposed to date have drawbacks, interferometric switches are so far the most promising optical switch type for fast operation and with low energy requirements, particularly where a semiconductor nonlinear element is used. The large nonlinearity of the semiconductor materials from which SOAs are made can produce unwanted effects (e.g. cross-talk between channels or pulse profile distortion) when SOAs are used as amplifiers in photonic networks [9]. Such nonlinear effects in SOAs, combined with the addition of noise from amplified spontaneous emission and coupling losses, explain why fibre amplifiers are in general favoured, over SOAs, for inline amplification. However it is the magnitude of the nonlinearity that makes the SOA attractive for switching and other processing applications. Consider the following example.

With an SOA replacing the silica fibre, the TOAD configuration is based on the same Sagnac interferometer principle as the nonlinear optical fibre loop mirror (NOLM) and competes with this device for applications. However, the fibre NOLM requires long lengths of fibre and high pulse powers, due to the nonlinearities in the fibre being small. In addition to huge latency, a disadvantage of the long optical path length of fibre switches is increased sensitivity to environmental disturbance, for example thermally induced variation in fibre length, and there may be group-velocity walk-off between signal and switching pulses [9]. For a fibre NOLM to operate as a switch, of the order of 1 km of fibre and peak optical pulse powers of 1 W would be required [10]. By contrast, the higher nonlinearities of the semiconductor materials mean that a 1 mm SOA based switch could be operated using optical powers of a 1 mW or less. Indeed TOAD operation has been demonstrated using switching pulse energies below 200 fJ (for example, [11]), which even at a bit rate in excess of 100 Gbit/s would correspond to much lower average power than required for a fibre device.

The TOAD

To set the context for discussion of SOA characteristics with respect to applications, it is useful to consider the operation of an SOA-based switch in more detail. The example

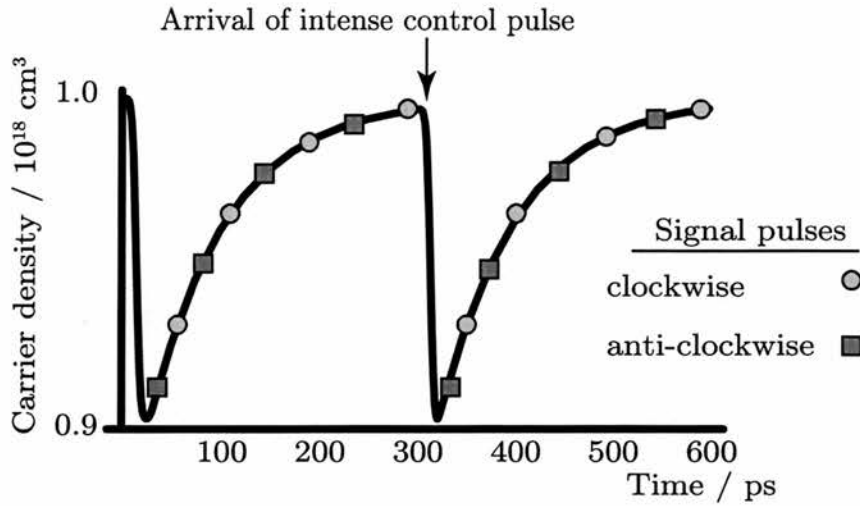


Figure 1.4: Change of carrier density induced by control pulse with respect to the arrival time of co- and counter-propagating signal pulses. The recovery occurs more rapidly than the spontaneous recombination time due to applied electrical bias.

of the TOAD is chosen since it raises issues common to many interferometric switching configurations and it is this Sagnac interferometer configuration that has been used in experiments, described in Chapter 8.

In the TOAD, shown in figure 1.3, the low power signal, input at A, is split by a 50:50 coupler and the two components are sent around the loop in opposite directions. The resulting counter-propagating pulses both pass through the SOA but they do so at different times. In the absence of any control pulses, the signal pulse pair interfere constructively at the coupler and the signal appears reflected (output at A). To operate the switch, a higher power control pulse is timed to arrive at the SOA between the two components of the original signal pulse, hence effecting only the latter. If, by altering the refractive index in the SOA, the control pulse causes the phase of second signal component to be shifted by π radians with respect to the phase of the first, the recombined components will be transmitted through the loop (emerging at B). For subsequent pairs of counter propagating signal pulses, both arriving after the control pulse, each component accumulates approximately the same phase change. Consequently, they are mostly reflected by the loop (emerging at A), similar to the case of pulse pairs arriving before the control. (Note that the coupler can also be set up such that the pulse is reflected when $\Delta\phi = \pi$ and transmitted for no differential phase change.)

Figure 1.4 illustrates the evolution of the carrier density in the SOA, due to a train of intense control pulses, with respect to the arrival time of weak clockwise and anti-clockwise propagating signal pulses. The curve is calculated using simple rate equations (of the form detailed in Chapter 5) which describe optical depletion of the carrier population in the SOA by intense control pulses and recovery through electrical injection of carriers. On occasions when the control pulse arrives between a pair of signal pulses the change in carrier density, and hence the phase difference induced between the two components of the pair, is large. Under these circumstances, the signal would be switched. Conversely when no control pulse arrives between the passing of the two components, the phase difference induced between them is small and the signal is not switched. In this way, depending on the pattern in the control pulse sequence, pulses in the original signal train can be preserved or annulled. In particular, if the control pulse train is periodic the TOAD is functioning as a demultiplexer. In order to be able to separate the control pulses from the signal, the control can be either of the opposite linear polarisation or at a different wavelength to the signal data.

Note that the carrier density change required to achieve a π phase change is small compared to the typical carrier inversion in an SOA. Consider that the control-induced refractive index change, Δn , gives a phase change, $\Delta\phi = \Delta n 2\pi L/\lambda$ where L is the path length in the device. For the SOA studied in this thesis the operating wavelength is around $1.5 \mu\text{m}$ and the waveguide is 1 mm long. Consequently taking the rate of change of index with electron-hole pair density to be approximately -2×10^{-20} [12], the carrier density change corresponding to $\Delta\phi = \pi$ is only $\sim 10^{17}$ compared to an equilibrium inversion density of $\sim 10^{18}$. These relatively small modulations in carrier density required for switching, combined with rapid rates of recovery of carrier density under conditions of high electrical bias, explain why SOA-based interferometric configurations are capable of achieving fast switching. This analysis is based on considering the simple picture of carrier density dependent index changes only; ultra-fast carrier dynamics which may be associated with even larger and more rapid index changes and tend to complicate this simple description are introduced in Chapter 2, included in the modelling described in Chapter 5 and discussed along with experimental results in later chapters.

In addition, the condition for interferometric switching is a difference in phase (an odd multiple of π) between the two components of the signal pulse; the device does not necessarily need to recover fully between switching events. Consequently, performance of switching functions using interferometric switches is possible at rates even faster than the recovery of gain in the semiconductor device [13] [14]. The establishment of a quasi-equilibrium, a regime of operation that can be used for such high rate switching, is demonstrated in Chapter 5.

The overall duration of the switching window in a TOAD is determined by the offset of the SOA from the point in the loop exactly opposite the coupler, and so can readily be adjusted. This ability to tune the width of the switching window is common to other SOA-based switching configurations [15] [16]. Note however that the characteristic shape of the switching window is device and configuration dependent [17], as is discussed extensively with experimental results in Chapters 7 and 8.

Other SOA-based configurations

In recent years many other configurations for SOA-based interferometric switches, without a loop structure, have been demonstrated. Several are based on the Mach-Zender interferometer with two SOAs, one in each arm of the interferometer [18] [19]. Examples, shown schematically in figure 1.5, include the symmetric Mach-Zender (SMZ) and the colliding pulse Mach-Zender (CPMZ) in which the control pulses co- or counter-propagate relative to the signal respectively. In these two arm configurations external stabilisation is required (e.g. tuning of the electrical bias to each SOA independently).

Partly in response to the complication of optimising configurations requiring two SOA devices, several single arm interferometers have been proposed. These include the polarisation-discriminating symmetric Mach-Zender switch (PD-SMZ) [20], the uniaxial nonlinear interferometer (UNI) [21] and, specifically for wavelength conversion, the delayed interference signal-wavelength converter (DISC) [22]. These single arm configurations function by differentially delaying two polarisation components of the signal pulse; whilst the number of optical elements is reduced, these configurations still require careful length matching.

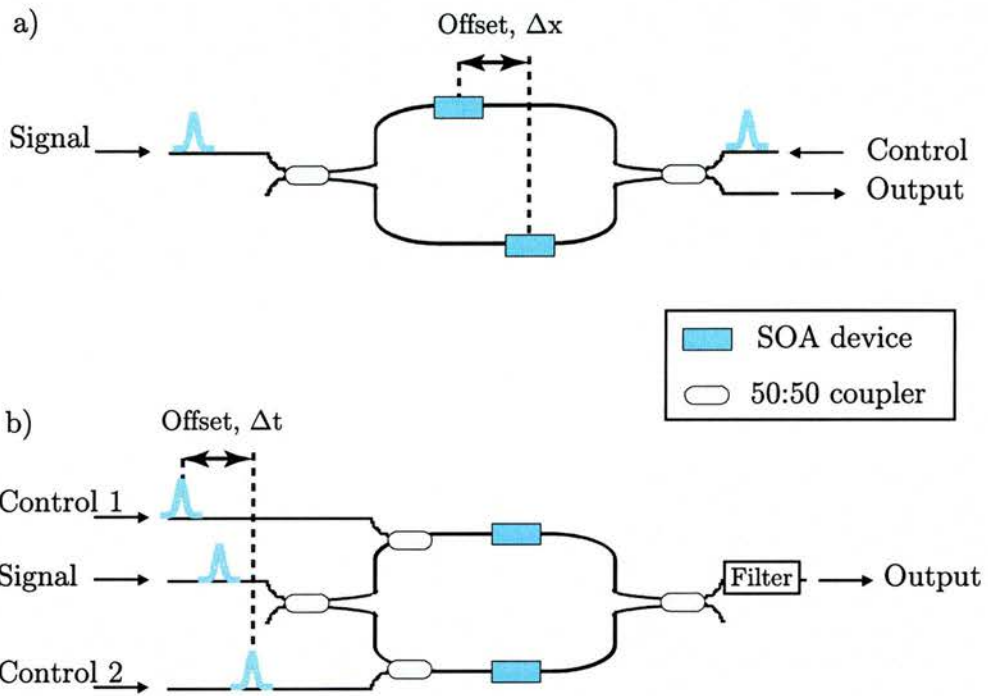


Figure 1.5: Schematics of (a) the Colliding Pulse Mach-Zender (CPMZ) and (b) the Symmetric Mach-Zender (SMZ) switching configurations each using two SOAs one in each arm of a two arm interferometer. Note that the required differential phase shift between the two components of the signal are introduced via a spatial offset, Δx , in path lengths and a temporal offset, Δt , between two control pulse trains in the CPMZ and the SMZ respectively.

Varied functions of SOA-based switches

The basic concept of the operation of a TOAD and other interferometric configurations is that of switching out individual pulses from a stream of signal data. However operation of these configurations as single bit switches is not necessarily the best niche they could occupy in the context of real world applications. Firstly, there are some drawbacks to their operation as single bit switches and, secondly, many other desirable functions have been successfully demonstrated.

Imperfect switching results from the fact that for signal pulses, subsequent to the switched signal, the two components will not acquire exactly the same phase or experience the same gain (see figure 1.4). The difference between the components becomes less severe with each successive signal pulse pair, until the arrival of the next control pulse. However, for as long the difference remains, there is amplitude modulation between pulses in the non-switched signal data train. Moreover, if the data is random, there may be a succession of 1's in the control pulse sequence. This can result in severe patterning of the switched signal data, since the device can not recover to the same degree between switching events [12]. These problems are allayed if the device can be made to recover more rapidly and various means of influencing the speed of recovery are discussed in Chapter 2, and elsewhere in this thesis. However, in general, the consensus has been to advance the use of configurations such as the TOAD for demultiplexing (as its name implies) where the control pulse is periodic [13] [1].

An alternative use of these SOA-based switches is for the regeneration of pulses. Not only can the optical field be amplified on passing through the SOA but quality of the data train can be improved in other ways, for example, pulses can be re-shaped and re-timed [10] [23]. The distortion that may be manifested when an SOA is used for direct amplification, due to nonlinear effects, can be compensated for when it is placed within a TOAD [24].

Another range of proposed applications of SOAs are in the field of wavelength conversion. If the control sequence is in fact the patterned data and the signal input to the switch is replaced by a regular clock or CW signal at some different wavelength, the pattern from the control can be imposed on this new wavelength. This can produce

a high quality data train and moreover effects the transfer of data from one wavelength channel to another, an important function for WDM network management [25].

In addition there are some reports in the literature of using an SOA to perform logic functions [26]. Configurations involving SOAs in a loop have even been proposed as one answer to the thorny problem of achieving optical memory [27]. These examples serve to illustrate the wide range of potential applications being envisaged for SOAs; many of those cited are related to switching, but are above and beyond the basic concept of switching a data bit from one channel to another.

1.2.4 Challenges in the optimisation of SOA-based switches

Key to minimising the power requirements and maximising stability of SOA-based switches is integration of the interferometric configurations. Indeed the potential for fully integrated switches is a major advantage of semiconductor-based optical processing devices over other bulkier switching mechanisms, e.g. MEMS. It remains a challenge to minimise the cross-talk between channels in an integrated device, and the growth and processing tends to be complex, but integrated switches have been demonstrated [28][29][30]. Clearly simplification of the fabrication such that they can be produced at a progressively lower cost will increase the competitiveness of SOA-based switches.

Beyond production costs, the implementation of optical switching in real world systems depends on optimisation of the operating characteristics of the optical elements. Factors of concern include deviation from the ideal of the characteristics of components, such as the splitting ratio of couplers, tolerances on energy of the control pulses and the degree of degradation of the signal to noise ratio by amplified spontaneous emission (ASE) [31]. Losses are another a key issue. Clearly with a forward biased device, such as an SOA, losses can be compensated for by gain. This ability to provide amplification as necessary is highly desirable. However the use of high electrical bias currents pushes up total power requirements of the system and may result in significant degradation of the signal if there is a large amount of ASE.

For switching, SOAs made from semiconductor materials such as InGaAsP and InGaAs seem highly promising by commonly applied figures of merit [2] [9]. These

are related to requirements of high device throughput and sufficiently large nonlinearity relative to attenuation with increasing length through the material. However these criteria form a bare minimum for acceptability.

For real applications, the switching process must satisfy the requirement of less than one error in 10^9 bits, referred to as 'error free'. Error free operation has been demonstrated using SOA-based switches for both demultiplexing and regeneration on data streams of at least 40 Gbit/s [23]. However degradation in the BER has been observed when the TOAD configuration is used for demultiplexing at higher rates (100 Gbit/s data stream to a 12.5 Gbit/s [32]). The explanation proposed [32] is that the switching pulse interacted with more than one data pulse due to the fact that transit time through the SOA was longer than half the bit period. In this way, the length of the nonlinear element limits the operational data rate in a TOAD, with the implication that for faster rates it would be necessary to use ever shorter waveguides. Other configurations such as the UNI or SMZ in which signal and control pulses co-propagate through the waveguide(s) can avoid this limitation. However, since in these configurations the pulses do not propagate along the same optical path, they are not intrinsically balanced, in contrast to the loop switches, making their implementation more complicated [33].

In the drive to develop devices for processing at high data rates it will be important to consider different, possibly totally new, configurations or new modes of operation of existing switches. One such concept is to use non-degenerate signal and control pulses. This has proved effective in improving the performance SOA-based interferometric configurations, producing higher contrast ratios by reduction of the noise added by amplified spontaneous emission at the signal wavelength and minimising the amplitude modulation of the output signal [34] [35].

Almost a decade ago, Ellis and Spirit [36] reported switching with TOADs of 10 GHz pulse trains. Specifically every fourth pulse was extracted from a 40 Gbit/s data sequence. The following year a demonstration of demultiplexing from 160 Gbit/s to 10 Gbit/s was achieved using a semiconductor amplifier [37], these ever faster operation rates being possible because of it not being necessary for the SOA to fully recover between interferometric switching events. More recently demultiplexing to 10 Gbit/s from extremely high rates has been demonstrated: from 640 Gbit/s with an NOLM [38]

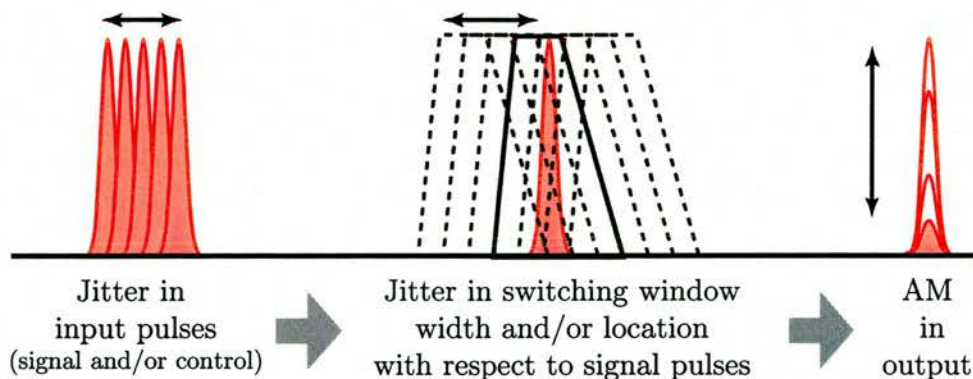


Figure 1.6: Schematic illustrating how timing jitter translates into amplitude modulation in the output from an interferometric switch.

and from 1.5 Tbit/s with a SMZ configuration including a semiconductor waveguide [39]. The NOLM had the weakness of introducing high latency due to the long fibre loop lengths and requiring relatively high optical powers and with the SMZ switch ultrafast turn on/off was only shown separately from the high repetition rate demultiplexing. Such results remain research laboratory demonstrations; their implementation in real world applications still far from being realised. For example, whilst Yamamoto et al. have successfully demonstrated a complete system with a 640 Gbit/s signal transmitted and subsequently demultiplexed, it was extremely complex and the maximum transmission distance achieved was less than 100 km [40].

After propagation down significant lengths of optical fibre jitter can be a problem even if the optical source was virtually jitter free. In particular at high rates where the period between consecutive bits is short, jitter in the arrival time of the control pulse with respect to the signal significantly degrades interferometric switching[18]. This is illustrated schematically in figure 1.6. The use of shorter pulses makes high jitter levels still more problematic, since the opening of the switching window is steeper, and the top of the switching window may not be flat or smooth [35] [41]. Experimental measurements of the switching window with a TOAD-like configuration are reported in Chapter 8. For practical devices the speed of switching and limits on the repetition rate, determined by the response time of the device and its recovery, are key. However other factors that have been mentioned are critical: for example, optimisation for operation with low optical energies may be more important than striving for ever faster

operation rates [42].

The research for this thesis has been conducted in the context of these application requirements. At the same time, the physics behind the observed behaviour of the device has been explored. A detailed study of the behaviour of an SOA under a wide range of conditions, electrical and optical, is reported. Some characterisation was undertaken using continuous wave light, however most measurements were conducted using sub-picosecond pulses, at a variety of wavelengths and pulse energies. The propagation of single pulses through an SOA was investigated and subsequent experiments were conducted with two and three pulse trains, with pulses both co- and counter-propagating through the device. This has allowed for investigation of many of the issues relevant to the applications discussed, and in particular the implications of ultra-fast index and gain changes for achieving rapid, low energy interferometric switching. The important semiconductor material processes behind observed behaviour of the device are introduced in Chapter 2 and the experimental measurements of the optical properties, including gain and index dynamics, are reported in subsequent chapters.

1.3 Introduction to propagation in optical media

For the discussion of the work reported in this thesis it is useful to introduce a general description of optical pulses and their propagation. In particular, propagation in non-absorbing and absorbing media and under linear and nonlinear conditions will be considered.

At weak intensities light propagates linearly; different wavelengths may propagate at different speeds or be differently absorbed, but there is no generation of a new wavelength. Specifically, the linear regime corresponds to conditions under which the response of the medium is linear with respect to the instantaneous value of the oscillating electric field, associated with the electromagnetic wave. On the contrary, at high light intensities, the polarisation of the medium may demonstrate components proportional to the square, and higher powers, of the instantaneous electric field. Under these conditions, light waves may interact with each other, as well as the medium they are travelling through, and new frequencies may be generated.

1.3.1 The wave equation

The wave equation deduced from Maxwell's equations, describing the propagation of electromagnetic waves, may be written in Cartesian coordinates in the form

$$\left(\frac{\partial^2}{\partial x^2} + \frac{\partial^2}{\partial y^2} + \frac{\partial^2}{\partial z^2} - \frac{n^2}{c^2} \frac{\partial^2}{\partial t^2} \right) E(x, y, z, t) = \mu \frac{\partial^2}{\partial t^2} P(x, y, z, t) \quad (1.1)$$

where μ is the magnetic permeability, ε is the dielectric constant, E represents the electric field and P the polarisation.

Solutions of equation 1.1, for a propagating electric field with spatial and time dependence, such as that associated with an optical pulse can be written

$$E(z, t) = E_0 \exp^{i(kz - \omega t)} \quad (1.2)$$

where k is the wavevector, ω the angular frequency and z distance in the direction of propagation.

1.3.2 Complex refractive index

In a non-absorbing medium the wavevector, k , is related to wavelength, λ , refractive index in the medium, n , and ω through

$$k = \frac{2\pi}{\lambda/n} = \frac{n\omega}{c} \quad (1.3)$$

For an absorbing medium equation 1.3 can be generalised by allowing the index, n , to be complex, of the form

$$k = (n + i\kappa) \frac{\omega}{c} \quad (1.4)$$

For an electromagnetic wave propagating through such a medium, changes in n correspond to changes in phase and changes in κ correspond to absorption or amplification of the field.

The absorption of light by a medium is usually quantified by a factor α per unit distance travelled through the medium. The evolution of a field of intensity, I , then expressed as

$$I(z) = I_0 \exp^{-\alpha z} \quad (1.5)$$

where z is distance in the medium and I_0 is the intensity at $z = 0$. Given that the intensity, I is proportional to the electric field, that is $I \propto |E(t)|^2$, it is possible to show that the variables κ and α are related [43].

$$\alpha = \kappa \frac{2\omega}{c} = \kappa \frac{2\pi}{\lambda} \quad (1.6)$$

In general, as this would suggest, absorption is strongly dependent on wavelength. Absorption in semiconductors relevant to the devices investigated in this project is discussed further in Chapter 2.

1.3.3 Polarisation and susceptibilities

The optical properties of materials can be characterised through the real and imaginary parts of the dielectric constant, ϵ . The electric displacement, D , of the medium is defined with respect to electric field, E , and polarisation, P , as

$$D = \epsilon_0 E + P \quad (1.7)$$

where the constant ϵ_0 is the permittivity of free space. It is then possible to write

$$D = \epsilon_0 \epsilon_r E \quad (1.8)$$

where

$$P = \epsilon_0 \chi E \quad (1.9)$$

and

$$\epsilon_r = 1 + \chi \quad (1.10)$$

where χ is the electric susceptibility of the medium. However in a nonlinear regime a more general form of equations 1.9 and 1.10 is required since the polarisation is not linear with respect to the electric field. In general the polarisation can be expressed as

$$P(E) = \epsilon \int \chi E dE \quad (1.11)$$

This is commonly approximated by a series expansion of the form

$$P = \epsilon_0 \chi^{(1)} E + \epsilon_0 \chi^{(2)} E^2 + \epsilon_0 \chi^{(3)} E^3 + \dots \quad (1.12)$$

where $\chi^{(1)}$ is the linear susceptibility and $\chi^{(j)}$ the higher (jth) order susceptibilities, which are generally weaker. Each χ is complex. The real parts give rise to frequency mixing, effects such as self-phase modulation (SPM) and the nonlinear refractive index, n_2 . The imaginary parts of χ describe optical processes including two photon absorption (TPA) and Raman scattering. Some of these processes, those most relevant to this project, will be discussed further in section 1.3.5.

1.3.4 Linear propagation

For low intensities the higher order effects are insignificant, and the propagation through an optical medium is governed by $\chi^{(1)}$. This linear susceptibility gives rise to linear effects such as refraction, diffraction and dispersion.

Linear refractive index

In this regime, the linear refractive index, n_0 is related to the first order susceptibility by

$$n_0(\lambda) = 1 + \frac{1}{2} \text{Re}[\chi^{(1)}(\lambda)] \quad (1.13)$$

Away from optical resonances, the dependence of the refractive index, n , on wavelength, λ may be expressed by an empirical Sellmeier equation of the form

$$n_0(\lambda) = 1 + \sum \frac{A_j \lambda^2}{\lambda^2 - B_j} \quad (1.14)$$

where the constants A and B are determined empirically by fitting the equation to experimental data for a given optical material (see for example, [44] which gives equations for a Lithium Niobate crystal of the sort used for the pulse generation outlined in Chapter 3). This is generally possible for optical materials from the visible to the near infrared; beyond these regions optical resonances reduce the accuracy of this type of expression.

The phase change experienced by a pulse on propagation through a uniform medium may expressed

$$\phi(\omega) = \text{Re}[k(\omega)]L = \frac{n(\omega_0)\omega}{c}L \quad (1.15)$$

where L is the length of the medium. Physically, this phase change between the incident and emitted radiation is due to the delay incurred by absorption and re-emission:

the interaction of the radiation with a material which is responsible for the speed of propagation being reduced with respect to propagation in free space.

Dispersion

The frequency dependent characteristic of the first order susceptibility and hence of the linear refractive index of a material gives rise to dispersive effects.

Consider that in general the electromagnetic waves of different wavelengths propagate in a medium at different velocities given by c/n_λ where n_λ is the index of refraction for each wavelength. In the case of an ultrashort pulse composed of many spectral components this can result in significant broadening, or shortening, of the pulse temporal duration.

To quantify dispersion, consider the electric field variation associated with an optical pulse written

$$E(z, t) = E(t) \exp^{i\phi(t)} \exp^{i\omega_0 t} \quad (1.16)$$

where $E(t)$ is the time varying electric field envelope, $\phi(t)$ represents the phase variation across the pulse and ω_0 is the optical carrier frequency. This expression (equation 1.16) uses the slowly-varying field approximation where the assumption is that the pulse envelope changes only slowly with respect to the carrier frequency. It is convenient to expand the phase in a Taylor series about the central frequency of the pulse, ω_0 as follows

$$\phi(\omega) = \phi_0 + \phi'[\omega - \omega_0] + \frac{\phi''}{2!}[\omega - \omega_0]^2 + \frac{\phi'''}{3!}[\omega - \omega_0]^3 + \dots \quad (1.17)$$

where $\phi_0 = \phi(\omega_0)$, ϕ' is the first order derivative of $\phi(\omega)$ evaluated at $\omega = \omega_0$ and so on. The terms can be used to describe the behaviour of a pulse in a dispersive medium.

The first two terms do not affect the pulse profile. The term ϕ_0 is a phase delay of the optical carrier and is related to the phase velocity of the pulse

$$v_\phi = \frac{\omega}{k} = L \frac{\omega}{\phi} \quad (1.18)$$

which is the speed at which the central carrier frequency travels through the medium. The second term gives the group velocity, v_g , which represents the speed at which the

pulse envelope will travel through the medium

$$v_g = \frac{d\omega}{dk} = L \frac{d\omega}{d\phi} \quad (1.19)$$

However the quadratic spectral phase, ϕ'' , in the third term is related to the first derivative of the group velocity, the group velocity dispersion (GVD) which leads to spectral broadening. Mathematically these quantities are related by

$$GVD = \frac{dv_g}{d\omega} = \frac{\omega^2 v_g^2 \phi''}{2\pi c L} \quad (1.20)$$

For most materials the value of GVD is positive at near infrared wavelengths, resulting in some degree of broadening of unchirped or positively chirped pulses (and acting against the chirp of negatively chirped pulses). Higher order terms (ϕ''' , ϕ'''' etc.) result in more complex pulse distortion.

It is possible to control pulse distortion accumulated on propagation through a dispersive medium by use of a material possessing different dispersive properties. For example, in an optical cavity pulses may be passed through glass prisms in order that the net dispersion in the cavity, arising from the prisms, together with the crystal and other optical elements, can be controlled (as described in section 1.3.4).

1.3.5 Nonlinear effects

In an intense electromagnetic field the higher order susceptibilities become significant. In some circumstances the resultant nonlinear effects may be exploited to practical advantage, in others it is desirable to minimise them. In any case, it is unavoidable that nonlinearities will be manifested when working with intense optical fields. Those relevant to this project are reviewed here.

Second order processes

The $\chi^{(2)}$ term has zero effect in centrosymmetric crystalline materials due to the high degree of symmetry in their structure [45]. In non-centrosymmetric crystals, this term gives rise to an induced polarisation which is weak, but can under sufficiently intense optical fields, give rise to the generation of new wavelengths. These $\chi^{(2)}$ non-resonant nonlinear processes include difference-frequency mixing in which the frequencies are

related by

$$\omega_3 = \omega_1 - \omega_2 \quad (1.21)$$

and second harmonic generation (SHG) in which the generated frequency is simply twice the input frequency according to

$$\omega_2 = \omega_1 + \omega_1 = 2\omega_1 \quad (1.22)$$

and the intensity of the generated signal is related to the square of incident intensity, I_ω , by

$$I_{2\omega}(L) = \frac{(2\omega)^2 |\chi^{(2)}|^2}{8\epsilon_0 c^3 n_\omega^2 n_{2\omega}} I_\omega^2 L^2 \text{sinc}^2 \left(\frac{\Delta L}{2} \right) \quad (1.23)$$

where L is the length of propagation through the material.

In this project these effects are exploited in the optical sources, (Chapter 3 details how optical parametric generation is used to produce pulses in the infrared wavelength range) and in diagnostics, where SHG is used for the measurement of the pulse durations (see section 3.5.2).

Third order processes

The third order susceptibility, $\chi^{(3)}$, is correspondingly related to third harmonic generation. In the context of this work however, the most evident effects of $\chi^{(3)}$ are on nonlinear propagation. Indeed in non-centrosymmetric crystals, for which $\chi^{(2)}$ is zero, the nonlinear polarisation response is dominated by $\chi^{(3)}$.

Nonlinear refractive index

In general, in the nonlinear regime, the refractive index can be expressed in the form

$$n = n_0 + \Delta n \quad (1.24)$$

where the index change, Δn is dependent on the electromagnetic field.

The Optical Kerr Effect

The real part of $\chi^{(3)}$ gives rise to a nonlinear refractive index change

$$\Delta n = \frac{3\text{Re}\chi^{(3)} E^2}{8n_0} = n_{2E} E^2 \quad (1.25)$$

where n_{2E} is in units of m^2V^{-2} [45]. Usually this effect requires electric field strengths that are extremely high ($> 100kVcm^{-1}$). However the electric field associated with a short optical pulse may be sufficiently large for a significant refractive index change to occur. It is convenient to define the index change with respect to the optical intensity

$$\Delta n = n_{2I}I(t) \quad (1.26)$$

where $I(t)$ represents the intensity profile of the pulse and $n_{2I} = \frac{3Re\chi^{(3)}}{4\epsilon_0n_0^2c}$ in units of m^2W^{-1} [45].

Self-phase modulation

Time and spatially dependent phase changes associated with the refractive index changes can have distorting effects on the optical pulse itself [46] [47]. The phase shift due to the Kerr effect may be expressed

$$\Delta\phi(t) = \frac{2\pi L\Delta n}{\lambda} = \frac{2\pi Ln_{2I}I(t)}{\lambda} \quad (1.27)$$

where L the propagation length through the material. Under these circumstances a pulse is imposing a change on itself, an effect called self-phase modulation. The time dependent phase change corresponds to an instantaneous frequency change of

$$\Delta\omega = -\frac{d\phi(t)}{dt} = -\frac{2\pi Ln_{2I}}{\lambda} \frac{dI(t)}{dt} \quad (1.28)$$

Where n_{2I} is positive, the resultant pulse is spectrally broadened. Experienced together with non-zero GVD, the temporal duration of a pulse may be significantly broadened or shortened [45] [48].

Absorption and gain

In addition to the pulse shaping effects described, the resonant nonlinearities associated with absorption and gain saturation are also due to $\chi^{(3)}$ and higher order susceptibilities. Absorption and gain processes in semiconductors are discussed Chapter 2.

1.4 Summary

In this chapter, types of switching for future optical networks have been discussed. In particular, the principle of SOA-based interferometric switches, such as the Terahertz

Asymmetric Optical Demultiplexer (TOAD), have been described in detail and a range of issues that need to be addressed to enable the optimisation of these switches have been presented. Relative to other optical switches, such SOA-based switches have the potential to be operated at high repetition rates with ultrafast, low energy pulses. Following on from this, Chapter 2 introduces the semiconductor optical properties which underly the characteristics of SOAs to be exploited for such switching applications.

Also in this first chapter, a general description of optical pulse interactions with optical media have been presented, including linear and nonlinear propagation. This background is key to understanding the principles that underly the system for ultra-short optical pulse generation, described in Chapter 3, that is the source of pulses for experiments detailed in later chapters. In addition, concepts are introduced which are relevant to the description of semiconductor optical properties in Chapter 2 and the modelling of these properties, described in Chapter 5.

Bibliography for Chapter 1

- [1] S Kawanishi. Ultrahigh-speed optical time-division-multiplexed transmission technology based on optical signal processing. *IEEE J. Quantum Elect.*, 34(11):2064, 1998.
- [2] R J Manning, A D Ellis, A J Poustie, and K J Blow. Semiconductor laser amplifiers for ultrafast all-optical signal processing. *J. Opt. Soc. Am. B*, 14(11):3204–3216, 1997.
- [3] O Wada. Femtosecond semiconductor-based optoelectronic devices for optical-communication systems. *Opt. Quant. Electron.*, 32:453–471, 2000.
- [4] N J Doran and D Wood. Nonlinear-optical loop mirror. *Opt. Lett.*, 13(1):56–58, 1988.
- [5] M E Fermann, F Haberl, M Hofer, and H Hochreiter. Nonlinear amplifying loop mirror. *Opt. Lett.*, 15(13):752–754, 1990.
- [6] A W O’Neill and R P Webb. All-optical loop mirror switch employing an asymmetric amplifier/attenuator combination. *Electron. Lett.*, 26(24):2008–2009, 1990.
- [7] M Eiselt. Optical loop mirror with semiconductor laser amplifier. *Electron. Lett.*, 28(16):1505–1507, 1992.
- [8] M G Kane, I Glesk, J P Sokoloff, and P R Prucnal. Asymmetric optical loop mirror: analysis of an all-optical switch. *Appl. Optics*, 33(29):6833–6842, 1994.
- [9] D. Cotter. Nonlinear optics for future high-speed photonic networks. *Non Linear Optics*, 13:185, 1995.
- [10] M Eiselt, W Pieper, and H G Weber. SLALOM: Semiconductor laser amplifier in a loop mirror. *IEEE J. Lightwave Technol.*, 13(10):2099, 1995.
- [11] R J Manning, A E Kelly, A J Poustie, and K J Blow. Wavelength dependence of switching contrast ratio of semiconductor optical amplifier-based nonlinear loop mirror. *Electron. Lett.*, 34(9):916, 1998.
- [12] D Cotter, R J Manning, K J Blow, A D Ellis, A E Kelly, D Nasset, I D Phillips, A J Poustie, and D C Rogers. Nonlinear optics for high-speed digital information processing. *Science*, 286(5444):1523–1528, 1999.
- [13] M Eiselt, W Peiper, and H G Weber. All-optical high speed demultiplexing with a semiconductor laser amplifier in a loop mirror configuration. *Electron. Lett.*, 29(13):1167–1168, 1993.
- [14] St. Fischer, M Dülk, E Gamper, W Vogt, W Hunziker, E Gini ad H Melchior, A Buxens, H N Poulsen, and A T Clausen. All-optical regenerative OTDM add-drop multiplexing at 40 Gb/s using monolithic InP Mach-Zender interferometer. *IEEE Photonic. Tech. L.*, 12(3):335–337, 2000.
- [15] K Tajima. All-optical switch with switch-off time unrestricted by carrier lifetime. *Jpn. J. Appl. Phys.*, 32 Part 2(12A):L1746–L1749, 1993.
- [16] R J Runser, D Zhou, C Coldwell, B C Wang, P Toliver, K L Deng, I Glesk, and P R Prucnal. Interferometric ultrafast SOA-based optical switches: from devices to applications. *Opt. Quant. Electron.*, 33:941–874, 2001.

- [17] K I Kang, T G Chang, I Glesk, and P R Prucnal. Comparison of Sagnac and Mach-Zender ultrafast all-optical interferometric switches based on semiconductor resonant optical nonlinearity. *Appl. Optics*, 35(3):471–426, 1996.
- [18] S Bischoff, A Buxens, St Fisher, M Dülk, A T Clausen, H N Poulsen, and J Mørk. Comparison of all-optical co- and counter-propagating high-speed signal processing in SOA-based Mach-Zender interferometers. *Opt. Quant. Electron.*, 33:907–926, 2001.
- [19] K Tajima, S Nakamura, and Y Ueno. Ultrafast all-optical signal processing with symmetric Mach-Zender type all-optical switches. *Opt. Quant. Electron.*, 33:875–897, 2001.
- [20] K Tajima, S Nakamura, and Y Sugimoto. Ultrafast polarization-discriminating Mach-Zender all-optical switch. *Appl. Phys. Lett.*, 67(25):3709–3711, 1995.
- [21] N A Patel, K A Rauschenbach, and K L Hall. 40-GB/S demultiplexing using an ultrafast nonlinear interferometer (UNI). *IEEE Photonic. Tech. L.*, 8(12):1695, 1996.
- [22] Y Ueno, S Nakamura, K Tajima, and S Kitamura. 3.8 thz wavelength conversion of picosecond pulses using a semiconductor delayed-interference signal-wavelength converter (DISC). *IEEE Photonic. Tech. L.*, 10(3):346–348, 1998.
- [23] I D Philips, A D Ellis, H J Thiele, R J Manning, and A E Kelly. 40 gbit/s all-optical data regeneration and demultiplexing with long pattern lengths using a semiconductor nonlinear interferometer. *Electron. Lett.*, 34(24):2340, 1998.
- [24] K Chan, C-K Chan, W Hung, F Tong, and L K Chen. Waveform restoration in semiconductor optical amplifier using fibre loop mirror. *IEEE Photonic. Tech. L.*, 14(7):905–997, 2002.
- [25] J Leuthold. Signal regeneration and all-optical wavelength conversion. In *IEEE/LEOS Annual Meeting Conference Proceedings*, volume 2, pages 107–108. IEEE/LEOS, IEEE, November 2002.
- [26] K E Stubkjaer. Semiconductor optical amplifier-based all-optical gates for high-speed optical processing. *IEEE J. Sel. Top. Quant.*, 6(6):1428–1435, 2000.
- [27] A J Poustie, K J Blow, and R J Manning. All-optical regenerative memory for long term data storage. *Opt. Commun.*, 140:184–186, 1997.
- [28] M Gustavsson, B Lagerström, L Thylén, M Janson, L Lundgren, A-C Möörner, M Rask, and B Stoltz. Monolithically integrated 4 X 4 InGaAsP/InP laser amplifier gate switch arrays. *Electron. Lett.*, 28(24):2223–2225, 1992.
- [29] E Jahn, N Agrawal, W Pieper, H-J Ehrke, D Franke, W Fürst, and C M Weinert. Monolithically integrated nonlinear Sagnac interferometer and its application as a 20 Gbit/s all-optical demultiplexer. *Electron. Lett.*, 32(9):782–784, 1996.
- [30] V K Menon, W Tong, C Q Li, F Xia, I Glesk, P R Prucnal, and S R Forrest. Monolithically integrated sagnac interferometer for all-optical wavelength conversion. In *IEEE/LEOS Annual Meeting Conference Proceedings*, volume 2, pages 447–448. IEEE/LEOS, IEEE, November 2002.
- [31] D Zhou, K I Kang, I Glesk, and P R Prucnal. An analysis of Signal-to-Roise Ratio and design parameters of a Terahertz Asymmetric Demultiplexer. *IEEE/OSA J. Lightwave Technol.*, 17(2):298–307, 1999.

- [32] K L Hall and B S Robinson. Bit error rate characterisation of 100 gbit/s all-optical demultiplexers. In *Proceedings of IEEE Conference on Lasers and Electro-Optics*, 1999.
- [33] C Schubert, J Berger, S Diez, H J Ehrke, R Ludwig, U Feiste, C Schmidt, H G Weber, G Toptchiyski and S Randel, and K Petermann. Comparison of interferometric all-optical switches for demultiplexing applications in high-speed OTDM systems. *IEEE/OSA J. Lightwave Technol.*, 20(4):618–624, 2002.
- [34] S Diez, R Ludwig, and H G Weber. All-optical switching for TDM and WDM/TDM systems demonstrated in a 640 Gbit/s demultiplexing experiment. *Electron. Lett.*, 34(8):803–805, 1998.
- [35] G Toptchiyski, S Randel, K Petermann, S Diez, E Hilliger, C Schimidt, C Schubert, R Ludwig, and H G Weber. Analysis of switching windows in a gain-transparent-SLALOM configuration. *IEEE/OSA J. Lightwave Technol.*, 18(12):2188–2195, 2000.
- [36] A D Ellis and D M Spirit. Compact 40 gbit/s optical demultiplexer using a GaInAsP optical amplifier. *Electron. Lett.*, 29(24):2115, 1993.
- [37] K Suzuki, K Iwasuki, S Nishi, and M Saruwatari. Error-free demultiplexing of 160 gbit/s pulse signal using optical loop mirror including semiconductor laser amplifier. *Electron. Lett.*, 30(18):1501, 1994.
- [38] T Yamamoto, E Yoshida, and M Nakazawa. Ultrafast nonlinear optical loop mirror for demultiplexing 640Gbit/s TDM signals. *Electron. Lett.*, 34(10):1013–1014, 1998.
- [39] S Nakamura, Y Ueno, and K Tajima. Ultrafast (200fs switching, 150-Tb/s demultiplexing) and high-repetition (10 GHz) operation of a polarisation-discriminating symmetric Mach-Zender all-optical switch. *IEEE Photonic. Tech. L.*, 10(11):1575–1577, 1998.
- [40] T Yamamoto, E Yoshida, K R Tamura, K Yonenaga, and M Nakazawa. 640-Gbit/s optical TDM transmission over 92 km through dispersion-managed fiber consisting of single-mode fiber and "reverse dispersion fiber". *IEEE Photonic. Tech. L.*, 12(3):353–355, 2000.
- [41] R P Schrieck, M H Kwakernaak, H Jäckel, and H Melchior. All-optical switching at multi-100-Gb/s data rates with Mach-Zender interferometer switches. *IEEE J. Quantum Elect.*, 38(8):1053–1061, 2002.
- [42] K Tajima, S Nakamura, Y Ueno, J Sasaki, T Sugimoto, T Kato, T Shimoda, H Hatakeyama, T Tamanuki, and T Sasaki. Ultrafast hybrid-integrated symmetric Mach-Zender all-optical switch and its 168 Gbps error-free demultiplexing operation. *IEICE T. Electron.*, E83-C(6):959–956, 2000.
- [43] M Fox. *Optical Properties of Solids*. Oxford Master Series in Condensed Matter Physics. Oxford University Press, New York, 2001.
- [44] D H Jundt. Temperature-dependent Sellmeier equation for the index of refraction, n_e , in congruent lithium niobate. *Opt. Lett.*, 22(20):1553–1555, 1997.
- [45] P N Butcher and D Cotter. *The Elements of Nonlinear Optics*, volume 9 of *Cambridge Studies in Modern Optics*. Cambridge University Press, UK, 1990.
- [46] P L Kelley. Nonlinear index of refraction and self-action effects in optical propagation. *IEEE J. Sel. Top. Quant.*, 6(6):1259–1264, 2000.

- [47] Y R Shen. *The Principles of Nonlinear Optics*. Wiley, New York, 1984.
- [48] G P Agrawal and N A Olsson. Self-phase modulation and spectral broadening of optical pulses in semiconductor laser amplifiers. *IEEE J. Quantum Elect.*, 25(11):2297, 1989.

Chapter 2

Optical properties of semiconductor devices

2.1 Introduction

This chapter serves as an introduction to the type of device studied for this project and specifically to the active semiconductor material. The optical properties of semiconductor materials are introduced and the special properties of quantum confined structures (quantum wells and superlattices) are discussed. Lastly, the range of nonlinear interactions relevant to this project which can occur between light and semiconductor materials are summarised.

2.2 SOA device design

The device type studied in this project was the semiconductor optical amplifier (SOA). A schematic of the structure of a typical SOA is shown in figure 2.1. In the device studied, the optical guiding was provided by a confinement heterostructure detailed in section 4.2. Essentially the structure of the SOA is similar to that of a semiconductor heterostructure laser. However, the gain efficiencies in heterostructures can be so high, as discussed in section 2.4.2, that when such a structure is forward biased reflections from the cleaved facets alone can provide sufficient feedback for the device to lase. At low bias currents, below the threshold for lasing, such a device amplifies at the Fabry-Perot modes of the cavity and is called a Fabry-Perot amplifier (FPA). However, to access the amplification potential it is necessary to match the input signal with these resonances; this is a considerable disadvantage for applications [1]. If the cavity is

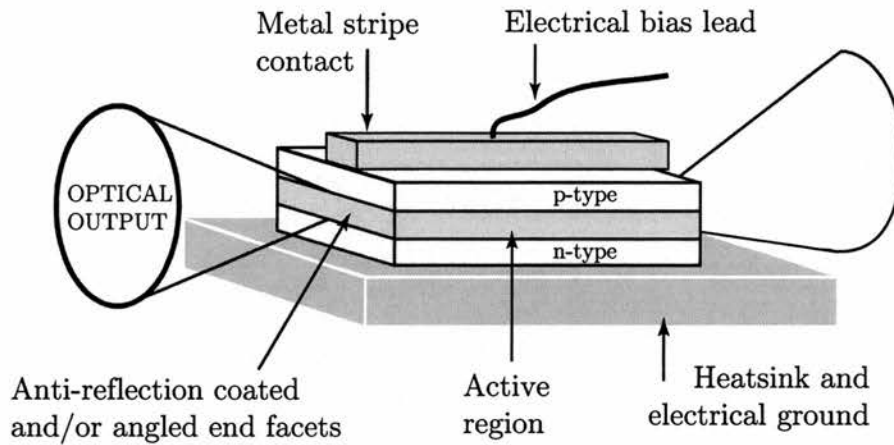


Figure 2.1: Schematic of the structure of an SOA

‘spoiled’ the light passes through the sample, extracting gain, only once. By contrast to the FPA, this regime of operation does not depend on resonating with cavity modes and has the advantage of offering gain over a broad bandwidth. In general ‘spoiling’ of the cavity is achieved by depositing anti-reflection coatings on the end facets of the sample and sometimes by cleaving the waveguide, from the as-grown wafer, at an angle. Such amplifiers are often called travelling wave amplifiers (TWA), however in this project the term SOA will be used to refer to this type of non-resonant amplifier, unless specified otherwise.

For the study of optical processes, waveguide devices have an advantage over thin samples in that, since effects can be cumulative with propagation distance, they enable sensitive measurements of nonlinearities in semiconductors. Moreover, SOAs are preferable to laser diode structures for several reasons [2]. Due to the inhibition of lasing, very high carrier densities can be achieved by injection, without the level being clamped by laser action. Under these conditions effects may be stronger and more readily observed. In addition, the carrier density dependence of dynamics can be readily investigated since the density can be changed without fundamentally changing the characteristics of the cavity. When feedback from end facets is successfully suppressed (i.e. no cavity), there are no standing wave effects within the device and periodic gain depletion (spatial hole burning) is avoided. Also under these conditions no interference occurs between multiple trips of the optical beams, which are being used to investigate

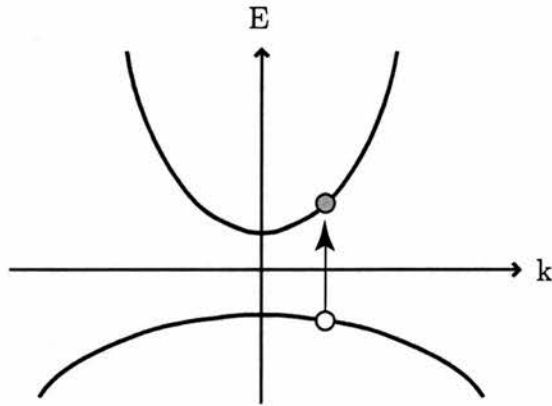


Figure 2.2: Schematic of dispersion relations for near the top of the valence band and the bottom of the conduction band. The promotion of an electron from the valence to the conduction band creates a hole in the valence band.

optical properties of the device. All these factors associated with SOAs are desirable in that they avoid what could be further complications in the interpretation of data.

The device structure investigated in this project contained multiple quantum wells. A benefit of using a QW device is that, compared to bulk materials, high gain is associated even with levels at the bottom of the band, due to the step like nature of the density of states, as discussed in section 2.6.2. Secondly, since the band gap of the material is dependent on the thickness of the quantum wells, the operating wavelength region may be chosen (within a certain range) at the growth stage. In this case, due to the intense current interest in SOAs for telecommunications application, the device focused on was one optimised for operation in the $1.55 \mu\text{m}$ region. The active material was a QW superlattice in which the barriers were strained material; a design that helped to minimise to some degree the polarisation dependence of the device, as discussed in section 2.8 and further detailed in Chapter 4. Additionally, some measurements were made on a device active in the other optical fibre window, $\sim 1.3 \mu\text{m}$.

2.3 Semiconductor basics

The behaviour of semiconductor materials is dominated by electrons in states near the bottom of the conduction band and the top of the valence band, where the terms conduction and valence band refer to the lowest unoccupied states and the highest occupied states at absolute zero, respectively. For states close to these minima

and maxima in energy, the dispersion curve, $E(k)$, can be taken to be parabolic, to a reasonable approximation, see figure 2.2. Under this assumption, the energies for the conduction and valence bands respectively can be expressed as

$$E(k) = E_G + \frac{\hbar^2 k^2}{2m_e} \quad (2.1)$$

$$E(k) = -\frac{\hbar^2 k^2}{2m_h} \quad (2.2)$$

where E_G is the energy gap and the zero of potential energy is taken to be the top of the valence band. Comparing these equations, 2.1 and 2.2, with the energy of a free electron, the masses m_e and m_h can be seen to correspond to the effective masses of the particles in the conduction and valence bands respectively [3]. In the case of the conduction band the electrons behave like free particles with a positive mass, m_e , a modified, effective electron mass. By the same reasoning, the valence band is taken to be occupied by particles of negative mass equal to m_h . These fictitious particles, corresponding to the vacancies left by absent electrons, are referred to as holes. (Note that this convention facilitates calculations of the properties of semiconductors, by contrast to the difficulty of working with the total distribution of electrons at lower energies.)

2.3.1 Interband transitions

The transition of an electron from the valence to the conduction band corresponds to an energy change of

$$\Delta E = E_G + \frac{\hbar^2 k_e^2}{2m_e} - \left(-\frac{\hbar^2 k_h^2}{2m_h} \right) \quad (2.3)$$

This transition can occur due to the absorption of a photon of energy $\hbar\omega_{\text{photon}} = \Delta E$, to satisfy the conservation of energy condition. In addition, momentum must be conserved. The photon momentum is very small, and for a vertical transition, as shown in figure 2.2, $k_e \approx k_h$, hence the momentum condition can readily be satisfied and strong absorption can occur. Transitions involving significant changes of momentum, require the contribution of lattice vibrations, phonons, and hence are less likely. In semiconductors where the maxima of the valence band and minima of the conduction band do not occur at the same value of k , this type of diagonal transition (requiring a

momentum change) is necessary even for the lowest energy transitions. Consequently, in these so-called indirect band gap materials, the onset of absorption (with increasing photon energy) is less strong. In general, the process of absorption results in the generation of an electron-hole pair; an electron in the conduction band and a hole in the valence band.

A transition in the opposite sense can occur if there are holes in the valence band and electrons excited to the conduction band. This process, recombination, results in the loss of an electron-hole pair. It can occur by a variety of mechanisms including transitions via impurity states (discussed in the following paragraph) and at surfaces. In some cases, so-called radiative recombination, the energy liberated is emitted as a photon, where $\hbar\omega_{\text{photon}} = \Delta E$. In non-radiative recombination the energy contributes towards the temperature of the system. In general following optical absorption or some other excitation process, the distribution of the electrons and holes evolves towards a steady state by interband recombination at a rate characteristic of the particular system (see section 2.9.1).

Impurities (or dopants) can be added to semiconductor materials by substitution. For example if arsenic is added to molten germanium, when it crystallises, some positions normally occupied by a germanium atom are taken by arsenic atoms. The net result of adding impurities is two fold. Firstly there are extra energy levels just above the valence band and just below the conduction band edges, so-called impurity states. Secondly there may be excess electrons or holes, such that the material is no longer neutral. Material in which the number of electrons exceeds the number of holes is known as n-type and where the converse is true it is called p-type.

The application of an electric field across the material corresponds to injection of electrons and holes; they move in opposite directions and the net movements of these particles, collectively usually called carriers, corresponds to the flow of electrical current.

2.3.2 Fermi distributions and bulk density of states

The number of carriers at a particular energy is given by the combination a Fermi distribution and the density of states in the conduction and valence bands (for this

form of description of a semiconductor see for example [4], and references therein). Specifically, the probability of an energy state, E , being occupied is given by the Fermi function,

$$f(E) = \frac{1}{e^{\frac{E-E_F}{k_B T}} + 1} \quad (2.4)$$

where E_F is the Fermi level energy, which corresponds to the chemical potential for temperature, T , and adjusted for the total number of carriers. The density of states per unit volume for the conduction and valence band, respectively are

$$\rho(E) = \frac{1}{2\pi^2} \left(\frac{2m_e}{\hbar^2} \right)^{\frac{2}{3}} (E - E_G)^{\frac{1}{2}} \quad (2.5)$$

and

$$\rho(E) = \frac{1}{2\pi^2} \left(\frac{2m_h}{\hbar^2} \right)^{\frac{2}{3}} (-E)^{\frac{1}{2}} \quad (2.6)$$

The number of electrons per unit volume in the conduction band can be calculated by making the sum of the density of electrons across all states weighted by the corresponding Fermi functions

$$n = \int_{E_G}^{\infty} f(E)\rho(E)dE \quad (2.7)$$

Substituting in equations 2.4 and 2.5, and considering that for an electron in the conduction band $(E - E_F) \gg k_B T$, an approximate analytical expression of equation 2.7 may be obtained

$$n = N_C e^{\frac{E - E_F}{k_B T}} \quad (2.8)$$

where

$$N_C = 2 \left(\frac{2\pi m_e k_B T}{h^2} \right) \quad (2.9)$$

The value of N_C corresponds to the effective number of levels per unit volume there would be were they all concentrated at the bottom of the conduction band i.e. $E = E_G$.

Correspondingly, the number of holes per unit volume may be approximated by

$$p = N_V e^{\frac{-E_F}{k_B T}} \quad (2.10)$$

where

$$N_V = 2 \left(\frac{2\pi m_h k_B T}{h^2} \right) \quad (2.11)$$

These approximations, equations 2.8 and 2.10, enable us to visualise the distribution of the carriers as a function of energy and the changes in this distribution due to

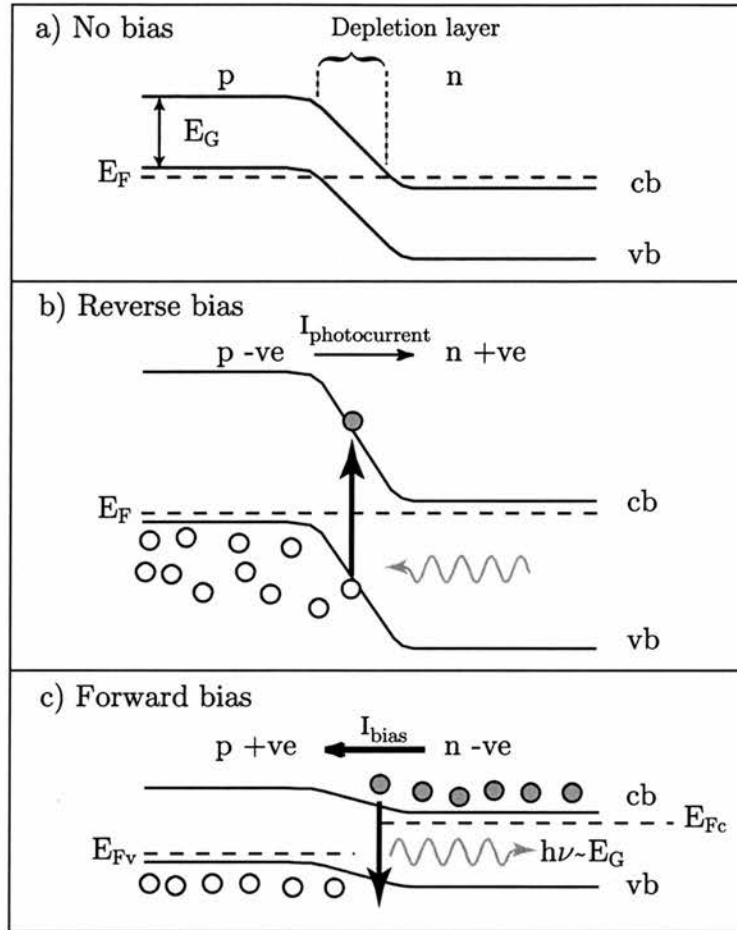


Figure 2.3: Schematic of a p-n junction, unbiased (a), reverse biased (b) and forward biased (c).

temperature changes. This proves to be important in the understanding of the dynamical properties of a semiconductor material under excitation.

2.4 Semiconductor devices

2.4.1 The p-n junction

At the core of the useful behaviour of devices, such as the SOAs studied in this thesis, is the concept of a p-n junction, a boundary where n-type and p-type materials are brought together. Under equilibrium conditions, electrons will travel from the n-type material into the p-type where they recombine with holes, with the result that there is a region near the interface with very few carriers, the so-called depletion layer. The electron energy level on the n side becomes lower and on the p side higher, as illustrated

in figure 2.3 (a). It follows that, to achieve a uniform chemical potential, there is a potential difference across the interface.

A p-n junction can be electrically biased by applying an additional potential difference across it. Where the positive connection is applied to the n side, the junction is said to be reverse biased, as shown schematically in figure 2.3 (b). In this case, there is little net flow of current. If however electron-hole pairs are created near the interface they are swept away from this central region and appear as an increased current flow. In this regime, a p-n junction may be used as an optical detector, since if incident photons excite electrons from the valence band to the conduction band, an electron-hole pair is created and this is detectable as current ($I_{photocurrent}$).

On the other hand, if an electrical bias is applied in the opposite sense, with the positive side applied to the p region, as shown in figure 2.3 (c), a net current readily flows (I_{bias}). This achieves the injection of electrons into the p-type region and holes into the n-type. These excess carriers recombine and, if they do so by a radiative mechanism, photons are emitted. When radiative recombination is prevalent the junction is acting as a light source, such as in light emitting diodes.

It is possible to forward bias a junction to a sufficient degree that a population inversion is achieved. A photon propagating through this region is more likely to cause recombination, resulting in the stimulated emission of a second, coherent photon, than to promote one of the valence band electrons and be absorbed. Consequently, the junction amplifies an incident optical field; in this regime, the junction is said to be operating in gain. Further more, if this process occurs in a cavity such that, rather than escaping from the system, generated photons are reflected back into the junction region, the coherent photon amplitude increases. This type of system with feedback and emitting coherent photons is a p-n junction laser.

2.4.2 Heterostructures

In a simple p-n junction, it is possible to achieve gain, but very high applied electrical biases are required. The development of techniques for fabricating semiconductor materials, such as molecular beam epitaxy (MBE), have made it possible to vary the composition of a sample on atomic scales. In particular it became possible to grow

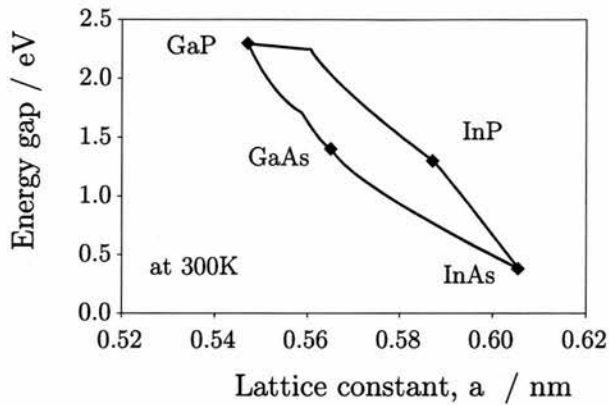


Figure 2.4: A map of lattice constants and the corresponding energy gaps for the III-V semiconductors used in the SOA

alternating layers of different compositions, so-called heterojunctions, where the layer thicknesses were as small as some hundreds of nanometres [5].

The most dramatic benefit of a heterostructure, over the basic p-n junction concept, is the addition of optical and electrical confinement. Optical waveguiding is achieved by the central semiconductor layer having a higher refractive index than the layers above and below, the cladding regions. The fact that band gap and refractive index usually are inversely related, results in there also being potential barriers at the material interfaces where there is an index change. Consequently, the lower index cladding layers also tend to confine the electrically injected carriers to the same region as the optical field; the so-called active region of the device.

The injected carriers and the optical field can additionally be confined in the lateral direction by etching away the sides of the waveguide to realise a narrow raised bar (a ridge waveguide), and by tailoring the shape of the electrical contact into a narrow metal stripe.

With these improved structural properties, forward biased heterojunctions can have much higher gain efficiencies by comparison with the simple p-n homojunctions. This is evident, for example, from the fact that heterojunctions tend to have much lower threshold currents for lasing. Indeed the devices lase very readily, with more than sufficient feedback for lasing obtained from reflection only from the cleaved facets of the material sample itself. Consequently, as mentioned in section 2.2, to ensure that an

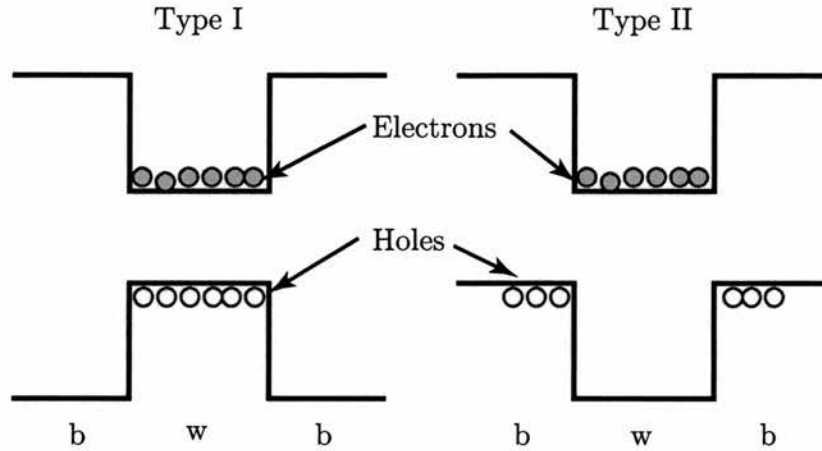


Figure 2.5: Band structure for a) type I heterostructures with the electrons and holes both localised in the well and b) type II heterostructures with the electrons and holes localised in the well and the barrier respectively

SOA is a single pass amplifier it is necessary to obstruct this feedback by the addition of antireflection coatings or cleaving angled facets.

Physically, the growing of one crystal composition directly on another, relies on identifying compositions in which the mismatch between lattice dimensions is not too severe. Too great a difference between the lattice constants results in dislocations in the crystal and may cause the sample to fracture. Figure 2.4 is a map of lattice constants and energy gaps for the III-V semiconductors used in the SOA investigated in this project. The device structure is grown from various compositions of these four elements (as detailed in section 4.2): the substrate is InP and the active region is composed of quantum wells and barrier layers of different compositions of InGaAs. Even slight mismatch between the lattice constants of adjacent layers causes strain and the implications of this are discussed in section 2.8.

In a heterostructure, the electrons and holes can be localised either in the same material layer, so called Type I heterostructures or in different layers, Type II structures, as shown in figure 2.5. The spatial separation of electrons and holes in Type II heterostructures results in greater tunability of the optical properties of the material, however the properties of are still poorly understood and further experimental studies are required [5].

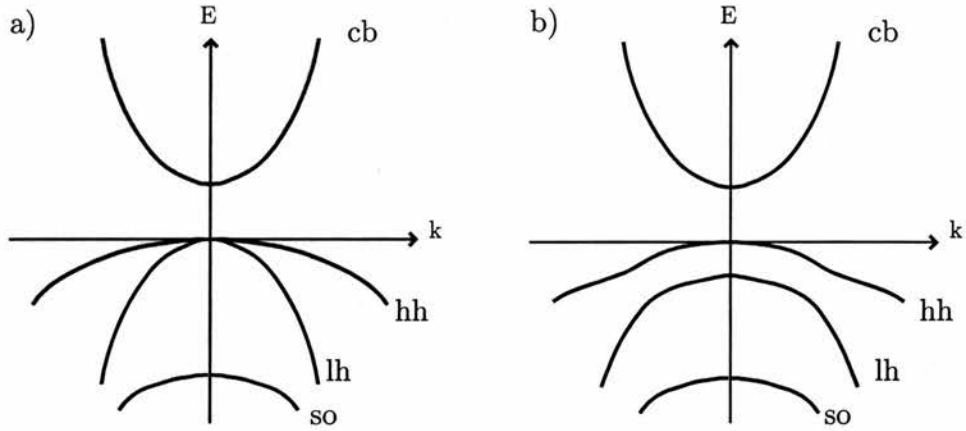


Figure 2.7: Schematic of the band structure of a direct gap III-V material near $k=0$, for (a) a bulk and (b) a QW structure. In both cases there are four bands, the conduction band, and three valence bands: the heavy hole (hh), the light hole (lh) and the split-off hole (so) bands. The degeneracy of the hh and lh bands around $k = 0$ in the bulk material is lost in the case of the QW.

light hole are degenerate at $k = 0$. Moreover, whilst the split-off band has influence on the calculation of optical properties, such as the gain, it lies at significantly lower energy than the light hole and heavy hole bands. It is transitions involving the light and heavy hole and the conduction bands which are of most relevance to the dynamic optical properties investigated in this project.

2.6 Quantum wells

Advances in the methods of growing semiconductor samples have made it possible to reduce the thickness of adjacent layers of semiconductor to such a degree that the properties of the material become affected by quantisation. Quantum well (QW) structures, are composed of a sandwich of layers some tens of angstroms thick.

As in the bulk heterostructures, the electrons and holes in quantum wells may be localised in different layers (as shown in figure 2.5). In general with regards to the designing of a device, the carriers are confined to the region of the quantum layers. It is desirable also to confine the optical field to this active region, this can be achieved by careful engineering of the structure. The confinement geometry used for the device studied for this work is detailed in section 4.2.

More fundamentally however, the material properties of these two dimensional

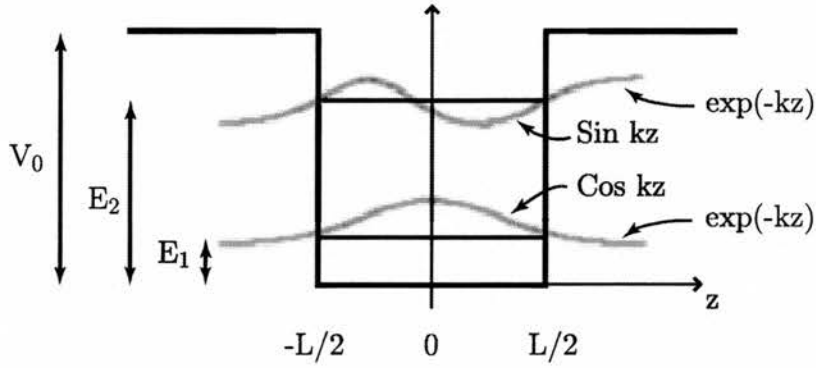


Figure 2.8: The energy levels and wavefunctions for the first two bound states in a quantum well

(2D) structures are significantly modified with respect to a three dimensional (3D) material. This is, for example, reflected in the band structure: the degeneracy of light and heavy hole valance bands that can be seen in bulk semiconductors is lost in 2D confined systems (illustrated in figure 2.7).

2.6.1 Energy levels in a quantum confined system

The condition necessary for quantum behaviour is that the motion of the electrons is restricted in (at least) one dimension to a distance comparable to or smaller than the Bohr radius of the electron-hole pair. The result is that that the electron and the hole behave like standing waves, as if they were trapped in a box. This can be understood by considering the wavefunction of a particle in a box and its solutions.

For one dimension, Schrödinger's equation may be written

$$\frac{-\hbar^2}{2m^*} \frac{\partial^2}{\partial z^2} \Psi_n(z) + V(z)\Psi_n = E_n \Psi_n(z) \quad (2.12)$$

where Ψ is the wavefunction of the particle, m^* is the effective mass and $V(z)$ is potential. For the simplest case of an infinite square well potential, the solutions for wave functions and the energy levels are of the form

$$\Psi_n = \sqrt{\frac{2}{L}} \sin \frac{n\pi z}{L_z} \quad (2.13)$$

and

$$E_n = \frac{-\hbar^2}{2m^*} \left[\frac{n\pi}{L_z} \right]^2 \quad (2.14)$$

where n is a positive integer.

However, in a real semiconductor QW structure the barriers are not infinite. Consequently, the wavefunctions penetrate into the barrier regions, exponentially decaying with distance away from the edge of the well, as illustrated schematically in figure 2.8. The solution of equation 2.12 for a finite potential, V_0 , is obtained by applying continuity conditions. The following transcendental equations are obtained

$$\frac{k}{m_a^*} \tan\left(\frac{kL}{2}\right) = \frac{K}{m_b^*} \quad (2.15)$$

$$\frac{k}{m_a^*} \cot\left(\frac{kL}{2}\right) = -\frac{K}{m_b^*} \quad (2.16)$$

where k_a^* and k_b^* are the effective masses in the confined well and the barrier regions respectively, $k^2 = 2m_a^*/\hbar^2(E_n - V_0)$ and $K^2 = 2E_n m_b^*/\hbar^2$. Since no analytical solution exists to these equations, solutions are found numerically or graphically.

Note that in the plane of the layers the electrons are not affected by the confinement. Consequently, the behaviour of electrons in the plane is similar to that in the bulk and so near $k=0$, under the parabolic approximation, the electron energies in the conduction band are of the form

$$E_{x,y}(k) = \frac{\hbar^2(k_x^2 + k_y^2)}{2m_a} \quad (2.17)$$

In QW materials, in addition to the valence light and heavy hole bands ceasing to be degenerate at $k = 0$, the bands are non-parabolic. This structure near $k = 0$ is commonly described by the Luttinger Hamiltonian [6] [7]. The nonparabolicity of the bands is due to the strong coupling between heavy hole and light hole. The main effects on the band structure of confinement of the carriers can be seen by comparing schematics of a band structure for a QW structure, figure 2.7 (b) with that for bulk material (a) (both schematics being typical for direct III-V materials).

2.6.2 QW density of states

The quantum confinement also causes the density of states to be modified with respect to that for a 3D material (given by equation 2.5). The density of states for a quantum well is expressed as

$$\rho(E) = \frac{nm^*}{\pi\hbar^2} \quad (2.18)$$

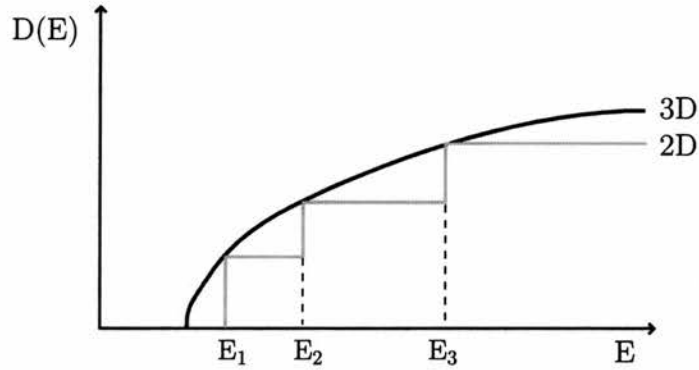


Figure 2.9: Schematic of the 2D and 3D density of states functions

where n is a positive integer and m^* is the effective mass (of electron or hole). By contrast with the 3D case, the 2D density of states does not depend on energy, nor does it depend on the thickness of the layers in the quantum well. For comparison, the 2D and 3D densities of states are shown schematically in figure 2.9.

2.6.3 Superlattices

In quantum well systems it is usually the case that the barriers are sufficiently broad that there is no significant coupling between the QW layers and the quantised levels are well defined in energy. However, in the limit of very thin barriers, down to a thickness of only a few monolayers, the density of states changes significantly from that of an ideal 2-D system [8]. In particular, as the distance between wells is reduced, the overlap of the wavefunctions increases with the result that the levels are broadened into bands [9]. Therefore the properties of a such a superlattice structure can be significantly different from an ideal QW material i.e. one in which the wells are spatially separated. Indeed in some respects a superlattice structure may appear more like a continuous bulk material.

Results presented this thesis, in Chapter 4, illustrate a Type II optical transition that is strong, contrary to what might be expected. The transition is indeed Type II in nature in the sense that it is between energy levels derived from different material layers (as illustrated in figure 2.5). However the active material in the SOA is a superlattice, the layers being thin, so the position of the carriers is not well defined. Hence it could be said that the transition is less strictly Type II and that, in this context, a strong transition

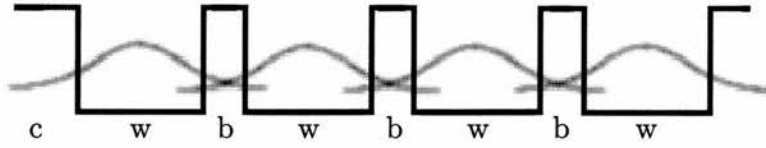


Figure 2.10: In a superlattice the barrier layers are so narrow that there is significant overlap between the wavefunctions in adjacent wells

is less surprising.

2.7 Optical transitions

The rates at which optical transitions occur can be expressed mathematically using Fermi's golden rule in terms of the densities of states in the semiconductor and the matrix element for the transition in question. Specifically, the probabilities of particular interband transitions actually occurring, between conduction and valence band states, are determined by the degree of overlap of the conduction and valence band wavefunctions. For a transition to occur the overlap integral between two states must be non zero.

Selection rules describing which optical transitions are allowed and the relative strengths of the allowed transitions can be derived from the matrix elements (see for example [10] and [11]). In general, from an initial state, i , to a final state, f , the matrix element is of the form

$$M = \langle f | r \cdot \eta | i \rangle = \int_{-\infty}^{\infty} \Psi_f(r) \Psi_i(i) d^3r \quad (2.19)$$

where η is the polarisation vector associated with the electromagnetic wave.

For an infinite well only transitions between states with the same quantum number would be allowed, due to the orthogonality of the wavefunctions. However in a real material, with a finite quantum well, this condition does not hold rigidly: whilst transitions for which $\Delta n = 0$ remain the strongest observed transitions, those for which $\Delta n \neq 0$ have finite probabilities of occurring.

In addition, to deduce the selection rules, the electric-dipole matrix element is considered. This indicates the possibility of a transition between two given states with the

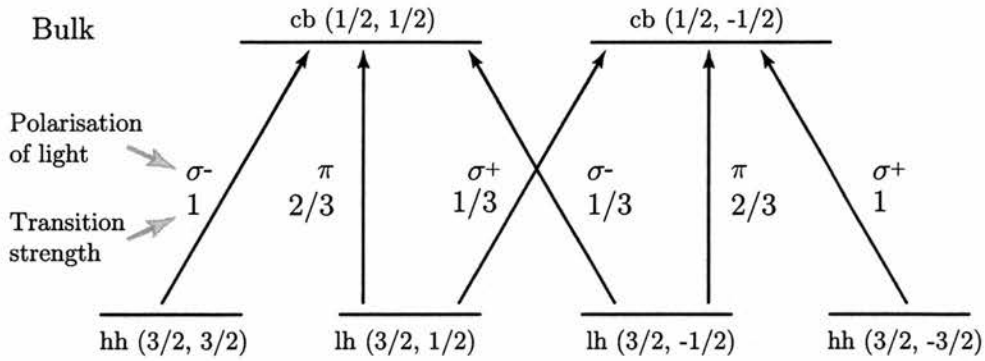


Figure 2.11: The selection rules for bulk GaAs. The transition probabilities are shown beside the corresponding transition.

required induced dipole; the polarisation direction of the absorption or radiation that may occur necessarily being related to the orientation of this dipole (see for example [12]).

Figure 2.11 illustrates the selection rules for bulk GaAs. Right and left circularly polarised light are indicated by σ^+ and σ^- respectively, and π represents linear polarisation. The optical absorption strengths of different possible transitions are indicated on the diagram.

2.7.1 Polarisation and QW selection rules

In 3-D bulk isotropic semiconductors x , y and z directions are equivalent. By contrast in 2-D materials such as quantum wells, whilst x and y remain equivalent, the z direction is different. Electrons and holes in the same subband have the same k_z wavevector and hence, in effect, the associated oscillator strength is ‘concentrated’ compared to the 3-D case. The lower dimensionality of the quantum well does not increase the oscillator strength per electron-hole pair, rather the effect of the confinement is manifested in polarisation dependence of certain transitions [13], as indicated in figure 2.12.

For the case of an SOA structure, of the type that this thesis is concerned with, the propagation of light is parallel to the layers of the quantum wells. According to the selection rules, the heavy hole transition can only occur with light polarised parallel to the layer i.e. the TE mode (which is the horizontal polarisation in a horizontal waveguide). By contrast, the light hole transitions are allowed for both linear polarisations

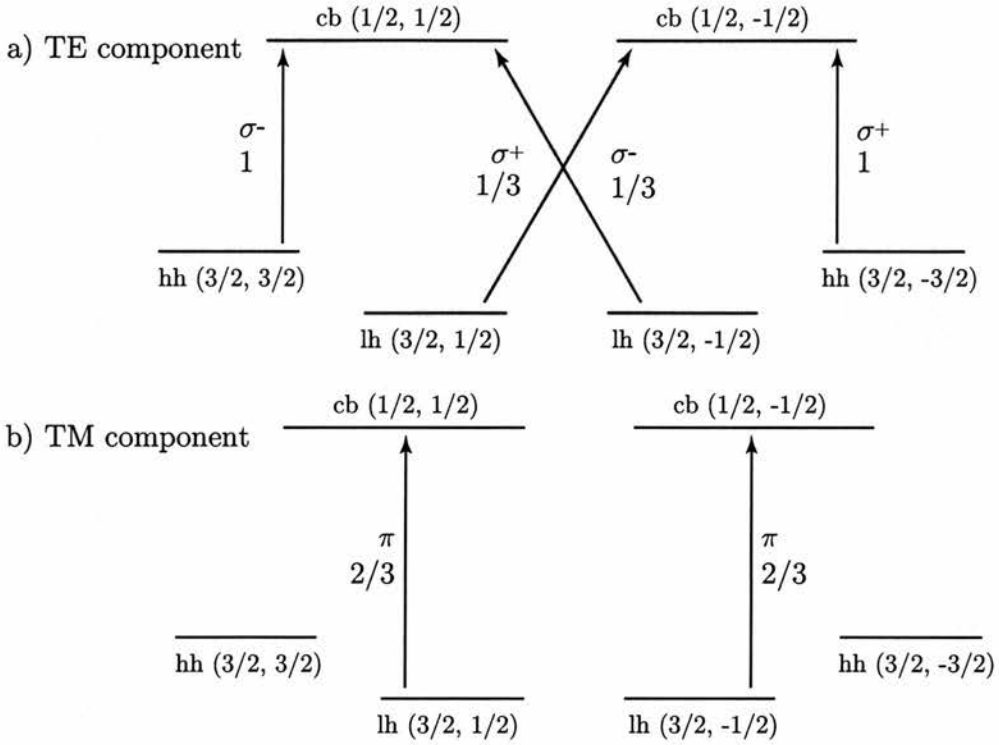


Figure 2.12: The selection rules for QW GaAs with the light propagating parallel to the QW layers for the cases where the optical field has components of (a) TE and (b) TM polarisations. Note that circularly polarised light can be considered to be composed of linear components.

of the light i.e TE and TM modes.

However the relative strengths of the heavy hole and light hole transitions are not reliably determined by simple analysis [9]. Indeed, the way in which these processes are manifested in the polarisation dependence of the optical properties of complex semiconductor structures merits investigation. Throughout the experiments reported in this thesis measurements with linear polarised light revealed polarisation dependence and the results are discussed in Chapters 4, 6 and 7.

2.7.2 Absorption and gain

In general, optical transitions may be associated with carrier generation (following optical absorption) or light generation (due to carrier recombination). Henry, using a derivation similar to that used by Einstein to derive his coefficients for transitions in a two level system, derived expressions for emission and absorption in semiconductors [14]. The key principle in this derivation being that emission and absorption processes

must lead to the same equilibrium values for optical density and population levels as determined by statistical mechanics. The net absorption rate between state 1 (in the valence band) and state 2 (in the conduction band) is the difference between the rate of transitions upwards and downwards in energy. This is given by

$$\alpha(E_{21}) = \frac{\text{Rate}_{12}(f_1 - f_2)}{c/n} \quad (2.20)$$

where f_j is the Fermi probability of state j being occupied.

By consideration of the matrix elements, relevant statistical factors and continuity conditions, absorption in a bulk semiconductor can be expressed as

$$\alpha_B = \alpha_{b0} \langle |p_{cv}|^2 \rangle (\hbar\omega - E_G)^{\frac{1}{2}} \quad (2.21)$$

where $\langle |p_{cv}|^2 \rangle$ is the average of the squared matrix element for transition rates between conduction and valence bands and

$$\alpha_{b0} = \frac{e^2 (2\mu)^{\frac{3}{2}}}{2\pi\epsilon_0 c n m_0^2 \hbar^3 \omega} \quad (2.22)$$

where $\mu^{-1} = m_e^{-1} + m_h^{-1}$ is the reduced mass [4]. Note that this absorption, as expressed by equation 2.21, is proportional to the bulk density of states function.

Likewise for quantum wells absorption is related to the appropriate density of states function, so the expression for absorption includes the Heavyside step function, $H(x)$. The absorption spectrum in QW material is of the form

$$\alpha_{QW} = \alpha_{qw0} \langle |p_{cv}|^2 \rangle C_{mn} A_{mn} (f_h - f_e) H(\hbar\omega - E_{gmn}) \quad (2.23)$$

where C_{mn} accounts for selection rules, A_{mn} is the anisotropy factor for the quantum confined system and

$$\alpha_{qw0} = \frac{e^2 \mu}{\epsilon_0 c n m_0^2 \hbar^2 \omega L} \quad (2.24)$$

where L is the quantum well width [4]. Under k -conservation the Fermi function f_e , for electrons, is of the form

$$f(E) = \frac{1}{e^{\frac{E_n + \frac{\mu \hbar^2 k^2}{m_e} - E_F}{k_B T}} + 1} \quad (2.25)$$

where E_n is the energy of the n^{th} subband, and for holes the expression is similar (where an h is substituted for e) [4].

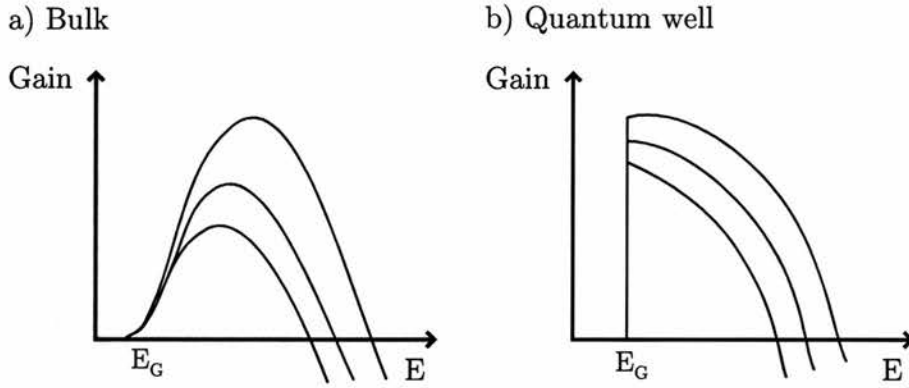


Figure 2.13: Schematic of ideal gain spectra (total gain for TE and TM modes) for (a) bulk and (b) QW laser structures

Absorption being defined as the rate of decrease of photon flux per unit distance in the direction of propagation, it follows that where the absorption coefficient is negative there is gain. From equation 2.20, this could be expected to occur when $f_2 > f_1$. Using the expressions for the Fermi probabilities, it can be shown that for gain, the photon energy, $\hbar\omega < E_{F_e} - E_{F_h}$ where E_{F_e} and E_{F_h} are the Fermi level energies in the conduction and valence band respectively. Also the gain threshold occurs for photon energies, $\hbar\omega = E_G$ i.e. at the band gap; in bulk material gain maxima occur at energies significantly away from the band gap, as illustrated in figure 2.13(a). Bringing these together, the condition for gain in semiconductors expressed by the Bernard-Durrafourg condition as

$$E_G < \hbar\omega < E_{F_e} - E_{F_h} \quad (2.26)$$

Analysis of the expression for absorption in quantum wells, equation 2.23, indicates that α is zero when $f_h = f_e$. Under the assumption that the injected electron and hole densities are equal, this condition is satisfied for a particular carrier density. For higher injected densities, $f_e > f_h$, and the Bernard-Durrafourg condition 2.26 is satisfied i.e. the material has been biased into gain. From examining equation 2.25, it can be deduced that the maximum of f_e and minimum of f_h occur at their respective subband edges [4]. This suggests that, in contrast to the bulk case, the QW maximum gain occurs at $\hbar\omega = E_G$, as illustrated in figure 2.13(b).

In a real QW material, gain is broadened by comparison to that illustrated in figure 2.13(b), in particular the band edge is not as sharp. A full model should consider

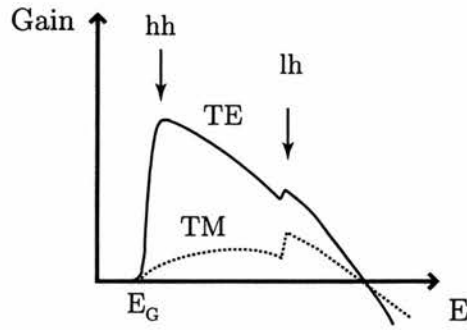


Figure 2.14: Schematic of typical gain spectra for QW laser structures detailing contributions from TM and TE polarisations and due to transitions involving first hh and lh bands

the broadening effects of processes including intraband relaxation, carrier-carrier scattering and well width fluctuations. There may be band gap shrinkage as a result of injected carriers and subband mixing may further complicate this simple picture. It remains the case that QW gain has different characteristics to that of a bulk material. In particular, as can be expected from the density of states, in a QW the gain tends to start at higher energies and it saturates at moderate values of carrier density, since all the available electron and hole states become fully inverted. However, due to the selection rules for transitions the value of A_{mn} in the gain expression for quantum wells (equation 2.23) is dependent on the light polarisation. Consequently the gain experienced by TE and TM polarisations tends to be significantly different. For example the gain for the two polarisations may be of the form illustrated schematically in figure 2.14 with a rise in TM gain with photon energy as the higher lh transition is accessed. Note that, contrary to what would be expected by application of the selection rules, there is a small component of gain for the TM mode even for energies below the allowed lh transition. This is due to fact that the selection rules are only strictly valid around $k = 0$. The reality is even more complex since the relative strengths of the gain for TE and TM may be reversed completely in strained materials as discussed below.

2.8 Strained materials

In designing a multilayer structure it is necessary to consider the lattice constants of adjacent layers. As noted in section 2.4.2, too large a difference between the lattice

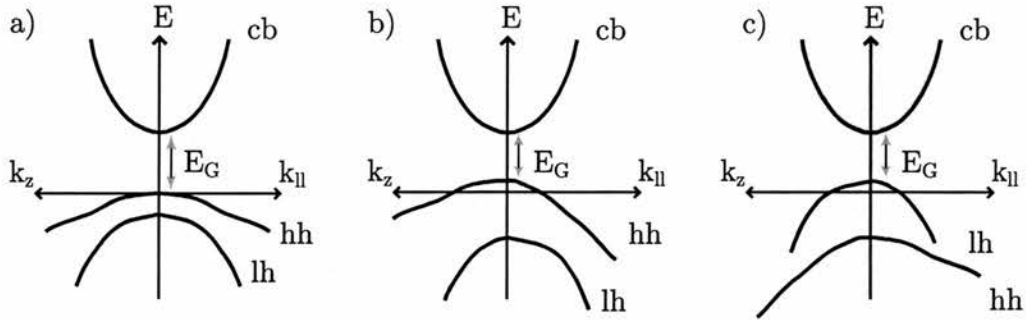


Figure 2.15: Schematic of the band structure of epitaxial layers (a) unstrained, (b) under compressive strain (c) under tensile strain, illustrating the relative changes in the light and heavy hole bands and a change in the band gap

constants can cause material defects and can even cause the sample to fracture. However stable epitaxial layers, whose lattice constants are similar but not equal, can be grown slowly, up to a critical thickness and maximum percentage strain [15]. This results in coherent strain, rather than fractures and other defects [4]. The pressure due to this strain, which can be compressive or tensile, effects the band structure and optical properties of the material.

Even in bulk materials strain can be used to balance the material gain difference for TE and TM polarisations, by introducing strain and at the same time as adjusting the shape of the active region and hence the confinement factor [16]. In quantum confined structures the wide choice of material compositions available, combined with the fact that the resultant electronic structure will depend also on layer thickness, allows real engineering of band structures [15] [17].

Band structure engineering can, for example, be used to move the band edge of the sample [18]. So, since some nonlinear effects are stronger near band edge (such as refractive index nonlinearities), the edge can be shifted to take advantage of, or avoid, those effects.

Another influence of strain which is very significant in the case of QW and superlattice structures is on the light and heavy hole bands. Depending whether the conditions are of compression or tension the heavy hole or light hole band can become higher with respect to the other [19][20][21]. This is illustrated in figure 2.15, where the unstrained structure (a) is of the general form shown in figure 2.7, and (b) and (c) demonstrate the effects of strain. These changes in band structure influence the po-

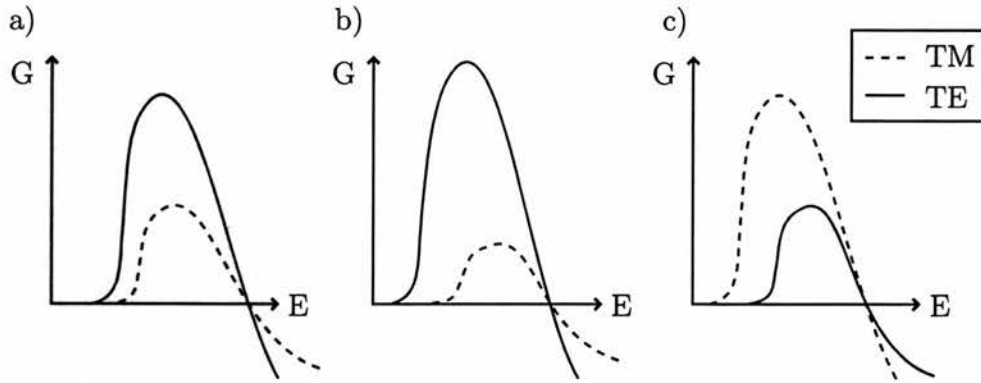


Figure 2.16: Schematic of the optical gain, G , for different material compositions resulting in material that is (a) unstrained, (b) under compressive strain (c) under tensile strain, corresponding to the bandstructures illustrated in figure 2.15

larisation dependence of the optical properties of the quantum well [22][23][24][17]. In figure 2.16 the shape of the gain is illustrated for band structures corresponding to those in figure 2.15. The relative changes in the light and heavy hole bands, in figure 2.15, translate into relative changes in the strengths of the TE and TM gains, in figure 2.16; in both figures a change in band gap is also shown.

Using strain, selection rules and transition strengths, a device can be designed to give strong emission of a particular polarisation, should this be desirable, for example for lasers [25]. However for SOAs it is the converse, namely isotropic amplification, that would have a premium for many optical processing applications [26] [27]. One of the first polarisation insensitive SOAs was achieved in the $1.3 \mu\text{m}$ range by Tiemeijer et al. [21] using different wells to provide the TE and TM gain. Reports of a plethora of developments of this and other strategies to design polarisation independent amplifiers have followed [28][29][30][31]. For example, structures with strong gain in both polarisations can be designed, by the introduction of strain to the barrier layers or by the use of alternating layers of compressive and tensile strain (see for example [18], [32] and references therein). In addition, note that in a structure which gives both TE and TM amplification, the modal TE and TM gain can be balanced by careful adjustment of the optical confinement [23][33].

2.9 Optical nonlinearities in semiconductors

The result of an optical transition occurring is a change in the number of carriers in the conduction and valence bands. In the case of the SOA investigated in this project, the device is usually electrically biased into gain and hence will amplify an incident optical field, contrary to an unbiased sample of material which will tend to absorb an optical field of the appropriate frequency. With an extremely weak optical field incident on the device, there is little or no bleaching of the available transitions and hence of the gain, even with the cumulative amplification of the light which occurs on propagation through the SOA. However for a stronger signal, the density of carriers can be significantly reduced, which has concomitant effects on the optical properties of the material and hence on the operation of the device. This can be achieved with an ultrashort pulse of moderate energies, less than 1 pJ, as will be reported in subsequent chapters.

Due to the optical interaction, the device is induced into a non-equilibrium state. After the removal of the perturbing optical field the carrier population will tend to recover towards equilibrium. In the case of an ultrashort pulse, as well as the peak and average optical power, the central wavelength, bandwidth and temporal duration of the optical pulse are all critical in determining the initial response of the device. A host of different carrier relaxation mechanisms determine the subsequent carrier dynamics and the observed changes in optical properties.

2.9.1 Nonlinear gain

At low energies the response of the material is generally linear, that is if the strength of the optical field is doubled the magnitude of the response will also double. At some point, as the strength of the optical field is increased, the response of the material begins to saturate; the material behaviour becomes nonlinear.

For a general discussion of nonlinearities in semiconductors, the dimensionality of the active region is not critically important. However some optical properties are subtly different in quantum confined structures. In particular, although by use of strained materials efforts have been made to design SOAs that can demonstrate polarisation

independent operation (section 2.8), optical nonlinearities in devices will tend to be affected by the polarisation of the optical field at least to some degree for some bias levels and at some wavelengths [22] [34] [35]. This is discussed further along with results in Chapters 6 and 7. Some other differences between bulk and QW SOAs will be noted where relevant in the following summary of nonlinear processes.

Interband transitions and band filling

The Pauli exclusion principle dictates that in a system containing many electrons no two electrons can be in states with identical quantum numbers. Consequently although it would appear to be energetically favourable for all the population of electrons in the conduction band to be located at the bottom of the band, this is not allowed. Rather the electrons fill up the conduction band from the lowest available states.

When carriers are excited from the valence band into the conduction band, through absorption of a photon, the free carriers created continue to fill the states inhibiting further transitions to those states. This is the so-called state or band filling effect. In the case of a forward biased SOA the analogous effect is that of gain depletion and eventual gain saturation: incident photons stimulate the radiative recombination of electrons in conduction band states, with holes in valence band states, thereby blocking a further optical transition between those states. The observable effect is that the potential of the SOA to amplify a subsequent pulse is reduced following this extraction of gain.

Any excess carriers recombine by radiative and non-radiative processes. The characteristic rate of spontaneous recombination due to the sum of these processes can be expressed as

$$R(N) = AN + B(N)N^2 + CN^3 \quad (2.27)$$

where N is carrier density, A is the non-radiative recombination rate at defects in the lattice and at interfaces, $B(N)$ is the radiative recombination rate and C is the coefficient associated with the higher order non-radiative Auger effect [36]. The rate of recovery of an SOA from gain depletion by carrier injection is also limited by this recombination rate.

With high quality materials, as fabricated for active devices such as an SOA, coefficient A may be small, reflecting the reduced recombination caused by defects. Indeed

for modelling of devices it can be reasonable to take $A \approx 0$ [2]. In particular in biased devices since carrier densities can be extremely high, the terms in equation 2.27 dependent on coefficients B and, particularly, C tend to dominate [37] [29]. Moreover the devices investigated in this project operate in the region of $1.3 \mu\text{m}$ and $1.5 \mu\text{m}$ and the Auger coefficient, C, tends to be large in narrow band semiconductors [38].

The carrier population in the active material recovers from the bandfilling nonlinearity with a time constant given by

$$\tau = \frac{1}{R(N)} \quad (2.28)$$

Typical values of τ vary from approximately 1 ns, for absorption bleaching in bare material samples, down to less than a hundred picoseconds, for gain depletion in biased devices. This time constant, which corresponds to the lifetime of carriers in the upper state, can be further reduced by carrier injection using very high electrical biases [39] or by applying an optical field [40] [41]. The relationship between the observed gain recovery of a device, the material parameters and electrical bias is further discussed with analysis of the results in Chapter 7.

Intraband transitions

In addition to the relaxation of excited carriers by interband transitions between the conduction and valence bands, carriers can also relax within the bands. It is these intraband transitions that are responsible for broadening gain spectra, as noted in section 2.7.2. Mechanisms by which this relaxation can occur are carrier-carrier scattering and carrier-phonon interactions [42].

Spectral hole burning

As has been mentioned, optical transitions occurring between specific states in the conduction and valence band block further transitions between these states. In an inhomogeneously broadened gain medium, light of a given wavelength stimulates transitions only between certain states with an equivalent energy separation, not across the entire range of energies over which absorption or gain could occur. The consequence in semiconductor materials is that these transitions effectively burn a hole in the Fermi

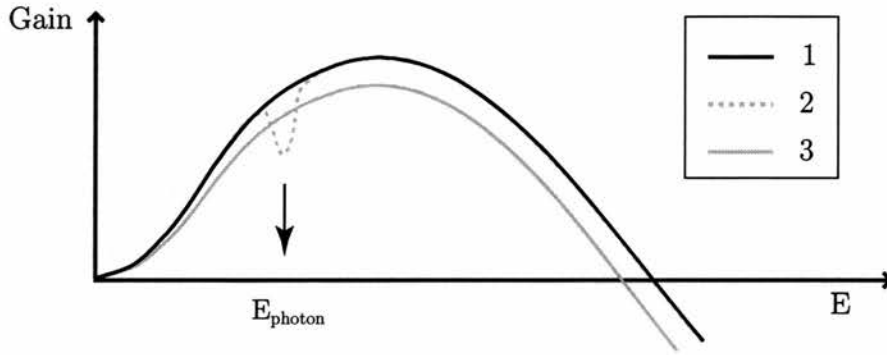


Figure 2.17: Schematic of the evolution of the carrier distribution when a hole is burnt in the gain spectrum by stimulated emission due to an optical beam at with central energy of E_{photon} . The initial distribution is smooth (1), spectral hole burning creates a dip over a range of energies (2) and subsequently the carriers evolve to a new distribution via carrier carrier scattering (3)

distribution. This is an effect called spectral hole burning (SHB). In an unbiased sample, the absorption is bleached over a spectrally narrow range. When the material is biased to transparency there are no net stimulated transitions, so in principle can be no spectral hole burning, although with a spectrally broad input pulse carriers may be more excited by some wavelengths and more depleted by others. In the gain regime the stimulated transitions burn a hole in the available gain, as illustrated in figure 2.17.

The characteristics of this hole depend on several factors: assuming a spectrally narrow optical excitation, the width of the hole will depend on the k-vector selectivity and the dephasing rate, which is thought to be very rapid at high carrier densities (<50 fs), such as those found in a forward biased SOA. The spectral hole disappears due to intraband carrier-carrier scattering, with a time constant of approximately 100-250 fs [2] [43]. On this time scale a new Fermi distribution evolves, which under gain conditions contains fewer carriers (as indicated by the dashed curve in figure 2.17) since the stimulated transitions have caused a net removal of carriers. The characteristic timescale of SHB and the fact that its contribution to the dynamics changes sign between the gain and absorption regimes, facilitate the identification of this process in time resolved pump-probe studies [44][45]. However, given the rapid time constants associated with the thermalisation following SHB, its effects can only be expected to be time-resolved in pump-probe studies with very short optical pulses (<300 fs), shorter than those used in the experiments reported here.

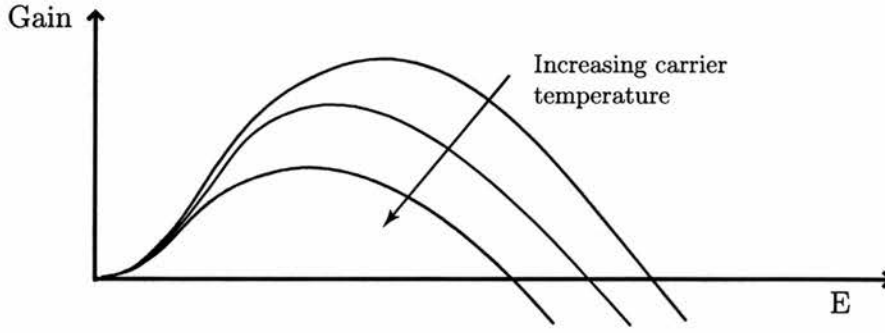


Figure 2.18: Schematic of the change of the carrier distribution when the temperature of the carriers is increased.

Carrier heating

The changes in the carrier distribution caused by optical transitions result in another nonlinearity due to the non-equilibrium carrier heating (CH) [46] [47], which can be longer lived than spectral hole burning. The new Fermi distribution, which evolves from carrier-carrier scattering (subsequent to SHB), may settle to a temperature which is different from that of the lattice. As shown schematically in figure 2.18, increasing the temperature reduces the gain at all energies [48]. Also at higher carrier temperatures, the peak of the gain moves to longer wavelengths, due to the strong temperature dependence of the Fermi function (equation 2.4). Significant changes in the gain are possible for moderate changes in the temperature of the carrier distribution (for example, a reduction of the gain by a quarter for a heating of 20 K [2]). This is illustrated by figure 2.19 in which the gain is plotted as a function of temperature using gain calculations for bulk InGaAs.

There are several mechanisms by which the carrier distribution can be changed. Consider that carriers are ‘hot’ or ‘cold’ depending on whether their energy is above or below the average energy of the distribution

$$\langle E \rangle = \frac{\int f(E)\rho(E)EdE}{\int f(E)\rho(E)dE} \quad (2.29)$$

where $\rho(E)$ is the density of states, $f(E)$ is the Fermi function probability and the denominator is equivalent to the carrier density. An optical beam incident on the semiconductor material can add or remove carriers, as discussed. If by this action, hot carriers are added or cold carriers are removed then the temperature of the distribution

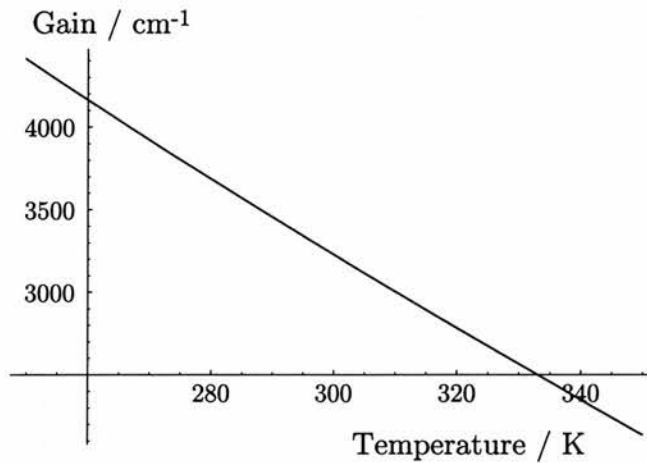


Figure 2.19: Calculated change in gain at a given energy near peak gain as a function of temperature.

is heated; vice versa then the distribution is cooled.

Free carrier absorption (FCA) which creates high energy carriers and stimulated emission (SE), by which cool carriers can be removed from low in the conduction band, have both been identified as processes which cause carrier heating in SOAs [49][46][50]. Stimulated transitions have a high probability of occurring relative to FCA, but the latter changes the total energy of the distribution more per occurrence [2]. Consequently is it not clear whether SE or FCA are more important. Generally, the degree of carrier heating is highly dependent on the energy of the photons in the optical beam.

An additional source of carrier heating which has been found in SOAs is the higher order process two photon absorption (TPA) [51]. This can occur in parts of the waveguide other than the active region and in all regimes: absorption, transparency and gain. The effect of TPA is always associated with a decrease in the available gain, however only where the TPA changes the carrier population in the active region will it contribute to the carrier heating dynamic. Whilst the behaviour of bulk and multiple quantum well (MQW) devices has been observed to be qualitatively similar, TPA may appear a more dominant component of the response in MQW SOAs [52]. This can be attributed to the lower confinement of the optical beam to the active region in MQW relative to bulk devices and TPA can occur strongly in cladding regions, whilst other processes responsible for gain dynamics such as stimulated transitions are expected to

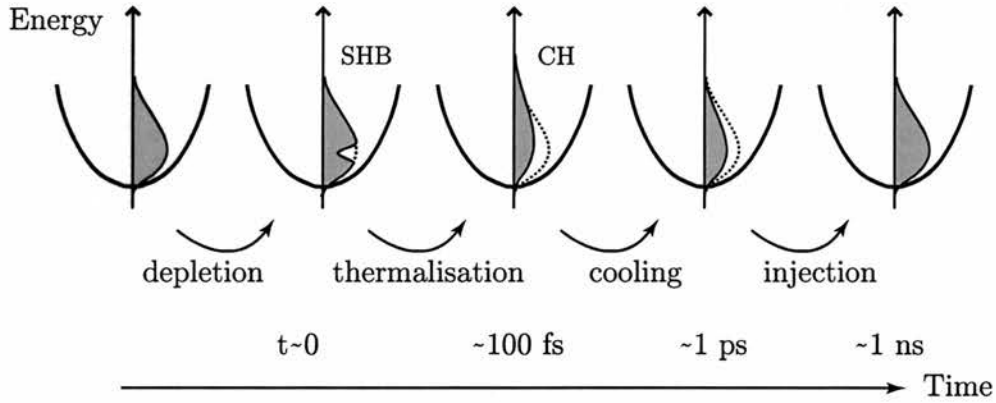


Figure 2.20: Schematic summarising the evolution of the carrier distribution over time following depletion by an optical pulse.

occur in the active region.

The characteristic time constants associated with carrier heating are of the order of 500fs up to 2ps [2][51] [53][54]. In this period the carrier distribution cools by the emission of optical phonons [55], a much slower process than the initial thermalisation to a new Fermi distribution by carrier-carrier scattering (following SHB).

Summary of carrier changes responsible for nonlinear gain

Figure 2.20 summarises the evolution of the carrier distribution subsequent to depletion of the carriers by an optical pulse with central wavelength around the peak of the gain. Initially the carrier population is reduced at the energies corresponding to the optical pulse energy (SHB). The carriers rapidly evolve towards a Fermi distribution, but at an elevated temperature with respect to the initial distribution. Subsequently the carriers thermalise to the lattice temperature. Finally the carrier population recovers by electrical injection of carriers.

2.9.2 Index nonlinearities

Long-lived and ultrafast refractive index changes

Along with the nonlinearities associated with changes in the carrier population there are concomitant refractive index nonlinearities. Gain and refractive index may be related mathematically using the Kramers-Kronig relation [56]

$$n(\omega) = 1 + \frac{c}{\pi} \int \frac{g_0(\omega')}{\omega'^2 - \omega^2} d\omega' \quad (2.30)$$

where g_0 is the linear gain. Also, ultrafast refractive index changes may be related to ultrafast gain nonlinearities by

$$\Delta n(\omega) = 1 + \frac{c}{\pi} \int \frac{\Delta g_0(\omega')}{\omega'^2 - \omega^2} \quad (2.31)$$

where $\Delta g_0 = g_0(\omega, N_1) - g_0(\omega, N_2)$ is a change in gain as a function of carrier density, N_i . This formalism is useful to describe the index changes associated with given changes in gain due to variations in the carrier population and its distribution. In general, the largest changes in index occur at energies around the band gap of the semiconductor. For energies above, but near, the band-gap, decreasing the carrier density increases the refractive index; conversely an increase in carrier density results in a reduction in index [52][57][58].

Carrier temperature changes and spectral hole burning have also been found to induce refractive index changes. This can be understood in terms of these processes effectively removing carriers from interaction with photons of certain energies. Specifically, at energies above, but near, the band-gap, experiments have found that increasing the carrier temperature and spectrally hole burning both have the effect of increasing the refractive index [57][58][59].

Instantaneous index changes

In addition to refractive index changes associated with changes in carrier density, there are also index changes attributed to rapid electronic or virtual processes [60], [61]. Experimentally it is observed that this instantaneous effect is enhanced as the wavelength is tuned towards and into the band and is reduced when the SOA is driven with higher biases [53] [61]. These higher biases correspond to increasing the carrier density and filling the states near band edge resulting in a shift of the absorption edge to higher energies. A reduced instantaneous nonlinearity in these circumstances is consistent with the theory of the optical Stark effect as manifested in SOAs [62]. In this paper [62], contributions from Raman transitions and two photon absorption (TPA), following the pulse profile, are also cited as possible contributory processes.

Experimentally, an instantaneous refractive index change may be observed as chirp added to a pulse which travels through an SOA. If the observed broadening of the pulse

spectrum is wholly attributed to an instantaneous index nonlinearity that follows the temporal profile of the pulse (the Kerr effect as described in section 1.3.5), measurement of the chirp may be used to calculate a value for the nonlinear refractive index coefficient

$$n_{2I} = \frac{\lambda L \Delta\phi}{2\pi I} \quad (2.32)$$

where λ is the centre wavelength of the pulse, I is the pulse intensity and L is the length of the SOA [52][63]. Note that spectral broadening may not be translated in a concomitant distortion of the temporal pulse profile, unless the device is very long, since the group velocity dispersion (GVD) in SOAs tends to be low [64] [65].

Effects of index changes

Dynamic changes in refractive index have been observed to cause changes in frequency [66][67] [68]. The instantaneous central frequency of a pulse can be described by

$$\omega = \omega_0 - \frac{\omega_0 L}{c} \left(\frac{\partial n(t)}{\partial t} \right) \quad (2.33)$$

where ω_0 is the carrier frequency, L is length of material and $n(t)$ is the time-dependent refractive index [69].

Weak pulses can be affected by index changes imposed by more intense pulses propagating through an SOA [52][70][71][72]. If pulses are sufficiently intense, they may significantly self distort by self-phase modulation (SPM) as introduced in section 1.3.5. To summarise the sources of SPM manifested in SOAs it is useful to consider three types: firstly, ‘slow’ SPM related to interband carrier density changes; secondly, that due to the carrier heating dynamic (following TPA, FCA, removal of cool carriers etc.); and thirdly, SPM from the instantaneous n_2 nonlinearity. The strength of all types of SPM, but especially the latter two sources, depends strongly on the pulse profile [65][73].

2.9.3 Link between gain and index effects

The amplitude gain and index, discussed so far in this chapter, correspond to the real and imaginary parts of the complex refractive index of the material, as introduced in section 1.3.2. The ratio of changes in gain, g and refractive index, n associated with

changes in carrier density, N , are related through a linewidth enhancement factor, also called Henry's α -factor [74][75]

$$\alpha_N = -\frac{\frac{\partial \chi_R}{\partial N}}{\frac{\partial \chi_I}{\partial N}} = -\frac{4\pi}{\lambda} \frac{\frac{\partial n}{\partial N}}{\frac{\partial g}{\partial N}} \quad (2.34)$$

where χ_R and χ_I are the real and imaginary parts of the complex susceptibility respectively and N is carrier density.

Values for the α -parameter can be derived experimentally, for example from the differential changes in gain and index via mode wavelength shifts for measured changes in applied current [76] [75] [77]. The value of α_N for MQW SOAs tends to be in the range 1.5 to 3, however there are some reports of values over 10; for bulk devices α_N is generally larger, 6 to 8 or above [25] [78] [75][76].

The linewidth enhancement factor is so-called since for semiconductor lasers it determines the enhancement of the spectral width of the laser, consequently, the lowest possible α_N may be the goal. In the case of an SOA to be used in an interferometric switch α_N is critical in determining the relative strength of amplitude gain and index dynamics; higher values tend to reduce the pulse energy required for switching. Additional α -parameters can be used to quantify the index changes induced by ultrafast gain changes. This approach is taken in modelling of the SOA described in Chapter 5.

2.9.4 Spatially dependent effects

In a complex structure such as an SOA the time it takes for carriers to diffuse from where they are injected to the active region depends on many factors such as the size of the active region and the confinement of the optical mode in the device. In analysis of carrier dynamics it is important to consider whether carrier capture times can be a limiting effect. It is not expected to be critical for the devices investigated in this project since the interband recovery times measured are in excess of 200 ps (as reported in Chapter 7) and ultrafast dynamics, such as carrier heating, can be considered separately since they are independent of carrier injection and occur on distinctly shorter timescales (≤ 1 ps).

Another type of spatial effect that can be of concern in some waveguide devices is longitudinal hole burning. If standing waves were set up along the length of the device

there would be sinusoidal variation in the carrier density. However there should not be this type of spatial hole burning of the gain in the SOA device since it is designed to be a travelling wave cavity, as described in section 2.2. That is not to say that longitudinal phenomena are not of interest with this device, on the contrary, as highlighted at the beginning of this chapter (section 2.2) nonlinear effects tend to be cumulative with longitudinal propagation. The results of the simulations of counter-propagating pump-probe measurements, reported in Chapter 7, highlight the importance of longitudinal effects.

2.10 Summary

This chapter has introduced the semiconductor optical properties relevant to the understanding of the behaviour of the device on which this thesis is focused: the semiconductor optical amplifier. The SOA is a particularly interesting device with which to investigate semiconductor optical processes, due to the fact that carrier density dependent optical properties can be altered by applying a range of electrical biases. This is in contrast to bare material, with no electrical contacts, or a laser diode in which the carrier density is clamped by the laser action.

The origin of optical amplification from interband carrier transitions has been outlined. Additionally ultrafast processes, including spectral hole burning, carrier heating and two-photon absorption, which modify the gain available for optical pulses propagating through the semiconductor have been introduced. The description presented in this chapter highlights the fact that although the behaviour of the SOA is controllable in some senses (e.g. the selection the initial level of gain for a particular wavelength by varying the carrier density via the level of applied bias), the carrier dynamics and associated changes in optical properties are highly complex.

Moreover, carrier dynamics originating from the same physical mechanism may manifest themselves differently under various operating conditions and in devices composed of varying materials and structures. In order to establish a general picture that is valid for a wide range of conditions, it is therefore necessary that experiments such as those reported in this thesis are undertaken. It is also important to measure both am-

plitude gain and index dynamics when investigating an SOA device, as it is the combination of both parameters that determines the overall changes in ultrafast pulse propagating through an SOA. In terms of applications, small changes in these parameters significantly affect the operation of SOA-based interferometric switches. Subsequent chapters of this thesis report the characterisation of an SOA, experiments to measure amplitude gain and phase changes on propagation through the device and modelling to aid the understanding of these complex dynamics.

The complexities of the semiconductor nonlinearities combined with the effects of propagation in a waveguide structure explain the interest in researching SOAs, work that is substantially motivated by the critical importance of these effects for realising reliable switches for telecommunications.

Bibliography for Chapter 2

- [1] T Saitoh and T Mukai. 1.5 μm GaInAsP traveling-wave semiconductor laser amplifier. *IEEE J. Quantum Elect.*, 23(6):1010–1020, 1987.
- [2] K L Hall, E R Thoen, and E P Ippen. *Semiconductors and Semimetals*, volume 59, chapter 2 Nonlinearities in Active Media. Academic Press, 1999.
- [3] J R Hook and H E Hall. *Solid state physics*. Manchester Physics Series. Wiley, Bristol, UK, 2nd edition, 1996.
- [4] P K Basu. *Theory of optical processes in semiconductors: bulk and microstructures*. Oxford University Press, New York, 1997.
- [5] Z I Alferov. Nobel lecture: The double heterostructure concept and its applications in physics, electronics and technology. *Rev. Mod. Phys.*, 73(3):767–782, 2000.
- [6] J M Luttinger. Quantum theory of cyclotron resonance in semiconductors: general theory. *Phys. Rev.*, 102(4):1030–1041, 1956.
- [7] S Seki, P Sotirelis, K Hess, T Yamanaka, and K Yokoyama. Theoretical analysis of gain saturation coefficients in InGaAs/AlGaAs strained layer quantum well lasers. *Appl. Phys. Lett.*, 61(18):2147–2149, 1992.
- [8] F Capasso. *Physics and applications of quantum wells and superlattices*, volume 170 of *NATO ASE Series B*, chapter Band-gap engineering for new photonic and electronic devices, pages 377–391. Plenum Press, 1987.
- [9] C Weisbuch and B Vinter. *Quantum semiconductor structures*. Academic Press, London, UK, 1991.
- [10] H C Casey Jr. and M B Panish. *Heterostructure lasers Part A: Fundamental principles*. Academic Press, 1978.
- [11] T Wenckebach. *Essentials of semiconductor physics*. Wiley, Chichester, UK, 1999.
- [12] J Willmott. *Atomic Physics*. Manchester Physics Series. Wiley, Bristol, UK, 1975.
- [13] M Yamanishi and I Suemune. Comment on polarization momentum matrix elements in quantum well lasers. *Jpn. J. Appl. Phys.*, 23(1):L35–L36, 1984.
- [14] C H Henry, R A Logan, and F R Merritt. Measurement of gain and absorption spectra in AlGaAs buried heterostructure lasers. *J. Appl. Phys.*, 51(6):3042–3061, 1980.
- [15] E P O'Reilly. Valance band engineering in strained-layer structures. *Semicond. Sci. Tech.*, 4:121–137, 1989.
- [16] M Itoh, Y Shibata, T Kakitsuka, Y Kadota, and Y Tohmori. Polarisation-insensitive SOA with strained bulk active layer for network device application. *IEEE Photonic. Tech. L.*, 14(6):765–767, 2002.
- [17] W W Chow and S W Koch. *Semiconductor laser fundamentals: physics of the gain of materials*. Springer-Verlag, Berlin, 1999.

- [18] J E M Haverkort, B H P Dorren, M Kemerink, A Yu Silov, and J H Wolter. Design of composite InAsP/InGaAs quantum wells for a 1.55 μm polarisation independent semiconductor optical amplifier. *Appl. Phys. Lett.*, 75(18):2782–2784, 1999.
- [19] M Sugawara, N Okazaki, T Fujii, and S Yamazaki. Conduction-band and valance-band structures in $\text{In}_{1-x}\text{Ga}_x\text{As}/\text{InP}$ quantum wells on (001) InP substrates. *Phys. Rev. B*, 48(11):8102–8118, 1993.
- [20] D Ahn and S-L Chuang. Optical gain in a strained-layer quantum-well laser. *IEEE J. Quantum Elect.*, 24(12):2400–2406, 1988.
- [21] L F Tiemeijer, P J A Thijs, T van Dongen, R W M Sloopweg, J M M van der Heijden, J J M Binsma, and M P C M Krijn. Polarisation insensitive multiple quantum well laser amplifiers for the 1300 nm window. *Appl. Phys. Lett.*, 62(8):826–828, 1993.
- [22] P Koonath, S Kim, Woon-Jo Cho, and A Gopinath. Polarization-insensitive optical amplifiers in AlInGaAs. *IEEE Photonic. Tech. L.*, 13(8):779–781, 2001.
- [23] D Ban and E H Sargent. Influence of nonuniform carrier distribution on the polarisation dependence of modal gain in multiquantum-well lasers and semiconductor optical amplifiers. *IEEE J. Quantum Elect.*, 36(9):1081–1088, 2000.
- [24] A Di Carlo, A Reale, L Tocca, and P Lugli. Polarization-independent δ -strained semiconductor optical amplifiers: a tight-binding study. *IEEE J. Quantum Elect.*, 34(9):1730–1739, 1998.
- [25] L F Tiemeijer, P J A Thijs, P J de Waard, J J M Binsma, and T B Dongen. Dependence of polarisation, gain, linewidth enhancement factor, and K factor on the sign of the strain of InGaAsP/InP strained-layer multiquantum well lasers. *Appl. Phys. Lett.*, 58(24):2738–2740, 1991.
- [26] A D Ellis and D M Spirit. Compact 40 gbit/s optical demultiplexer using a GaInAsP optical amplifier. *Electron. Lett.*, 29(24):2115, 1993.
- [27] C Schubert, J Berger, U Feiste, R Ludwig, C Schmidt, and H G Weber. 160-Gb/s polarisation insensitive all-optical demultiplexing using a gain-transparent ultrafast nonlinear interferometer (GT-UNI). *IEEE Photonic. Tech. L.*, 13(11):1200–1202, 2001.
- [28] J Y Emery, T Ducellier, M Bachmann, and P Doussière. High performance 1.55 μm polarisation-insensitive optical amplifier based on low-tensile strain bulk GaInAsP. *Electron. Lett.*, 33(12):1083–1084, 1997.
- [29] A Reale, A Di Carlo, P Lugli, D Campi, C Cacciatore, A Stano, and G Fornuto. Study of gain compression mechanisms in multiple-quantum-well $\text{In}_{1-x}\text{Ga}_x\text{As}$ semiconductor optical amplifiers. *IEEE J. Quantum Elect.*, 35(11):1697–1703, 1999.
- [30] M Silver, A F Philips, A R Adams, P D Greene, and A J Collar. Design and ASE characteristics of 1550 μm polarization-insensitive SOAs containing tensile and compressive wells. *IEEE J. Quantum Elect.*, 36(1):118–122, 2000.
- [31] W P Wong and K S Chiang. Design of waveguide structures for polarization-insensitive optical amplification. *IEEE J. Quantum Elect.*, 36(11):1243–1250, 2000.

- [32] M Okamoto, K Sato, H Mawatari, F Kano, K Magari, Y Kondo, and Y Itaya. TM mode gain enhancement in GaInAs-InP lasers with tensile strained-layer superlattice. *IEEE J. Quantum Elect.*, 27(6):1463–1469, 1991.
- [33] S Seki, T Yamanaka, W Lui, Y Yoshikuni, and K Yokoyama. Theoretical analysis of pure effects of strain and quantum confinement on differential gain in InGaAs/InP strained-layer quantum-well lasers. *IEEE J. Quantum Elect.*, 30(2):500–510, 1994.
- [34] K Magari, M Okamoto, H Yasaka, K Sato, Y Noguchi, and O Mikami. Polarization insensitive traveling wave type amplifier using strained multiple quantum well structure. *IEEE Photonic Tech. L.*, 2(8):556–558, 1990.
- [35] R J Manning, A Antonopolous, R Le Roux, and A E Kelly. Experimental measurement of non-linear polarisation rotation in semiconductor optical amplifiers. *Electron. Lett.*, 37(4):229–231, 2001.
- [36] S Hausser, G Fuchs, A Hangleiter, K Streubel, and W T Tsang. Auger recombination in bulk and quantum well InGaAs. *Appl. Phys. Lett.*, 56(10):913–915, 1990.
- [37] G Eisenstein, R S Tucker, J M Wiesenfeld, P B Hansen, G Raybon, B C Johnson, T J Bridges, F G Storz, and C A Burrus. Gain recovery of travelling-wave semiconductor optical amplifiers. *Appl. Phys. Lett.*, 54(5):454–456, 1989.
- [38] W K Metzger, M W Wanlass, R J Ellingson, R K Ahrenkiel, and J J Carapella. Auger recombination in low-band-gap n-type InGaAs. *Appl. Phys. Lett.*, 79(20):3272–3274, 2001.
- [39] R J Manning, D A O Davies, and J K Lucek. Recovery rates in semiconductor laser amplifiers: Optical and electrical bias dependancies. *Electron. Lett.*, 30(15):1233–1235, 1994.
- [40] M A Dupertuis, J L Pleumeekers, T P Hessler, P E Selbmann, B Deveaud, B Dagens, and J Y Emery. Extremely fast high-gain and low-current SOA by optical speed-up at transparency. *IEEE Photonic Tech. L.*, 12(11):1453–1455, 2000.
- [41] R J Manning and D A O Davies. Three-wavelength device for all-optical signal processing. *Opt. Lett.*, 19(12):889, 1994.
- [42] M Asada. Intraband relaxation time in quantum-well lasers. *IEEE J. Quantum Elect.*, 25(9):2019–2026, 1989.
- [43] R A Indik, R Binder, M Mlejnek, J V Moloney, S Hughes, A Knorr, and S W Kock. Role of plasma cooling, heating and memory effects in subpicosecond pulse propagation in semiconductor amplifiers. *Phys. Rev. A*, 53(5):3614–3620, 1996.
- [44] K L Hall, G Lenz, E P Ippen, U Koren, and G Raybon. Carrier heating and spectral hole burning in strained-layer quantum-well laser amplifiers at 1.5 μm . *Appl. Phys. Lett.*, 61(21):2512, 1992.
- [45] M Willatzen, J Mark, and J Mork. Carrier temperature and spectral holeburning dynamics in InGaAsP quantum well laser amplifiers. *Appl. Phys. Lett.*, 64(2):143–145, 1994.
- [46] D Bimberg and J Mycielski. The recombination-induced temperature change of non-equilibrium charge carriers. *J. Phys. C: Solid State Phys.*, 19:2363–2373, 1986.

- [47] K L Hall, J Mark, E P Ippen, and G Eisenstein. Femtosecond gain dynamics in InGaAsP optical amplifiers. *Appl. Phys. Lett.*, 56(18):1740, 1990.
- [48] G Belenky and C L Reynolds Jr. and L Shterengas and M S Hybertsen and D V Donetsky and G E Shtengel and S Luryi. Effect of p-doping on the temperature dependence of differential gain in FP and DFB 1.3 μ m InGaAsP-InP multiple quantum well lasers. *IEEE Photonic. Tech. L.*, 12(8):969–971, 2000.
- [49] C-K Sun, H K Choi, C A Wang, and J G Fujimoto. Studies of carrier heating in InGaAs/AlGaAs strained-layer quantum well diode lasers using a multiple wavelength pump probe technique. *Appl. Phys. Lett.*, 62(7):747, 1993.
- [50] B N Gomatam and A P De Fonzo. Theory of hot carrier effects on nonlinear gain in GaAs-GaAlAs lasers and amplifiers. *IEEE J. Quantum Elect.*, 26(10):1689–1704, 1990.
- [51] J Mork, J Mark, and C P Seltzer. Carrier heating in InGaAsP laser amplifiers due to two-photon absorption. *Appl. Phys. Lett.*, 64(17):2206, 1994.
- [52] K L Hall, G Lenz, A M Darwish, and E P Ippen. Subpicosecond gain and index nonlinearities in InGaAsP diode lasers. *Opt. Commun.*, 111:589–612, 1994.
- [53] C P Hultgren, D J Dougherty, and E P Ippen. Above- and below-band femtosecond nonlinearities in active AlGaAs waveguides. *Appl. Phys. Lett.*, 61(23):2767, 1992.
- [54] C K Sun, B Golubovic, J G Fujimoto, H K Choi, and C A Wang. Heterodyne nondegenerate pump-probe measurement technique for guided-wave devices. *Opt. Lett.*, 20(2):210–212, 1995.
- [55] A Uskov, J Mørk, and J Mark. Theory of short-pulse gain saturation in semiconductor laser amplifiers. *IEEE Photonic. Tech. L.*, 4(2):443–446, 1992.
- [56] D C Hutchings, M Sheik-Bahae, D J Hagan, and E W Van Stryland. Kramers-kronig relations in nonlinear optics. *Opt. Quant. Electron.*, 24:1–30, 1992.
- [57] C T Hultgren and E P Ippen. Ultrafast refractive index dynamics in AlGaAs diode laser amplifiers. *Appl. Phys. Lett.*, 59(6):635–637, 1991.
- [58] J Mork and A Mecozzi. Response function for gain and refractive index dynamics in active semiconductor waveguides. *Appl. Phys. Lett.*, 65(14):1736–1738, 1994.
- [59] K L Hall, G Lenz, E P Ippen, and G Raybon. Heterodyne pump-probe technique for time-domain studies of optical nonlinearities. *Opt. Lett.*, 17(12):874–879, 1992.
- [60] K K Anderson, M J LaGasse, C A Wang, J G Fujimoto, and H A Haus. Femtosecond dynamics of the nonlinear index change near the band edge in AlGaAs waveguides. *Appl. Phys. Lett.*, 56(17):1834–1836, 1990.
- [61] M J LaGasse, K K Anderson, C A Wang, H A Haus, and J G Fujimoto. Femtosecond measurements of the nonresonant nonlinear index in AlGaAs. *Appl. Phys. Lett.*, 56(5):417–419, 1990.
- [62] M Sheik-Bahae and E W Van Stryland. Ultrafast nonlinearities in semiconductor laser amplifiers. *Phys Rev B*, 50(19):14171, 1994.

- [63] R S Grant and W Sibbett. Observations of ultrafast refraction in an InGaAsP optical amplifier. *Appl. Phys. Lett.*, 58(11):1119–1121, 1991.
- [64] K L Hall, G Lenz, and E P Ippen. Femtosecond time domain measurement of group velocity dispersion in diode lasers at 1.5 μm . *IEEE J. Lightwave Technol.*, 10(5):616–619, 1992.
- [65] M Y Hong, Y H Chang, A Dienes, J P Heritage, and P J Delfyett. Subpicosecond pulse amplification in semiconductor laser amplifiers: Theory and experiment. *IEEE J. Quantum Elect.*, 30(4):1122–1131, 1994.
- [66] G P Agrawal and N A Olsson. Self-phase modulation and spectral broadening of optical pulses in semiconductor laser amplifiers. *IEEE J. Quantum Elect.*, 25(11):2297, 1989.
- [67] N Finlayson, E M Wright, and G I Stegeman. Nonlinear optical pulse propagation in a semiconductor medium in the transient regime - i: Temporal and spectral effects. *IEEE J. Quantum Elect.*, 26(4):770–777, 1990.
- [68] M Y Hong, Y H Chang, A Dienes, J P Heritage, P J Delfyett, S Dijaili, and F G Patterson. Femtosecond self- and cross-phase modulation in semiconductor laser amplifiers. *IEEE J. Sel. Top. Quant.*, 2(3):523–539, 1996.
- [69] Y R Shen. *The Principles of Nonlinear Optics*. Wiley, New York, 1984.
- [70] P J Delfyett, Y Silberberg, and G A Aphonse. Hot-carrier thermalisation induced self-phase modulation in semiconductor traveling wave amplifiers. *Appl. Phys. Lett.*, 59(1):10, 1991.
- [71] K Sutkus, K Shum, R R Alfano, and P J Delfyett. Effect of carrier heating on the wavelength chirp of ultrashort laser pulses in semiconductor travelling wave amplifiers. *IEEE Photonic. Tech. L.*, 6(3):372–375, 1994.
- [72] R Schrieck, M Kwakernaak, H Jckel, E Gamper, E Gini, W Vogt, and H Melchior. Ultrafast switching dynamics of Mach-Zender interferometric switches. *IEEE J. Quantum Elect.*, 37(6):603–605, 2001.
- [73] P P Vasil'ev, I H White, and J Gowar. Fast phenomena in semiconductor lasers. *Rep. Prog. Phys.*, 63:1997–2042, 2000.
- [74] C H Henry. Theory of the linewidth enhancement factor. *IEEE J. Quantum Elect.*, 18(2):259–264, 1982.
- [75] M Osiński and J Buus. Linewidth broadening factor in semiconductor lasers - an overview. *IEEE J. Quantum Elect.*, 23(1):9–29, 1987.
- [76] J Stohs, D J Bossert, D J Gallant, and S R J Brueck. Gain, refractive index change, and linewidth enhancement factor in broad-area GaAs and InGaAs quantum-well lasers. *IEEE J. Quantum Elect.*, 37(11):1449–1459, 2001.
- [77] W Rideout, B Yu, J LaCourse, P K York, K J Beerink, and J J Coleman. Measurement of the carrier dependence of the differential gain, refractive index and linewidth enhancement factor. *Appl. Phys. Lett.*, 56(8):706–708, 1990.
- [78] L F Tiemeijer, P J Thijs, J J M Binsma, and E J Jansen. Self-phase modulation coefficient of multiple-quantum-well optical amplifiers. *IEEE Photonic. Tech. L.*, 8(7):876–878, 1996.

Chapter 3

Optical sources: principles and operation

3.1 Introduction

Ultrashort pulse sources were required for the study of the ultrafast dynamics in semiconductor optical amplifiers conducted in this project. This chapter discusses the sources used, in particular an all-solid state synchronously-pumped optical parametric oscillator system, and the optimisation of this system.

The set-up for monitoring the sources, including the spectral and temporal characteristics of the pulses, is also detailed. This monitoring was critical in establishing stable output and maintaining low noise and drift for experiments. Moreover it was important to track the spectral and temporal profile of the input pulses during experiments and to be able to match changes in these parameters to measurements of the output from the SOA.

3.2 Overview of optical sources

Infrared optical pulses were required for the measurement of dynamics in Semiconductor Optical Amplifiers (SOAs) that is described in this thesis. The major part of the work has been carried out on devices operating around $1.5 \mu\text{m}$. In addition, some experiments have been carried out on devices in the region of $1.3 \mu\text{m}$. In both cases, the pulses were provided by an Optical Parametric Oscillator (OPO).

For characterisation of the SOAs, as described in Chapter 4, tunable CW diode lasers were also used.

3.3 Optical Parametric Oscillators

Optical parametric oscillators (OPOs) have developed, particularly over the past decade, to become highly versatile sources of tunable coherent light in the infrared. The potential of OPOs, in which new wavelengths are generated through difference-frequency mixing (introduced in section 1.3.5), was recognised more than 30 years ago [1]. However, technical advances were necessary to facilitate the realisation of OPOs as sources for a range of applications, from spectroscopy to biomedical research and environmental monitoring. The critical developments included the ability to grow and microengineer structures from a plethora of new optically nonlinear crystals, the improved stability and increased power of pump laser systems, and novel optical cavity configurations for the OPOs themselves [2].

3.3.1 The principle of the OPO

Usually OPOs involve coherent three-wave nonlinear optical processes and the generation is resonated within an optical cavity, much like that of a laser. A high power, high frequency pump wave is passed through a crystal generating two lower energy waves. Conventionally, the high power wave is known as the pump wave, at frequency ω_p , and the two other frequencies are designated the signal, centred at frequency ω_s and the idler, at ω_i . These frequencies, according to the requirement for conservation of energy in the system, must obey the following condition

$$\omega_p = \omega_s + \omega_i \quad (3.1)$$

The cavity resonance of the OPO is designed to correspond to an integral number of half wavelengths of the signal (and sometimes the idler as well, in a so-called doubly resonant cavity). If the gain corresponding to the resonant frequency exceeds the losses in the cavity, initial optical noise at that frequency will be amplified on successive round trips, building up a coherent signal wave, and the associated idler.

For gain to be experienced at the frequencies ω_s and ω_i , the contributions from all the three frequencies must add up constructively i.e. in phase. The criterion for this phase matching is

$$\Delta k = k_p - k_s - k_i \quad (3.2)$$

where k_p , k_s and k_i represent the wavevectors in the nonlinear material for pump, signal and idler, respectively, and where Δk is ideally zero. This condition corresponds to the conservation of momentum. Using $k = \frac{\omega}{c}n$, and taking $\Delta k = 0$, this can be expressed as

$$\omega_p n_p = \omega_s n_s + \omega_i n_i \quad (3.3)$$

where n_p , n_s and n_i are the refractive indices of the nonlinear medium at the pump, signal and idler wavelengths, respectively.

For the new wavelengths, ω_s and ω_i to be generated from ω_p , and to be amplified, the conditions expressed by equations 3.1 and 3.2, both need to be met. Maximum intensity generation occurs when $\Delta k = 0$. The reduction in the efficiency of the conversion process for a given system is expressed in terms of the phase mismatch corresponding to the value of $\Delta k l$, where l is the length of the crystal.

In addition, in any given nonlinear medium, the magnitude of signal and idler generated will depend on the pump frequency and on the dispersion characteristics of the medium.

3.3.2 Phase matching and wavelength tuning

In general, different wavelengths propagate at different velocities in the crystal due to dispersion. For the parametric process this results in a low conversion efficiency, since the pump, signal and idler do not propagate together. As mentioned in section 3.3.1, the efficiency of conversion in an OPO is determined by how closely the phase matching condition is adhered to. As a consequence, the strengths and energies of signal and idler can be adjusted by a number of methods related to changing the relative refractive indices of the different waves in the direction of propagation.

A direct method is through changing the pump wavelength. Also changing the temperature, pressure or electric field conditions of the crystal can be used to modify the refractive index. Alternatively, by adjusting the angle of the crystal with respect to the incident direction of the pump beam, crystal birefringence may be used to satisfy the phase matching condition.

Birefringent phase matching exploits the different values of refractive index experienced by orthogonal polarisations propagating in an arbitrary direction through a

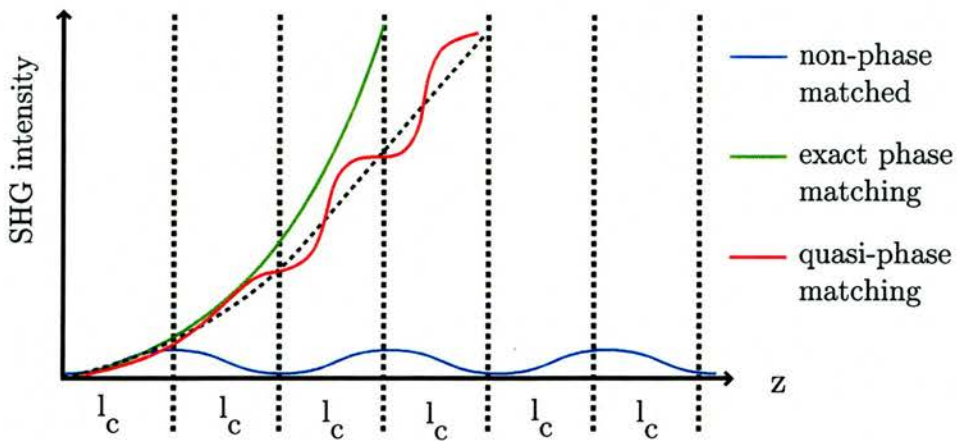


Figure 3.1: Second Harmonic Generation (SHG) under conditions of no phase matching, exact phase matching and quasi-phase matching

birefringent material. Phase matching using this effect is restricted in that it is dependent on achieving the right combination of polarisation and propagation direction. The effective interaction length in the material is limited by the fact that the direction of the wave vector, k , and that of the flow of energy through the crystal do not generally coincide, an effect called Poynting vector walk-off. What is more, only a certain pair of wavelengths can be phase matched for a given propagation direction and the range of wavelengths which can be generated from a single material is limited. Overall birefringent phase matching is restrictive, since it is inherently dependent on the material properties.

Significant advances, in recent years, in the fabrication and engineering of materials, have allowed quasi-phase matching to be used [3]. The concept of this technique is modulation of the nonlinear coefficient of the material to periodically compensate for the accumulating phase mismatch.

Consider the case of imperfect phase matching: the effect of the waves slipping out of phase is that they will interact less strongly. The generated signal and idler begin to back convert. If this process proceeds unchecked, the phase may revert to favour forward conversion and the cycle repeats itself, with the result that the generated power oscillates. In this cycle, the maximum for the generated wave is reached when a phase difference of π has accumulated. At this stage the gain is reduced by half and the corresponding distance over which this occurs is known as the coherence length.

In quasi-phase matching it is at this distance that the sign of the nonlinear coefficient is reversed, which in turn reverses the sign of the phase mismatch. In this way, the interaction is brought back into phase and the conversion efficiency can be substantially improved, as illustrated by figure 3.1.

The condition for optimisation of the conversion is minimisation of phase mismatch defined as in equation 3.2, with an additional term due to the periodic nature of the crystal structure

$$\Delta k_{QPM} = k_p - k_s - k_i - \frac{2\pi m}{\Lambda} \quad (3.4)$$

where Λ is the period of the modulation (grating period) and m the order of the interaction.

It is possible to engineer crystals to achieve phase matching for a broad range of wavelengths by selection of the grating period and nonlinear material, and additionally controlling conditions, such as temperature. This flexibility has allowed optical generation with OPOs from interactions for which birefringent phase matching is impossible.

3.3.3 Optical properties of the OPO crystal

The transparency, optical nonlinearity and refractive index are all important optical properties of a crystal for optical parametric generation. In Niobates, Phosphates and other ferroelectric materials it has been found that electric field poling can be used to reverse the nonlinear coefficient, as required for quasi-phase matching. In the OPO designed for the work in this thesis, a periodically poled Lithium Niobate (PPLN) crystal has been used. Lithium Niobate has a broad range of transparency, extending from 0.33 to 6.0 μm , and hence is suitable for generation in the mid-infrared.

To calculate the quasi-phase matching criteria in a crystal it is necessary to know the precise refractive indices in the material as function of optical wavelength and material temperature. The following Sellmier equation has been derived from measurements of PPLN [4], and is valid for the calculation of refractive indices for the near infrared wavelengths of interest in this project

$$n^2 = a_1 + b_1 F + \frac{a_2 + b_2 F}{\lambda^2 - (a_3 + b_3 F)^2} + \frac{a_4 + b_4 F}{\lambda^2 - a_5^2} - a_6 \lambda^2 \quad (3.5)$$

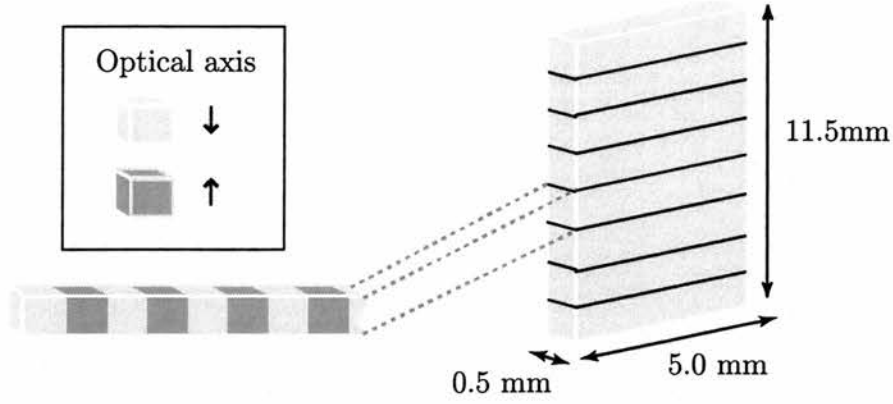


Figure 3.2: Schematic of the PPLN crystal, illustrating schematically the periodic reversal of the optical axis that is imposed with a different period in each of the eight grating layers.

where $F = (T - T_0)(T + T_0 + 546.32)$. The reference temperature $T_0 = 24.5^\circ\text{C}$ and the values of the constants are

$$a_1 = 5.35583, a_2 = 0.100473, a_3 = 0.20692$$

$$a_4 = 100, a_5 = 11.34927, a_6 = 1.5334 \times 10^{-2}$$

$$b_1 = 4.629 \times 10^{-7}, b_2 = 3.862 \times 10^{-8}$$

$$b_3 = -0.89 \times 10^{-8}, b_3 = 2.657 \times 10^{-5}$$

Wavelength tuning curves for a given periodic structure crystal can be calculated using this approximation (equation 3.5) for the refractive index combined with the quasi-phase matching condition (equation 3.4). The phase matching condition can be met for a range of signal wavelengths if the pump wavelength or the temperature of the crystal are varied.

The PPLN crystal which produced the pulses used for most of the experiments reported in this thesis is illustrated in the schematic in figure 3.2. It was 5 mm long and has eight gratings with periods ranging from 21.0 to 22.4 μm . The crystal was mounted in an oven to allow temperature control, and the pump wavelength could be changed. Figure 3.3 shows the calculated range of tuning of the signal wavelength for the eight grating periods of this PPLN crystal. It can be seen that by changing the pump wavelength by 30 nm and using the different gratings it is possible to generate wavelengths from below 1350 nm to above 1550 nm, at a fixed crystal temperature.

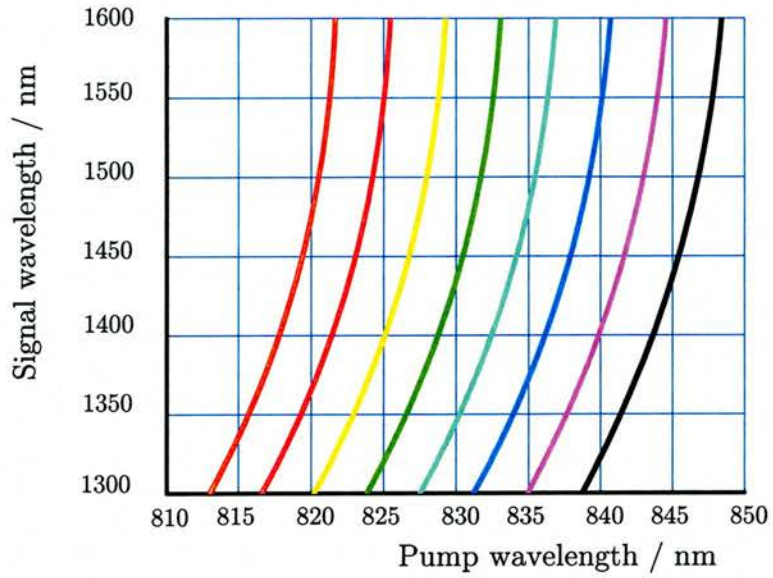


Figure 3.3: Calculated OPO tuning curve at 150° : signal wavelength as a function of pump wavelength for gratings $21.0 \mu\text{m}$ (black) to $22.4 \mu\text{m}$ (red) in steps of $0.2 \mu\text{m}$

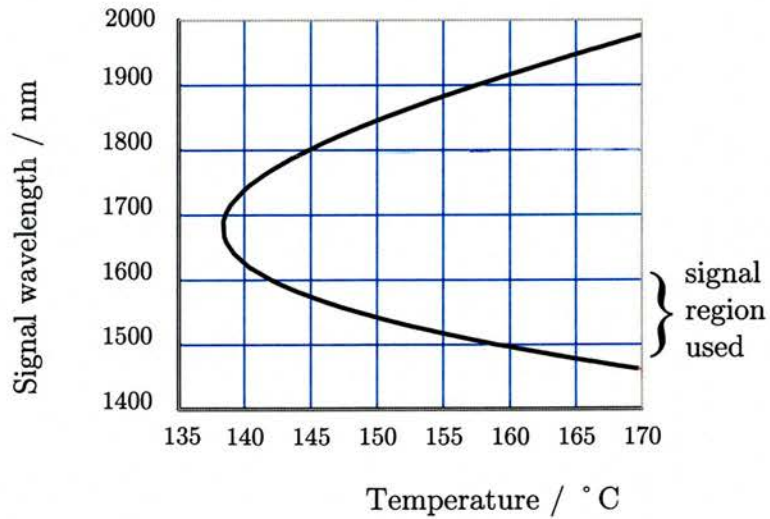


Figure 3.4: Calculated OPO tuning curve for grating period $22 \mu\text{m}$: signal wavelength as a function of temperature

Allowing the crystal temperature also to be varied widens the possibilities for successful generation. Figure 3.4 illustrates range of signal wavelengths achievable using a single pump wavelength of 840 nm and changing the temperature of a single grating (in this case, with a period of 22 μm). Note that for the experiments reported in this thesis the resonant signal was in the lower range of the tuning curve shown in figure 3.4; the idler was at the longer wavelengths of the upper part of the curve.

The variation in the value of refractive index with wavelength also has an impact on the propagation velocity of an optical pulse. In the context of designing a crystal for this OPO, it was important that the temporal overlap of signal and the pump pulses was not lost as they propagated along the crystal, since high conversion efficiency in this system relies on this overlap (as discussed in section 3.3.5). Setting a temporal offset limit equal to half the pump pulse width leads to an expression for the maximum crystal length, L of the form

$$L = \frac{\tau_p}{2(\nu_p^{-1} + \nu_s^{-1})} \quad (3.6)$$

where τ_p is the pump pulse duration (full-width half maximum) and ν_p and ν_s are the group velocities of the pump and signal waves respectively. Using a longer crystal ($> L$) will result in a reduction of the gain.

3.3.4 Dispersion compensation

The ultrashort (≤ 1 ps) pulses propagating in the OPO are composed of a spread of frequencies. Consequently, the crystal and other cavity elements may give rise to considerable dispersion of the pulses. (Note that the term dispersion may be used in the context of describing the wavelength dependent properties of a crystal (material dispersion) or, secondly, the degree of change of the characteristics of a particular optical pulse.) This may result in a combination of pulse compression or broadening and distortion.

In order to be able to control the characteristics of the output signal pulse, it is necessary to include in an OPO cavity some means of compensating for this dispersion. To this end various geometrical optical systems have been devised. These include diffraction gratings, Gires-Tournois interferometers, chirped mirrors and systems of prisms. The latter is the standard method of intracavity dispersion compensation in

OPOs. Whilst the angular dispersion prisms provide is much smaller than that from a grating, they can provide more than sufficient compensation for the OPO used and are readily integrated into the design of an optical cavity of the dimensions of this OPO.

The concept of the technique is that by virtue of the different angles of refraction of each wavelength on entering the glass, each spectral component of a pulse will experience a different optical path length through the prism. By translating more or less prism glass into the path of the beam, this difference can be adjusted so as to recompress the temporal envelope of the pulse.

The OPO used in this work, was first operated (when constructed for a previous project) with only a single prism to effect dispersion compensation. The prism was placed in the cavity just before the output coupler. With this juxtaposition of the optical elements, the signal output wavelength could readily be selected by changing the angle of the output coupler since, after the prism, the different wavelengths were spatially divergent. However, the disadvantage of this configuration was that tuning the wavelength also resulted in slightly altering the direction of the output beam from the OPO.

By contrast, in some optical cavities a four prism sequence is used [5]. This results in no deviation or dispersal of the beam spatially, which may, for example, be important to sustain the broad bandwidth necessary for very short femtosecond pulses. However in the OPO cavity in this project, zero dispersal of the optical path was not a critically important factor in cavity design. In addition, retaining some spatial separation of the wavelengths assists with wavelength tuning.

A compromise of inserting two prisms was chosen. With this configuration, the approximately collinear spatial separation of wavelengths after the prisms was exploited for wavelength selection by insertion of a slit (shown in the schematic of the cavity in figure 3.5). The total dispersion in the cavity was calculated as the sum of contributions from the PPLN crystal and the glass from two prisms with a given separation, using the Sellmier equation for the PPLN (equation 3.5, following [4]) and second order phase derivatives for the crystal and the prism glass (see for example [6]). Only the second order dispersion was considered; the contribution of the third order dispersion being assumed to be insignificant for the duration of pulses in this cavity (~ 700 fs).

The calculated distance between the prisms for which the total dispersion was zero was used as a starting value for inserting the prisms in the cavity. Note however that the calculation depended strongly not only on the material parameters but on the estimate of the beam size, which was known only approximately. For example, at a crystal temperature of 150°C and wavelength of 1.5 μm , changing the beam spot size by a factor of 2 (from 1 mm to 0.5 mm) altered the result by $\sim 8\%$, and using an alternative empirical Sellmeier for PPLN [7] changed the length by $\sim 12\%$. Fortunately, the degree of dispersion contributed by the prisms was tunable by translating more or less prism glass into the beam path. This had to be balanced by the fact that continuing to increase the length of glass in the cavity introduced excessive losses. With the material used being SF10 glass, the prisms were set 200 mm apart in the cavity and approximately 6 mm (half from each prism) was found to provide satisfactory dispersion compensation.

3.3.5 Synchronously pumped singly resonant OPO

For the nonlinear conversion which generates the signal and idler waves to resonate, feedback is required. A plethora of different cavity configurations are possible for an OPO, as with laser systems. In this project, the signal frequency, and not the idler, was resonated. With this type of singly-resonant oscillator (SRO), it is generally possible to achieve a higher quality of output pulse and greater stability, since cavity elements can be adjusted more freely (only needing to favour a resonance of one wavelength).

When the single-pass gain experienced by the resonating wave exceeds the losses in the cavity oscillation occurs. However when only one wave is resonated the overall gain in the system is decreased (with respect to the case of there being both signal and idler resonant). Consequently, the threshold conditions in a SRO are higher. Nevertheless, the penalty of higher threshold was worth paying, since the superior output qualities, cited above, were very important for the experiments for which the OPO output was to be used.

The high threshold was overcome by intense pumping of the system. To this end, the cavity was constructed in a way such that the resonant signal wave was synchronous with the pulses of the pump laser. This design, called a synchronously pumped resonator, requires precise matching of the optical lengths of the OPO and pulsed laser

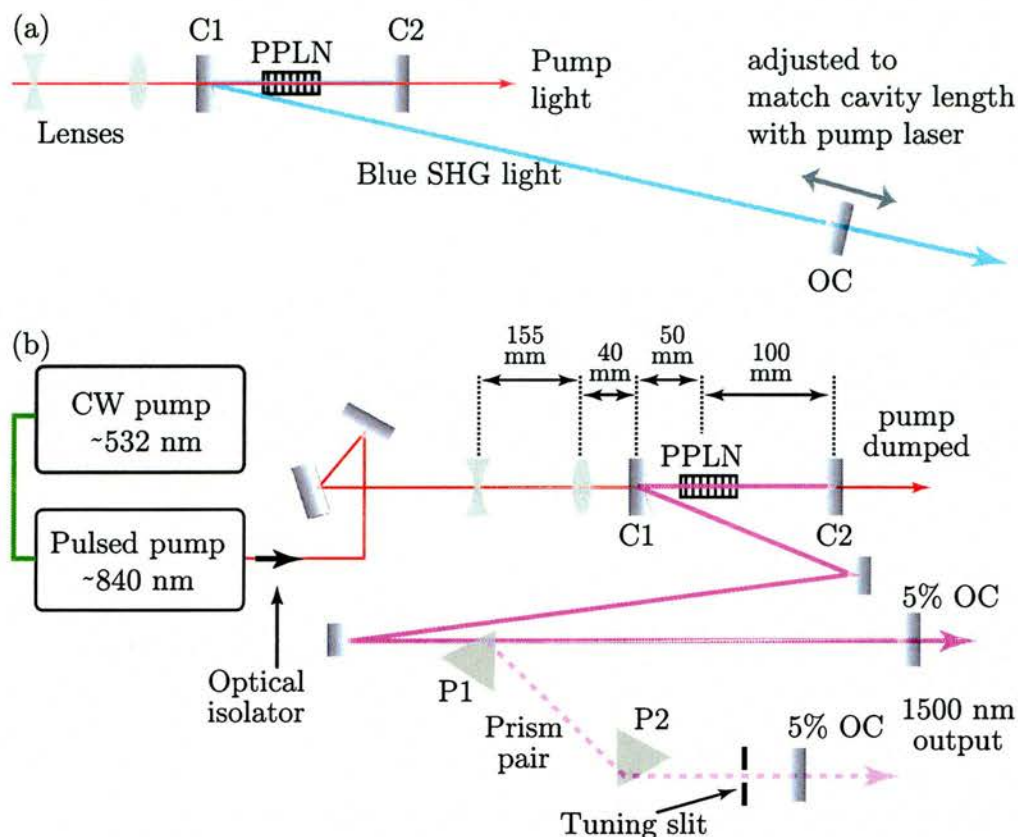


Figure 3.5: Cavity configuration of the OPO: the initial ‘V’ cavity (a) used for building the OPO and the subsequent ‘W’ cavity (b) to which the prism pair were added (dashed line) to complete the final OPO cavity.

cavities. In effect, the signal pulse is met by an arriving pump pulse on each round trip such that the gain experienced by the signal is replenished each time it returns to the OPO crystal. Commensurate with this, length matching of the OPO and laser cavities was required to an accuracy of hundreds of microns or better i.e. in order that pulses with durations 1 ps or less overlap in the crystal. Any mismatch leads to a reduction in conversion efficiency and, when too large, to cessation of the oscillation. However this sensitive operating criteria also corresponded to a tuning mechanism for the generated signal wavelength.

The underlying cavity used for the OPO, shown in figure 3.5(a), was a three mirror ‘V’ configuration: from the second curved mirror (C2) to the output coupler (OC). The PPLN crystal was situated between two focusing mirrors; the third mirror being set at a distance such that the length of the cavity was extended to match that of the

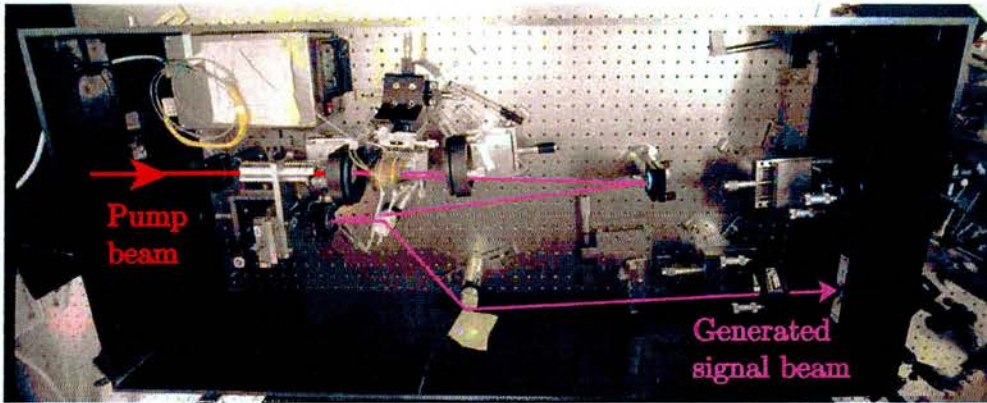


Figure 3.6: Photograph of the complete OPO cavity, as shown schematically in (b) in figure 3.5

pump laser (approximately 1.83 m). With the pump pulses focused into the crystal, frequency doubling occurs, generating blue light, which facilitates alignment of the cavity elements. The OPO was initially built in this shape and the alignment of beam expanding optics and focusing mirrors was optimised to maximise the signal power. The PPLN crystal was antireflection coated for the pump wavelength, to maximise the focused power in the PPLN; the pump light which passed through the crystal leaked out of the curved mirror on the far side (C2).

Subsequently the cavity was folded into a 'W' configuration, as illustrated schematically in figure 3.5(b). This final OPO cavity is shown in figure 3.6. The folding angles were kept as small as possible ($< 3^\circ$), to minimise astigmatism and losses at each reflection. After folding, the footprint of the cavity was only $\sim 1 \text{ m}^2$, even with the addition of the dispersion compensating prisms.

The prisms were added one at a time, each inserted at Brewster's angle to the beam path, to keep the losses to a minimum. The first prism (P1 in figure 3.5(b)) was used to pick off just a small part of the beam and allow the existing cavity to remain above threshold. The diverted beam could be used to align an output coupler in the new position i.e. such that it sent the beam back along its incident path to the prism. Only at this stage was the prism translated fully into the path of the beam. With the cavity length re-adjusted to match that of the pump laser, the generation would resume. This process was then repeated with the second prism (P2).

Once the cavity was assembled and access could be restricted, the OPO was boxed

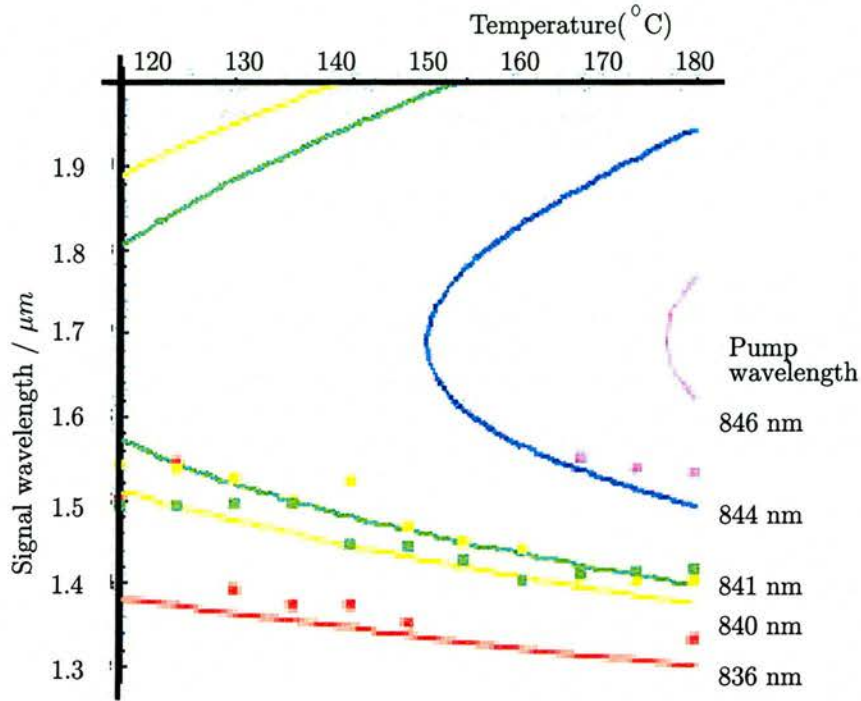


Figure 3.7: Calculated OPO tuning curve for grating $22.2 \mu\text{m}$: signal wavelength as a function of temperature for pump wavelengths between 836 and 844 nm. Data points (squares) indicate experimentally realised operation.

to minimise air currents, so improving stability. It was also important to reduce the chance of dust particles being caught in the higher power focused beams and burnt onto the optics.

3.3.6 Summary of methods for wavelength tuning

In the previous sections, a wide variety of mechanisms for tuning the wavelength of the OPO signal have been mentioned. To highlight the flexibility of the system, these mechanisms are reviewed.

As mentioned above, phase matching conditions can be altered by varying the temperature of the crystal and by adjusting the pump wavelength. In practice, these are used to optimise operation of the OPO in windows within an overall range, dictated by the chosen grating. For example, data points in figure 3.7 illustrate signal wavelengths achieved with grating period of $22.2 \mu\text{m}$, by adjustment of the temperature and pump wavelength. The curves in figure 3.7 are the phase matched operating points of the OPO calculated for the corresponding pump wavelengths and crystal temperatures.

For substantial changes in signal wavelength, the prisms in the cavity could be adjusted to maintain clean spectral and temporal characteristics of the pulse. Where possible the prisms were set to achieve near transform limited operation.

In addition a slit was added between the second prism and the output coupler (indicated in figure 3.5(b)). Due to slight spatial separation of the paths of different wavelengths, this gave an additional tuning mechanism. In particular using the slit it was found to be possible to disrupt generation of certain strong modes, which made operation at otherwise very weak modes sufficiently stable for the generated signal to be used for experiments. This was a very significant benefit of the redesign and rebuild of the OPO. In general, it is possible to tune to these ‘difficult’ wavelengths by other means, i.e. without the use of a slit, however it would take more time, making the acquisition of a set of data quickly, before other conditions change, hard to achieve.

In practice, small variations in wavelength were most readily achieved by alteration of the cavity length. When other elements in optical cavity were aligned to permit the oscillation of a range of wavelengths, the actual wavelength of operation could be selected by translating the position of the output coupler as long as the phase-matching criteria were maintained. Whilst the output power would tend to fall off at the edges of the range, tuning over tens of nanometres could be obtained. Since often the required output was only a few milliwatts average power, this was useful for many experiments.

3.4 The pump laser system

3.4.1 Optical pumping of the OPO

Implementation of the type of pulsed OPO used in this project is critically dependent on the availability of a stable, pulsed pump source. Indeed synchronous pumping of parametric generation was first demonstrated in 1972 [1], but practical systems have only been made possible by improvements in pulsed lasers. In this regard, the discovery of new techniques for modelocking, the mechanism for sustaining ultra short pulse generation in lasers, was key. (An explanation of mechanisms for modelocking can be found in reference [8].) In particular, in the 1990s, the development of self-modelocked Titanium:Sapphire lasers brought vastly improved stability [9]. In

addition the realisation of OPO systems suitable for use as a research tool was facilitated by the introduction, as the CW pump for the Ti:Sapphire, of all-solid-state lasers. These boast improved beam quality with respect to the gas lasers (e.g. Argon ion) that they replaced, and effect more efficient pumping of the Ti:Sapphire system.

The optical pulses to drive the OPOs used in this project were generated by a commercial all-solid-state laser system. The pump pulses for the OPOs were from a Titanium-Sapphire laser (*Spectra-Physics Tsunami*). This in turn was pumped by a diode-pumped, CW frequency doubled $Nd : YVO_4$ laser (*Spectra-Physics Millennium V* and subsequently *Millennia X*).

At the beginning of the work only one OPO (that described in section 3.3) was in operation. Although it was tunable to as low as $1.3 \mu\text{m}$, this OPO was optimised for working in the $1.5 \mu\text{m}$ wavelength range. Having a threshold of approximately 700 mW, it was pumped with pulses with average optical power of just over 1 W, generated by 5 W of CW pump (*Millennia V*). Subsequently, following the acquisition of a more powerful CW pump (*Millennia X*), which gave 10 W of optical power, it was possible to achieve 1.8 to 2.1 W of output from the Ti:Sapphire laser. This represented enough power to pump two OPOs to above threshold, and a second OPO designed to operate in the $1.3 \mu\text{m}$ range was built. Average OPO output powers were tens of milliwatts ($< 80\text{mW}$), depending on the chosen operating wavelength.

3.4.2 The CW pump laser

The 5 W and 10 W versions of the CW pump laser, despite construction differences, were based on the same diode-pumped four level laser system. The active medium was a Yttrium Vanadate crystalline matrix doped with Nd^{3+} ions ($Nd : YVO_4$). This has principal absorption bands in the red and near infrared, an accessible region for laser diodes to be used as the primary pump. The *Millennia V* and *Millennia X* lasers use custom designed laser diode bars (*Spectra-Physics FcbarTM*) to pump the absorption band at approximately 815 nm. The 10 W output is achieved by doubling the power of these diode pump bars.

In the $Nd : YVO_4$, the excited electrons drop quickly to the upper level of the lasing transition, the $F_{3/2}$ level, where they remain for a relatively long time (appxi-

mately 60 μs). From this inverted state, the most probable transition is by emission of a photon at 1064 nm, to the $I_{1/2}$ state. Cavity optics are used, in the *Millennia* lasers, to limit lasing to this transition. The 1064 nm beam was frequency doubled, in a Lithium Triborate crystal, to produce an output in the green, at 532 nm.

3.4.3 The Titanium:Sapphire pulsed laser

The crystal in the Ti:Sapphire laser (*Spectra-Physics Tsunami*) is made by introducing Ti_2O_3 into a melt of Al_2O_3 , in order that some of the Ti^{3+} ions are substituted for by Al^{3+} ions. As a result, the electronic ground state is split into a pair of broad vibrational levels. Absorption transitions in the crystal can occur over a wide range of wavelengths from 400 to 600 nm. In the case of using a *Millennia* laser, the absorption is pumped at 532 nm. Subsequent fluorescence transitions occur from the vibrational levels of the excited state to the upper vibrational levels of the ground state. The resultant emission occurs in a range from 670 to 1100 nm. Due to the set of mirrors chosen for the cavity, lasing could be obtained in the range of 720 to 850 nm, however pulsed operation was optimum for the longer wavelength part of this range.

Wavelength tuning is achieved by means of a birefringent filter. The filter consists of a stack of crystalline quartz plates, which have been cut parallel to their optical axis. The filter is placed in the laser cavity, at Brewster's angle, and birefringence of the quartz causes the polarisation of the incident cavity beam to become, in general, elliptical. For a given thickness of the plates, a narrow range of wavelengths experience a complete 180° polarisation rotation, or multiple thereof; these wavelengths remain linearly polarised. All other wavelengths are left elliptically polarised and consequently suffer losses at each Brewster angled surface in the cavity. Only those wavelengths which remain linearly polarised, and as a result experience relatively lower losses on each round trip through the cavity, reach lasing threshold. Altering the wavelength for which these conditions are met was achieved by rotating the filter about an axis normal to the plates.

The pulses are sustained through a modelocking process, assisted by an acousto-optic modulator. For the experiments described in this thesis, the Ti:Sapphire laser was configured to produce picosecond pulses (~ 1 ps). In this configuration, the negative

group velocity dispersion (GVD), necessary to give sufficient dispersion compensation to obtain near transform limited pulses, is provided by a Gires-Tournois interferometer (GTI). This is similar to a Fabry-Perot interferometer except that, instead of high reflector, the first mirror in a GTI is a partial reflector. Consequently the GTI is highly reflective over a broad spectral range, but still provides an optical phase shift which is wavelength dependent. This was adjusted by changing the separation of the mirrors, to optimise output pulse characteristics.

Due to the cavity length (~ 1.8 m), the repetition rate of the pulsed operation was set at 81.3 MHz (corresponding to 12.3 ns between output pulses). The output of the laser being linearly polarised vertically, due to the nature of its cavity, half-wave plates were used to obtain the horizontal polarisation required for the OPOs. Also, an optical isolator was placed directly after the Ti:Sapphire laser to prevent any instability caused by feedback from the OPOs.

3.5 Diagnostics

3.5.1 Spectrum measurements

The spectrum of the pulses from both the Ti:Sapphire pump laser and the OPO could be measured using a spectrometer (*Rees Instruments, Laser λ meter*, spectral range from 800 to 1600 nm). This was used for tuning the sources, since with the output of the spectrometer connected to an oscilloscope a real time image of the spectrum could be viewed. Ideally an approximately Gaussian spectrum was obtained. Asymmetry in the pulse shape, side bands or other distortions were indicative of the pulse being significantly chirped. Adjustments in the cavity, in particular of the amount of prism glass, were made to improve the profile of the pulses.

For higher resolution measurement of spectra a scanning monochromator was available, however due to the slower acquisition time this was mostly reserved for single pulse spectral experiments (described in Chapter 6). However, the calibration of the small spectrometer was checked against the higher resolution monochromator (and data corrected accordingly).

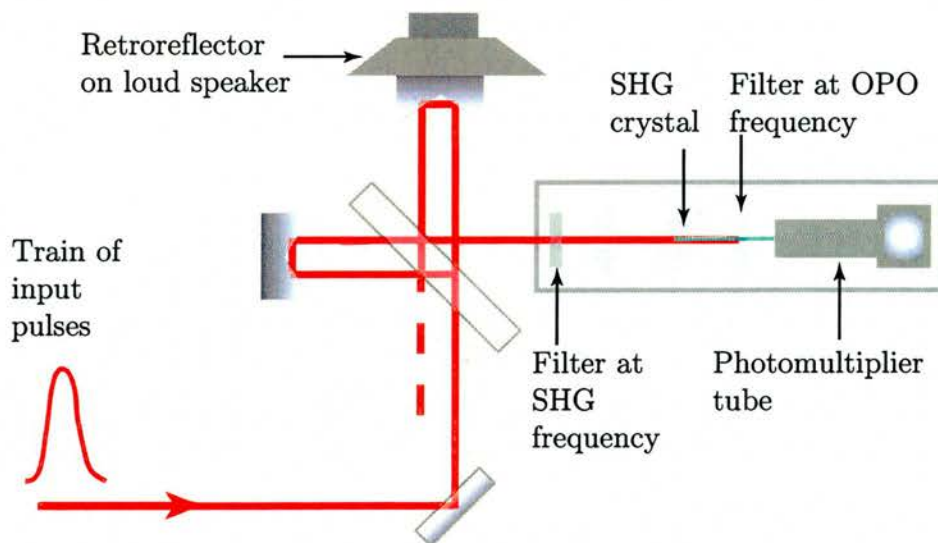


Figure 3.8: Schematic of the experimental configuration used to measure the autocorrelations.

3.5.2 Autocorrelation for temporal measurements

The choice of method used routinely for temporal measurements merits some discussion. In order to measure the duration of an event in time it is usual to compare it with a shorter event. However ultrashort optical pulses are the fastest man-made events so measuring them presents significant challenges.

Information about a train of pulses can be obtained using a photodiode and oscilloscope, if the repetition rate is sufficiently slow. However, the fastest photodetectors operate at 50 GHz giving too slow a response time to give temporal information about actual pulses with durations of a less than several tens of picoseconds or shorter. Streak cameras can provide direct linear measurements of pulses as short as 1 ps, or even 0.5 ps in single-shot mode. However it was imperative to have routine, preferably real time, measurements of the pulses from the Ti:Sapphire pump laser which had durations of around 1 ps and from the OPO from which pulses could be even shorter; for this we used an autocorrelation technique. This is a simple technique that is widely used and enables real-time pulse characterisation [10] [11] [12].

Mathematically an autocorrelation compares two copies of a data set with each other, running one through the other and detecting the degree of correlation at each point. In the case of an optical pulse, the signal is split into two copies and recombined

with a variable delay between them. That is to say, since there is no readily harnessable shorter event, a copy of the pulse is used as the reference in the measurement process. This is a neat concept, but it does introduce an ambiguity: it is necessary to make assumptions about the shape of the pulse being measured.

In practice the optical autocorrelation was performed using a Michelson type delay arrangement, illustrated schematically in figure 3.8. The pulses were split equally at a beamsplitter, one travelling to a fixed retroreflector (corner cube mirror) and the other to a retroreflector mounted on an oscillating loud speaker cone. On reflection the pulses recombined at the beamsplitter and were made to interfere on a nonlinear detector, which due to the nonlinearity was very sensitive to the degree of overlap of the pulses. When there was zero delay between the copies, there was a maximum detector response; no overlap gave the minimum background level of signal. In this way, a temporal measurement was transformed into a spatial measurement. For example, a time of 1 ps, too fast to be measured by regular electronics, corresponds to light covering a distance of 0.3 mm, a magnitude visible even to the naked eye and certainly readily measurable.

The nonlinear detectors were constructed from crystals which gave a Second Harmonic Generation (SHG) signal, KDP and BBO for pump pulse and OPO output wavelengths respectively [11][13]. Photomultiplier tubes, preceded by filters, were used after the crystals to increase sensitivity to the generated signal. This detector combination remains the more sensitive, but semiconductor devices that can detect to two-photon absorption of the OPO wavelength can be used for autocorrelation measurements and appropriate devices have become commercially available [14][15]. These have been implemented as the nonlinear detector for the cross-correlation of pulses input and output from the SOA. A practical advantage of moving to the use of semiconductor two-photon detectors is that it obviates the use of the long photomultiplier tubes, which means that diagnostics need not take up so much space on the optical bench. Moreover, the semiconductor detectors for the near infrared are polarisation insensitive and inexpensive, relative to the photomultiplier tube option.

In all cases, the signal from the optical detector was displayed on an oscilloscope, triggered by the electrical signal driving the loudspeaker. The autocorrelator was cal-

ibrated by translating the normally stationary mirror and observing the movement in the autocorrelation trace on the oscilloscope display.

The type of autocorrelation recorded depends on the response time of the total configuration. In order to understand this, consider that the electric field corresponding to the two overlapping pulses may be expressed as

$$E(t) + E(t - \tau) \quad (3.7)$$

where τ is the delay of the second pulse with respect to the first and $E(t) = \xi(t) \cos(\omega_0 t + \phi(t))$. The nonlinear signal, due to the overlap of the two pulses, is given by

$$G(\tau) = \int_{-\infty}^{\infty} |[E(t) + E(t - \tau)]|^2 dt = \int_{-\infty}^{\infty} |[\xi(t) \cos(\omega_0 t + \phi(t)) + \xi(t - \tau) \cos(\omega_0(t - \tau) + \phi(t - \tau))]|^2 dt \quad (3.8)$$

In the case of slow frequency response of the detection system, which was generally the case, the rapidly varying terms in equation 3.8 cannot be resolved. Consequently the autocorrelator records the time-averaged intensity autocorrelation described by

$$G_i(\tau) = 1 + 2g(\tau) \quad (3.9)$$

where $g(\tau)$ is the back-ground free intensity autocorrelation function defined by

$$g(\tau) = \frac{\int_{-\infty}^{\infty} [I(t) + I(t - \tau)] dt}{\int_{-\infty}^{\infty} I(t)^2 dt} \quad (3.10)$$

Since these expressions, equations 3.9 and 3.10, are dependent only on intensity, no information about the chirp of the pulse remains. In aligning the optical elements, care is taken to achieve a ratio between the background and the peak as close as possible to the ideal (3:1) since deviations from this correspond to degradation of the measurement.

The relationship between a measured intensity autocorrelation width Δt_i and the full width half maximum (FWHM) pulse duration $\Delta \tau_p$ is given by

$$\Delta \tau_p = \frac{\Delta t_i}{k_i} \quad (3.11)$$

Field envelope	Intensity profile	k_i	$\Delta\tau_p\Delta\nu$
Gaussian	$\exp(-\frac{t^2}{\tau^2})$	$\sqrt{2} \simeq 1.414$	0.441
Sech ²	$\text{sech}^2(-\frac{t^2}{\tau^2})$	1.543	0.315

Table 3.1: Correction factors, k_i , for autocorrelations of Gaussian and sech² pulse shapes

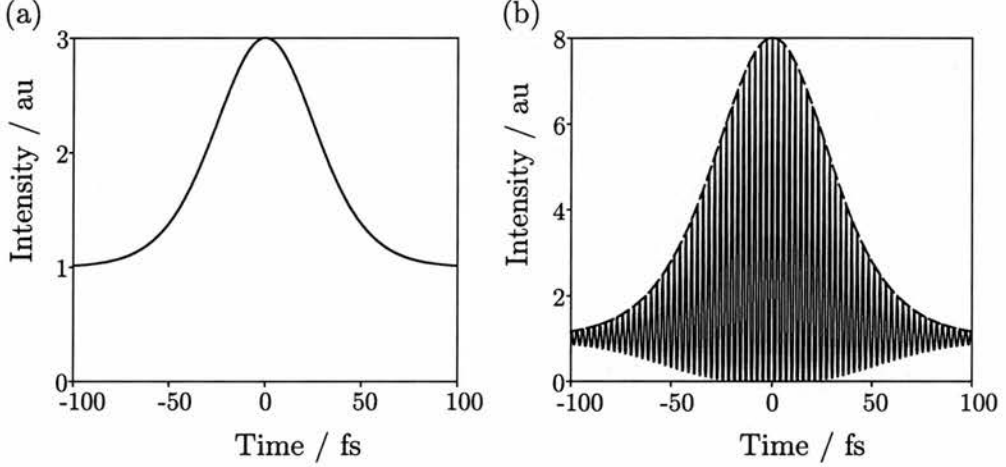


Figure 3.9: Ideal (a) intensity and (b) interferometric autocorrelation traces.

where k_i is a constant depending on the pulse shape [16].

Since the autocorrelation is symmetric about $\tau = 0$ it contains no useful information about pulse shape. It is therefore necessary to assume a pulse shape and k_i factors for typical pulse shapes are shown in table 3.1. Simultaneous spectral information can corroborate the assumed shape, through the time-bandwidth product associated with different pulse shapes. It should be noted however that this gives only a qualitative assessment of chirp of the pulse.

An autocorrelation in which the interference fringes are resolved, can be obtained by improving the response time of the measurement system. This was achieved by impedance matching the oscilloscope with the detector and photomultiplier tube. The resulting signal, known as an interferometric autocorrelation is given by

$$G_f(\tau) = \frac{\int_{-\infty}^{\infty} |[\xi(t) \cos(\omega_0 t + \phi(t)) + \xi(t - \tau) \cos(\omega_0(t - \tau) + \phi(t - \tau))]|^2 dt}{2 \int_{-\infty}^{\infty} \xi^4(t) dt} \quad (3.12)$$

This corresponds to $G(\tau)$ (given in equation 3.8) normalised to give a background of one. For an unchirped pulse the contrast ratio, given by the envelope of the fringes,

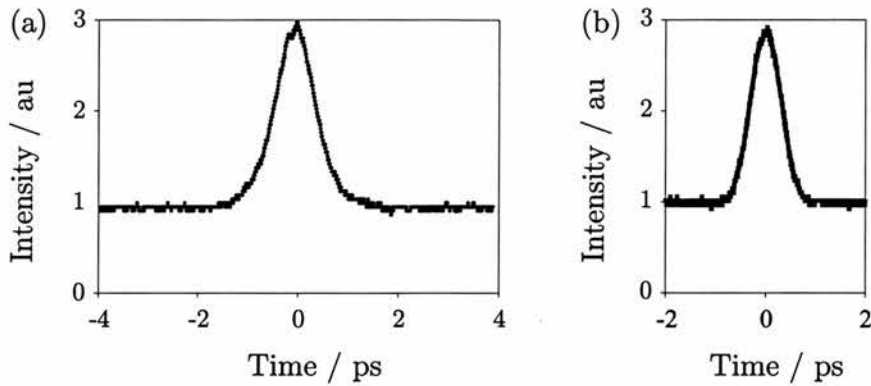


Figure 3.10: Typical autocorrelations of pulses from (a) the Titanium:Sapphire Laser and (b) the Optical Parametric Oscillator. The pulse shortening in the OPO is such that the Full Width Half Maximum of (b) is less than that of (a)

yields a contrast ratio of 8:1, in contrast to the 3:1 ratio for the intensity case. For comparison ideal intensity and interferometric autocorrelations, for a Gaussian shaped input pulse, are shown in figure 3.9.

The higher peak to background ratio, relative to the intensity measurement, and the fact that phase information is not averaged out, make the interferometric measurement more sensitive to pulse shape. Chirp can be manifested as interference between individual fringes, and interpreting the autocorrelation can be complicated. In addition, due to the faster response time of the set-up the pulse-to-pulse stability also has more influence on the trace. From time to time, the interferometric autocorrelations were set up. In general however, since the OPO output was not power or directionally stable, routine monitoring of pulse duration was performed using intensity autocorrelations.

Figure 3.10 shows typical autocorrelation traces for pulses from the Titanium:Sapphire pump source (a), and from the OPO (b). In practice, the peak to background ratio was not always ideal for the OPO trace used for monitoring. This was due to the fact that the monitoring autocorrelation measurement was taken using a very small fraction of the total OPO output power; the rest of the power being taken for experiments. This adds a larger margin of uncertainty into the measurement of the OPO pulse width. However it is believed that any additional error introduced in this way was small since the low power monitoring measurements were compared with the values obtained using all the output power of the OPO, and the pulse widths obtained

were not significantly different.

In general, as illustrated in figure 3.10, the temporal width of the pulse from the OPO is significantly shorter than that of the pulses with which it is pumped. Optimisation of the cavity elements for operation at a particular wavelength determined the degree of this pulse shortening effect. The OPO pulse duration, calculated from an autocorrelation measurement with the assumption of Gaussian pulse shape, was sometimes less than 400 fs, compared with pump pulses of ~ 1 ps.

3.5.3 Monitoring program

The knowledge of the output from OPO source was critical to the experimental analysis and unfortunately pulse characteristics could not be prevented from changing over time. For example, the commercial systems (used as pump sources) claim a warm up period of at least half an hour, during which time the optical power and beam direction in particular are likely to change. Although the laboratory was air conditioned, environmental factors seemed to cause such drift to continue at all times, to greater or lesser degrees. Whilst the mode-locking of the pump laser was generally fairly stable, on occasion it 'dropped out' leading to a momentary fall in power from the OPO. In addition, variation in cavity length of the pump laser, attributed to thermal effects, was apparent throughout operation. This caused changes in OPO wavelength by the same mechanism as that exploited for tuning (described in section 3.3.6). There tended to be a corresponding change in OPO output power, as phase-matching became non optimal. Additionally, if the change brought the signal wavelength away from dispersion compensated conditions the pulse became severely chirped.

For some measurements, for example single pulse propagation, information about the source pulses at an instant could be sufficient. However for the pump-probe experiments, described in Chapter 7, more continuous information was required. Consider that to monitor time dynamics over 500 ps took several minutes with a mirror moving 15 cm (the distance light travels in 500 ps) in micrometre steps, pausing at each step to allow the signal to settle and the lock-in amplifier to obtain data. Moreover, if a series of experiments is to be performed which might be highly dependent on input pulse characteristics, it is critically important to determine if the input used is the same for

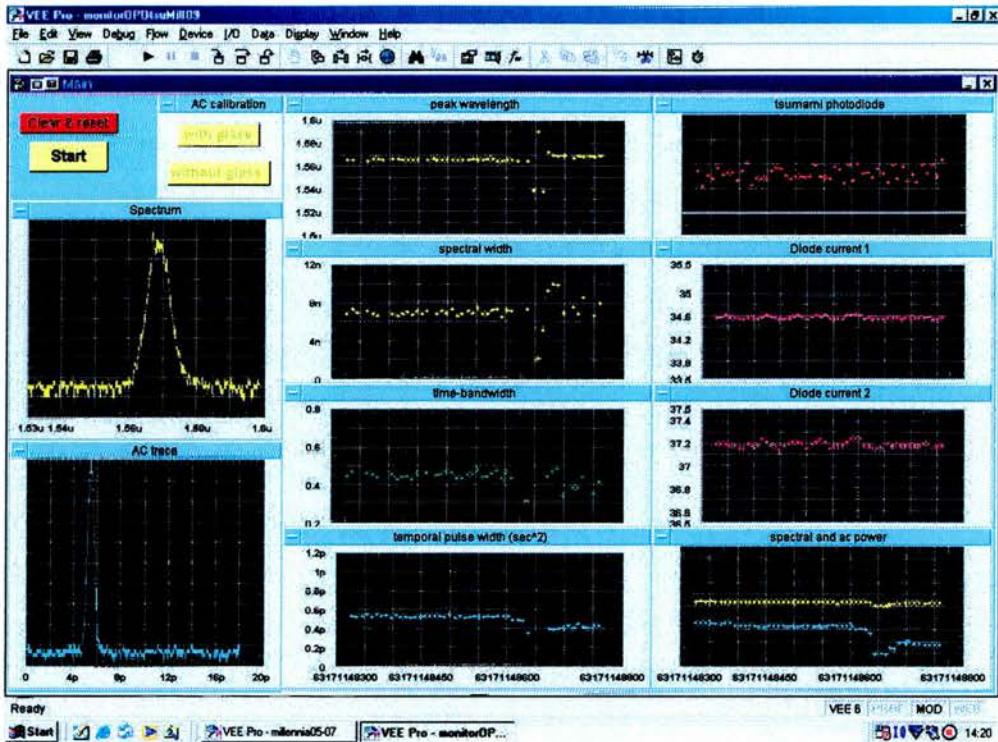


Figure 3.11: The front panel of the program (VEE) for continual monitoring of the characteristics of the pulses from the OPO, and the operating conditions of the CW and pulse pump lasers.

each measurement.

Consequently, it proved very important to develop a system of monitoring the optical source. The front panel of the program used to view monitoring data, in near real time, is shown in figure 3.11 and summarises the types of data recorded. The program was written in *Agilent VEE*, a visual programming language, suitable for interfacing with equipment through GPIB connections.

The data feed into the program was as follows:

- From the OPO: the spectrum, autocorrelation and corresponding trigger signals
- From the pulsed pump source: the signal from the internal photodiode monitoring the output signal
- From the CW pump source: currents drawn by the two diode bars and the optical output power

All data was time stamped using the computer's internal clock. The clocks of the

computers used for the collection of this monitoring data and for experiments were regularly synchronised. This was performed using AboutTime [17], a program which takes signals from a networked time server for synchronisation of networked computers (with accuracy of ± 50 ms).

The signals from the spectrometer provided spectrum and calibration thereof. Approximately every eight seconds (depending on the time taken to trigger correctly), the peak wavelength, the spectral full-width half maximum (FWHM) and the integral of the spectrum were calculated, displayed and saved to file. Likewise, the FWHM of the autocorrelation and integral of the temporal pulse were displayed and recorded every eight seconds. The signals from the autocorrelator were calibrated with respect to a time delay incurred by introducing into the beam path a glass slide of known thickness and refractive index. Full spectrum and autocorrelation traces were only recorded approximately four times per minute to reduce the total accumulation of data.

The spectral FWHM and temporal FWHM, with use of a factor for conversion to a temporal pulse width, were used to calculate a time-bandwidth product. As discussed above, the factor relating temporal FWHM to pulse width depends on the pulse profile. In post experiment analysis, the autocorrelation traces were fitted to decide which factor to apply and usually the best fit was Gaussian. Variation in this estimate of the time-bandwidth product was useful since it was indicative of changes in the chirp of the pulses, during experiments. If the value was far from the transform limited value it was indicative that the OPO was producing significantly chirped pulses and the dispersion could be adjusted. Moreover, if this value was suddenly seen to change, it was a warning that a trend appearing in an experiment at that point might be due to change in pulse characteristics as opposed to any other parameter being purposefully varied. Measurements could then be repeated, in order that a full data set was obtained under stable input conditions.

The diode currents from the CW source primarily gave an indication of environmental changes. In particular, despite air conditioning, the main laboratory was not immune to external conditions e.g. weather or settings of the heating system for the entire building being altered. The currents were found to be a useful indicator of when the influence of swings in temperature and humidity became so severe that stability

in pulse characteristics, sufficient for use in experiments, could not be achieved. Also very rapid increases in the currents indicated failure of the diode bar itself. Since the lifetime of these components did not prove to be very reliable during the course of this project, this was useful information; steps could be taken to prepare for the installation of a replacement part, minimising downtime of the system.

The photodiode signal from the pulsed pump source increased as the laser warmed up to full power. Over subsequent hours this signal indicated variations in the output which could be due either to change in the beam direction or change in power. However both changes represented a reduction of the power correctly focused into the OPO crystal and a resultant fall in output from the OPO. Significant falls in this photodiode signal tended to indicate that the Ti:Sapphire laser need to be realigned or cleaned. In extremis, falls in this signal gave an early warning that the quality of the CW pump beam was degrading e.g. the beam profile was changing (and this facilitated prompt repairs, as noted above).

To facilitate use of the wealth of data from the monitoring during data analysis, a program was written to select the monitoring data corresponding to a given window of experimental time. For example, an experimental data file could be plotted on the same time axis as peak wavelength, temporal pulse width and optical power (as indicated by the integral of the autocorrelation and spectral measurements). For this time window, mean and standard deviation values of the monitoring data were automatically calculated and displayed, as shown in figure 3.12.

A set of criteria could then be used for an experiment, such as requiring a standard deviation of the peak wavelength no greater than 2 nm. This was particularly useful in circumstances where each of several experiments yielded a single value for a parameter (e.g. pump-probe traces fitted to ascertain a time constant). When using the data from all experiments the trend in the parameter was often ambiguous; if data from those experiments which did not meet the criteria, for stable pulse characteristics throughout the measurement, were rejected, the subset of data retained tended to present a much clear trend. In this way anomalous data could be discarded during processing, using objective criteria.

The effort expended on setting up this monitoring system has paid off, by reducing

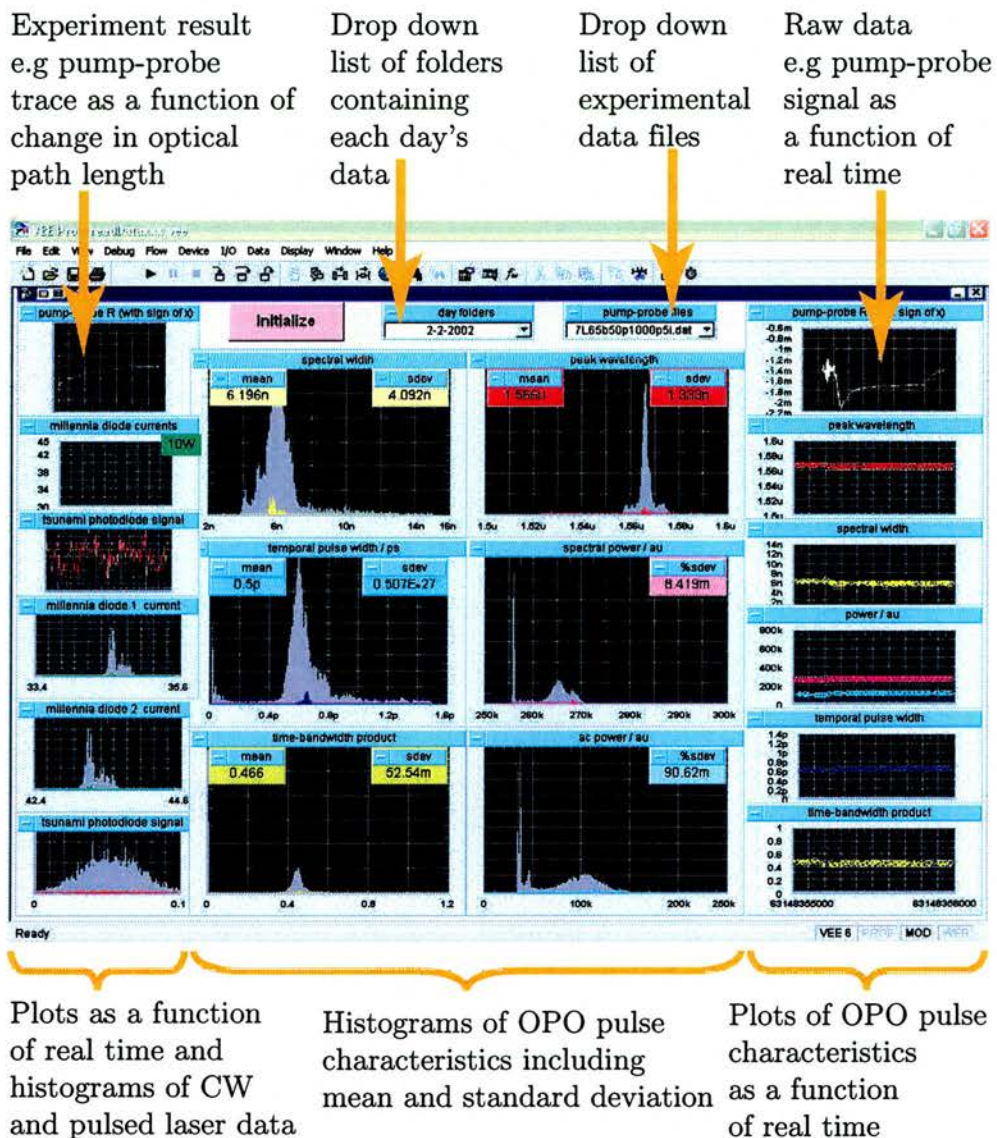


Figure 3.12: The front panel of the program (VEE) for viewing the characteristics of the optical pulse source during the time period of a given experiment. The histograms in bright colours correspond to the data collected during the experiment; the grey histograms in the background are the data collected during a full day. Note that the x axis of the six graphs on the right hand side corresponds to computer time in seconds.

the time spent trying to achieve experimentally usable output from the OPO, since it was possible to rigorously assess the stability of the system at any time. Far fewer excessively noisy data sets were acquired and even those that appeared dubious did not need to be rejected outright since sufficient monitoring data was recorded to filter out the unreliable experiments. As a check, even for data which appeared 'clean' the pulse input characteristics were assessed using the data acquired using this monitoring system. Most importantly then, the continual monitoring of the OPO pulses has made possible a high degree of confidence that trends observed in the experimental data are real, not due to systematic changes in the pulse source.

3.6 Summary

In this chapter, the development of the optical pulse sources, for experiments detailed in subsequent chapters, has been described. It was highlighted that advances in both nonlinear materials and ultrashort pulse lasers, have been critical in realising synchronously-pumped optical parametric oscillator systems suitable for studying semiconductors, as well as many other applications. The OPO system was optimised to give 10-80 mW average power, with pulse durations of 350-1000 fs, over wavelengths from 1490 to 1580 nm. The use of a prism pair in the OPO cavity to control dispersion of the pulses has been explained.

Measurement of the output pulses from the OPO, in spectral and temporal domains, has also been described. Stability in these characteristics over the time necessary for conducting experiments was critical, but was not readily obtained. The system that was therefore developed to monitor the all of the key parameters of the pulse generation system has been detailed. Lastly, the method by which the monitoring data was used to certify that changes in the characteristics of the output pulses from the OPO were within reasonable limits, and did not distort experimentally measured trends, has been outlined.

Bibliography for Chapter 3

- [1] K Burneika, M Ignatavichyus, V Kabelka, A Piskarskas, and A Stabinis. Parametric light amplification and oscillation in KDP with mode-locked pump. *IEEE J. Quantum Elect.*, 8:574, 1972.
- [2] M H Dunn and M Ebrahimzadeh. Parametric generation of tunable light from continuous-wave to femtosecond sources. *Science*, 286:1513–1517, 1999.
- [3] D T Reid, G T Kennedy, A Miller, W Sibbett, and M Ebrahimzadeh. Widely tunable, near- to mid-infrared femtosecond and picosecond optical parametric oscillators using periodically poled $LiNbO_3$ and $RbTiOAsO_4$. *IEEE J. Sel. Top. Quant.*, 4(2):238–248, 1998.
- [4] D H Jundt. Temperature-dependent Sellmeier equation for the index of refraction, n_e , in congruent lithium niobate. *Opt. Lett.*, 22(20):1553–1555, 1997.
- [5] R L Fork, O E Martinez, and J P Gordon. Negative dispersion using pairs of prisms. *Opt. Lett.*, 9(5):150–152, 1984.
- [6] R L Fork, C H Brito Cruz, P C Becker, and C V Shank. Compression of optical pulses to six femtoseconds by using cubic phase compensation. *Opt. Lett.*, 12(7):483–485, 1987.
- [7] M Lawrence. Short communication - A temperature dependent dispersion equation for congruently grown Lithium Niobate. *Opt. Quant. Electron.*, 16:373–374, 1984.
- [8] A Yariv. *Quantum Electronics*. Wiley, New York, 3rd edition, 1989.
- [9] D E Spence, P N Kean, and W Sibbett. Regeneratively initiated self-mode-locked Ti:Sapphire laser. *Opt. Lett.*, 16(42), 1991.
- [10] M Maier, W Kaiser, and J A Giordmaine. Intense light bursts in the stimulated Raman effect. *Phys. Rev. Letts.*, 17(26):1275–1277, 1966.
- [11] R L Fork and F A Beisser. Real-time intensity autocorrelation interferometer. *Appl. Optics*, 17:3534–3535, 1978.
- [12] J-C Diels and W Rudolph. *Ultrashort laser pulse phenomena*. Academic Press, London, 1996.
- [13] M Raghuramaiah, A K Sharma, P A Naik, G P Gupta, and R A Ganeev. A second-order autocorrelator for single-shot measurement of femtosecond laser pulse durations. *Indian Academy of Sciences: Sadhana-Academy Proceedings in Engineering Sciences*, 26(6):603–611, 2001.
- [14] Y Tomita, M Shibata, and J Bergquist. Pulswidth dependence of the time-resolved two-photon absorption with picosecond pump-probe excitation. *J. Appl. Phys.*, 71(5):2102–2105, 1992.
- [15] D T Reid and W Sibbett. Commercial semiconductor devices for two photon absorption autocorrelation of ultrashort light pulses. *Opt. Photonics News*, 9(5):SupL6–8, 1998.
- [16] K L Sala, G A Kenney-Wallace, and G E Hall. CW autocorrelation measurement of picosecond laser pulses. *IEEE J. Quantum Elect.*, 16(9):990–996, 1980.
- [17] AboutTime. <http://www.arachnoid.com/abouttime>. CareWare synchronisation program, March 2003.

Chapter 4

Device characterisation

4.1 Introduction

This chapter reports a range of experiments undertaken to measure the spectral characteristics of the SOA device. The degree of difference in the device properties for TE and TM polarisation directions is discussed, with reference to the band structure of the active material, a strained InGaAs superlattice.

Measurements of the amplified spontaneous emission and transmission of a continuous wave beam yield information about the wavelength and bias dependence of the gain. More sensitive information about the state of the material, whether it is absorbing, amplifying or transparent to an optical beam, are obtained from measurements of the electrical signal across the device. The wavelength and optical power dependence of the electrical bias required for transparency are investigated.

4.2 Description of SOA structure

The SOA device focused on in this project is an InGaAs multiple quantum well (MQW) superlattice structure. The substrate is InP and the active region consists of a stack of 10 wells and 11 barriers of InGaAs: the wells are 4 nm of unstrained material and the barriers are 6 nm with -0.67% strain. This unstrained well/strained barrier combination results in strong gain in the TM mode, whilst retaining significant gain the TE mode, as is seen in the results discussed in this chapter.

Figure 4.1 shows the complex design of the SOA structure. The structure was grown by atmospheric pressure metallo-organic vapour phase deposition (MOVPE)

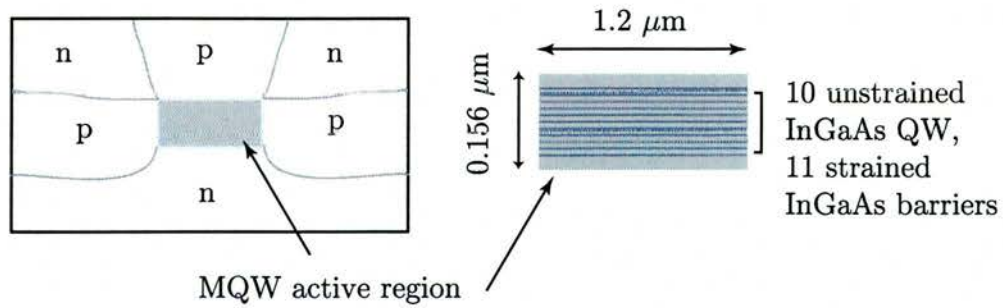


Figure 4.1: End view of the waveguide illustrating the buried heterostructure composed of n- and p-type material. This provides electrical and optical confinement.

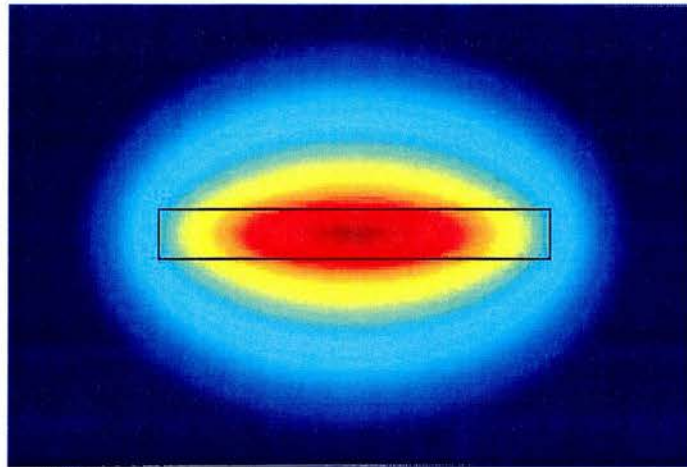


Figure 4.2: Calculated field, E_z for the TM mode in the SOA waveguide.

[1]. This pattern of n- and p-type material around the active region creates a separate confinement heterostructure [2], which provides carrier and optical confinement to the active region. Calculations demonstrate that light at $1.56 \mu\text{m}$ is waveguided in a single mode by the structure illustrated in figure 4.1, with the effective refractive index of the active region taken to be between 3.2 and 3.4 and values for the cladding between 3.5 and 3.65. For example, figure 4.2 illustrates the field, E_z for the TM mode with the indices for core set to 3.2 and the cladding to 3.6. These calculations were carried out by Michael Mazilu using *Femlab* (a *Matlab* based software package).

The waveguide, including the active region, is oriented at an angle of 10° . The purpose of this orientation, which creates angled end facets to the waveguide, is to inhibit lasing under conditions of forward electrical bias [2]. In addition, a single layer antireflection coating was grown on the end facets to further optimise the device as a travelling wave SOA [3].

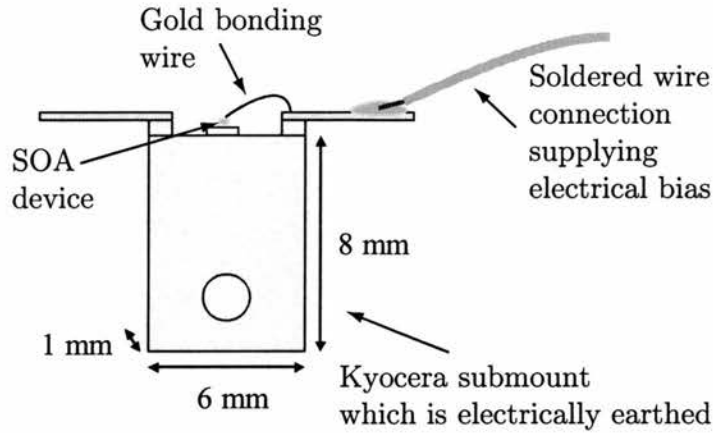


Figure 4.3: Schematic of the SOA on a *Kyocera* submount with bonding wires

4.3 Mounting of the device

To ensure thermal stability when the device was driven with high electrical currents, and under intense optical pumping, a brass mount was designed to hold the SOA. A Peltier cooler, driven by a temperature controller, was sandwiched between two electrically isolated layers of the brass mount and a thermistor was located close to the device itself. A *Kyocera* submount was used as the base in direct contact with the device, providing good thermal and electrical conductivity. Bonding wires were attached to the submount and thence to the top of the device, as illustrated schematically in figure 4.3. The *Kyocera* submount was coated with thermal paste and held in place in the brass mount by a retaining plate to ensure good thermal contact.

A factory-aligned three-block waveguide manipulator was used for coupling light in and collimating output from the device. The brass mount, holding the SOA device, was secured to the central block which had x and y positioning and rotation. Microlenses, used to couple light into the waveguide and collimate the output, were mounted on each end block, with x, y and z adjustment. This complete set-up is shown in figure 4.4.

For some experiments the light arrived at and left from the waveguide manipulator as a free space beam. In other cases, as illustrated in figure 4.5, mounts for FC connected fibres and fibre couplers were added to the end blocks. There remained space, in the centre of the end blocks, for half-wave plates to adjust the linear polarisation in

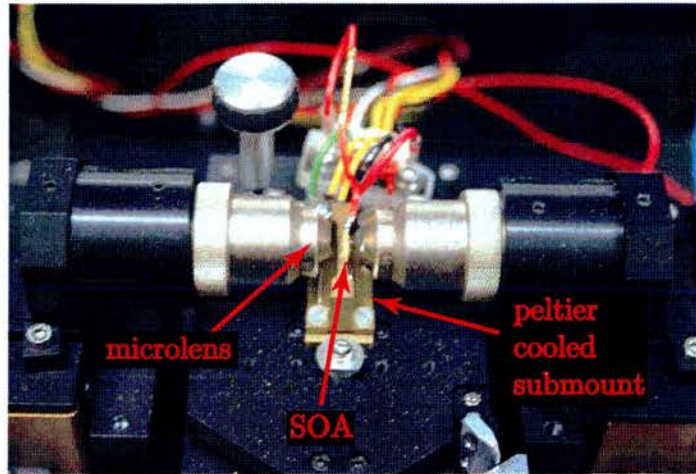


Figure 4.4: Photograph of the mounting of the SOA

and out of the device.

Fibres were used to couple light out of the device into connectorised diagnostic equipment, for example a spectrometer, and to isolate the coupling of the light into the device from variation in the beam direction of the light from the OPO pump source. The length of fibre used was 1 metre or less, and the dispersive effect of the fibre was expected to be minimal. This was confirmed by comparison of the input and output pulse characteristics, as illustrated in figure 4.6. In addition, the fibres used were polarisation maintaining in order that the linear polarisations of the optical beams used would be preserved. A strong advantage of using fibres was that the coupling of light into the waveguide was isolated from changes in the direction of the beam from the optical source, since the coupling of light into the device was independent of the coupling into the fibre. This was particularly important when major adjustments were made to the OPO cavity during a series of experiments, for example to tune the wavelength by tens of nanometres.

4.4 Coupling efficiencies

Coupling efficiencies to the SOA were estimated using the amplified spontaneous emission to assess the coupling of light between the fibre and the active region of the device, combined with measurements of the coupling of the source light into the fibre, as illustrated schematically in figure 4.7. The output coupling efficiency,

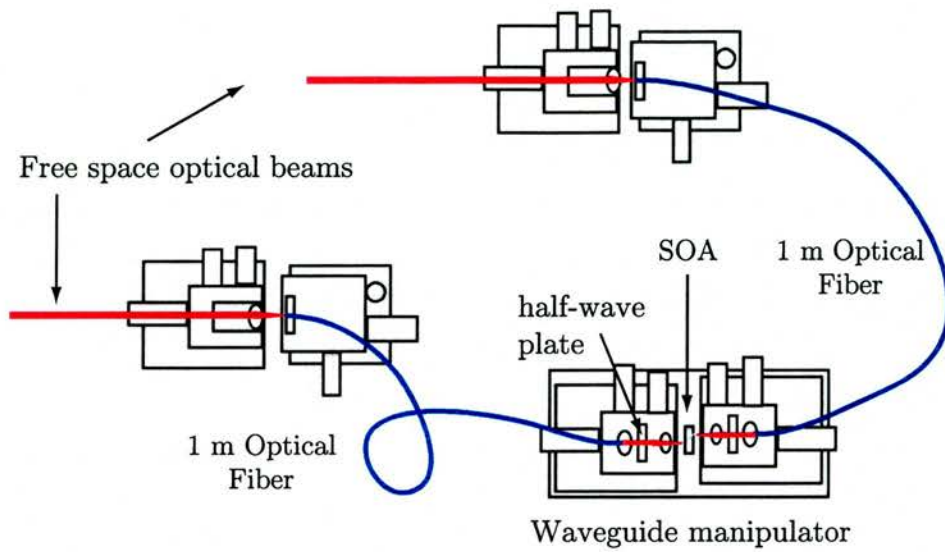


Figure 4.5: Schematic illustrating the experimental set-up for coupling into the device. Half-wave plates mounted on the waveguide manipulator enable the angle of the linear polarisation to be rotated with respect to the device.

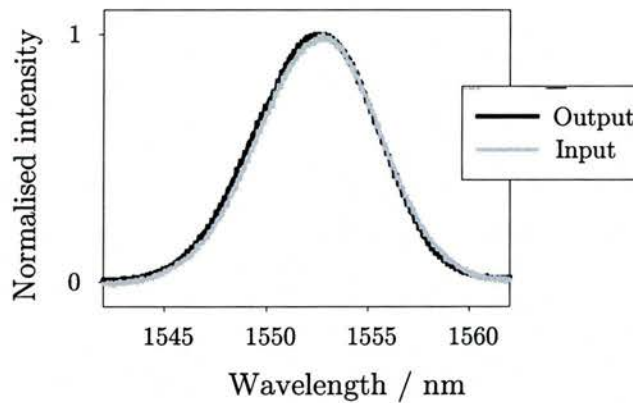


Figure 4.6: Comparison of the output spectra from 1 m of fibre with the input illustrating the negligible pulse shaping effect of propagation through this short length of fibre. The small difference is attributed to jitter in the OPO pulse source.

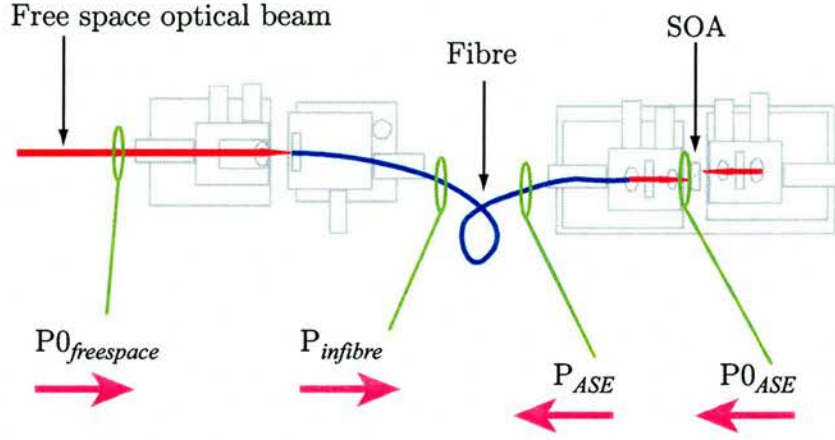


Figure 4.7: Schematic illustrating the manner in which the coupling efficiencies were assessed: coupling of OPO light into one end of the fibre and ASE light from the device into the other end of the fibre.

$\eta_{device-to-fibre}$ was calculated by

$$\eta_{device-to-fibre} = \frac{P_{ASE}}{P0_{ASE}} \quad (4.1)$$

where $P0_{ASE}$ is the optical power of the ASE measured immediately after the microlens, which collects the light from the device, and P_{ASE} is the ASE power coupled into the fibre.

The coupling of light into the other end of the fibre, $\eta_{freespace-to-fibre}$ was given by

$$\eta_{freespace-to-fibre} = \frac{P_{in\,fibre}}{P0_{freespace}} \quad (4.2)$$

where $P0_{freespace}$ is the optical power of the freespace input beam e.g. from the OPO, and $P_{in\,fibre}$ is the power coupled into the fibre.

It was assumed that $\eta_{fibre-to-device} = \eta_{device-to-fibre}$. The total input coupling efficiency was then given by

$$\eta_{total} = \eta_{freespace-to-fibre} \eta_{fibre-to-device} \quad (4.3)$$

Using a 'x 40' microlens, it was found that $\eta_{device-to-fibre}$ was generally only 10%. With $\eta_{freespace-to-fibre}$ of $\sim 25\%$, the total coupling efficiency, η , was typically 2.5%.

Similar methods are cited in the literature (see for example [4]). However one should add the caveat that there remains a degree of uncertainty in this measurement due, for example, to unknown losses such as power reflected from the device. It is

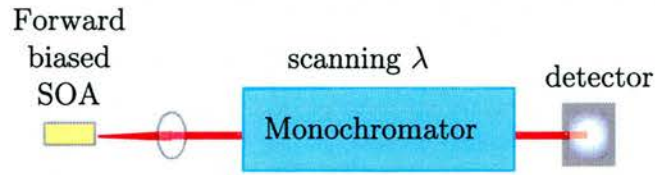


Figure 4.8: Schematic of the experimental set-up used for the measurement of the ASE spectra

reasonable to expect that reflections from the angled-facet device are low. Nevertheless such inherent unknowns correspond to a margin of error for all power measurements. Extreme care was taken to optimise the alignment of coupling optics at the beginning of experiments to minimise additional potential losses due to relaxation of optical mounts.

4.5 Amplified Spontaneous Emission

4.5.1 ASE from an SOA

Under conditions of forward electrical bias the spontaneous emission in the material is amplified. In an SOA the total amplified spontaneous emission (ASE) can be significant since it is cumulative along the length of the device, in this case 1 mm.

4.5.2 Experimental set-up for ASE measurements

The power of the ASE from the SOA was measured as a function of electrical bias, where the power meter (*Melles Griot, Universal Optical Power Meter* with a Germanium detector head) was calibrated for a wavelength in the centre of the spectral range of the ASE.

To measure the ASE spectra a quarter metre scanning monochromator (*CVI Digikrom DK240*) and large area Germanium detector (*New Focus, Model 2033*) were used, as shown schematically in figure 4.8. A polarising beamsplitter cube and a halfwave plate were used to resolve TE and TM components of the emission.

4.5.3 ASE results

Spectrally integrated emission

The increase in total ASE power measured as the electrical bias was ramped up as illustrated in figure 4.9. With increasing bias the difference in TE and TM emission

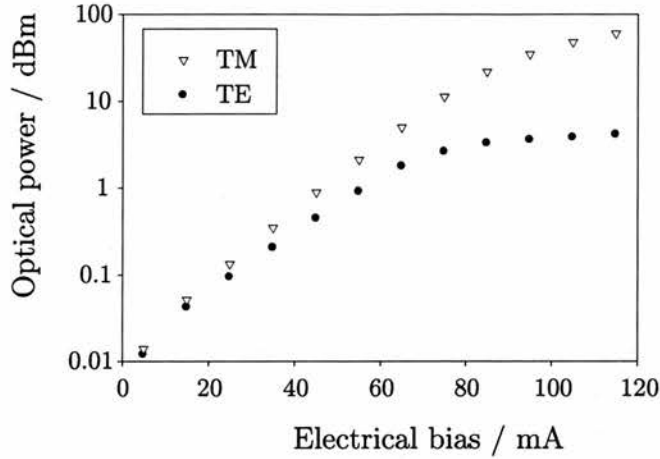


Figure 4.9: The optical power of the ASE as a function of applied electrical bias for TE (black circles) and TM (white triangles) polarisations

grew: at a bias of 35 mA the difference is only 0.3 dBm; by 100 mA the difference has increased to 20 dBm.

It was necessary to work in the lower range of biases for some experiments, especially during the latter stages of the research since the longitudinal modes appeared more strongly, perhaps due to degradation of the AR coated facets. However, in general, the measurements demonstrate that the device provides significant amplification across the range of biases from 50 to 120 mA. The amount of gain imparted to an optical field propagating through the waveguide is quantified by the results reported in Chapter 6.

ASE spectra

Figure 4.10 shows the broad spectral range over which there was significant ASE, from approximately 1510 to 1610 nm. The TM emission was more intense than TE over the full spectral range, as shown in figure 4.10. At the highest biases a narrow peak can be seen to emerge from the TM spectra. This peak is attributed to an emerging cavity mode, and suggests that if driven to higher biases the SOA would lase. Carrier dynamics in the presence of lasing are very different to those in a device operating as an amplifier and consequently in pump-probe experiments (described in Chapter 7) very high biases were avoided.

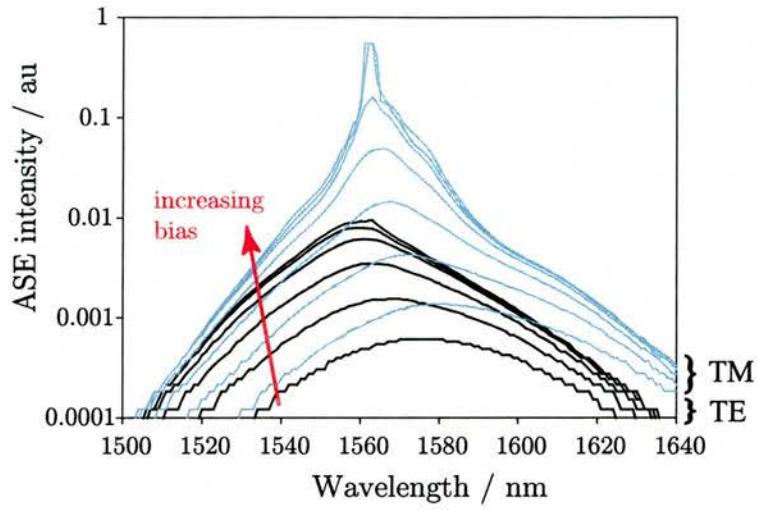


Figure 4.10: ASE spectra for TE (solid lines) and TM (dashed lines) as a function of electrical bias. The bias increases in steps of 10 mA from 5 mA (lowest curves) to 95 mA (highest curves)

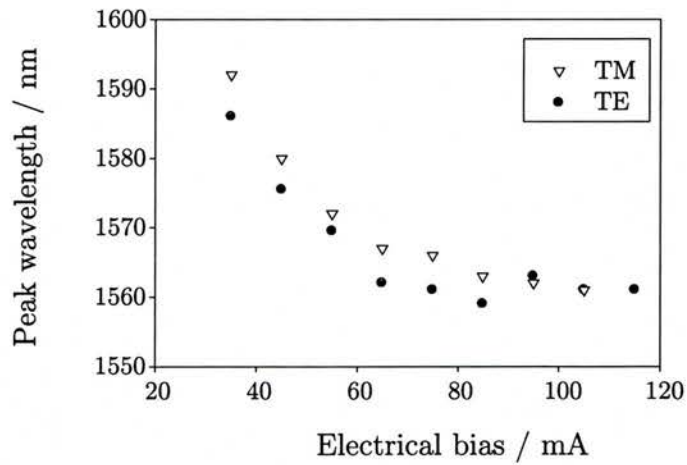


Figure 4.11: The wavelength of the peak of the ASE for TE and TM emission as a function of electrical bias. The TE peak occurs at shorter wavelengths than the TM.

For both TE and TM the ASE spectra not only grow but also move with applied bias as figure 4.11 illustrates. The observed peak shift is towards lower wavelengths, as the bias is increased. This effect is commonly seen and is attributed to the band filling effect (for example, [5]). These curves indicate the degree to which the peak gain can be tuned by setting the applied bias level.

The peaks in the ASE for TE emission occur at slightly shorter wavelengths than for TM. This characteristic could be due to some contribution to the TE gain coming from a relatively higher energy transition than the TM gain. Evidence of this was found from the transmission measurements, as discussed in section 4.6.3.

For higher biases, the spectral offset between TE and TM emission reduces, and eventually the wavelength shift in the position of the peaks seems to saturate, as expected for band filling. Note that at high biases, when the cavity modes are appearing, the location of the peaks in ASE are more ambiguous. Consequently the marginal crossover of TE and TM peaks under these conditions is not regarded as significant.

4.6 CW transmission measurements

4.6.1 Amplification of CW source

Whilst ASE spectra are very readily obtained, they differ from the true gain spectra of a device [6]. There are a variety of methods by which the gain of a material can be determined experimentally including measurements of the spontaneous emission perpendicular to the waveguide propagation direction (through a top contact or a transparent substrate) [7], by using a segmented contact device [8] [9], the single-pass stripe length method [10] and the Hakki-Paoli method [11][12][13]. However these methods depend on the fabrication of a complex structure or having multiple samples of the same wafer differently processed: for example, before and after antireflection coating, different lengths of waveguide and windows etched to allow ASE out of the side of the cavity. Since such samples were not available for the SOA studied in this work, measurements of the transmission as function of wavelength, made using a CW tunable laser, were used to obtain additional information about the gain characteristics of the SOA.

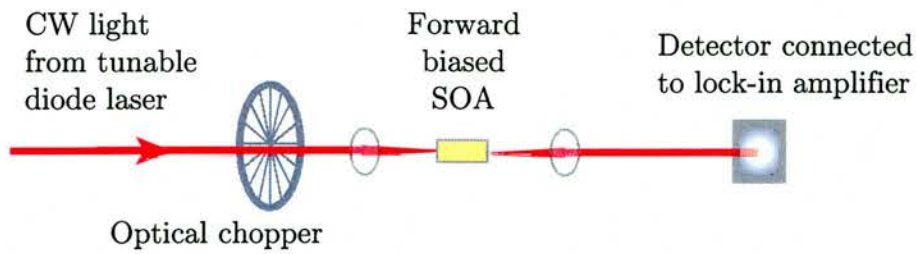


Figure 4.12: Schematic of the experimental set-up used for the measurement of the CW transmission

4.6.2 Experimental set-up for transmission measurements

The laser used for the transmission experiments was a $1.5\ \mu\text{m}$ tunable diode laser (*Photonetics Tunics*), giving CW light from 1480 to 1580 nm. These experiments were undertaken in the Department of Electrical and Electronic Engineering in Glasgow University (with assistance from Marc Sorel).

The beam from the diode laser was passed through a polarising beamsplitter to ensure clean linear polarisation characteristics of the light. The system was calibrated as a function of wavelength in order that the data could be corrected for the sensitivity of the detector over this wavelength range.

The experimental set-up is shown schematically in figure 4.12. The light was coupled into the SOA and collected and collimated after it by microlenses. To distinguish the amplified throughput from the ASE signal an optical chopper was used to modulate the input beam and the signal from the detector (measuring the output) was passed to a lock-in amplifier. Wavelength scanning of the laser was driven by a *LabVIEW* (*National Instruments*) program which also recorded the signal from the lock-in.

4.6.3 CW transmission results

The relative strength of transmission as function of wavelength for TE and TM polarisations at a range of input powers is shown in figure 4.13.

The transmission spectra are consistent with ASE spectra in that maximum amplification is found to occur at similar wavelengths for the same biases as illustrated in figure 4.14. However, by contrast to the smooth ASE spectra, figure 4.13 of the transmission spectra demonstrates that the TE gain has two peaks occurring at differ-

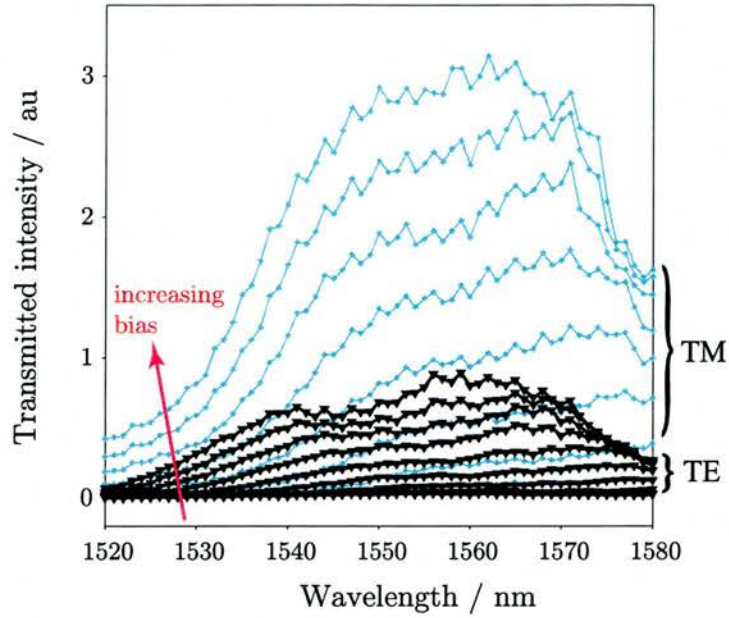


Figure 4.13: Intensity of the TE (solid lines) and TM (dotted lines) transmission of a CW beam as a function of wavelength.

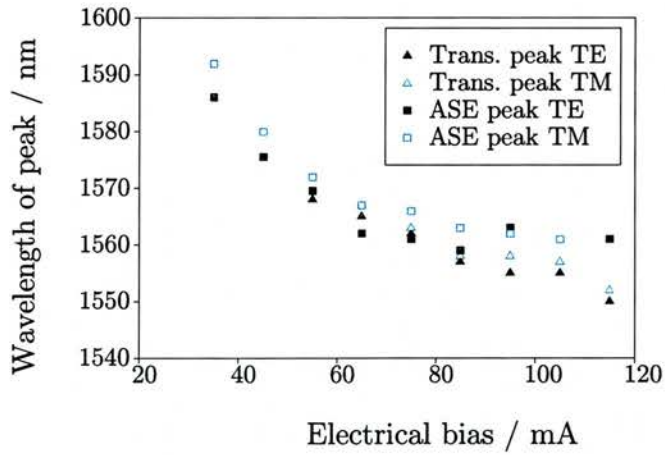


Figure 4.14: The peak of transmission and ASE spectra for both TE and TM polarizations, demonstrating the consistency of the two measurements. Note that this agreement is despite the ambiguity in defining a maxima of the transmission spectra, due to their roughness as shown in figure 4.13.

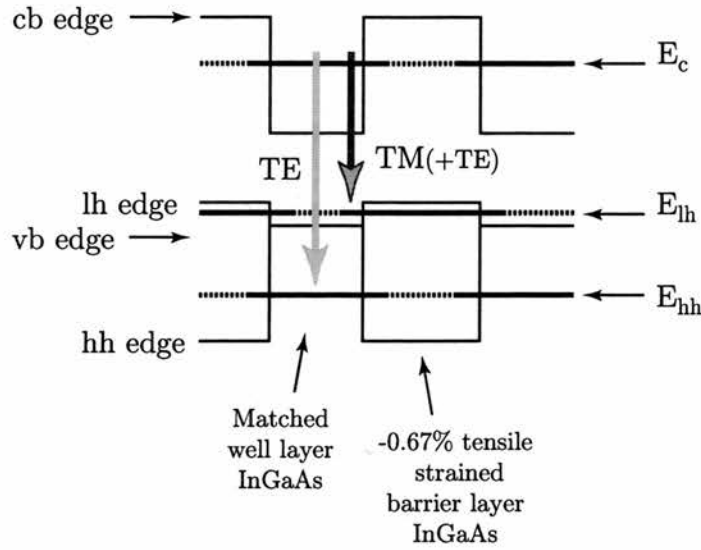


Figure 4.15: Schematic of the band structure of the SOA unstrained well/strained barrier superlattice.

ent wavelengths whilst the TM direction has a single peak and is broad. To explain these more detailed characteristics of the transmission measurements it is necessary to consider the theory of optical properties of semiconductors introduced in chapter 2.

Firstly, to understand the location of features of transmission spectra in figure 4.13 as function of energy, it is necessary to consider the form of the band structure of the SOA active layer material. As discussed in section 2.8, the tensile strain causes the heavy and light hole bands, which are degenerate at $k = 0$ in the unstrained material, to separate; the light hole is shifted up with respect to the heavy hole (see figure 2.15). Figure 4.15 illustrates schematically the band structure of the InGaAs unstrained well and strained barrier superlattice which constitutes the active region of the SOA. This is based on band structure calculations carried out by Jian Zhong Zhang and Ian Galbraith at Heriot Watt University, Edinburgh [14]. The valence band structure from such calculations is shown in figure 4.16 (note that the parabolic band approximation agrees with the k.p theory around $k = 0$). In both cases, the energy separation between the first light and heavy bands is predicted to be of the order of 25 meV.

Secondly, as described in section 2.7.1, the selection rules for TE and TM polarisations in a quantum confined material are different. For an SOA device, in which the propagation direction is parallel with the quantum well layers, transitions between

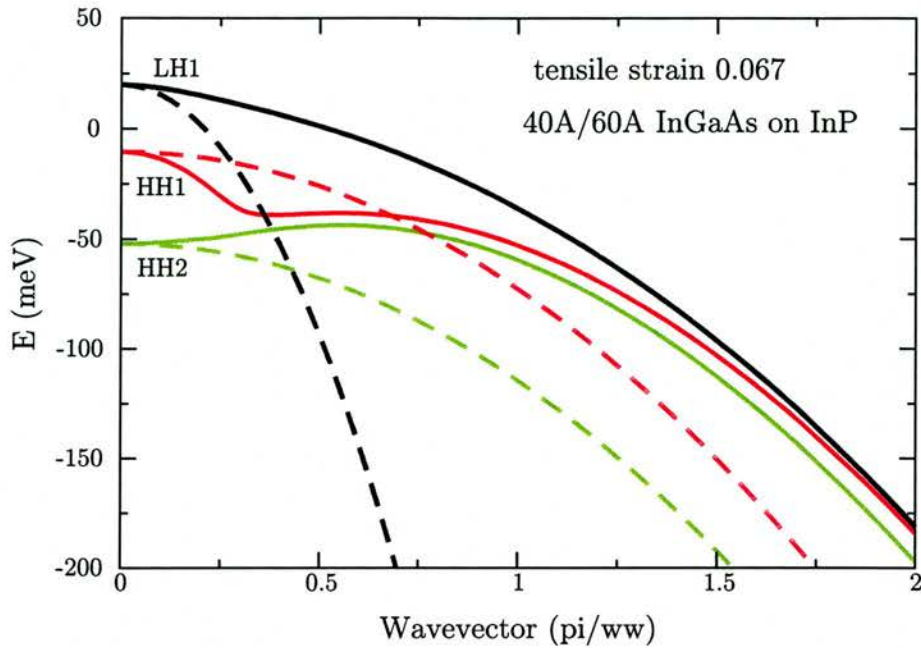


Figure 4.16: Calculated valence band structure for the SOA superlattice. The dashed curves were calculated within the parabolic band approximation; the solid curves are from k.p theory. As a result of the strain the light hole is higher than the heavy hole [14].

the conduction band and light hole (lh) valence band are allowed for both TE and TM polarisations, however transitions to the heavy hole (hh) are only allowed for the TE mode. The strength of transitions is related to the dipole moments for the given transitions.

Figures 4.17 and 4.18 show the results of dipole moment calculations carried out for the strained InGaAs superlattice structure of the SOA by Zhang et al. Figure 4.17 illustrates that for the TM polarisation the only strong transition is to the lh band. In contrast, figure 4.18 shows that, around $k = 0$ the dipole moment for the TE polarisation is strong for both the first lh and first hh bands, and even the second hh band appears to have a non negligible transition strength. Consequently, whilst the gain in the TM direction is dominated by lh1 transitions only, the TE gain is composed from significant contributions from both lh1 and hh1 transitions.

Returning to consider the transmission spectra, figure 4.13, the experimental data is found to be consistent in the light of the transition rules and the band structure calculations. The two peak TE transmission is attributed to contributions from the lh

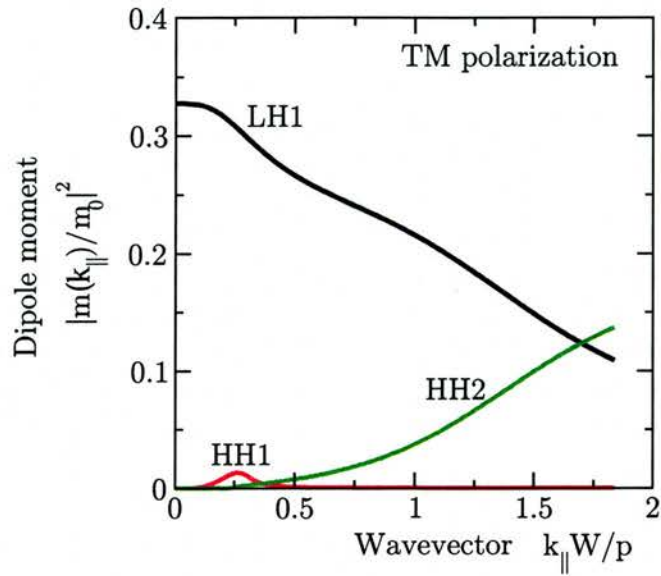


Figure 4.17: The strength of the dipole moment for the TM polarisation calculated for an InGaAs superlattice with the same specifications as the active material of the SOA device. This indicates that only the light hole (lh) transition is strong [14].

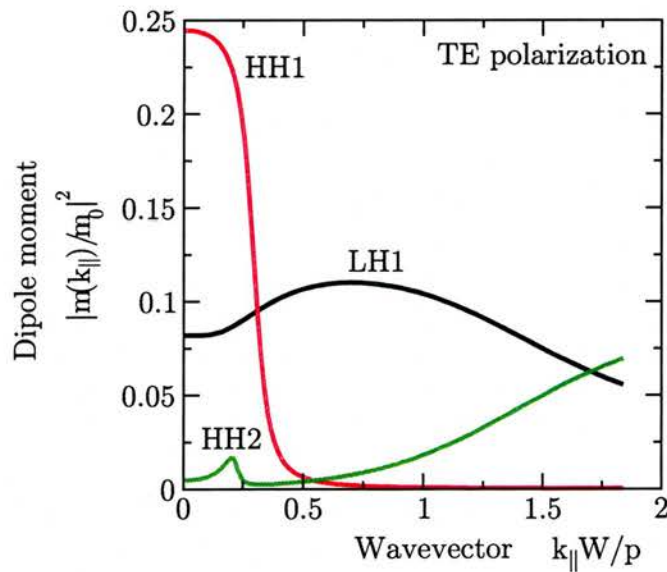


Figure 4.18: The strength of the dipole moment for the TE polarisation for the same material in figure 4.17. This indicates that both heavy hole (hh) and light hole (lh) transitions are significant [14].

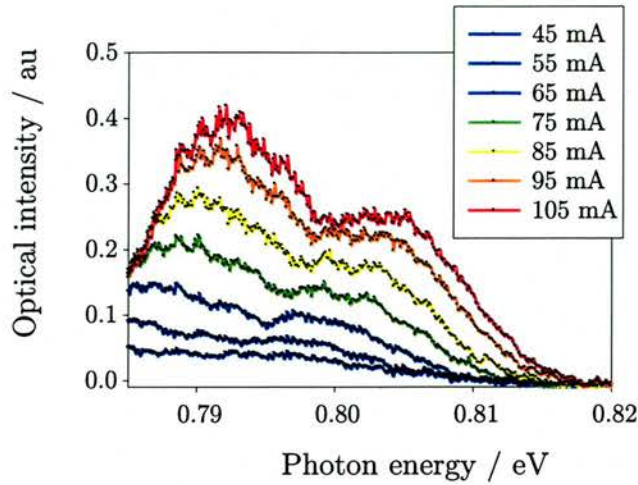


Figure 4.19: Measured transmission of a CW beam in the TE mode as a function of photon energy. The two peaks are attributed to light hole and heavy hole transitions, both of which are allowed for the TE polarisation.

transition and, at higher energies, the hh transition. By contrast, the single TM peak is consistent with the single allowed transition, that involving the lh; at low biases it is centred over the same energy range as the lower energy TE peak, also thought to be due to the lh transition.

Note that the TM transition is a quasi Type II transition in that it occurs between a conduction band energy level in the well and the light hole valence band due to the barrier material. However, as discussed in section 2.6.3, the layers are very thin and the carriers are not tightly localised. Therefore transitions can occur, as suggested by the vertical line in figure 4.15, in the region of overlap of the wavefunctions.

Figure 4.19 illustrates the TE transmission re-plotted as a function of photon energy. The peaks shift with electrical bias but can be estimated to occur at energies of $\sim 800 \pm 5$ meV and $\sim 788 \pm 5$ meV. This suggests a lh to hh separation of 12 ± 10 meV. This is less than the value from the band structure calculations, but the agreement is reasonable, given sources of error, including the fact that the transmission peaks move as a function of carrier density in the device (as controlled by the applied electrical bias). Moreover, the actual level of strain in the material may differ from the value of -0.67% used in the calculations. Calculated offset energies of the heavy and light hole bands as a function of Gallium content give a difference between the heavy and light hole energies of between zero (unstrained case) and 37 meV (for 90% Gallium)

[15]. The energy difference determined from the transmission measurements reported here lies well within this range.

In general these results are consistent with both theory and experimental results published for tensile-strained MQW structures [6][15][16]. Specifically, Okamoto et al. [15] report single and two peak photoluminescence curves for a tensile-strained barrier InGaAs SOA for the orthogonal polarisations, qualitatively similar to the transmission measurements presented here.

4.7 Photo-induced voltage

4.7.1 Three regimes: absorption, transmission and gain

The ASE and transmission experiments have provided information about the strength of the gain and how it varies as a function of wavelength and polarisation. However it is by looking at the electrical signal across the device that it is most readily ascertained whether the active material is absorbing or amplifying. The three regimes of absorption, transparency and gain may be defined in terms of the photo-induced voltage signal, also called the bias-lead or junction voltage [17].

The photo-induced voltage is the change in the potential difference across the device from it being in a state of quasi-equilibrium to the state imposed by an incident optical beam. When the SOA is unbiased or biased only very slightly, an optical beam of sufficiently short wavelength is absorbed and carriers are thereby created. This increase in carriers is observed as an increase in the voltage across the SOA. On the contrary, at higher biases when the device is in gain, the same incident optical beam will be amplified as it propagates through the SOA. The stimulated emission removes carriers and as a consequence the potential difference across the device is reduced. The point at which there is sufficient bias to achieve balancing of gain and absorption is the transparency point [18]. At transparency there is no net increase or decrease in carrier density, consequently this condition is indicated by the photo-induced voltage signal being zero.

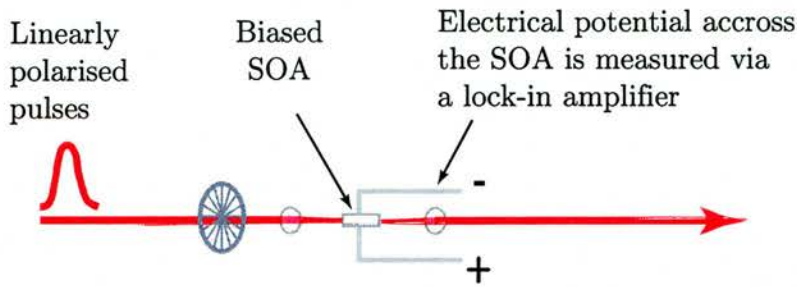


Figure 4.20: Schematic of the experimental configuration used for the photo-induced voltage measurements. Both CW and pulsed optical sources were used

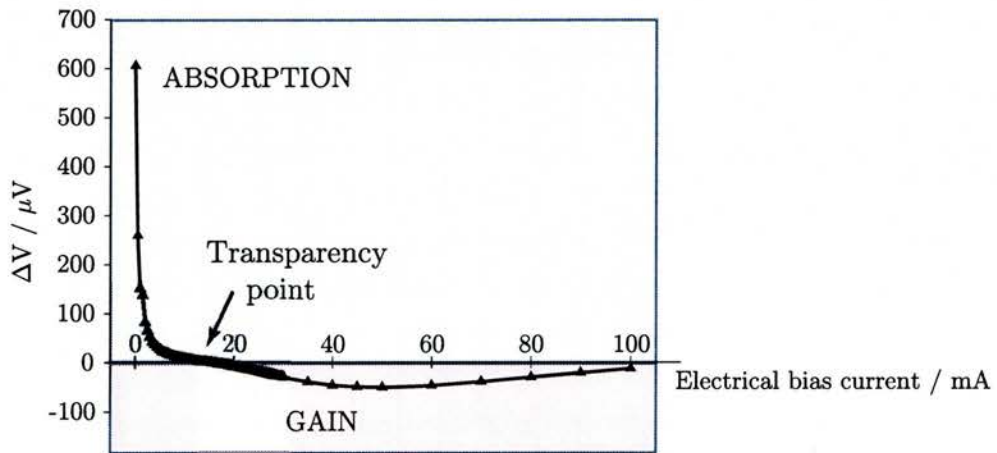


Figure 4.21: The photo-induced voltage signal as function of applied electrical bias for 0.7ps pulses at 1565nm. The average optical power was $12.5 \mu\text{W}$, corresponding to 150 fJ pulses at the repetition rate of 82 MHz

4.7.2 Experimental set-up for voltage measurements

Electrical connections are made across the device for the purpose of applying the electrical bias. The voltage signal across these connections corresponds to the potential difference across the device, and this signal was fed to a lock-in amplifier, triggered at the frequency of the optical chopper. Figure 4.20 illustrates this experimental set-up.

Measurements of the photo-induced voltage signal were made as a function of applied electrical bias and at a range of wavelengths, using both sub-picosecond pulses from the OPO and a CW tunable diode laser.

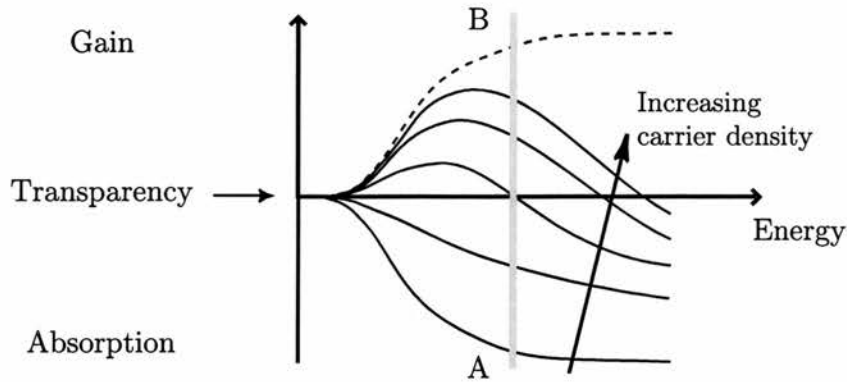


Figure 4.22: Schematic of the available gain/absorption as a function of optical energy. The curves represent different carrier densities, where the interval between them is the same in each case. Note however that the curves are not equally spaced.

4.7.3 Photo-induced voltage with pulses

Photo-induced voltage signal as a function of bias

The change in the photo-induced voltage (ΔV) as the applied electrical bias was increased is illustrated in figure 4.21 for optical pulses of 0.7 ps at 1565 nm, in the middle region of the gain spectrum. The high positive ΔV values at low biases correspond to the SOA being in the absorption regime; the negative values correspond to the SOA being in gain. At 17 mA applied bias the curve, in figure 4.21, crosses zero: the transparency point.

The change of regime from absorption into gain for a particular optical frequency corresponds to moving from A to B along the grey line in figure 4.22. This schematic illustrates gain/absorption as a function of photon energy at different carrier densities; changes in carrier density in this experiment being effected by varying the electrical bias. With the application of forward bias the effect on the conduction and valence bands is a reduction of the offset of the levels in the p-type layer with respect to those n-type layers (as in figure 2.3). The rapid change in ΔV as the bias is increased from zero, in figure 4.21, is consistent with the small applied potential difference that is required to reach the flat band condition. This also corresponds to the changes between curves in moving from A to B in figure 4.22: for equal changes in carrier density, the vertical differences between the curves become progressively smaller as the device moves from absorbing to amplifying.

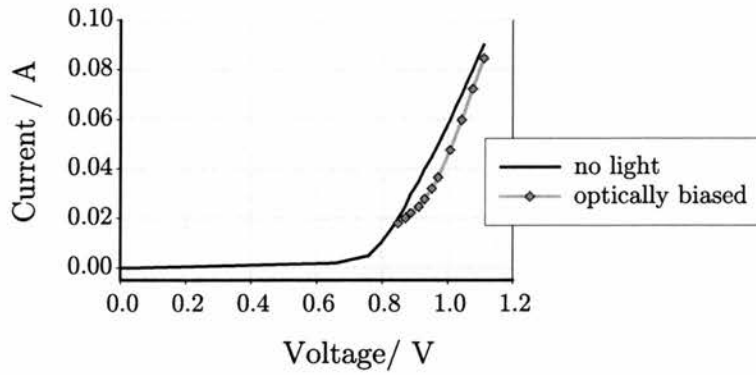


Figure 4.23: The I-V (current-voltage) curve for the SOA device with no optical bias (black curve) and the condition of the device induced by an incident optical field at a wavelength central to the gain, which corresponds to an offset by ΔI and ΔV with respect to the case of no optical bias (black diamonds).

Once the device is in gain the ΔV signal (in figure 4.21) becomes more negative very gradually, tending to a minimum at a bias of around 50 mA. This can be understood with reference to figure 4.23 which shows the optically biased state with respect to the I-V curve for the SOA in the absence of light. The effect of light is to move the device to a state offset from the state it is in under the zero light condition. However at higher bias levels, the no-light and optically-biased states converge. Note that the calculated offset values are approximate and only reasonable for the range over which the I-V curve is linear, since the ΔI values were calculated using the measured ΔV (due to the optical signal) and a resistance calculated from the slope of the linear region of the no-light I-V curve.

Lastly, increase in ΔV for still higher biases (in figure 4.21) implies a reduction in the gain under these conditions and is attributed to a longitudinal effect. The ΔV signal yields a measure of the state of the SOA averaged over the device. At high electrical biases the optical signal is sufficiently strongly amplified to itself extract the available gain and drive the device, on average, back towards the transparency condition. This was the first manifestation of longitudinal saturation in this SOA, a phenomena that was subsequently investigated with counter-propagating pump-probe experiments and simulations, reported in Chapter 7.

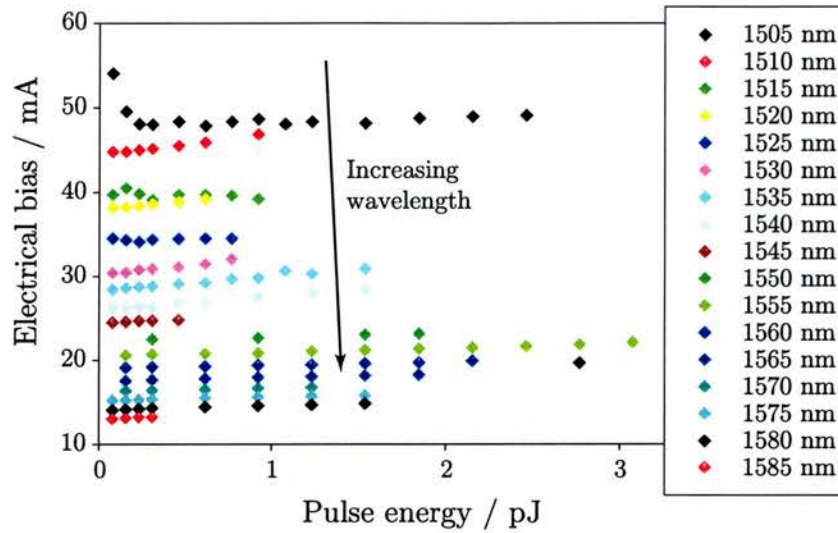


Figure 4.24: The variation in electrical bias required for transparency as determined by the zero photo-induced voltage condition is plotted as function of wavelength and optical pulse energy

The transparency condition

The transparency point of the SOA is investigated at different positions in the gain spectrum using pulses of different energies. Figure 4.24 shows the experimentally determined bias at transparency for a wide range of wavelengths and as a function of the input pulse energy.

The range of pulse energies over which data was obtained was limited by the tuning characteristics of the OPO, especially since care was taken to preserve clean pulse profiles. It was not always possible to obtain transform-limited pulses, but the pulse duration was kept at 700 ± 150 fs and the spectral profile and autocorrelation of the pulses were maintained approximately Gaussian. This was important since the behaviour of the device can be altered significantly due changes in the input pulse characteristics [19][20].

It can be seen clearly from figure 4.25 (which is composed of selected data from figure 4.24), that the transparency bias increases as a function of pulse energy. This is attributed to the change in carrier density caused by the optical field and appears linear for this range of pulse energies. Kao et al. [21] also report a power dependent transparency condition: for a MQW amplifier they observe a nonlinear increase in the

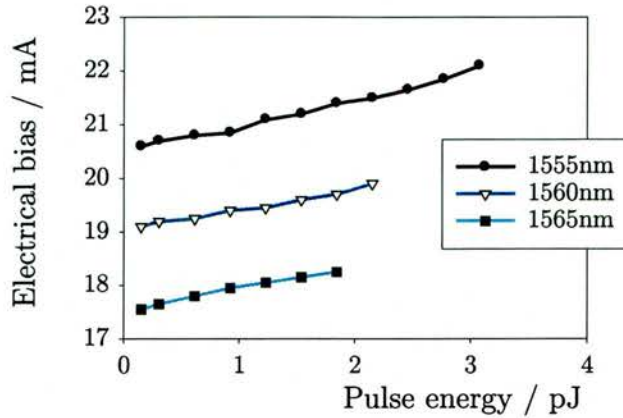


Figure 4.25: The variation in electrical bias required for transparency as shown in figure 4.24 for just three wavelengths to highlight the change in transparency conditions as a function of input pulse energy.

bias required for transparency which they attribute to two photon absorption (TPA). The data presented by Kao extends to high input pulse intensities, up to 10 pJ for 0.8 ps pulses. This is significantly more than the intensities available for the measurements presented in this thesis and it is not possible to conclude definitively whether a nonlinear change in the transparency bias indicative of TPA would have been seen had it been possible to use higher pulse energies. What is clear however is that that the condition of transparency has to be defined with respect to given operating conditions. It follows that for a bias which corresponds to a regime significantly ‘into gain’ for a low power input, the SOA may provide no significant gain to a pulse with an order of magnitude higher energy.

Figure 4.26 shows the experimentally determined transparency biases for 300 fJ pulses at a range of wavelengths. (This corresponds to a vertical slice through the data shown in figure 4.24.) The variation of the transparency current as a function of wavelength is very smooth; the characteristic has even been proposed as a method of wavelength discrimination for WDM communication systems [22].

In order to compare the data presented in figure 4.26 with theoretical calculations of transparency it is necessary to make an estimate of the carrier density as a function of applied electrical bias. It is very difficult to know accurately the actual carrier densities in the SOA. Here estimations are made on the basis of a simple rate equation that describes the evolution of the carrier density (see Chapter 5 and equations therein).

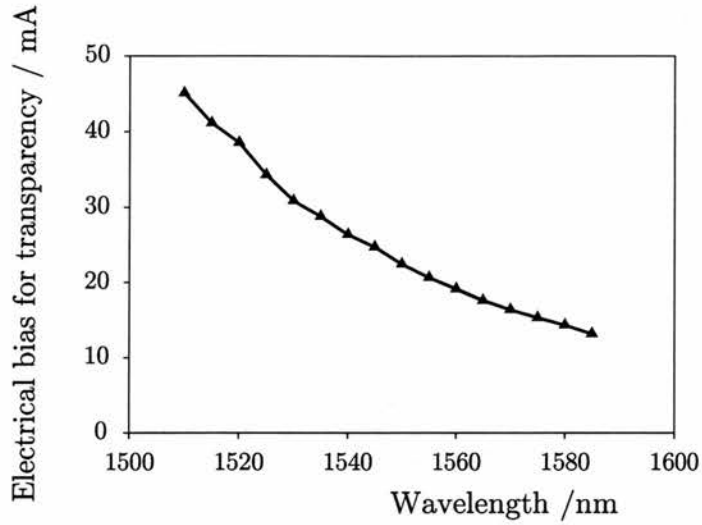


Figure 4.26: The variation in electrical bias required for transparency increases as function of wavelength, for a constant input pulse energy of 300 fJ.

Under steady state conditions, the relationship between carrier density and current, J , can be expressed approximately by

$$N(J) = \frac{J\tau(J)}{eV} \quad (4.4)$$

where e is the electronic charge and V is the volume of the active region. The current dependent carrier recombination time, $\tau(J)$, is determined empirically from a fit to experimental measurements of gain recovery (reported in chapter 7).

Simple gain calculations were carried out based on the equations introduced in section 2.7.2 (for analytical expressions see for example [23], [24], [25] and references therein). Material parameters such as the effective masses and the energy gap for the InGaAs active layer were taken from the literature ([26], [27], [28] and references therein). The transparency point, which corresponds to the zero crossing point of the gain spectra as shown in figure 4.27, is ascertained for different carrier densities. The calculated carrier density at transparency was consistent with the trend found experimentally, that is for lower frequencies (longer wavelengths) it is necessary to apply a higher electrical bias to reach the transparency condition. This trend is understandable as a band filling effect: the higher energy photons are able to interact with carriers further away from band edge and consequently it is necessary to fill up more states for the material to appear transparent.

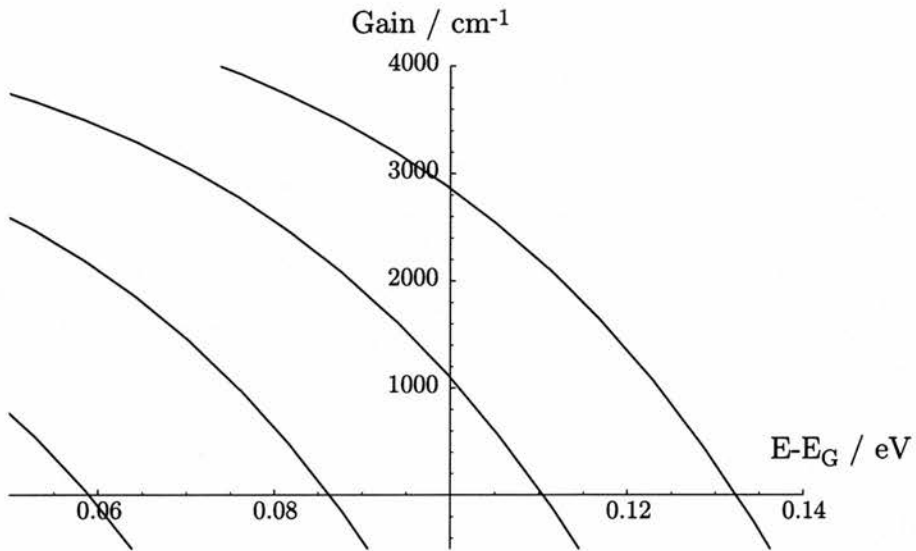


Figure 4.27: Transition from gain to absorption, through a transparency point for carrier densities from 1.4 to $2.6 \times 10^{18} \text{ cm}^{-3}$

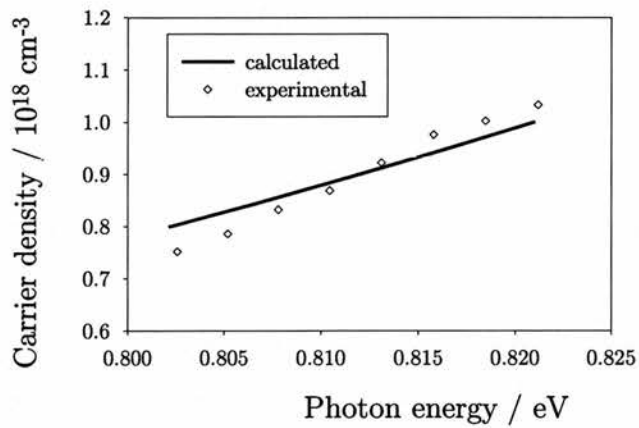


Figure 4.28: Carrier density at transparency as a function of photon energy. The diamonds are the experimentally determined transparency points and the curve is the calculated density for transparency from gain curves such as those illustrated in figure 4.27

In figure 4.28, experimental data from figure 4.26 (converted to carrier density and photon energy) is plotted together with the theoretical values for the transparency condition, assuming a band gap of 0.78 meV, a reasonable value for the InGaAs compositions in the device. Given the many approximations, the degree of agreement between the experimental data and the simple model is astonishing. The behaviour is qualitatively the same and the greater steepness of the theoretical curve may be due to differences between the material parameters used and those in the actual device with its complicated superlattice structure.

4.7.4 Photo-induced voltage with CW light

It was difficult to build up a three dimensional data set of the photo-induced voltage as a function of bias and photon energy with the pulsed source, since the OPO had to be tuned manually to different wavelengths. By contrast, this could be readily achieved with a tunable CW source. Figure 4.29 (a) and (b) illustrate the photo-induced voltage (ΔV) as a function of applied electrical bias and wavelength of the optical field, for TM and TE polarisations respectively.

For the lowest biases, the device is absorbing or provides negligible gain (red/orange); at higher biases the device moves progressively further into the gain regime, ΔV moves to more negative values and correspondingly the surface curves downwards (yellow to blue). The largest magnitude ΔV (most negative values) occurs for the highest biases, as would be expected, and around 1560 nm, corresponding to the spectral region of peak gain. At the longest wavelengths for which measurements were taken, the ΔV starts to decrease. Indeed it would be expected that the photo-induced signal would reduce in magnitude as the photon energy approached the band edge; unfortunately it was not possible to tune the laser to still longer wavelengths to clearly demonstrate this.

These 3-D plots illustrate how the voltage across the device is a guide to how altering conditions moves the state of the SOA through the wide parameter space of gain/absorption as a function of bias, optical wavelength and polarisation; this is especially the case in the region near transparency. Note however that two peaks found in the TE transmission spectra are not found in TE voltage signal. This is attributed to

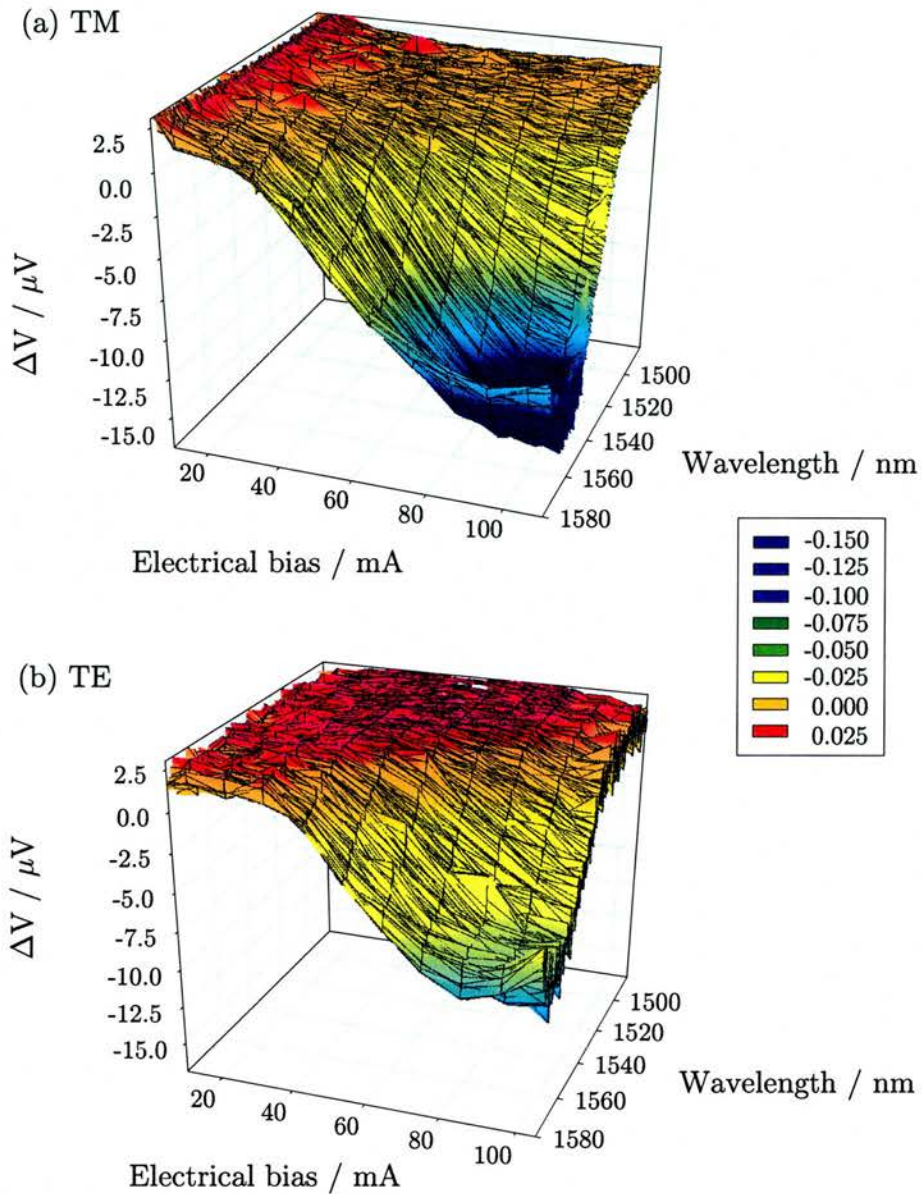


Figure 4.29: The photo-induced voltage signal induced by a CW optical field in (a) the TM and (b) the TE mode as a function of optical wavelength and electrical bias. The maximum magnitude of signal (minimum of the surface) occurs for the highest biases and wavelengths in the region of 1560 nm for both TM and TE. However the magnitude of signal is larger (more negative) for TM, corresponding to the larger available gain for this mode.

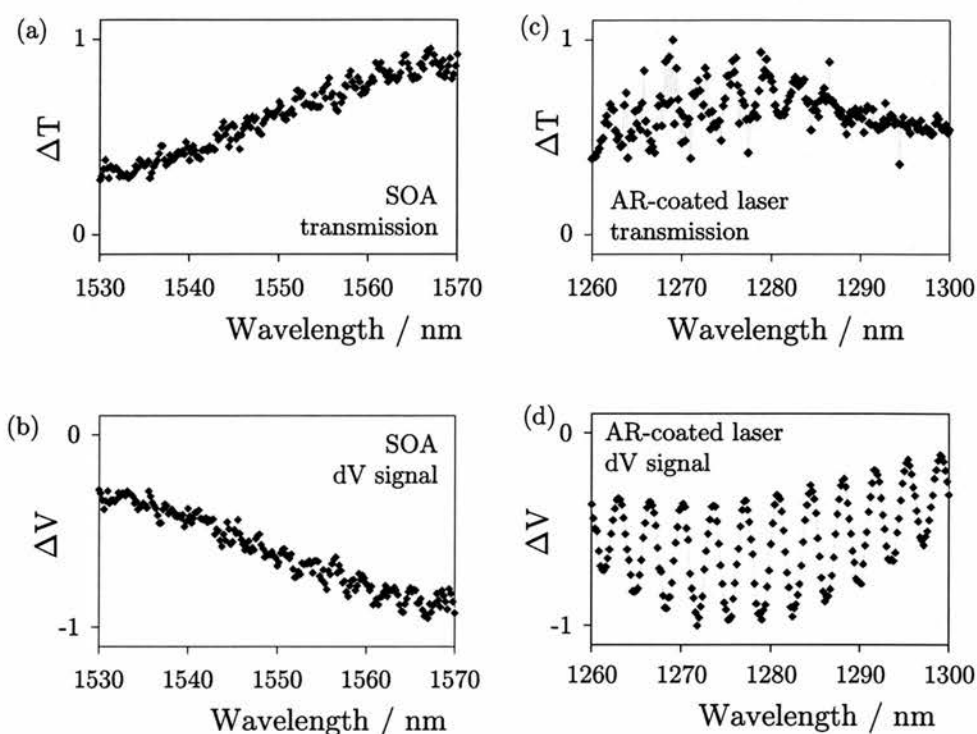


Figure 4.30: Transmission spectra measured for (a) angled-facet travelling wave SOA (the device focused on in this project) and (c) an AR coated laser. The photo-induced voltage spectra, for the two devices respectively, are shown in (b) and (d).

the nonlinearity of the photo-induced voltage (for example, as demonstrated in figure 4.21): once the device is in gain ΔV does not vary in magnitude over a wide range so it is understandable that the details of changes in gain with wavelength are obscured.

4.8 Oscillations in the spectra

As discussed in section 2.2, if no efforts are made to minimise feedback, SOAs demonstrate Fabry-Perot resonances. By contrast, travelling-wave amplifiers (TWA) have angled facets as well as (or instead of) antireflection (AR) coatings to minimise reflections. However, either due to residual reflections or even internal reflections, there may be ripples in the gain of so-called TWAs.

Figure 4.30 shows the transmission through a device in which feedback has been successfully suppressed (a) and one in which the Fabry-Perot resonances are still significantly modulating the transmission (c): the first was designed as a travelling wave

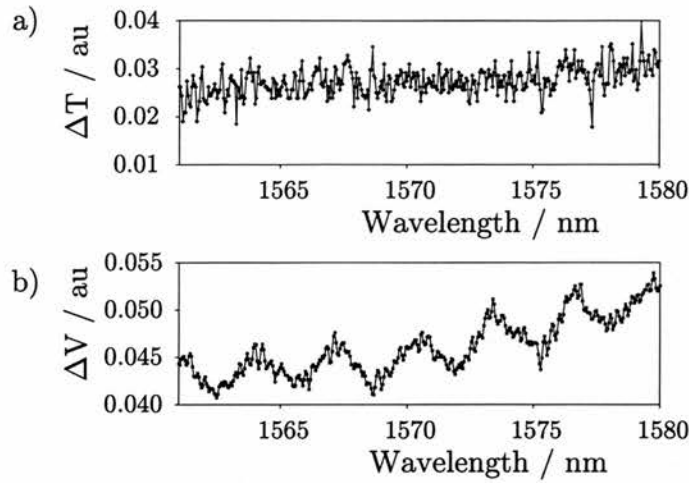


Figure 4.31: Transmission (a) and photo-induced voltage (b) of the travelling wave SOA as a function of wavelength with a step size of 0.05 nm

SOA, the second is an anti-reflection (AR) coated laser. The difference is more vividly illustrated by comparison of figure 4.30 (b) and (d) which show the photo-induced voltage measurements for the same pair of devices. In the case of the AR coated laser the modulation is very deep, by contrast with the angle-faceted and AR coated SOA device.

The length, L , of the cavity giving the resonances is given by

$$L = \frac{\Delta m}{2\left(\frac{n_1}{\lambda_1} - \frac{n_2}{\lambda_2}\right)} \quad (4.5)$$

where $\Delta m = m_1 - m_2$ is the number of modes between wavelengths λ_1 and λ_2 and n_i is the effective index at those wavelengths [12]. The data in the 1.5 μm region, shown in (a) in figure 4.30 pertains to the device that is the focus of this thesis. Since it is optimised as an SOA, the observed ripples are small and it is difficult to read the location of the maxima directly from these graphs, in which the step size used for the scan was 1 nm. To obtain greater accuracy additional wavelength scans were taken of both transmission and photo-induced voltage with progressively smaller step sizes. In the ΔV scans with a step size of 0.05 nm, shown in figure 4.31, ripples visible on the long step size scans were clearly resolved, however a shorter period oscillation also became visible. Consequently short scans were taken using even smaller step sizes. Figure 4.32, illustrates oscillations in the ΔV signal over a very small portion of the spectrum using a step size of 0.02 nm.

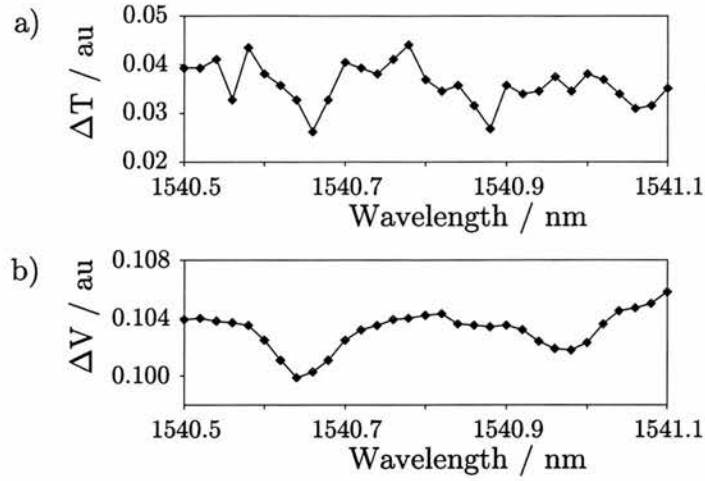


Figure 4.32: Transmission (a) and photo-induced voltage (b) of the travelling wave SOA as a function of wavelength with a step size of 0.02 nm

Periods of these oscillations can be measured off the graphs. However, since the strength of the resonances are weak and there appear to be two periods superimposed, the data was Fast Fourier Transformed to identify the frequencies. The change in the period with wavelength can be assumed to be small across this narrow range and the slow overall curvature of the spectra falls at low frequencies (near zero). Peaks are found which correspond to wavelength intervals $\Delta\lambda = \lambda_2 - \lambda_1$, of 0.34 ± 0.05 nm and 3.44 ± 0.05 nm.

With some assumptions, equation 4.5 can be used to calculate the lengths of the cavity responsible for the resonances from the wavelength intervals. It is assumed that for such a small wavelength range $\lambda_1\lambda_2 \approx \lambda_{mid}^2$ where λ_{mid} is the central wavelength of the data range. Also $n_1 = n_2$ with n between 3.17 and 3.57 (reasonable values for a range of compositions of materials from InGaAsP to InGaAs and InP [28]). Using these approximations, values of L obtained from the frequencies found by Fourier transforming the data are 1080 ± 200 nm and 104 ± 10 nm; calculations using the periods directly off the graphs also give cavity lengths which fall within this range. The longer cavity, derived from the short period resonance, can be attributed to the length of the device which is nominally 1 mm (noting that since the waveguide is diagonal across the chip any geometrical correction to the optical path length would yield a slightly longer length by a few percent).

The strength of these oscillations due to the SOA cavity is so weak that they can not be used as a means of quantifying the refractive index changes, due to changes in carrier density imposed by current injection, a technique commonly used with Fabry-Perot amplifiers [12] [29]. However, more importantly, it is clear that the measures taken to reduce feedback from the natural cavity of the chip itself, namely angling the waveguide and additionally applying antireflection coatings have been very successful, at least for bias levels up to about 100 mA.

The origin of the longer period oscillation is less clear. The depth of this oscillation does not appear to increase proportionally with electrical bias, which suggests that it is due to a cavity external to the active region. Further spectral scans of the power, taken in the absence of the device, also manifested this slow oscillation. These confirmed that it is not a feature of the device and it is attributed to multiple reflections in the optical set-up. Correction of the data using these power scans does not render the curves completely smooth, but has some effect on reducing the amplitude of the oscillations (this processing was carried out on the data shown in figure 4.13).

The strength of the oscillations in the ΔV signal, shown in figures 4.31 and 4.32, illustrates the greater sensitivity of photo-induced voltage measurements to resonances, compared to the transmission, under the same conditions, and the ASE spectra. Since the gain ripples can seriously degrade the functioning of SOAs in high speed operation (see for example the analysis in [30]), an additional conclusion is that in assessing the characteristics of an SOA it is useful to measure not just ASE and transmission spectra but also photo-induced voltage spectra.

4.9 Summary

In this chapter, spectral measurements that demonstrate the broad gain spectrum of the SOA stretching from below 1520 to beyond 1600 nm have been presented. The total gain is higher in the TM than the TE direction of polarisation. This difference diverges rapidly for biases in excess of 100 mA. Moreover, at higher biases the gain increases strongly at certain wavelengths, suggesting that it was nearing the threshold for lasing. Consequently the optimum range of biases for this device ranges from about 50 mA to

100 mA, and accordingly this range was used for most of the measurements reported in later chapters.

Whilst the TM gain appeared smooth, the nature of the TE transmission spectra suggested that it has contributions from more than one optical transition. Band structure and dipole moment calculations of the InGaAs superlattice active material support the conclusion that the TE gain originates from interband transitions involving both the light and heavy hole valance bands. On the other hand, consistent with selection rules, the only strong transition for the TM mode is between the conduction band and the light hole band.

Also in this chapter, results from measurements of the photo-induced voltage across the SOA circuitry by both ultrashort pulses and CW light has been reported. It is demonstrated to be a very sensitive technique for assessing changes in the state of the SOA as bias conditions are changed. It is clear that the SOA is most readily biased into gain, requiring the lowest level of electrical injection to cross the transparency point, at larger photon energies i.e. short wavelengths. Also the turn over of the photo-induced voltage signal was an early indication of how readily the gain of the SOA could be saturated by sub-picosecond pulses; gain saturation in this device was subsequently investigated extensively as reported in Chapters 6 and 7.

In particular, the combination of spectral and photo-induced voltage results, presented in this chapter, have demonstrated that oscillations in the gain as a function of wavelength were small, over a moderate range of electrical biases (from ~ 20 to 100 mA). Such oscillations are a signature of feedback due to surface reflections from the waveguide facets; their absence confirmed that the SOA was operating as a travelling wave amplifier.

Bibliography for Chapter 4

- [1] C P Seltzer, A L Burness, M Stevenson, M J Harlow, D M Cooper, R M Redstall, and P C Spurdens. Reliable 1.5 μm buried hetrostructure, separate confinement, multiple quantum well (BH-SC-MQW) lasers entirely grown by MOCVD. *Electron. Lett.*, 25(21):1449–1451, 1989.
- [2] A E Kelly, I F Lealman, L J Rivers, S D Perrin, and M Silver. Polarisation insensitive, 25 dB gain semiconductor laser amplifier without antireflection coatings. *Electron. Lett.*, 32(19):1835–1836, 1996.
- [3] A E Kelly, I F Lealman, L J Rivers, S D Perrin, and M Silver. Low noise figure (7.2 dB) and high gain (29 dB) semiconductor amplifier with a single layer AR coating. *Electron. Lett.*, 33(6):536–538, 1997.
- [4] L F Tiemeijer, P J A Thijs, T van Dongen, J J M Binsma, and E J Jansen. Polarisation resolved, complete characterisation of 1310 nm fiber pigtailed multiple-quantum-well optical amplifiers. *IEEE J. Lightwave Technol.*, 14(6):1524–1533, 1996.
- [5] M Itoh, Y Shibata, T Kakitsuka, Y Kadota, and Y Tohmori. Polarisation-insensitive SOA with strained bulk active layer for network device application. *IEEE Photonic. Tech. L.*, 14(6):765–767, 2002.
- [6] C-S Chang and S L Chuang. Modeling of strained quantum-well lasers with spin-orbit coupling. *IEEE J. Sel. Top. Quant.*, 1(2):218–229, 1995.
- [7] P Blood, A I Kucharska, J P Jacobs, and K Griffiths. Measurement and calculation of spontaneous recombination current and optical gain in GaAs-AlGaAs quantum-well structures. *J. Appl. Phys.*, 75(3):1144–1156, 1991.
- [8] G M Lewis, P M Smowton, J D Thomson, H D Summers, and P Blood. Measurement of true spontaneous emission spectra from the facet of diode laser structures. *Appl. Phys. Lett.*, 80(1):1–3, 2002.
- [9] G M Lewis, P M Smowton, P Blood, G Jones, and S Bland. Measurement of transverse electric and transverse magnetic spontaneous emission and gain in tensile strained GaInP laser diodes. *Appl. Phys. Lett.*, 80(19):3488–3490, 2002.
- [10] J D Thomson, H D Summers, P J Hulyer, P M Smowton, and P Blood. Determination of single-pass optical gain and internal loss using a multisection device. *Appl. Phys. Lett.*, 75(17):2527, 1999.
- [11] B W Hakki and T L Paoli. Gain spectra in GaAs double-heterostructure injection lasers. *J. Appl. Phys.*, 46(3):1299–1306, 1975.
- [12] C-S Chang, S L Chuang, J R Minch, W-C W Fang, Y K Chen, and T Tanbun-Ek. Amplified spontaneous emission spectroscopy in strained quantum-well lasers. *IEEE J. Sel. Top. Quant.*, 1(4):1100–1107, 1995.
- [13] J Stohs, D J Bossert, D J Gallant, and S R J Brueck. Gain, refractive index change, and linewidth enhancement factor in broad-area GaAs and InGaAs quantum-well lasers. *IEEE J. Quantum Elect.*, 37(11):1449–1459, 2001.
- [14] J-Z Zhang and I Galbraith. Private communication. Heriot Watt University, Edinburgh, 2002.

- [15] M Okamoto, K Sato, H Mawatari, F Kano, K Magari, Y Kondo, and Y Itaya. TM mode gain enhancement in GaInAs-InP lasers with tensile strained-layer superlattice. *IEEE J. Quantum Elect.*, 27(6):1463–1469, 1991.
- [16] K Magari, M Okamoto, Y Suzuki, K Sato, Y Noguchi, and O Mikami. Polarisation-insensitive optical amplifier with tensile-strained-barrier MQW structure. *IEEE J. Quantum Elect.*, 30(3):695–701, 1994.
- [17] V Văn Lục and P G Eliseev and M A Manko and G T Mikelian. Electrical diagnosis of the amplifier operation and feasibility of signal registration on the basis of voltage saturation effects in junction laser diodes. *IEEE J. Quantum Elect.*, 18(6):1080–1083, 1983.
- [18] S-L Lee. Analytical formula wavelength-dependent transparent current and its implications for designing wavelength sensors and wdm lasers. *IEEE J. Sel. Top. Quant.*, 7(2):201–209, 2001.
- [19] G P Agrawal and N A Olsson. Self-phase modulation and spectral broadening of optical pulses in semiconductor laser amplifiers. *IEEE J. Quantum Elect.*, 25(11):2297, 1989.
- [20] N Finlayson, E M Wright, and G I Stegeman. Nonlinear optical pulse propagation in a semiconductor medium in the transient regime - i: Temporal and spectral effects. *IEEE J. Quantum Elect.*, 26(4):770–777, 1990.
- [21] Y-H Kao, T J Xia, M N Islam, and G Raybon. Limitations on ultrafast optical switching in a semiconductor laser amplifier operating at transparency. *J. Appl. Phys.*, 86(9):4740–4747, 1999.
- [22] S-L Lee. Wavelength measurement and tracking using semiconductor laser amplifiers for applications in photonic networks. *IEEE Photonic. Tech. L.*, 10(3):439–441, 1998.
- [23] W B Joyce and R W Dixon. Analytic approximations for the fermi energy of an ideal fermi gas. *Appl. Phys. Lett.*, 31(5):354–356, 1977.
- [24] H C Casey Jr. and M B Panish. *Heterostructure lasers Part A: Fundamental principles*. Academic Press, 1978.
- [25] P K Basu. *Theory of optical processes in semiconductors: bulk and microstructures*. Oxford University Press, New York, 1997.
- [26] S Adachi. Material parameters of $In_{1-x}Ga_xAs_{1-y}P$ and related binaries. *J. Appl. Phys.*, 53(12):8775–8792, 1982.
- [27] S Adachi. Optical properties of $In_{1-x}Ga_xAs_yP_{1-y}$ alloys. *Phys. Rev. B*, 39(17):12612–12621, 1989.
- [28] G P Agrawal and N K Dutta. *Semiconductor lasers*. Van Nostrand Reinhold, New York, 2nd edition, 1993.
- [29] S E H Turley, G H B Thompson, and D F Lovelace. Effect of injection current on the dielectric constant of in built waveguide in twin-transverse-junction stripe lasers. *Electron. Lett.*, 15(9):256–257, 1979.
- [30] M Z Iqbal, K B Ma an C E Zah, T P Lee, and N K Cheung. Effects of gain ripples in semiconductor optical amplifiers on very high speed lightwave systems. *IEEE Photonic. Tech. L.*, 2(1):48–50, 1990.

Chapter 5

Modelling the SOA dynamics

5.1 Introduction

The SOA behaviour is highly complex and is sensitively dependent on a vast range of factors: from precise material composition to the intensity of an incident optical field. It is therefore instructive to explore the effects of varying given parameters within the confines of a model.

In this chapter, different approaches to modelling the SOA are discussed. Various types of model, with different structures and input parameters, prove to be useful for investigating different questions. The development of two versions of a phenomenological, rate equation based description of the SOA is outlined. The former serves to introduce the dynamic behaviour of the device; the latter version was designed to assist with the interpretation of the experimental data and can be readily extended to include ultrafast gain dynamics. The results of some calculations from the modelling are presented in this chapter; others are deferred to later chapters for discussion along with experimental results.

5.2 Different approaches: what is the model for?

Underlying the SOA interaction with light are the optical properties of its constituent materials, InGaAs and InP. The characteristics of bulk compounds such as these, and in general the changes of their properties with parameters such as temperature and optical wavelength, are known following research over several decades (see for example, [1] [2] [3]). However, as emphasised in Chapters 2 and 4, the SOA is not just composed of

bulk material, rather it is a precisely engineered 3-D waveguide structure with a superlattice active region and it is a device that is electrically biased into gain. Moreover the properties are changing dynamically due to fluctuations in the carrier population and, the device being a waveguide, propagation effects are important. For these reasons, the behaviour manifested by the SOA is highly complex.

One approach to understanding the interaction of a semiconductor device with light is to start from a many-body description of the active material and calculate the effect of an electro-magnetic wave propagating through it [4]. In connection with the work reported in this thesis, a collaboration has been developed with Jian Zhong Zhang, Javier Molina Vazquez and Ian Galbraith, at Heriot Watt University. Zhang et al. have been developing a many-body approach to modelling an SOA. Some results of the initial calculations, shown in Chapter 4 (figures 4.16, 4.17 and 4.18), have proved useful in interpreting experimentally determined spectra, i.e. static characteristics of the device [5]. Linear and nonlinear propagation in the superlattice (in one dimension) are being simulated and other results are pending [6]. Comparing experimental measurements with the results of many-body models is important, to test the consistency of explanations given for observations against the predictions of theory describing the way fundamental processes are believed to be manifested. However a many-body description of the SOA is beyond the scope of this thesis.

At the other extreme, models can focus on calculating the propagation of an optical field in a given 3-D waveguide (for example, [7]). Such models are particularly valuable for designing the device structure when, for example, fine tuning the geometry is of prime importance. In this case, steady state solutions to equations describing the electro-magnetic field in the waveguide may be satisfactory. On the other hand, in the research reported in this thesis, dynamics are of key interest.

The approach to modelling the SOA adopted for this thesis was based on rate equations that describe the dynamics phenomenologically. This modelling was intended to assist with the understanding and analysis of experimental data; simplifying assumptions, justified for the conditions under consideration, have been made, and it is not claimed that the description of the SOA is theoretically complete.

In general, rate equation type descriptions of semiconductor carrier dynamics can

be derived from semiclassical density matrix equations [8]. Such density matrix equations are themselves obtained from treating the semiconductor as an inhomogeneously broadened set of two-level systems (see for example, [9][10]). The evolution of the carrier populations towards Fermi distributions is accounted for by modifying the equations to include phenomenological time constants. This is valid so long as the deviations from the Fermi distribution are not too large, and results in a problem much simpler than a full many-body description [11]. However the solution of the full set of density matrix equations is still difficult and is beyond the scope of this thesis.

In particular, further simplifications are necessary to reach the concept of material gain. By assuming that the polarisation dephasing time (~ 50 fs) is much shorter than the pulse width, the off-diagonal elements in the matrices corresponding to atomic polarisation can be eliminated adiabatically [12]. This is reasonable since in all the experiments detailed in this report, the pulses used had temporal durations of 350 fs or longer. Also in the pump-probe experiments for which multiple pulse trains were used, all the input pulses were from the same optical pulse source and so were centred on the same wavelength. Since they therefore interact with the same carrier population, further levels of simplification are justified. Rate equations for the carrier densities can be obtained by summing over the diagonal elements in the density matrices which correspond to transition energies in the region around the relevant photon energy [11].

Note that in this description of the SOA gain dynamics, any coherent interaction between beams is neglected. The so-called coherent artifact between pump and probe beams, when they overlap temporally, is negligible for beams of the same polarisation [12]. In the experiments with multiple beams reported in this thesis orthogonal polarisations were used. Under real experimental conditions, linear polarisations tend to be marginally elliptical, due to imperfections in optical elements. Nevertheless, the 'leaked' collinear components of pump and probe were weak. Moreover, any coherent artifact overlaps with ultrafast dynamics around zero delay, and along with spectral hole burning would require a temporal resolution far higher than was available in the experiments detailed in subsequent chapters [13].

It is assumed that the amplitude gain and refractive index changes in the material are largely due to electron dynamics (equivalent to assuming that the electron and

hole dynamics are the same). The equations describing carrier dynamics are therefore implemented only for conduction band electrons.

If the dynamics of the occupation probabilities, from the full density matrices, are retained the description includes ultrafast dynamics, such as carrier heating [12]. It is density matrix calculations of this form that support the way in which ultrafast dynamics are included in the second version of rate equation based model, described in this chapter, which is referred to as the sliced-propagation model.

5.3 A tale of two versions

The model has been implemented in two stages. Firstly, the set of rate equations describing the evolution of the electric field (amplitude and phase) and the carrier population were defined. Solutions to this set of equations enabled the depletion of the gain and concomitant amplification of the field with propagation to be investigated. The evolution of the state of the SOA was simulated under conditions that corresponded to those that can be used for interferometric switching. Single pulses and pulse trains at variable repetition rates can readily be implemented. This version of the model was used to explore the behaviour of the equations with realistic values for the input parameters.

Secondly, a sliced propagation model, based on the rate equation description of the SOA, was developed. With this structure of model, detailed in section 5.6, the solutions are not sought to the full set of differential equations, rather they are used to formulate difference equations. The SOA is sliced into sections perpendicular to the direction of propagation, and the evolution of the carrier population and optical field are calculated iteratively. This facilitates the calculation of the evolution of pulses propagating in both directions, which is important for the evaluation of the SOA's properties in the context of proposed applications. For example in the TOAD interferometric switch (described in section 1.2.3), one half of the optical signal propagates through the SOA in the same direction as an intense control signal and the other half of the signal propagates in the opposite sense. There is a clear difference in dynamics observed with these co- and counter-propagating pulses and it has a significant impact on switching. This

Parameter	Typical value	Units	Description
J	100	mA	Electrical bias current
μ	0.75	–	Current efficiency
α_{int}	15	cm^{-1}	Internal loss
Γ	0.3	–	Optical confinement factor
σ	0.2	μm^2	Active cross-sectional area
L	1000	μm	Length of device
N_{tr}	1e18	cm^{-3}	Transparency carrier density
τ_N	500	ps	Slow time constant
$\left. \frac{\partial g}{\partial N} \right _{N_{tr}}$	2.4e-16	cm^2	Differential gain
$\left. \frac{\partial n}{\partial N} \right _{n_0}$	-2e-20	cm^3	Differential index
E_{satN}	2	pJ	Slow saturation energy

Table 5.1: Input parameters for rate equations

issue is further discussed later in this chapter and along with relevant results in subsequent chapters. In addition to assisting with the analysis of gain dynamics observed with counter-propagating pulses, the sliced-propagation model is readily extended to include the effects of ultrafast dynamics with those dynamics being described by physically meaningful parameters, time constants and saturation energies.

The definition of the equations and the implementation of the model in *Mathematica* was carried out in collaboration with Michael Mazilu. Both versions of model operate in one dimension only. In the limit of small slices, the results arrived at by the two methods should be equivalent. Indeed comparison of results from the iterative calculations with the solution of the simultaneous equations supports the validity of the iterative method.

5.4 Introducing the rate equations

5.4.1 The basic set of rate equations

The rate of change of carrier density, $\frac{\partial N}{\partial t}$, in the SOA is defined as

$$\frac{\partial N(z, t)}{\partial t} = \frac{\mu J}{e\sigma L} - \frac{N(z, t)}{\tau_N} - g_N(z, t) \frac{\Gamma}{\hbar\omega\sigma} |A(z, t)|^2 \quad (5.1)$$

where τ_N is the time constant governing the recovery of carrier density following population depletion and g_N is the carrier density dependent gain described by

$$g_N(z, t) = \left. \frac{\partial g}{\partial N} \right|_{N_{tr}} (N(z, t) - N_{tr}) \quad (5.2)$$

where $\left. \frac{\partial g}{\partial N} \right|_{N_{tr}}$ is the differential carrier density dependent gain with respect to the carrier density at transparency, N_{tr} and other parameters are as defined in table 5.1 (see section 5.7 for discussion of the choice of input parameters).

The first term of equation 5.1 describes the increase in carrier density from current injection (where e is electronic charge). This increase in carriers is always balanced by recombination of the carriers, described by the second term. Finally, the last term accounts for the interaction of the optical field, $A(t)$, with the carrier population.

Under conditions of gain, the usual mode of operation of the SOA, the carrier density is higher than its value at transparency, N_{tr} . Therefore $N(z, t) - N_{tr}$ is positive and it follows that an optical field (with photon energies within the gain bandwidth) depletes the conduction band carrier population, by stimulating photon emission. On travelling through the device such an optical field is amplified.

To describe the propagation of an optical field through the SOA, knowledge of the refractive index of the material is also required, and it does not have a constant value since there are index changes concomitant with the carrier dynamics. The refractive index is taken to be of the form $n(z, t) = n_0 + \Delta n(z, t)$ (as in equation 1.24) where n_0 is the background index at carrier equilibrium and the change in index due to dynamic changes in the carrier population is given by

$$\Delta n(z, t) = \left. \frac{\partial n}{\partial N} \right|_{n_0} \Delta N \quad (5.3)$$

where $\left. \frac{\partial n}{\partial N} \right|_{n_0}$ is the refractive index change per carrier pair [14].

For interferometric applications the changes in the phase of the optical field that result from this refractive index change are of critical importance. It is therefore necessary to consider a complex optical field. However, separate rate equations can be written for the evolution of the amplitude and phase [15]. A propagation equation for the amplitude of the field can be defined as follows

$$\frac{\partial A(z, t)}{\partial z} + \frac{n(z, t)}{c} \frac{\partial A(z, t)}{\partial t} = (\Gamma g - \alpha_{int}) A(z, t) \quad (5.4)$$

where $A(z, t) = \sqrt{P}$, with P being the optical power in the mode, and internal device losses, accounted for by α_{int} , balance the gain, g . A corresponding equation describing

the evolution of the phase can be written in the following form

$$\frac{\partial \phi(z, t)}{\partial z} + \frac{n(z, t)}{c} \frac{\partial \phi(z, t)}{\partial t} = \left. \frac{\partial n}{\partial N} \right|_{n_0} \frac{(N(z, t) - N_0)}{c} \quad (5.5)$$

As a first approximation it is assumed that the gain changes are due solely to changes in the carrier population (the addition of other gain dynamics is discussed subsequently). It follows that

$$g = g_N \quad (5.6)$$

With this assumption, equations 5.1, 5.4 and 5.5 taken simultaneously form a complete set describing the interaction of optical pulses with the SOA active material.

5.4.2 Implementing the rate equation model

For use in a computer model, these equations were re-expressed in a simpler form which was arrived at by

- converting all parameters to appropriate units (ps, μm , pJ etc.) such that the numbers were computationally manageable
- normalising the parameters with respect to the saturation energy, E_{satN}
- making a transformation into the moving frame of the pulse.

This latter simplification, the change of frame of reference, is equivalent to assuming that the pulse is stationary and has the effect of eliminating the explicit dependence of the pulse amplitude and phase on time. Running the model in this moving frame was computationally easier, and the results were readily transformed to the dynamics that would be seen by a stationary observer, i.e. such that the pulse appears to take a finite time to propagate through the device. This transformation is effected by a change of variables as follows

$$function(z, t) \rightarrow function(z, t') \text{ where } t' = t + zn/c \quad (5.7)$$

where t is 'real time' and t' is the time in the frame moving with the pulse.

The numerical method used for computation is Runge-Kutta over z (space) and then incrementing, by a two point finite difference method, through time. The results

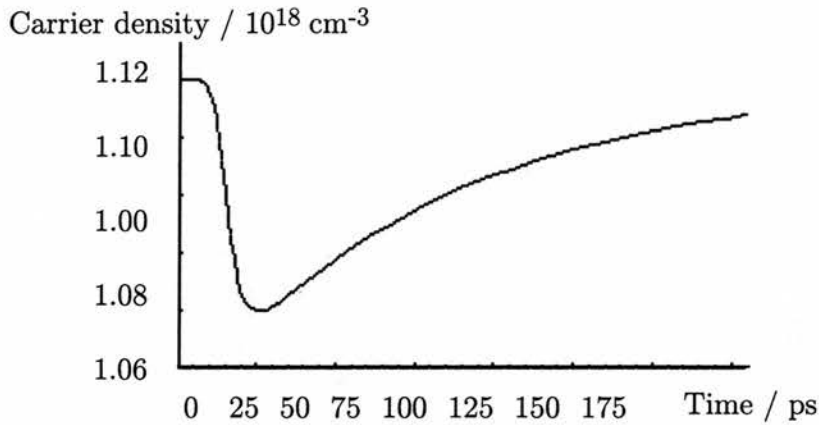


Figure 5.1: The calculated depletion of the carrier population by an intense pulse and subsequent recovery of the density towards its equilibrium value.

from this calculation were compared with the alternative procedure, that is applying Runge-Kutta to calculate over t and then incrementing over z . The maximum difference between the results by these two routes was less than 2% confirming the validity of the calculation method.

5.5 Results from solving the rate equations

5.5.1 Interband recombination

Figure 5.1 illustrates the evolution of carrier density due to the arrival of an intense pulse calculated using the set of simultaneous rate equations. The turn on of the carrier change is rapid, following the pulse profile; the exponential recovery is slow, governed by the time constant, τ_N . Typically τ_N in forward-biased SOAs is hundreds of picoseconds or less, much faster than the spontaneous emission lifetime of the material, due to carrier injection. Chapter 7 details the experimental measurement of the characteristic recovery of the SOA studied as a function of electrical bias.

5.5.2 A quasi-equilibrium regime

The evolution of the carrier density towards a quasi-equilibrium regime, due to a train of pulses, is illustrated in figure 5.2. The carrier density recovers between pulses but

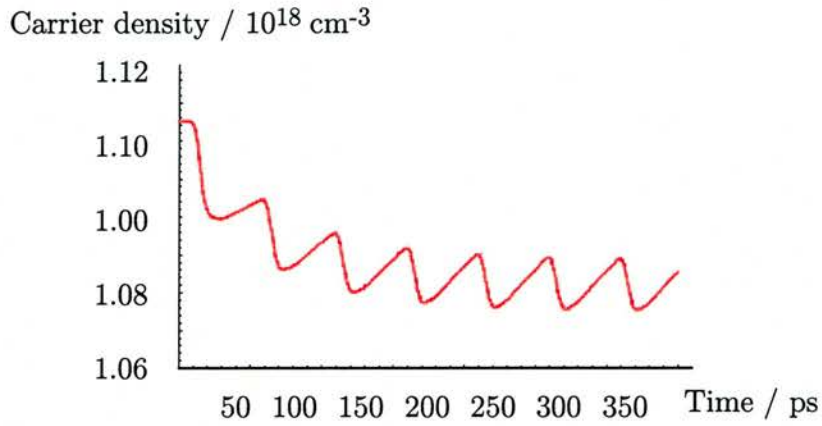


Figure 5.2: The carrier density changes calculated for a train of intense pulses, with the period between them being shorter than the time recovered for full recovery of the carrier population to the initial equilibrium value. Instead the carrier density settles to a quasi-equilibrium value at which the amount of carrier depletion caused by one pulse matches the carrier recovery achieved before the next pulse arrives.

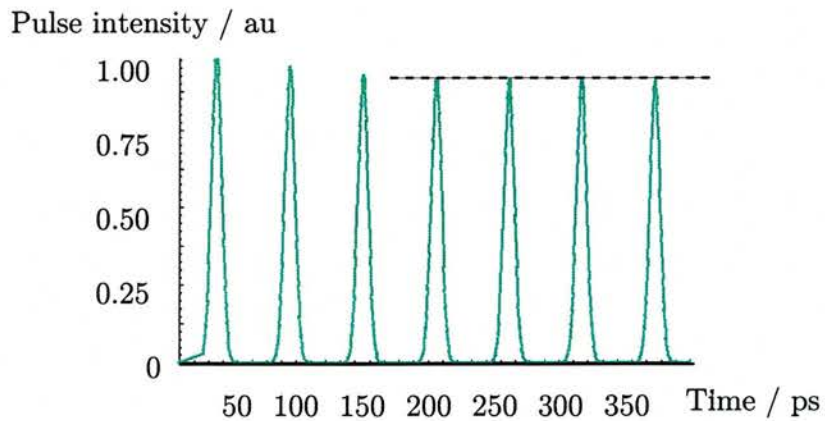


Figure 5.3: The calculated amplitude of output from a train of low intensity input pulses which arrive at the device relatively delayed by 15 ps but at the same repetition rate as the train of pulses causing the carrier density changes plotted in figure 5.2.

never to the initial equilibrium value since the interval between pulses is less than the device recovery time. Initially, the magnitude of the depletion effected by each pulse exceeds the degree of recovery between pulses; the carrier density is therefore successively depleted. However from the fourth pulse onwards, the amount of recovery exactly matches the amount of depletion i.e. the carrier population oscillates within a fixed range. This quasi stable mode of operation is what is meant by a quasi-equilibrium regime.

The pulse train effecting this depletion corresponds to the control pulse in an interferometric switch such as the TOAD (detailed in section 1.2.3). For the signal, a second train of pulses is required at the same clock rate but sufficiently low input intensity that the pulses do not induce significant changes in the carrier density.

During the initial stabilisation period, en route to quasi-equilibrium, the gain available in the SOA immediately following each intense pulse is successively reduced, eventually settling to a fixed value. Figure 5.3 shows this trend manifested in modulation in the output intensity of the train of weak pulses that follow the intense pulse train through the device. Each successive pulse experiences less gain, with the output intensity settling to a fixed value after the third pulse.

The establishment of a quasi-equilibrium can be effected by a low repetition rate pulse train with high energy in each pulse or, equivalently, by a high repetition rate pulse train whilst retaining low energy per pulse. The latter being exactly the conditions desirable for optical network applications i.e. high line rates and low optical powers to avoid nonlinearities in transmission. The process of establishing a quasi-equilibrium and the associated amplitude modulation lasts only as long as it would take for the device to fully recover. Instead of limiting the maximum repetition rate of operation, as would be the case if the device needed to recover fully between switching events, the slow gain recovery dynamic only limits the turn on time for optimum switching.

5.6 Definition of the sliced propagation equations

5.6.1 The simplest equations - interband transitions only

The expression used in the sliced-propagation model to relate gain changes to carrier population changes is derived from a rate equation describing the evolution of the carrier population, of the form of equation 5.1. The assumption that the carrier density dependent gain can be expressed in the form of equation 5.2 continues to apply. Inserting equation 5.2 into the rate equation for carrier density, equation 5.1, yields an expression for the rate of change of carrier density dependent gain, $\frac{\partial g_N}{\partial t}$ of the form

$$\frac{\partial g_N}{\partial t} = \frac{g_0 - g_N}{\tau_N} - g \frac{|A|^2}{E_{satN}} \quad (5.8)$$

The slow saturation energy, E_{satN} , due to saturation of such carrier density changes is given by

$$E_{satN} = \frac{\hbar\omega\sigma}{\Gamma \left. \frac{\partial g}{\partial N} \right|_{N_{tr}}} \quad (5.9)$$

The magnitude of the phase shifts associated with carrier density dependent gain changes may be calculated through use of the α -parameter, the ratio of the rates of change of the real and the imaginary susceptibilities (equation 2.34). It is thereby possible to describe the carrier density dependent phase changes over distance Δl with an expression of the form

$$\Delta\phi = -\frac{1}{2}\alpha_N g_N \Delta l \quad (5.10)$$

This relates phase changes directly to gain changes instead of to carrier density changes via refractive index changes quantified by the parameter $\left. \frac{\partial n}{\partial N} \right|_{n_0}$ (as in equation 5.3).

Considering only gain changes due to interband transitions g_N is the only contribution to the total gain, g i.e. at this stage it is assumed that equation 5.6 is still true. However the form of equations 5.6 and 5.10 are readily extendable to account for amplitude gain and phase changes due to processes other than interband carrier transitions - as is demonstrated later in this chapter.

For propagation through a small slice of the SOA, of thickness Δl , it is assumed that the output amplitude, A_{out} is given by

$$A_{out} \approx A_{in} \exp((\Gamma g(z_i, t) - \alpha_{int} + i\Gamma \Delta\phi(z_i, t)) \Delta l) \quad (5.11)$$

where z_i is the position of the i^{th} slice.

5.6.2 Implementing the iterative calculations

Equations 5.6, 5.8, 5.10 and 5.11 constitute the sliced model in its simplest form, with gain amplitude and phase changes being due only to interband transitions. These equations enable the evolution of the optical field on propagation through the long SOA waveguide to be calculated iteratively.

The gain in each slice is initialised at its equilibrium value and a Gaussian pulse is incident on the first slice. The change in the complex gain of this first slice, due to the passing of the input pulse, is calculated using equations 5.6, 5.8 and 5.10. The output on the far side of the slice, of width dl , is then calculated using equation 5.11. The output becomes the input to the next slice. This process is repeated to accumulate propagation through the full length of the device. At any later time the complex gain can also be calculated as the gain at the level it is immediately after the pulse passed, modified by the degree to which it would have recovered during the time which has elapsed since the optical field passed.

By introducing relative time delays, one or more additional optical pulses can be arranged to be incident on the device at any time with respect to this first field. In the case that these subsequent pulses are sufficiently weak (probes) that it can be assumed that they do not themselves modify the gain, their evolution on propagating through the SOA can be rapidly calculated. What is more, with this iterative model structure, it is no more difficult to implement the calculations for this weak pulse propagating in the opposite direction, through the stack of slices, to the initial, gain-change inducing pulse, than it is to calculate for both fields co-propagating.

5.6.3 Including ultrafast dynamics

Contribution of different ultrafast processes

The equations presented so far in this chapter introduce the structure of the model, but include no ultrafast dynamics. To date, as described in the next part of this chapter, the model has been developed such that the effects of the ultrafast dynamics of carrier heating (CH), spectral hole burning (SHB) and two-photon absorption (TPA) can be considered. These processes are all of interest when discussing the behaviour of the

SOA on which this study focuses for the following reasons.

Pump-probe transmission measurements, reported in Chapter 7, manifest an ultrafast dynamic gain change with the characteristics consistent with CH; the ultrafast dynamic adds to that induced by carrier density changes and occurs on a time scale of a few picoseconds. Consideration of the order of magnitude of time constant associated with SHB (150 fs), with respect to the duration of pulses used in the experimental work reported (~ 700 fs), would suggest that it would not be strongly manifested [16]. Indeed no clear signature of SHB is observed with even the shortest pulses used in the experiments reported in this thesis (350 fs). It is, nevertheless, interesting to explore the effect of an additional ultrafast dynamic with the characteristics of SHB, since it has been suggested in the literature that a full understanding of the dynamics associated with any pulses shorter than 10 ps may require the inclusion of SHB [17]. This is borne out by the calculations of gain saturation, reported in Chapter 6. Lastly, experimental results do not prove the role of TPA. However pulse energy dependent transparency characteristics (reported in section 4.7.3) have previously been associated with TPA in SOAs [18]. In addition, the strength of the ultrafast pump-probe transmission change suggests that TPA may be significant in the device studied.

In practice, since the characteristic contributions of SHB and TPA with this device have not been determined by experiments as yet, the model was generally run with a single ultrafast dynamic, with the characteristics of carrier heating. SHB and TPA were included to observe their effect and some examples of their potential influence on gain dynamics are presented.

Amplitude gain changes

These ultrafast processes which alter the gain are added as additional terms to equation 5.6. Carrier heating (CH) and spectral hole burning (SHB) do not actually change the number of carriers, rather they redistribute the population, potentially removing carriers from the gain region accessible by the optical field under consideration. Hence the contribution of these processes can be thought of through the concept of virtual populations, which deplete or supplement the gain with respect to the contribution from the real carrier population density. TPA directly reduces the available gain if it

τ_T	1.2	<i>ps</i>	CH time constant
τ_{SHB}	0.2	<i>ps</i>	SHB time constant
E_{satT}	0.5	<i>pJ</i>	CH saturation energy
E_{satSHB}	0.15	<i>pJ</i>	SHB saturation energy
β_{TPA}	75	<i>cmGW⁻¹</i>	TPA coefficient
α_N	8	–	Slow α -parameter
α_T	2	–	CH α -parameter
α_{SHB}	0.1	–	SHB α -parameter
α_{TPA}	-2	–	TPA α -parameter

Table 5.2: Supplementary input parameters required for the sliced-propagation model. As discussed in section 5.7, where possible parameters were determined from experiments, e.g. τ_T ; other values were taken from the literature.)

occurs in the active region of the device. The input parameters required to describe these ultrafast dynamics are listed in table 5.2.

Including ultrafast effects, the total gain in the SOA may be defined as

$$g = g_N + g_T + g_{SHB} + g_{TPA} \quad (5.12)$$

where g_T , g_{SHB} and g_{TPA} are additional contributions due to the processes of carrier heating, spectral hole burning and two-photon absorption, respectively [12] [19] [20].

An expression to describe the evolution of the carrier heating contribution to the gain is found by a method parallel to the derivation of the expression for the carrier density gain (outlined above). Specifically, the carrier temperature gain, g_T , is taken to be given by

$$g_T = \left. \frac{\partial g}{\partial T} \right|_{T_L} (T - T_L) \quad (5.13)$$

where T_L is the equilibrium temperature of the lattice. This expression is inserted into a rate equation for carrier temperature, $\frac{\partial T}{\partial t}$, of the form

$$\frac{\partial T}{\partial t} = -\frac{T - T_L}{\tau_T} + \left(\frac{\partial T}{\partial U} \right) \left[\sigma_{fca} N \hbar \omega + \left(\frac{\partial U_c}{\partial N} - E_c \right) g \right] \frac{\Gamma |A|^2}{\hbar \omega \sigma} \quad (5.14)$$

where U_c is the carrier energy density [19]. The three terms in the square brackets account for mechanisms by which the temperature of the carriers may be increased: free carrier absorption (through the coefficient σ_{fca}), hot injected carriers ($\frac{\partial U}{\partial N}$) and stimulated emission taken to occur at band edge (E_c).

This yields an expression for the change in the carrier temperature dependent gain,

$\frac{\partial g_T}{\partial t}$ of the form

$$\frac{\partial g_T}{\partial t} = -\frac{g_T}{\tau_T} - g \frac{|A|^2}{E_{satT}} \quad (5.15)$$

where a temperature saturation energy, E_{satT} is defined as

$$E_{satT} = \frac{\hbar\omega\sigma g}{\Gamma \left. \frac{\partial g}{\partial U_c} \right|_{U_c} \left[\sigma_{fca} N \hbar\omega + \left(\frac{\partial U_c}{\partial N} - E_c \right) g \right]} \quad (5.16)$$

A similar approach is taken to introducing dynamic gain changes due to the redistribution of carriers by spectral hole burning (SHB). The change of SHB dependent gain is expressed as

$$\frac{\partial g_{SHB}}{\partial t} = -\frac{g_{SHB}}{\tau_{SHB}} - g \frac{|A|^2}{E_{satSHB}} \quad (5.17)$$

Note that the SHB saturation energy, E_{satSHB} would be expected to be wavelength dependent, tending to zero at transparency; it is given values from the literature which have been determined by experiments.

The effect on the gain of two-photon absorption is through the absorption of photons from the optical field propagating through the SOA. The resultant reduction in the gain is instantaneous and is proportional to the two-photon coefficient, β_{TPA} and the square of the optical field. Hence it is reasonable to express the change in gain due to TPA as

$$g_{TPA} = -\frac{\beta_{TPA}}{\sigma} |A|^2 \quad (5.18)$$

Refractive index and phase changes

To describe the relationship between changes in index and gain due to these ultrafast processes further α -parameters are used. For carrier heating, a temperature parameter, α_T , has been defined (see for example [16] [21] [22])

$$\alpha_T = -\frac{4\pi}{\lambda} \left. \frac{\partial n / \partial T}{\partial g / \partial T} \right|_{T_L} \quad (5.19)$$

Values of α_T quoted in the literature are of a similar order of magnitude to α_N , 1.9 to 3 [16] [23]. In the same way phase changes due to SHB can be quantified with an SHB α -parameter, with $\alpha_{SHB} < 1$, to account for its weak contribution to refractive index dynamics [19].

To account for the relative changes due to TPA, an α_{TPA} is defined as

$$\alpha_{TPA} = \frac{4\pi}{\lambda} \frac{n_{2I}}{\beta_{TPA}} \quad (5.20)$$

where n_{2I} is the coefficient for the intensity dependent refractive index change (discussed in section 2.9.2).

The total phase change is given by $\Delta\phi = \frac{2\pi L}{\lambda} \Delta n$ where the change in index, Δn is given by the sum of the contributions from carrier population changes, CH, SHB and TPA. Substituting for Δn in terms of the gain factors and α -parameters, yields an expression for the phase change over distance Δl as a function of the different gain changes

$$\Delta\phi = -\frac{1}{2} (\alpha_N g_N + \alpha_T g_T + \alpha_{SHB} g_{SHB} + \alpha_{TPA} g_{TPA}) \Delta l \quad (5.21)$$

5.7 Defining the input parameters

For the results of calculations from the model to be a useful aid in interpreting the experimental results, it was important to tie the behaviour of the model to experimental observations. As outlined in this section, measured values for time constants and small signal gain were used to determine reasonable values for associated input parameters. The magnitude of the unsaturated gain and the input for which this gain was reduced by 3 dB, with CW light and with pulses, were used to calibrate the powers/energies in the model.

The α -parameters were not measured, but the values used in the model were adjusted within the range of values reported in the literature for this type of SOA, to give a ratio between the magnitude of the ultrafast and slow dynamics which corresponded to that observed experimentally. Other input parameters were given values appropriate for an SOA with an active region consisting of MQWs, or a superlattice where available, taken from the literature (including [12][14][19] [24][25][26][27] [28][29]).

5.7.1 Time constants

As described in Chapter 2, the rate of carrier recombination in a semiconductor is the sum of contributions from radiative and non-radiative process, but it is reasonable to consider that in an SOA biased into gain the dominant process is Auger recombination.

However, as reported in Chapter 7, this assumption is found to break down at high biases.

Consequently the value of the slow time constant, τ_N for different biases is ascertained by fitting curves to the gain recovery observed in the pump-probe experiments. An important caveat is that this was only possible over the parameter range corresponding to the experimental conditions for which experiments had been conducted. However this was not problematically restrictive since the model is being used to explore the dynamics associated with these same experimental conditions.

It also appeared from experiments that the fast time constant varies with bias current: contrary to the slow recovery by recombination, the experimental results suggest that the rate of ultrafast recovery increases with bias. However the data is not conclusive, and in the modelling the ultrafast time constants are kept fixed. Specifically, τ_T is given the average value from fits to the pump-probe data, 1.2 fs, and τ_{SHB} is set at 200 fs, which is reasonable given the range of values reported in the literature [19][28].

5.7.2 Unsaturated gain as a function of current

Under steady state conditions and with no perturbing field (i.e. $A = 0$) equation 5.1 leads to the definition of an equilibrium carrier density, N_0 of the form

$$N_0 = \frac{\mu J \tau_N}{q \sigma L} \quad (5.22)$$

It follows that unsaturated gain, g_0 , the so-called small signal gain, can be expressed as

$$g_0 = \left. \frac{\partial g}{\partial N} \right|_{N_{tr}} (N_0 - N_{tr}) = \left. \frac{\partial g}{\partial N} \right|_{N_{tr}} \left(\frac{\mu J \tau_N}{q \sigma L} - N_{tr} \right) \quad (5.23)$$

This expression would result in an increase in the small signal gain value that is linear with current, if it were not for the fact that recovery governed by τ_N is not constant: at higher currents the gain recovery is faster and the increase in g_0 saturates.

It was decided to describe the small signal gain as a function of current by an empirical equation of the form

$$g_0 = \frac{J_s N_{tr}}{J_{tr}} \left. \frac{\partial g}{\partial N} \right|_{N_{tr}} \frac{J - J_{tr}}{J + J_s} \quad (5.24)$$

where J_{tr} , the current for which $g_0 = 0$, and J_s , the turn over point for the saturation, are determined by fits to experimental measurements of small signal gain.

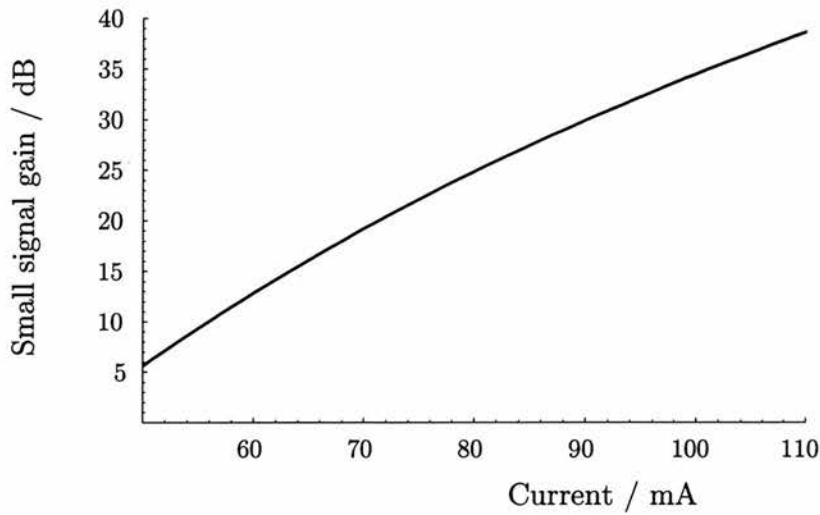


Figure 5.4: The SOA small signal gain as a function of current of the form given by the empirical expression in equation 5.24.

From measurements at several different wavelengths, J_s was found to be approximately 180 mA, and J_{tr} approximately 40 mA. This is consistent with the trend in magnitude of transmission changes observed with pump-probe measurements (section 7.4.1). However, in both cases the transparency current differs from the (lower) values found by the dV measurements (reported in Chapter 4). The apparent discrepancy is attributed to the fact that the gain and transmission measurements both include losses the optical field experiences on coupling and propagation through the device (α_{int}). That is, the transparency currents (~ 10 to 25 mA) found from the dV measurements do indeed put the material into a state of gain, however the amplification of the optical field at levels of bias just above this material transparency are insufficient to overcome the waveguide losses. Figure 5.4 illustrates the total small signal gain of the SOA device as function of bias, including the waveguide losses, as given by equation 5.24.

5.7.3 Gain saturation as a function of the optical field

As discussed more extensively in Chapter 6, the strength of optical field necessary to saturate the device differs substantially depending on whether the optical field is CW or pulsed, and, if pulsed, on the pulse duration. To explore, with the sliced-propagation model, the gain saturation with CW light, the steady state solutions were found to the equations for pulses (equations 5.8 and 5.15).

The level of the device gain as a function of the strength of the input field was calculated for both CW and pulsed input to obtain the 3 dB saturation points. The saturation energies, E_{satN} and E_{satT} were adjusted, within reasonable values, to achieve agreement between the ratio of the calculated peak powers for 3dB of gain saturation and the ratio determined experimentally. This was readily achieved since for the short pulses the saturation behaviour was dominated by value given to the smaller saturation energy, E_{satT} . Subsequently the larger saturation energy, E_{satN} was varied to achieve the necessary ratio.

Finally, the relationship between the experimentally determined energies (for pulses) and powers (for CW) for which the gain was saturated by 3 dB and the corresponding input coefficients, used in the model, were used to calibrate the model. The energies (or powers) in and out of the device were thereby defined as a fraction or multiple of the total experimentally determined saturation energy (or power).

5.8 Results from sliced propagation calculations

Sample results from calculations with the sliced-propagation model are presented in this chapter to demonstrate the operation of the model and the type of calculations that it has been used for. Further results however are deferred to be shown along with discussion of experimental results in subsequent chapters. Unless stated otherwise, input parameters were as defined in tables 5.1 and 5.2.

5.8.1 Pump-induced gain changes

The first stage of evaluating the model was to propagate a single pulse through the device. For example, figure 5.5 illustrates the pulse amplitude at each slice through the device (in this case, at intervals of $25 \mu\text{m}$) firstly considering only gain dynamics dependent on carrier density, g_N and, secondly, including the influence on gain of carrier temperature changes, g_T . The same input pulse, with an energy of a tenth of the saturation energy and duration of 700 fs, was used in both cases and the electrical bias was fixed at 90 mA.

The energy of the pulse, with duration, τ_p , was obtained by integrating over the

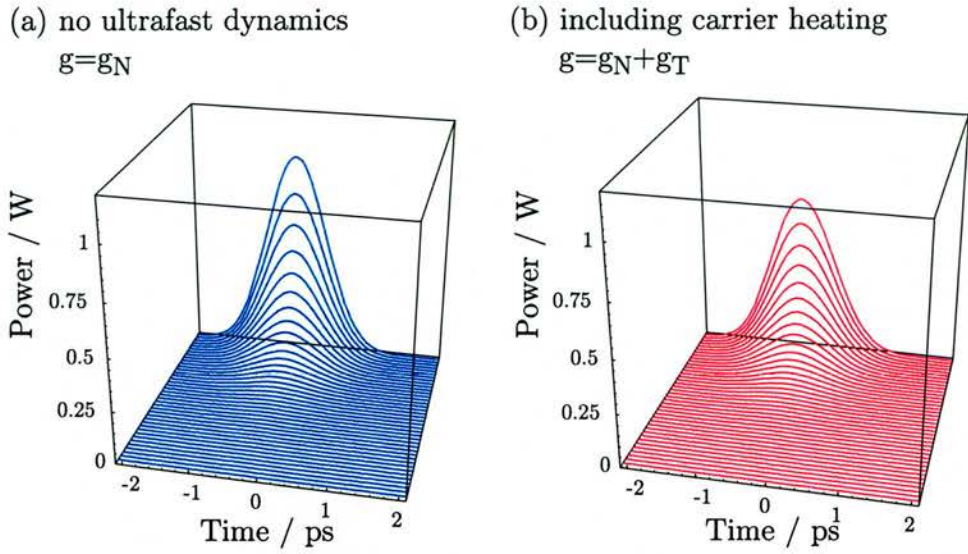


Figure 5.5: The pulse amplitude as it propagates through the SOA for gain dynamics dependent only on carrier density changes (a - blue) and with the additional gain dynamic of carrier heating (b - red). Note the depth corresponds to distance along the waveguide, successive curves being the calculated output after each 25 μm slice.

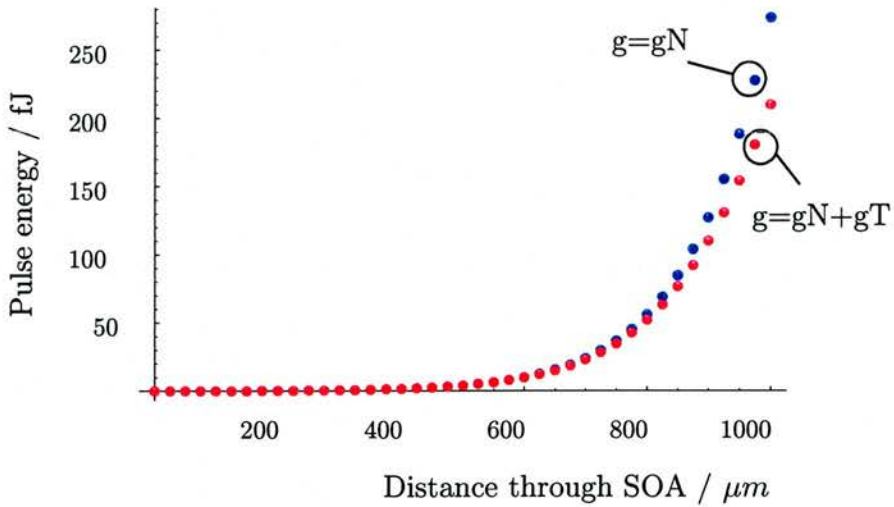


Figure 5.6: The growth in pulse energy through the SOA corresponding to the two cases illustrated in figure 5.5.

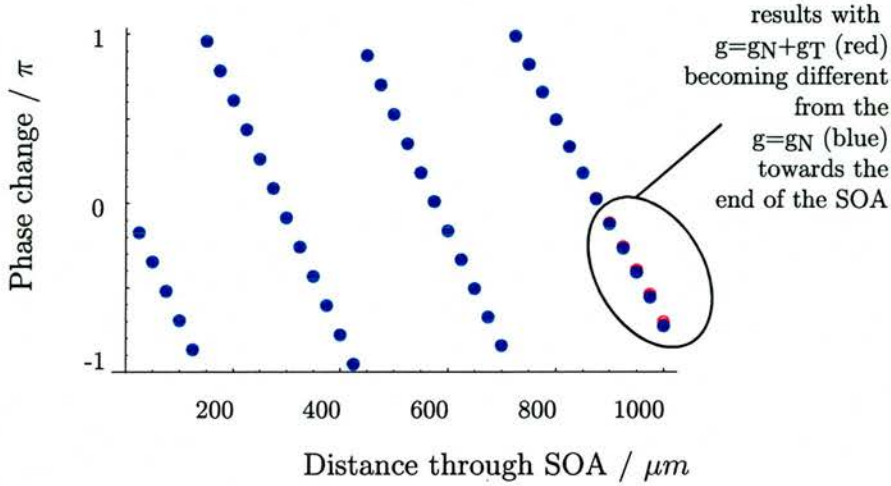


Figure 5.7: The accumulation of phase change on propagation through the SOA (after each slice) with gain dynamics dependent only on carrier density changes (blue) and with the additional gain dynamic of carrier heating (red).

pulse: from $-7\tau_p$ to $5\tau_p$, with wider bounds towards longer delays to allow for shift in the peak of the pulse to later times due to the induced index change. Figure 5.6 illustrates the growth of this energy along the device for the pulses shown in figure 5.5.

The phase change accumulated by the pulse as it travels through the SOA is shown in figure 5.7, for the two cases illustrated in figure 5.5. In both amplitude and phase, the total change through the device is smaller for the case where carrier heating term is included. This trend is shown more clearly by looking at the gain per unit length experienced by the pulse at different places in the device.

The amplification experienced by the pulse on propagation through each slice was calculated according to

$$G = \frac{E_{out}}{E_{in}} \quad (5.25)$$

Figure 5.8 illustrates the evolution of the gain per unit length along the device for just g_N and for the case of g_T also included. It is clear from this plot that the gain is saturated more rapidly where carrier heating is included. This is consistent with the saturation for low input intensities that is found with ultrafast pulses - a characteristic that is explored more extensively to understand the gain saturation results in Chapter 6. Subsequently the amplification per slice at different points along the length of the device is investigated in more detail, in section 7.4.2, to explore the longitudinal saturation observed with counter-propagating pump-probe experiments.

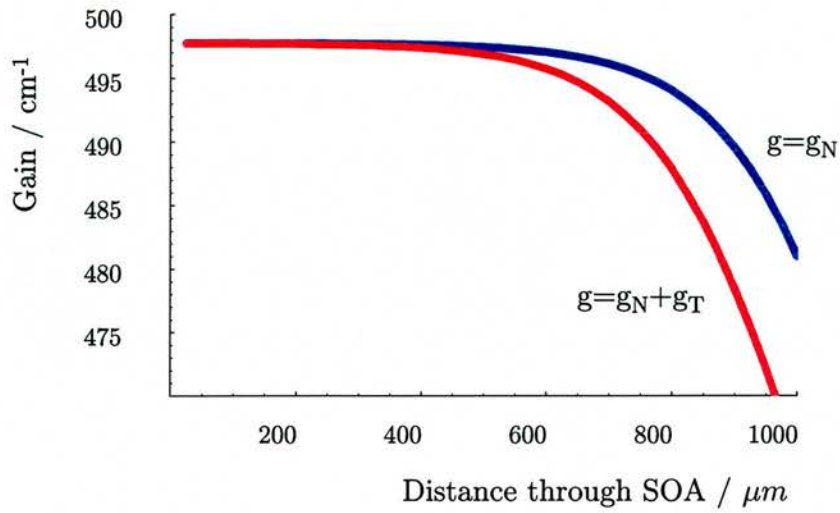


Figure 5.8: The amplification given by the available gain as a function of distance through the device with gain dynamics dependent only on carrier density changes (blue) and with the additional gain dynamic of carrier heating (red).

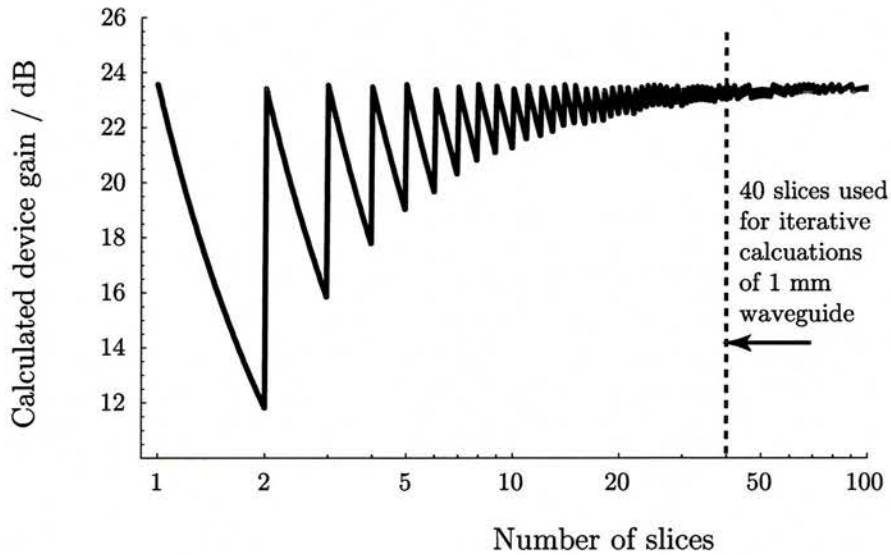


Figure 5.9: Device gain calculated using the sliced propagation model as function of the number of slices used.

The total gain experienced by a pulse on propagation through the SOA is given by equation 5.25, where the input and output are the amplitude of the pulse input to the first slice and output from the last slice. Keeping the length of the device constant, the number of slices was increased until the value of this gain approached a constant, as shown in figure 5.9. It was concluded that 40 slices, which for the 1 mm long waveguide corresponds to slices 25 μm thick, was a reasonable balance between accuracy and computation time. Using a higher number of slices does not qualitatively change the solution. Under these conditions, if only slow carrier changes are considered the results from the iterative calculations and solution of the set of rate equations are equivalent. Note, for comparison, that Blow et al. [30] in their calculations of propagation in a 1 mm SOA with a sliced model found that calculations with 20 slices agreed well with the exact result (from a non-iterative calculation) and therefore concluded that 20 slices were sufficient.

5.8.2 Co-propagating probe dynamics

Figure 5.10 illustrates the change in transmission of a probe, that propagates through the SOA in the same direction as the pump (co-propagating), as a function of the probe delay with respect to the pump. The SOA biased into gain with a current of 70 mA and the different colour curves correspond to calculations including different dynamic gain changing mechanisms, as indicated in the key. With only the carrier density dependent gain changes, $g = g_N$ (blue curves), the calculation reproduces the solution to the rate equations for co-propagation (for example, figure 5.1). The gain contributions g_T , g_{SHB} and g_{TPA} correspond to the ultrafast dynamics of carrier temperature (carrier heating - CH), spectral hole burning (SHB) and two-photon absorption (TPA), respectively.

The curves in figure 5.10 (a) illustrate the ultrafast dynamics adding to the magnitude of the ultrafast gain change, under conditions of gain (note that TPA always contributes in the same sense and therefore subtracts from the other dynamics under absorption). Under these gain conditions, the inclusion of first SHB, and subsequently TPA, tend not to qualitatively change the nature of the trace with respect to the case of including only carrier density and temperature changes. What is significant how-

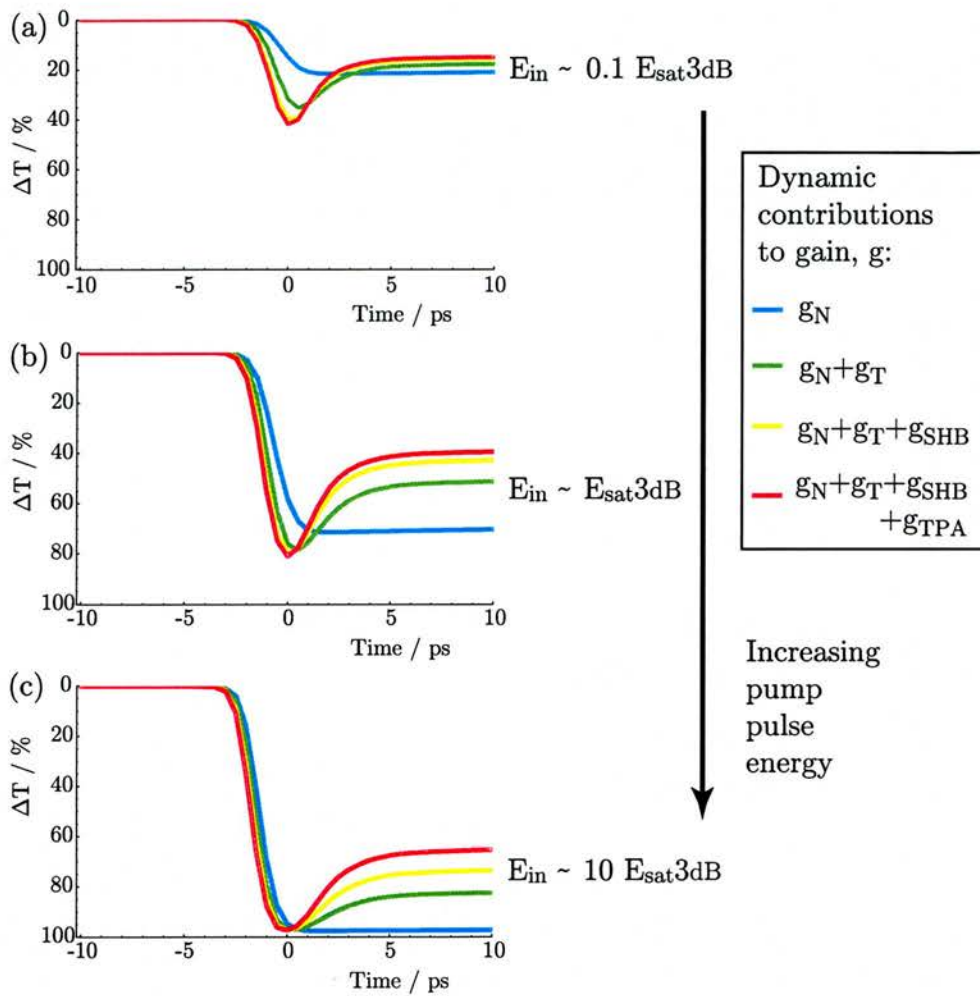


Figure 5.10: The calculated change of transmission of a probe co-propagating with the pump as a function of the pump delay.

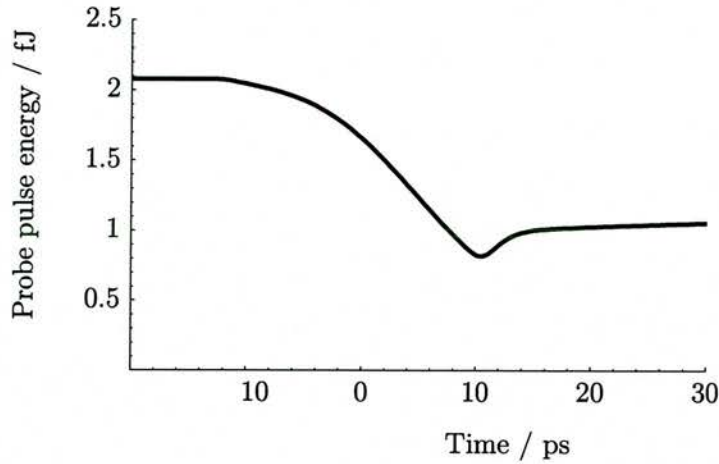


Figure 5.11: The calculated change of transmission of a probe counter-propagating with respect to the pump as a function of their relative delay.

ever is that the additional dynamics alter the ratio between the ultrafast and slowly recovering portions of the gain change. Between (a) to (c) of figure 5.10 the energy of the pump pulse is increased and the fraction of the change in transmission that is long-lived increases is found to increase. Notably, the effect of including the additional ultrafast contributions was to retain a more significant ultrafast component to the traces even with a high pump pulse energy ($10 E_{sat}3dB$). In particular, the contribution of TPA increases with the strength of the pump pulse; this consideration is returned to to explain pump-probe results in section 7.4.1. In general though, since the separate contributions of each ultrafast process have not been identified experimentally, it is not instructive to present simulations of all experimental results with multiple ultrafast dynamics. Consequently, in the analysis that follows the ultrafast dynamic is given by a single component, with characteristics consistent with the process of carrier heating.

5.8.3 Counter-propagating probe dynamics

Figure 5.11 illustrates the change in transmission of a probe counter-propagating with respect to the pump (including carrier density and temperature gain changes). Note the slow turn on of the changes, limited by time to propagate through the device. Plots from further calculations of this counter-propagating pump-probe dynamic successfully reproduce the experimental measurements and are shown in Chapter 7.

Since the difference in co- and counter-propagating experiments is only with re-

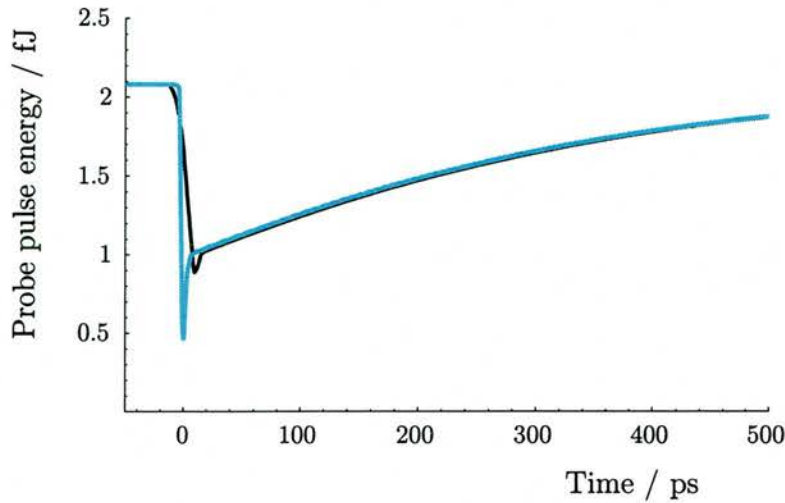


Figure 5.12: The calculated change of transmission co- and counter-propagating probes with respect to the pump as a function of the their relative delay.

spect to propagation through the device, the characteristic recovery should be the same for both. This was confirmed by comparison of the calculated results: as illustrated in figure 5.12 the co- and counter-propagating traces overlap at longer delays.

5.8.4 Interference signal

Pump-induced transmission changes can be detected directly, by measuring intensity changes in the probe; this is not the case for phase changes. As described in Chapter 8, phase changes can be monitored experimentally with an additional probe, which passes through the device at a different time, as a reference. Differential phase changes are then related to changes in the strength of interference of the two probes.

Setting up the loop

The calculations with the sliced propagation model were tailored to correspond to the actual experimental conditions. Specifically, with no differential phase introduced between the probes by changes in the SOA, the signals transmitted through the loop interfered destructively, and conversely those reflected interfered constructively. To understand why this was, it is necessary to consider the effect of each reflection and transmission from the beamsplitter, as follows.

With a 50:50 beamsplitter at 45° the coefficients of transmission and reflection are

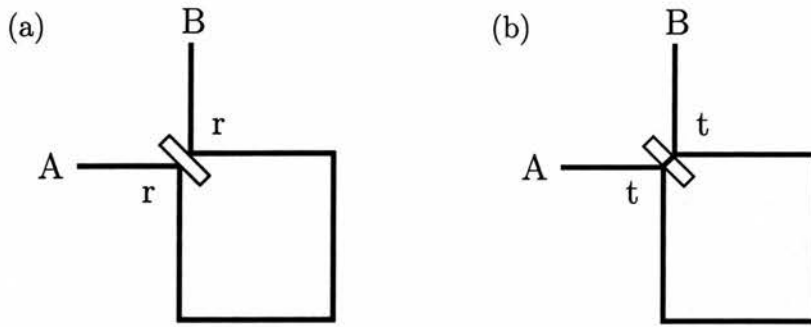


Figure 5.13: Schematic illustrating that for pulses to pass through the loop, input at A and emerge at B, they must either be twice reflected (a) or twice transmitted (b) through the beamsplitter.

nevertheless different as given by equations 5.26 and 5.27 respectively; reflection being imaginary.

$$t = \frac{1}{\sqrt{2}} \quad (5.26)$$

$$r = \frac{1}{\sqrt{2}}i \quad (5.27)$$

The light which passes through the loop, illustrated schematically in figure 5.13, has either been twice reflected or twice transmitted. In the context of the TOAD (described in detail in 1.2.3), the twice transmitted and twice reflected components correspond to the clockwise and anticlockwise probe pulses seen at the output port of the loop (B). Their magnitudes are given by

$$tt = \frac{1}{2} \quad (5.28)$$

$$rr = -\frac{1}{2} \quad (5.29)$$

In contrast the components transmitted and then reflected, or reflected and then transmitted correspond to pulse re-emerging at the input to the loop (A) and their magnitudes are

$$tr = \frac{1}{2} \quad (5.30)$$

$$rt = \frac{1}{2} \quad (5.31)$$

Hence in case of no differential effect of the SOA on the signal pulses (due to there being no control pulse or all the pulses being so low in intensity that they do not modify

the carrier population), a high signal is seen in reflection. Under these conditions, the transmitted intensity is low. It is only the ideal case of zero if the co- and counter-propagating signals are of identical magnitude at the point where they interfere. This corresponds to the practical requirement of using an ideal 50:50 beamsplitter and there being no directional dependence to the losses on propagation through any other optical components in the loop; in practice these two criteria tend not to be met exactly, so the minimum is greater than zero, as discussed further in Chapter 8.

Interference equations

In general, for two degenerate complex pulses, $E_1(z, t)$ and $E_2(z, t)$ the interference signal at their point of overlap is merely their sum. However in the experiments reported here it is the case that these fields correspond to the components of a signal pulse that have both passed through the SOA, but the interference takes place on the far side of the beamsplitter. The preceding analysis of the transmission and reflection coefficients has shown that in addition to the effect of propagating through the SOA, they are necessarily shifted out of phase by the beamsplitter. It follows that the interference signal resultant after the beamsplitter is given by

$$E_3(t) = E_1(t) - E_2(t) \quad (5.32)$$

where the strength of the interference determines whether the signal appears switched through the loop or annulled (having been reflected back to the input).

The power of this interference signal, $P_{out}(t)$, can be expressed as

$$P_{out}(t) = \frac{1}{2} [A_1(t)^2 + A_2(t)^2 - 2A_1(t)A_2(t)\cos(\phi_1(t) - \phi_2(t))] \quad (5.33)$$

where $A_{1,2}$ are the pulse amplitudes and $\phi_{1,2}$ their phase. The first maxima of $P_{out}(t)$ occurs when the difference in phase, $\Delta\phi$ is π , since then $\cos(\Delta\phi) = -1$ which reverses the sign of last term in equation 5.33. Subsequent maxima occur for $\Delta\phi = n\pi$ where $n = 3, 5, 7, \dots$ i.e. an odd integer. Conversely, if the magnitudes of the pulses are equal ($|A_1(t)| = |A_2(t)|$) then $P_{out}(t) = 0$ if $\Delta\phi = n\pi$, where $n = 0, 2, 4, \dots$ i.e. n is zero, the case of no control pulse, or an even integer.

From this analysis it follows that the experimentally measured interference signal can be expected to move from a minima to a maxima by increasing the pump energy

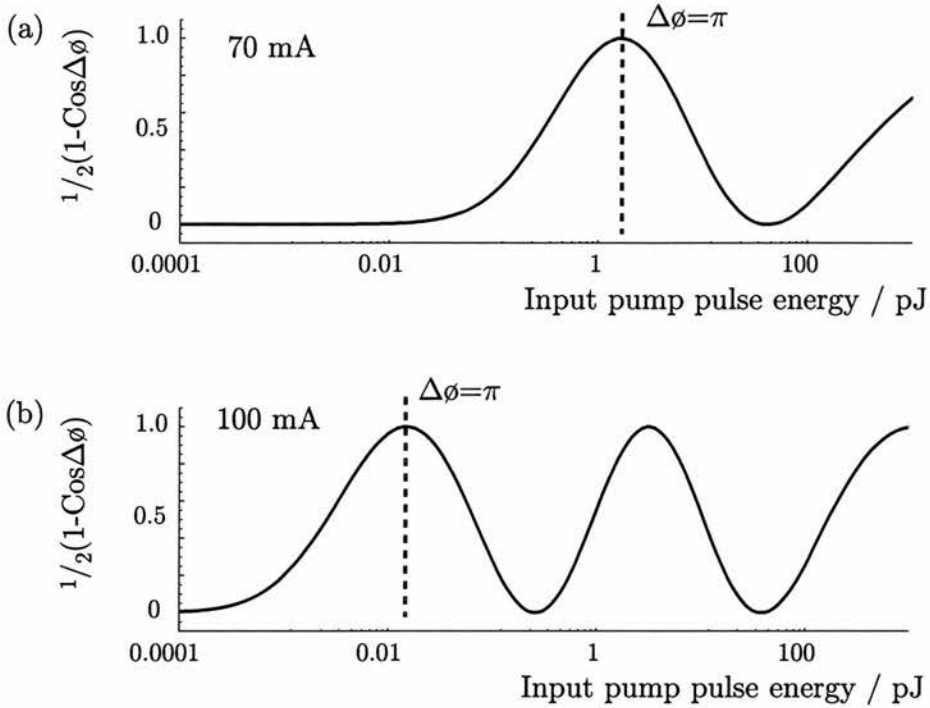


Figure 5.14: The maximum interference signal (normalised) calculated as a function of the pump pulse input energy with an electrical bias of (a) 70 mA and (b) 100 mA. Note that a maximum in the interference signal, corresponds to $\Delta\phi = n\pi$ where n is an odd integer and the first a maximum ($n=1$) occurs at a much lower energy for the higher bias.

by an amount that induces a π phase change. The intensity of the interference signal switching between high and low, corresponds, for example, to switching the transmission on and off in a TOAD demultiplexer.

In the ideal case of the amplitudes of the two probes being equal ($|A_1(t)| = |A_2(t)|$ in equation 5.33), the maximum normalised interference signal is proportional to $\frac{1}{2}(1 - \cos(\Delta\phi))$ [27]. Figure 5.14 illustrates the evolution of this signal as a function of the energy of the pump pulse, where gain changes due to carrier density and carrier temperature are included with α_N and α_T given values of 10 and 2 respectively. The probe pulse energy was fixed energy at 1 fJ. The calculations shown in figure 5.14 indicate that to achieve switching a pump pulse energy of between 10 fJ and a few pJ would be required. The latter is high with respect to the energies available from the optical pulse sources used in experiments.

Note also that the minimum pump energy to achieve a π phase change is reduced if

the strength of the amplitude gain to phase coupling is increased, via the values given to the α -parameters. That is, the change between figure 5.14 (a) and (b) was due to changing the electrical bias from 70 to 100 mA, but could also have been achieved by changing the values used for the α -parameters.

Switching characteristics

Remembering the fields $E_1(z, t)$ and $E_2(z, t)$ are the output fields from the SOA, it is clear that the actual strength of the transmitted interference signal at any time, t , depends on when they propagate through the SOA with respect to each other and with respect to the intense control pulse, the pump. The three-dimensional plot shown at the top of figure 5.15 illustrates the transmitted signal as a function of the two delays: the delay between probe 1 and the pump and the delay between probe 1 and probe 2.

Since the nature of the interference is complex, in this 3D plot only slow gain dynamics, due to carrier density changes, are considered i.e. $g = g_N$ (plots including ultrafast processes are included with discussion of experimental results in Chapter 8). The pump pulse energy is given a value such that the phase of the first probe is changed by a maximum of π . The probe pulse input energies are equal, and less than one hundredth the energy of the pump pulse i.e. the probes are in the linear, small signal gain region by a safe margin (as required, since in the model the probes do not alter the gain).

With a fixed delay between the two probes, the interference signal as a function of pump delay corresponds to taking diagonal slices through the 3-D plot at the top of figure 5.15, such that the intersection of the slice with the plane of the x and y axes forms a line with a gradient of 1 with respect to those axes. The crossing points on the x and y axes determine the relative arrival times of the two probes. For example, this yields the curves shown in the lower part of figure 5.15. With the counter-propagating probe preceding the co-propagating one (a), the less steep transition is from low to high transmission rather than vice versa; with the co-propagating probe preceding the counter-propagating one (c), these features are reversed. In the centre, where the delay between the probes is very small (b), less than the time required for the full change in transmission to occur, the window is reduced to a small triangle. These curves map

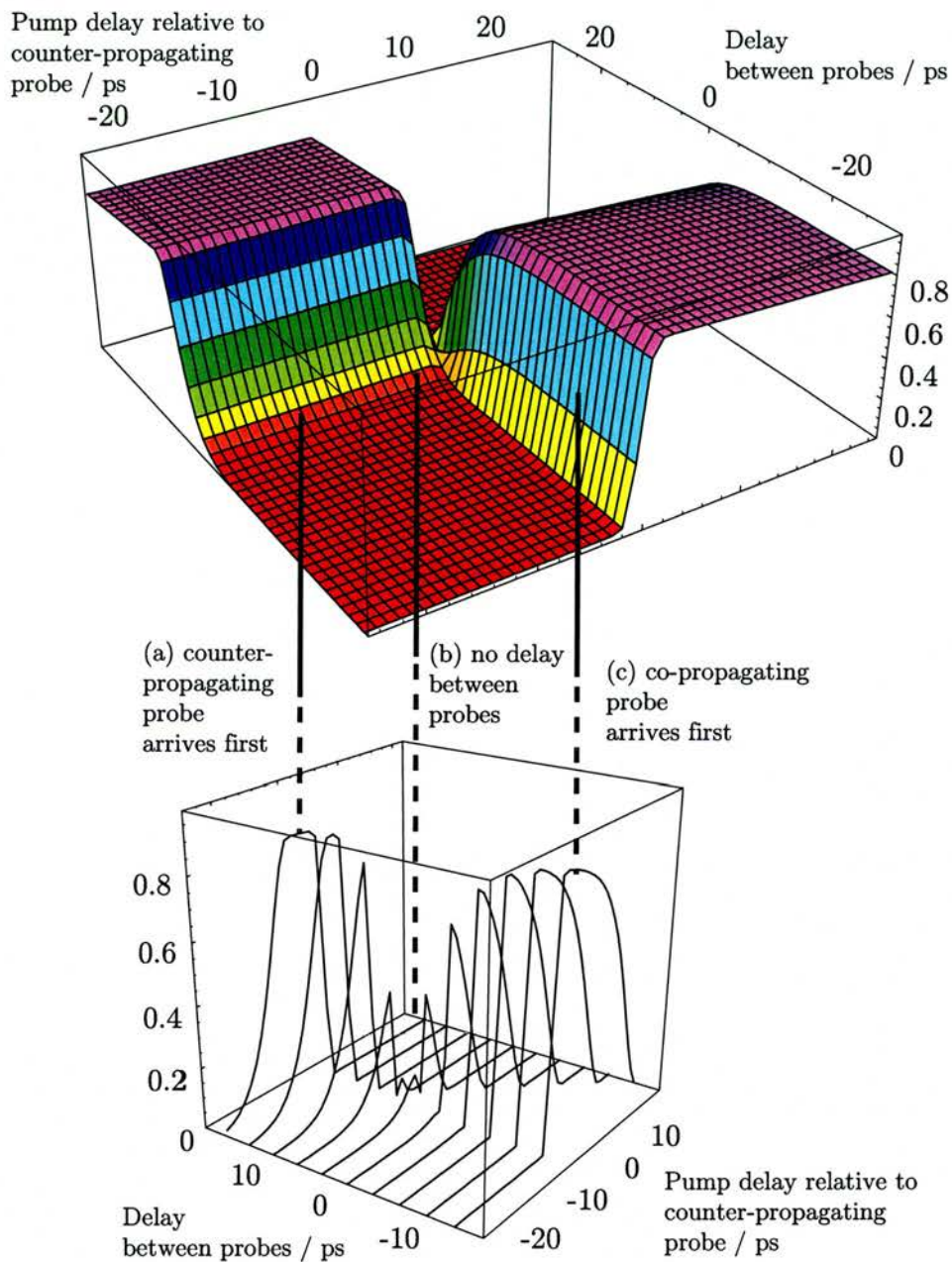


Figure 5.15: At the top, the calculated interference signal as a function of the relative delays of the two probes and the pump, where changes in gain and phase are due to carrier density changes only ($g = g_N$). Below, slices through this surface, which correspond to the switching window: the interference signal as a function of pump delay, with a fixed delay between the two probes.

out the switching window for the TOAD interferometric switching configuration and correspond to the measurements made in the three-beam pump-probe measurements reported in Chapter 8. Note that, in the plots of the switching window, the peak values reached are less than one and in some regions outside the ‘window’ the background is greater than zero. The maximum is reduced by the fact that the second pulse experiences less amplitude gain in the device, consequently the magnitudes of the two probes are not equal at the point that $\Delta\phi = \pi$ (as assumed in the calculations of the ideal case, illustrated in figure 5.14); the magnitude of the maximum constructive interference is therefore reduced. Outside the window it is not necessarily the case that $\Delta\phi = 0$ so the destructive interference does not reduce the signal to zero. Optimisation of the switching window, to maximise the contrast between the on and off states of the interferometric switch, is discussed in more detail with experimental results in section 8.3.5.

5.9 Summary

This chapter has described the development and implementation of two versions of rate-equation based models describing gain dynamics. The models assist with the understanding of the complex behaviour of the SOA device.

In the first model, the solutions to a set of simultaneous equations describing the evolution of the optical field (amplitude and phase) and the carrier population were found. In particular, the establishment of a quasi-equilibrium regime, under which the carrier density oscillates about a fixed level, has been demonstrated. This regime can be used for high bit rate demultiplexing, using control pulse trains with an inter-pulse period of less than the slow gain recovery time, so long as the gain change imposed by the control and subsequent periodic gain recovery (i.e. between control pulses) corresponds to a differential π phase change.

The second model that has been presented is a sliced-propagation model. With sufficiently small slices ($\leq 25 \mu\text{m}$) this model produces the same device behaviour as the solution based on a set of simultaneous equations. However the iterative structure of the sliced-propagation model is designed to facilitate the calculation of the gain

dynamics induced and experienced by pulses propagating in contrary directions, and possibly crossing in the device. In particular it has been outlined how this model can be used to calculate the strength of interference between two weak pulses (probes) which have counter-propagated through the SOA, where each experiences different degrees of amplification and refractive index change due to the carrier dynamics induced by a third (control or pump) pulse. This calculation corresponds to the switching function in the TOAD configuration, introduced in Chapter 1, for which experimental results are presented in Chapter 8.

In addition it has been described how ultrafast processes, that create rapidly changing gain (in addition to the slow carrier density dependent gain changes), can be successively added to the sliced-propagation model. The timescales and relative strengths of carrier heating, spectral hole burning and two-photon absorption are described by meaningful parameters such as time constants and saturation energies.

In this chapter, the complex behaviour of the SOA has been illustrated with sample plots from this sliced-propagation model. Further results are presented along with experimental results in subsequent chapters. In particular the model has been used to calculate gain dynamics that correspond closely to the pump-probe and switching experiments reported in Chapters 7 and 8. The model is also used to support explanations of the gain saturation characteristics reported in Chapter 6.

Bibliography for Chapter 5

- [1] S Adachi. Material parameters of $In_{1-x}Ga_xAs_{1-y}P$ and related binaries. *J. Appl. Phys.*, 53(12):8775–8792, 1982.
- [2] B Broberg and S Lindgren. Refractive index of $In_{1-x}Ga_xAs_yP_{1-y}$ and InP in the transparent wavelength region. *J. Appl. Phys.*, 55(9):3376–3381, 1984.
- [3] S Adachi. Optical properties of $In_{1-x}Ga_xAs_yP_{1-y}$ alloys. *Phys. Rev. B*, 39(17):12612–12621, 1989.
- [4] J V Moloney, R A Indik, J Hader, and S W Koch. Modeling semiconductor amplifiers and lasers: from microscopic physics to device simulation. *J. Opt. Soc. Am. B*, 16(11):2023–2029, 1999.
- [5] J-Z Zhang and I Galbraith. Private communication. Heriot Watt University, Edinburgh, 2002.
- [6] J-Z Zhang, J M Vazquez, M Mazilu, A Miller, and I Galbraith. Dispersion induced ultrafast pulse re-shaping in 1.55 μm InGaAs/InGaAsP optical amplifiers. *IEEE J. Quantum Elect.*, submitted 2003.
- [7] J Shim, J Kim, D Jang, Y Eo, and S Arai. Facet reflectivity of a spot-size-converter integrated semiconductor optical amplifier. *IEEE J. Quantum Elect.*, 38(6):665–673, 2002.
- [8] J Mork and A Mecozzi. Theory of the ultrafast optical response of active semiconductor waveguides. *J. Opt. Soc. Am. B*, 13(8):1803–1816, 1996.
- [9] J Verdeyen. *Laser electronics*. Prentice-Hall, 1989.
- [10] A Yariv. *Quantum Electronics*. Wiley, New York, 3rd edition, 1989.
- [11] J Mark and J Mork. Subpicosecond gain dynamics in InGaAsP optical amplifiers: Experiment and theory. *Appl. Phys. Lett.*, 61(19):2281, 1992.
- [12] M Y Hong, Y H Chang, A Dienes, J P Heritage, P J Delfyett, S Dijaili, and F G Patterson. Femtosecond self- and cross-phase modulation in semiconductor laser amplifiers. *IEEE J. Sel. Top. Quant.*, 2(3):523–539, 1996.
- [13] P Borri, F Romstad, W Langbein, A E Kelly, J Mørk, and J M Hvam. Separation of coherent and incoherent nonlinearities in a heterodyne pump-probe experiment. *Opt. Express*, 7(3):107–112, 2000.
- [14] R J Manning, A D Ellis, A J Poustie, and K J Blow. Semiconductor laser amplifiers for ultrafast all-optical signal processing. *J. Opt. Soc. Am. B*, 14(11):3204–3216, 1997.
- [15] J M Tang, P S Spencer, and K A Shore. The influence of gain compression on picosecond optical pulses in semiconductor optical amplifiers. *J. Mod. Optic.*, 45(6):1211, 1998.
- [16] M Y Hong, Y H Chang, A Dienes, J P Heritage, and P J Delfyett. Subpicosecond pulse amplification in semiconductor laser amplifiers: Theory and experiment. *IEEE J. Quantum Elect.*, 30(4):1122–1131, 1994.
- [17] A Uskov, J Mørk, and J Mark. Theory of short-pulse gain saturation in semiconductor laser amplifiers. *IEEE Photonic. Tech. L.*, 4(2):443–446, 1992.

- [18] Y-H Kao, T J Xia, M N Islam, and G Raybon. Limitations on ultrafast optical switching in a semiconductor laser amplifier operating at transparency. *J. Appl. Phys.*, 86(9):4740–4747, 1999.
- [19] R P Schrieck, M H Kwakernaak, H Jäckel, and H Melchior. All-optical switching at multi-100-Gb/s data rates with Mach-Zender interferometer switches. *IEEE J. Quantum Elect.*, 38(8):1053–1061, 2002.
- [20] G Toptchiski, S Randel, K Petermann, C Schubert, J Berger, and H G Weber. Characterisation of switching windows of an 160 Gb/s all-optical demultiplexer with data rates of 10 and 40 Gb/s. *IEEE Photonic. Tech. L.*, 14(4):534–536, 2002.
- [21] K L Hall, G Lenz, A M Darwish, and E P Ippen. Subpicosecond gain and index nonlinearities in InGaAsP diode lasers. *Opt. Commun.*, 111:589–612, 1994.
- [22] A Dienes, J P Heritage, M Y Hong, and Y H Chang. Time- and spectral-domain evolution of subpicosecond pulses in semiconductor optical amplifiers. *Opt. Lett.*, 17(22):1602–1604, 1992.
- [23] P J Delfyett, A Dienes, J P Heritage, M Y Hong, and Y H Chang. Femtosecond hybrid mode-locked semiconductor laser and amplifier dynamics. *Appl. Phys. B*, 58:183–195, 1994.
- [24] G P Agrawal and N A Olsson. Self-phase modulation and spectral broadening of optical pulses in semiconductor laser amplifiers. *IEEE J. Quantum Elect.*, 25(11):2297, 1989.
- [25] L F Tiemeijer, P J A Thijs, P J de Waard, J J M Binsma, and T B Dongen. Dependence of polarisation, gain, linewidth enhancement factor, and K factor on the sign of the strain of InGaAsP/InP strained-layer multiquantum well lasers. *Appl. Phys. Lett.*, 58(24):2738–2740, 1991.
- [26] M Eiselt. Optical loop mirror with semiconductor laser amplifier. *Electron. Lett.*, 28(16):1505–1507, 1992.
- [27] K J Blow, R J Manning, and A J Poustie. Nonlinear optical loop mirrors with feedback and a slow nonlinearity. *Opt. Commun.*, 134:43–48, 1997.
- [28] S Bischoff, A Buxens, St Fisher, M Dülk, A T Clausen, H N Poulsen, and J Mørk. Comparison of all-optical co- and counter-propagating high-speed signal processing in SOA-based Mach-Zender interferometers. *Opt. Quant. Electron.*, 33:907–926, 2001.
- [29] L Occhi, Y Ito, H Kawaguchi, L Schares, J Eckner, and G Guekos. Intraband gain dynamics in bulk semiconductor optical amplifiers: measurements and simulations. *IEEE J. Quantum Elect.*, 38(1):54–60, 2002.
- [30] K J Blow, R J Manning, and A J Poustie. Model of longitudinal effects in semiconductor optical amplifiers in a nonlinear loop mirror configuration. *Opt. Commun.*, 148:31–35, 1998.

Chapter 6

Single pulse propagation

6.1 Introduction

This chapter reports investigation of the propagation of single pulses through the SOA. In practice, a train of pulses is coupled into the SOA but the period between pulses is 12.3 ns, which is sufficiently long that the device has fully recovered by the time the next pulse arrives (as confirmed by the recovery times reported in chapter 7).

Firstly, the small signal gain and saturation characteristics of the device are discussed; measurements of the saturation with a CW beam are reported for comparison. Also the difference in short pulse gain saturation for TE and TM polarisations is demonstrated. Secondly, in this chapter, changes to the pulse profile on propagation through the SOA are discussed.

6.2 Single pulse propagation

6.2.1 From the linear regime to gain saturation

If the optical power of an input beam is doubled, the output power after passing through an SOA will also double, if and only if the optical powers are low. When exhibiting this behaviour, the SOA is said to be in the linear gain regime. However, the gain available at any given wavelength and bias level is determined by the size of the carrier population accessible for stimulated emission, and is therefore limited. Increasing the optical input power has the effect of depleting the carrier population inversion in the active region of the device. Whilst the population will recover under conditions of forward bias in an SOA, the recovery is in competition with carrier recombination

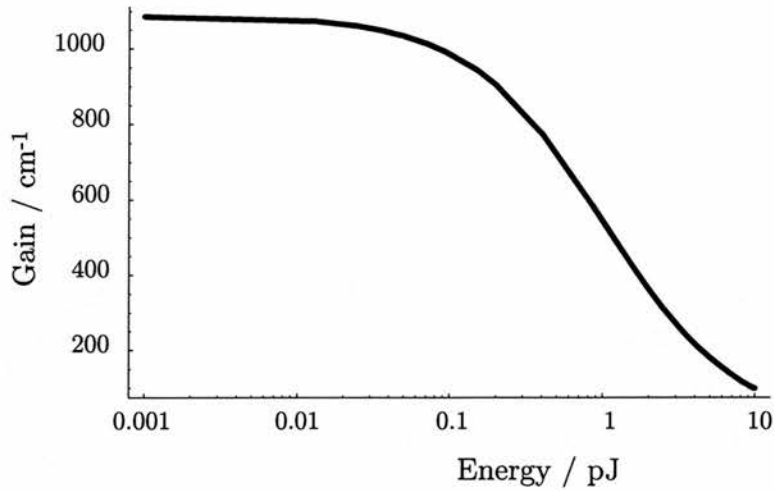


Figure 6.1: Gain as a function of pulse energy illustrating saturation of the gain with respect to its small signal value

and is not instantaneous. Consequently, the available gain is progressively exhausted; under these conditions the gain is said to be saturated.

From a simple rate equation model an expression can be derived for the material gain per unit length in an active material of the form of

$$g = \frac{g_0}{1 + I/I_{sat}} \quad (6.1)$$

where g_0 is the unsaturated gain coefficient, I is the optical intensity and I_{sat} is the saturation intensity (for the derivation see for example [1] [2] [3] [4]). For a four level system, the saturation intensity is given by

$$I_{sat} = \frac{\hbar\omega}{\Sigma\tau_{SE}} \quad (6.2)$$

where τ_{SE} is the carrier recombination time due to spontaneous emission and Σ is the stimulated emission cross-section [4].

For pulses in an SOA, where the pulse repetition period is long with respect to the device recovery time, a saturation energy can be defined as

$$E_{sat} = \frac{\hbar\omega\sigma}{2g_d\Gamma} \quad (6.3)$$

where σ is the cross-sectional area of the device, Γ is the mode confinement factor, and g_d is the semiconductor differential gain [5]. (Note that is equivalent to the saturation

energy used in Chapter 5 to describe gain changes due to changes in carrier density, E_{satN}).

Gain saturation as a function of pulse energy takes a similar form to equation 6.1 describing saturation with intensity. Specifically, defined with respect to E_{sat} , the level of gain as a function of pulse energy, E , can be expressed as

$$g = \frac{g_0}{1 + E/E_{sat}} \quad (6.4)$$

Figure 6.1 illustrates saturation behaviour as expressed in equation 6.4.

Parameters that are more phenomenological than P_{sat} and E_{sat} , and which are readily measurable are the 3 dB saturation power, P_{3dB} and energy, E_{3dB} for CW signals and pulses respectively. The E_{3dB} energy (P_{3dB} power) is defined as the output energy (power) for which the gain is reduced by a factor of 2 (i.e. by 3 dB) with respect to its small signal value. The saturation energy, E_{sat} , can be related to the E_{3dB} by the following expression

$$E_{3dB} = \left[\frac{1.38}{1 + \alpha_l/g_0} \right] E_{sat} \quad (6.5)$$

where α_l is the loss coefficient.

Experiments reported in the literature have demonstrated that these simple expressions are valid for CW optical beams and for long pulses (see for example [6][7] and references therein). Exceptionally, these same saturation characteristics may be found with shorter pulses down to sub-picosecond full-width half-maximum durations, if the pulses have certain temporal characteristics, for example if the pulses have a broad pedestal, such that the power is distributed over a longer duration [2]. However it has been shown that, in general, shorter pulses will cause saturation at lower powers [8] [9] [10] [11]. Calculations to explore these trends are presented with experimental results.

6.2.2 Pulse shaping under different conditions

The output pulse profiles were measured for a range of input pulses. Characteristics that were changed included the pulse energy, the central wavelength (equivalent to peak for clean, single peak pulses) and the temporal duration of the pulse. In all cases, the spectral profile of the input was maintained approximately Gaussian. Unless stated otherwise, in these single pulse train experiments the input polarisation was set at TM

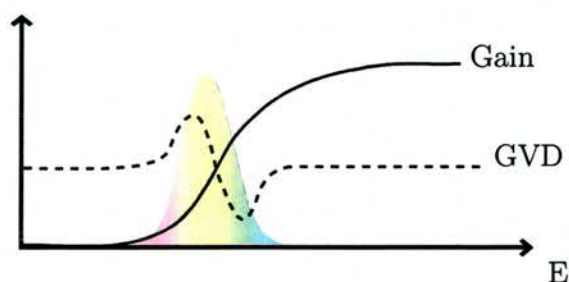


Figure 6.2: Schematic of an extreme case of gain and group velocity dispersion (GVD) changes with respect to the frequency distribution within a short optical pulse.

i.e. the polarisation providing the strongest gain. The gain conditions were adjusted by changing the applied electrical bias current.

With the pulse energy of only a few femtojoules and electrical bias just above its value at transparency nonlinear effects are expected to be minimal. Under such linear propagation conditions, it is assumed that the propagating field does not modify the properties of the material. However the pulses are as short as 350 fs and consequently are spectrally broad. For such pulses the gain and refractive index can potentially be significantly different for different components of the pulse. Essentially, if the region of the pulse that is most amplified also travels at a significantly different speed to other spectral components of the pulse, the peak of the pulse will shift towards this spectral region of high gain. An example of this is shown schematically in figure 6.2: there is more gain available for the higher frequencies of the input pulse than the lower frequencies and also, over the same range of frequencies, the GVD changes rapidly; under these conditions a pulse may be spectrally shifted towards higher frequencies.

With higher input energies, especially amplified under conditions of higher gain, the propagation of a pulse through an optical medium is nonlinear (as described in section 1.3.5). In particular the pulse may be distorted due to self-phase modulation (SPM) and dynamic changes in the refractive index may cause instantaneous frequency shifts.

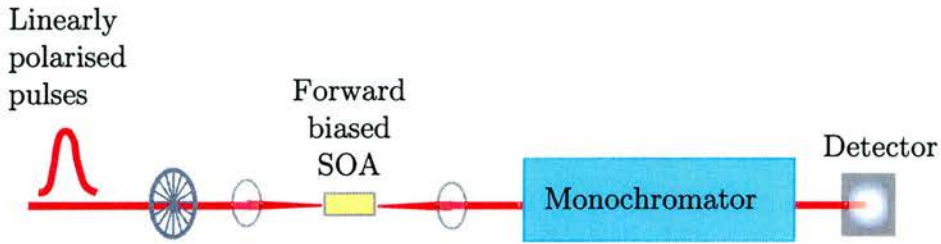


Figure 6.3: Schematic of the experimental set-up used for gain saturation and spectral measurements (the optical chopper was removed for the latter)

6.3 Input/output power experiments

A single train of pulses was coupled into the SOA and the output was collected by a microscope objective and directed into a scanning monochromator (*CVI Digikrom DK240*), as shown schematically in figure 6.3. In the free space path between the SOA and lens focusing into the monochromator, a pin-hole was used to spatially filter the output. This helped to remove the unguided light, for example that which had propagated through the cladding. The output from the monochromator was collected by a broad area Germanium detector.

For integrated power measurements, the monochromator was not scanned, rather it was used as a spectral filter to remove as much of the ASE as possible. This was necessary because under conditions of high electrical bias and with intense input pulses, as well as the input pulse experiencing progressively less gain, the amplification of the spontaneous emission is suppressed [12]. With the ASE removed, saturation of the detector was also avoided. For slit widths which are large with respect to the resolution of the monochromator, the bandpass is approximately given by

$$\Delta\lambda = dD \quad (6.6)$$

where d is the slit width and D is the reciprocal linear dispersion. Consequently with $D = 3.2 \text{ nm/mm}$, the maximum slit width of 3 mm gives a bandpass larger than the spectral width of the pulses ($\leq 7 \text{ nm}$).

In order to check the wavelength filtering, the electrical bias was set to zero, so that there was no ASE, and the input pulse was set to a high intensity with the result that, despite the device absorbing, a detectable signal reached the monochromator. With the coupling optimised, the slit width was decreased and the alignment re-optimised

(in case the slit had closed asymmetrically with respect to the optical beam) until narrowing it further was found to decrease the strength of the signal coupled through. As expected, this was found to correspond to the spectral width of the pulse, as measured by scanning the monochromator with a slit size of $50\ \mu\text{m}$. This configuration achieves a compromise keeping low both the intensity of ASE reaching the detector and the fraction of the output pulse intensity lost.

In addition, the input beam was chopped and the detector signal passed to a lock-in amplifier triggered at the chopping frequency. The input power was measured with both a power meter and the detector used to measure the output. In this way the detector was calibrated and the ratio of input and output signals yielded the gain. Note that stating input and output powers requires estimation of the coupling efficiencies and, in particular, the use of a monochromator as a spectral filter resulted in additional losses en route from the output of the device to the detector. Careful optimisation of the alignment eventually yielded repeatable values for the small signal gain using different optical set-ups and on different days. This gave confidence in the reliability of the measurements, at least to an accuracy of 20%.

The gain was measured using a beam of 700 fs pulses and CW light at different wavelengths and bias levels for a wide range of input energies/powers (peak power over the range ~ -20 to 20 dBm). Note that the gain would be clamped if the device were to lase, however the saturation measurements were taken well away from the bias levels at which lasing modes started to appear (as seen in ASE spectra). Indeed, relatively low bias levels were used in order that the optical input intensities necessary to cause saturation would not be too high. This meant that the level of power necessary to cause over 3 dB of saturation was available from the OPO. Moreover, it avoided concern of damaging the devices by the use of overly high optical intensities.

6.4 Results of gain measurements

6.4.1 Small signal gain

Figure 6.4 illustrates the values of small signal gain measured as function of wavelength for three different bias levels and both polarisations. As expected the small

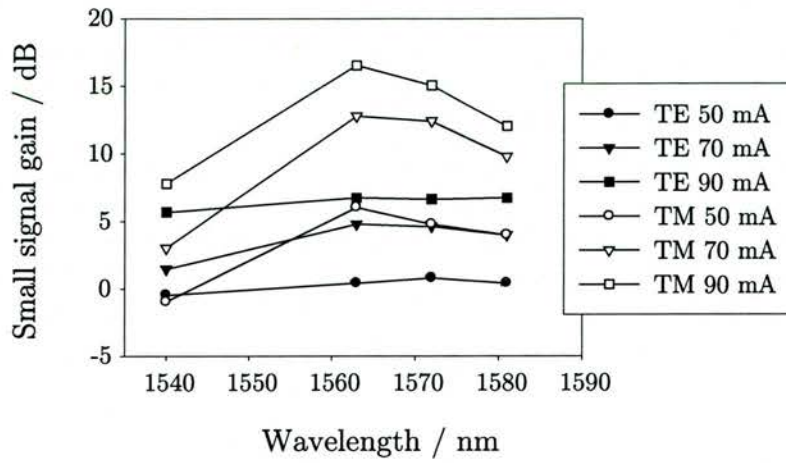


Figure 6.4: Small signal gain at different wavelengths for TE and TM polarisations on propagation through the SOA

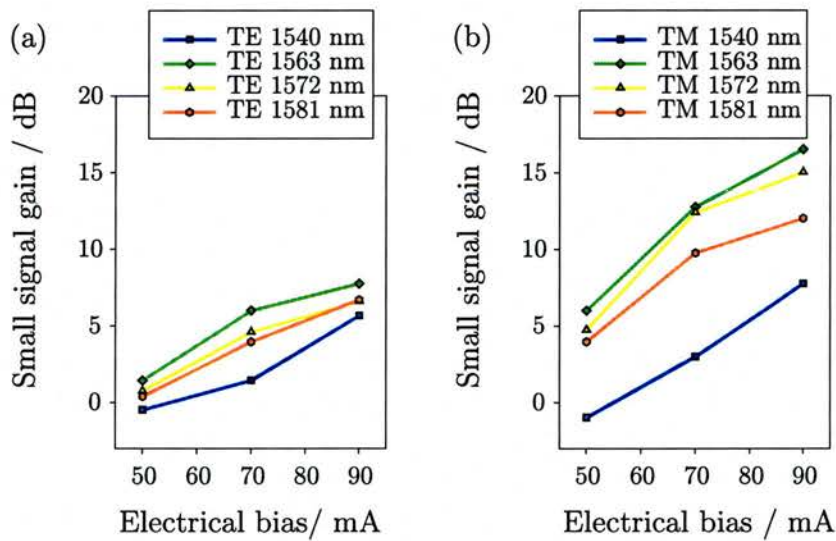


Figure 6.5: Small signal gain as a function of bias at different wavelengths, for (a) TE and (b) TM polarisations

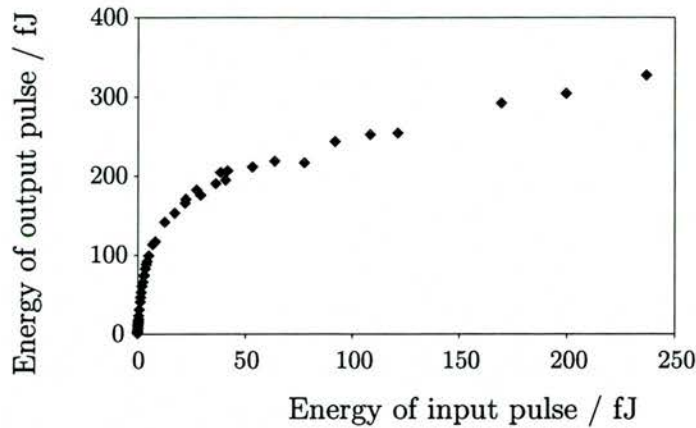


Figure 6.6: Output pulse energy as a function of input pulse energy. The electrical bias to the device was 90 mA, the input pulses were centred at 1563 nm, TM polarised and had a temporal duration of ~ 700 fs.

signal gain increases with electrical bias. The highest gains are found in the spectral region of 1565 nm to 1573 nm, and TM gains are higher than TE gains; both characteristics consistent with the ASE spectra and CW transmission measurements reported in Chapter 4.

The differential gain, dg/dJ corresponds to the slope of the gain with electrical bias, J , and this can be estimated from the data shown in figure 6.5. For the TM polarisation this yields a value of between 4 and 6 $cm^{-1} mA^{-1}$, and for TE from 3 to 5 $cm^{-1} mA^{-1}$. These values are of a similar order of magnitude to data reported in the literature, though considerably lower than in quantum well material optimised for lasers [13][14]. This is reasonable, since, in the case of an SOA device, what is required is not high amplification, but large phase changes. As demonstrated by results in later chapters, sufficient phase changes for interferometric switching can be achieved with this SOA using low input pulse energies. (Data such as that in figure 6.5 was also used to ascertain input parameters for the modelling.)

6.4.2 Pulsed gain saturation

Saturation as a function of pulse energy

For a fixed bias level, as the average input pulse energy was increased, the output pulse energies grew, but by progressively smaller amounts, as illustrated in figure 6.6. The input and output energies are used to calculate the total device gain and this is plotted

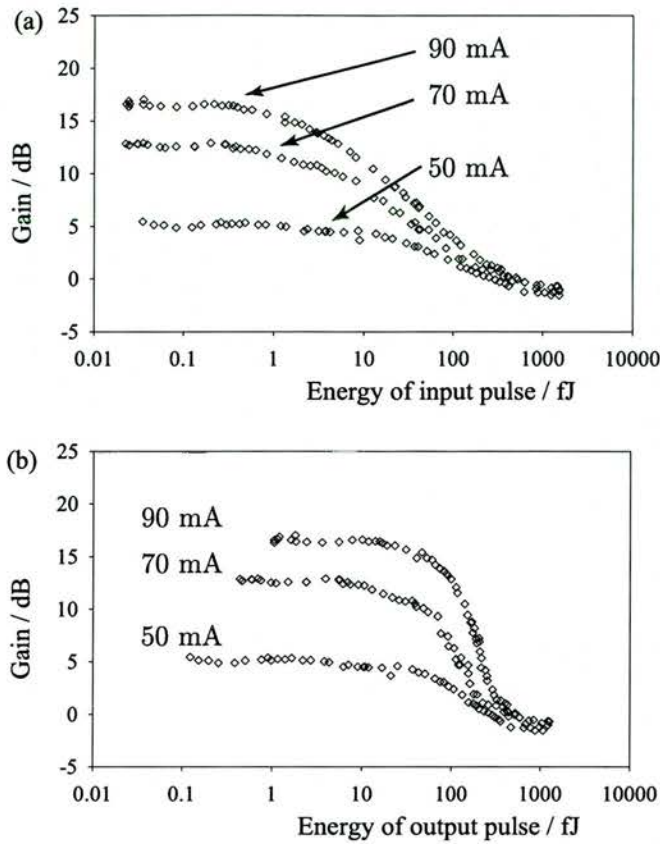


Figure 6.7: Gain as a function for three different bias currents (50 mA, 70 mA and 90 mA) as a function (a) of input and (b) of output pulse energy. Input pulses characteristics as for the data in figure 6.6.

as a function of input or output pulse energy. An example of the former, gain as a function of input pulse energy, is shown in figure 6.7(a) for three levels of bias. The curves have the characteristic shape of saturation behaviour i.e. switching between two linear limits. In the case of gain saturation, the curves are initially flat at some value of gain (>0 dB), for the lowest pulse energies, curving down to lower gains with increasing energy, and subsequently tailing off, tending again towards a flat line at the highest input energies.

Note that the limit towards which the gain saturates in figure 6.7 is slightly lower than 0 dB, i.e. less than an amplification factor of $\times 1$. This implies that despite the electrical forward bias applied, the SOA is absorbing. This is contrary to what would be expected, under the assumption that changes in gain were due to single photon interband transitions alone ($g = g_N$, in terms of the model), when it would be expected

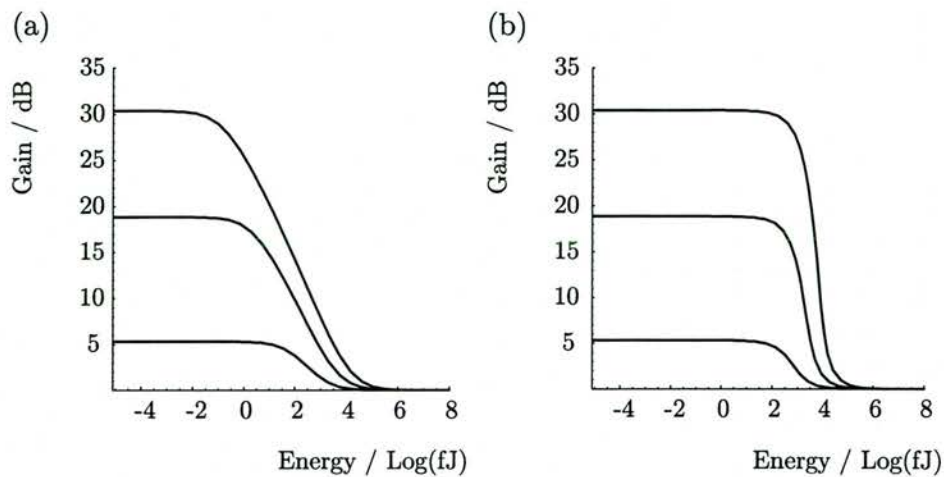


Figure 6.8: Calculated gain as a function for three different bias currents (50 mA, 70 mA and 90 mA) as a function (a) of input and (b) of output pulse energy, using the sliced-propagation model.

that the device would be driven to transparency. However even a small amount of two photon absorption could become significant at a critical input intensity level and take the amplification factor to less than $\times 1$.

The SOA device gain is reduced from its small signal level more easily, that is by lower levels of input pulse energy, when the electrical bias is high. This is demonstrated in figure 6.7(a) in which the gain is reduced from its maximum level (that found with low energy input pulses) sooner i.e. at lower energies, in the 90 mA curve than the 50 mA curve. What is not clear from the data plotted in this way is whether a higher output power is achieved for the high bias case, where the high gain is compressed with a lower input, or for the low bias case, when the maximum level of gain is available for relatively higher energy inputs.

To this end, gain is plotted against output pulse energy. For example, figure 6.7(b) illustrates the same data as in (a) but re-plotted as a function of output pulse energy for a range of electrical bias currents. This has the effect of reducing the horizontal offset between the three curves, with the implication that similarly high levels of output power can be achieved with all three biases. Figure 6.8 illustrates that the sliced-propagation model produces curves of the same form as the experimental results.

Saturation as a function of bias current

In the literature it is reported that for a travelling wave amplifier the saturation output power increases when the available gain is increased by ramping up the electrical bias [5][15][16]. This compares with the behaviour of laser amplifiers in which there is significant feedback (e.g. FPAs): although they tend to provide higher gain at the device resonances, this is at the price of the gain saturating at lower input energies [6]. What is more, increasing the injected current to FPAs has been found to lower the saturation energy still further [17][18].

In the experiments conducted for this thesis, the trend of change of output saturation energy with bias was not clear. As illustrated in figure 6.7 (b), the curves stack approximately one above the other; the saturation is neither offset significantly to higher nor to lower energies. No strong trend was found from analysing data obtained for bias currents of 50 to 90 mA at four different wavelengths across the gain spectrum.

The small ripples in the spectra in Chapter 4 confirm that the SOA is not an FPA; the cavity modes have been successfully suppressed by AR coatings and angled facets. It is concluded that there was not a sufficiently large difference between the minimum bias used (50 mA) and the maximum (90 mA) for the change in saturation energy to be resolved.

The conclusion that the range of biases used was the reason for the lack of trend is backed up by calculations using the sliced-propagation model. Figure 6.9 illustrates the calculated peak power for 3 dB of saturation of the device gain as a function of bias, for pulses of 700 fs and CW light (for which experimental results are presented later in this chapter).

Over the range of 50 to 70 mA the saturation energy is relatively flat as a function of bias. This is explained by the fact that, at these biases, increases in carrier density (via changing the current) increase the small signal gain very nearly linearly. It is also the case that, as the current density is increased, the rate of device recovery increases approximately linearly (as illustrated by pump-probe results presented in Chapter 7). Overall, it is expected that the power/energy to cause saturation of the gain would increase steeply only once the increase in gain with current becomes severely sublinear

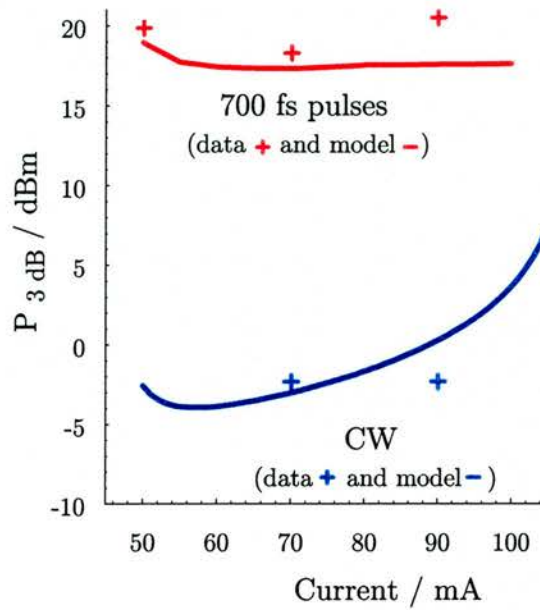


Figure 6.9: The calculated output power where the small signal gain has been compressed by 3 dB as a function bias, for 700 fs pulses using peak power (red curve) and CW light (blue curve). Results from experimental measurements taken near peak gain (~ 1560 nm) with 700 fs pulses and CW light are marked with red and blue crosses, respectively

[5]. For the SOA used in these experiments the current for which this occurs is estimated to be of the order of 150 to 250 mA (the turn over point determined from the fits to define an empirical expression for small signal gain, described in section 5.7.2), a level of bias beyond what was used in the experiments (≤ 90 mA). An applied current of 200 mA corresponds to a high current density of the order of $5 \times 10^3 A cm^{-2}$ (depending on the current injection efficiency) for the 1 mm device used and in the literature significant changes in saturation power/energy are reported for comparable or higher current densities [5][19] [20].

The curves in figure 6.9 were not extended further because the empirical description of the small signal gain is limited to the range of biases that have so far been investigated experimentally. It would be interesting to investigate these trends further using the model over a wider range of carrier densities; in particular this would require a description of device small signal gain and rate of device recovery covering the full range of bias conditions.

Unfortunately to date, it has not been possible to conduct experiments over a wider

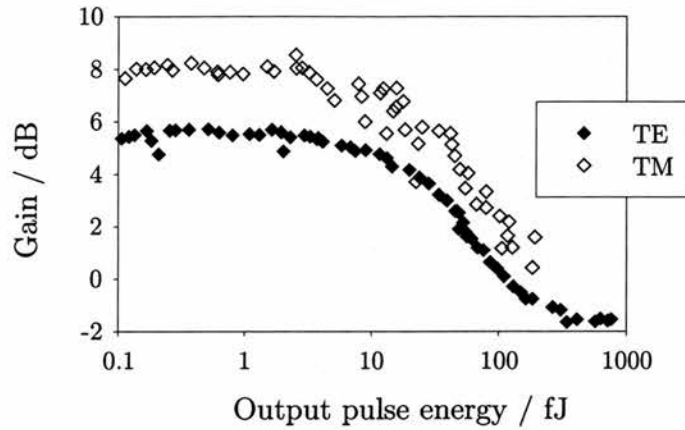


Figure 6.10: Gain as a function of output pulse energy for TE and TM polarisations. The electrical bias to the device was 90 mA, the input pulses were centred at 1572 nm and had a temporal duration of ~ 800 fs.

range: for lower biases the signal levels were so low that the signal to noise became very poor; for higher biases it was concluded that the ASE became too strong (such that ASE became a significant component of the signal measured after the spectral filter and thereby rendered the calculation of the gain by the experimental method being used invalid).

Saturation with different polarisations

Differences in the gain for TE and TM modes were shown in the ASE, transmission spectra and photo-induced voltage results presented in Chapter 4. The consequence of this polarisation dependent gain, for the saturation characteristics of the SOA, is clearly seen in figure 6.10, which shows the gain as a function of input pulse energy for TE and TM modes. The small signal gain of the device was 5.5 dB and 8 dB for the TE and TM modes respectively. For increasing input energy, the TM gain remains greater than the TE, but the curves converge at high levels of saturation.

The difference between the E_{3dB} energies of the TE and TM modes is not significant (given the margin of experimental error). This lack of difference is likely to be for similar reasons to that given for the lack of trend in E_{3dB} with bias.

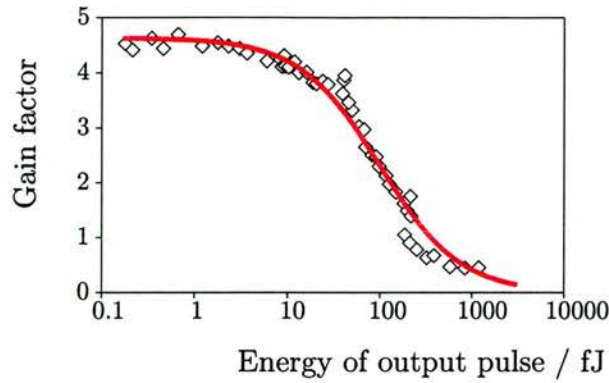


Figure 6.11: An example of fit to gain versus output pulse energy with a curve of the form of equation 6.4. (Note that the gain expressed as the raw multiplication factor, instead of in dB.)

6.4.3 Comparison of saturation due to pulses and CW light

Figure 6.11 shows the experimentally measured gain saturation fit with the form of equation 6.4. This yields saturation energies for TE of just 30 fJ; fits to other curves, TE and TM at different wavelengths, yield values of the same order of magnitude, up to about 150 fJ. This compares with a saturation energy, from equations 6.3 and 6.5, of over 1 pJ. This ‘early’ gain saturation, that is at lower pulse energies than predicted by the simple theory, is attributed to gain compression by ultrafast processes.

For comparison with these results for sub-picosecond pulses, the saturation behaviour of the device was also investigated using CW light. As demonstrated in figure 6.12 (a) the gain saturation with continuous wave (CW) light occurs at much higher powers than the equivalent average power of the pulses used. There are several sources of error in the measurement of the input and output powers (as noted previously), but the difference between the CW and pulsed cases was much larger than the margin of error: the measured gain saturation occurring at average powers of approximately 1 mW and 0.01 mW respectively, two orders of magnitude apart. This is a similar order of magnitude of difference as between the saturation energy predicted by simple theory (equation 6.3) and the saturation energies measured with sub-picosecond pulses.

In figure 6.12 (b), the data is re-plotted in terms of maximum output energy flux. This is equivalent to the the CW power (no change) and the peak power for the pulses (as opposed to the average power). Viewing the data in this way emphasises the com-

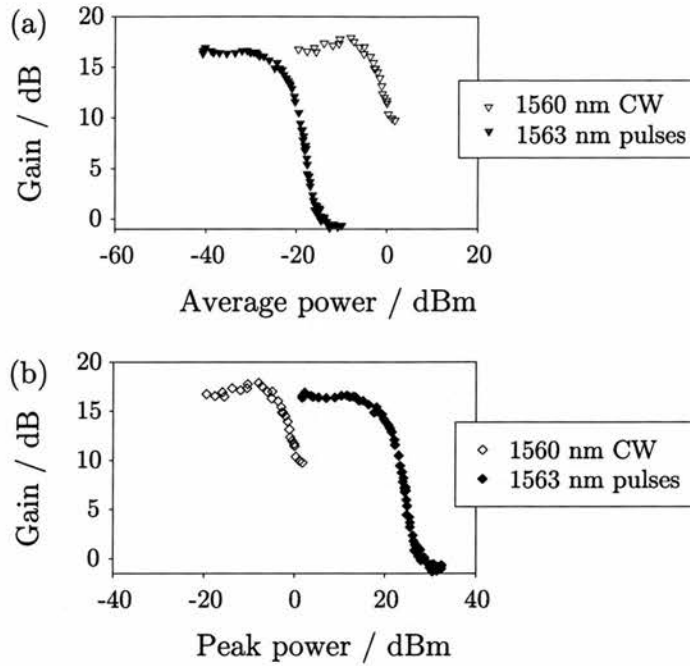


Figure 6.12: Gain saturation of the SOA comparing the effect of CW light and 700 fs pulses. The gain is plotted as a function of (a) average power and (b) peak power for the pulses and CW power in both cases.

paratively low power required to cause saturation with the CW light (~ 1 mW), whilst saturation using the 700 fs pulses required high peak powers (~ 100 mW). This approach enables saturation with CW light and pulses with a range of durations to be compared. Moreover, peak power for the pulses is independent of pulse repetition rate and allows for the possibility of distorted temporal profiles (i.e. peak power is used not just E_p/τ_p).

6.4.4 Calculations of saturation as a function of pulse duration

The experimental results demonstrate the very different saturation characteristic of the SOA with 700 fs pulses and CW light; the sliced-propagation model reproduces this trend. Using the model the gain of the device was calculated for CW input and pulses with a range of different temporal durations. Figure 6.13 illustrates the calculated saturation for CW light and pulses with durations of 200ps, 20 ps, 2 ps and 0.2ps where carrier density and temperature changes are considered ($g = g_N + g_T$). Figure 6.14 compares the P_{3dB} saturation points of the curves in figure 6.13. In general the shorter the pulse, the higher the peak power at 3 dB of saturation; at the other extreme,

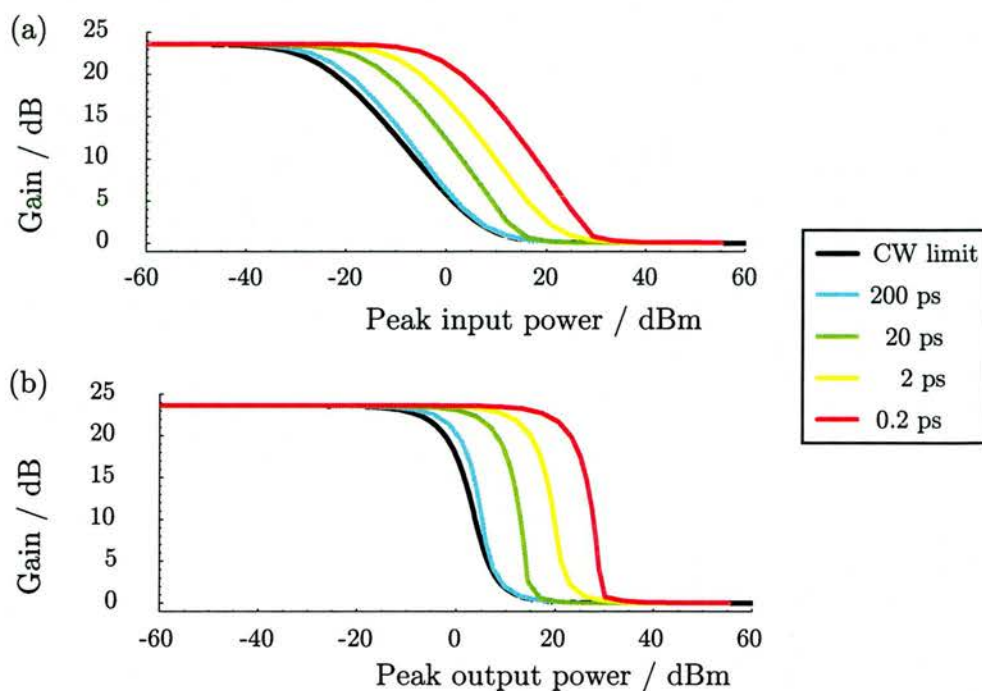


Figure 6.13: Calculated gain saturation of the SOA as a function of peak (a) input and (b) output power for pulses, with durations from 200 ps to 0.2 ps, compared to the power for saturation with CW light.

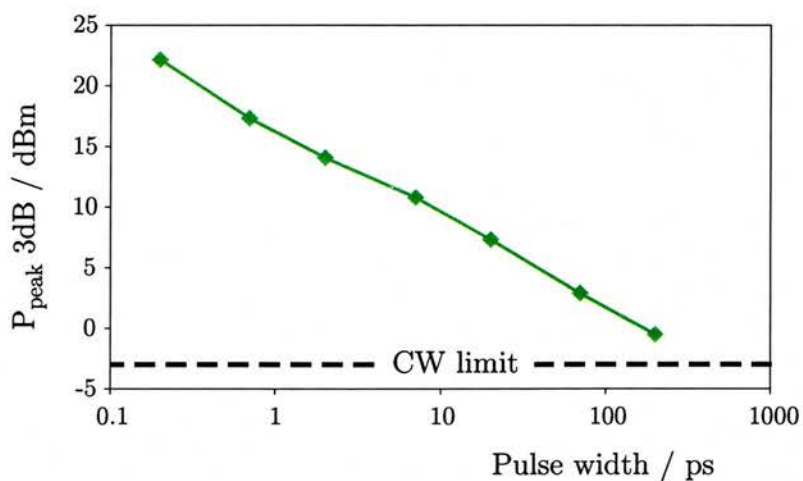


Figure 6.14: Calculated peak output power at which the gain is saturated by 3 dB with respect to its small signal value for different pulse durations, corresponding to the curves in figure 6.13 with additional data points from intermediate pulse durations. The CW 3 dB gain saturation output power is also plotted and is the limit for long pulses.

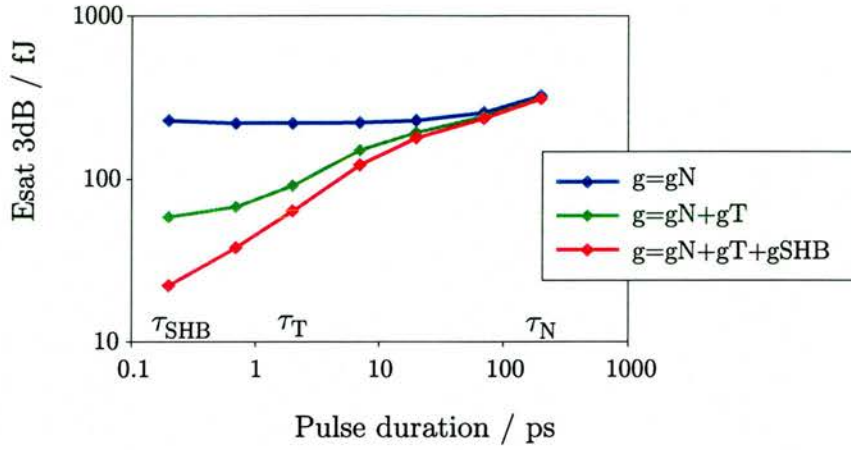


Figure 6.15: Calculated pulse energy for the gain to be saturated by 3 dB with respect to its small signal value different pulse durations.

with long pulses the peak power at 3 dB of saturation tends to the level of CW power at which the device gain is similarly saturated.

In the experiments reported in this thesis the pulse durations were ~ 700 fs. Mechanisms associated with gain dynamics in SOAs include ultrafast carrier heating and spectral hole burning in addition to slowly recovering, carrier density dependent changes. Figure 6.15 illustrates the calculated saturation energy (assuming a Gaussian pulse profile) with the successive addition of gain dynamics with characteristics of these processes. For the longest pulses illustrated, their duration ($\tau_p = 200$ ps) is only slightly less than $\tau_N = 250$ ps and all three curves converge. However for shorter pulses their saturation energies calculated from the different expressions for gain diverge; each additional process shifting the saturation to lower pulse energies. It becomes necessary to include each gain process in the calculation as the pulse duration is reduced towards the characteristic time constant of the process. Note that calculations using the sliced-propagating model for shorter pulses are not valid with this model because the pulse duration approaches the dephasing time (~ 50 fs) and the model is based on equations from which polarisation has been eliminated.

This trend in the point of the 3 dB with shorter pulses has been discussed in the literature [9] [11] [21] [22] [23]. A critical pulse width, τ_{crit} has been defined as the point at which the ‘slow’ carrier density dependent and ultrafast processes, governing

gain dynamics, contribute equally to gain saturation [11] [23]. The value of this critical pulse width can be expressed as

$$\tau_{crit} = 2\eta_2 \frac{\epsilon}{v_g \left. \frac{\partial g}{\partial N} \right|_{N_{tr}}} \quad (6.7)$$

where η_2 is a constant that depends on the pulse temporal shape, v_g is the group velocity in the device, $\left. \frac{\partial g}{\partial N} \right|_{N_{tr}}$ is the carrier density dependent differential gain, and ϵ is a parameter characterising the ultrafast response. For example, the contribution to ϵ from the ultrafast dynamic carrier heating is dependent on the associated characteristic time constant, τ_T , and the carrier temperature dependent differential gain, $\left. \frac{\partial g}{\partial T} \right|_{T_L}$. (For a full derivation of this expression for τ_{crit} refer to [23]). Note that the pulse shape is important because it is the spread of the pulse with respect to time constants associated with different gain dynamics that determines which of the processes makes the dominant contribution to the saturation of the available gain.

The critical pulse duration can be estimated to be approximately 10 ps, for Gaussian pulses around 1.5 μm . This value of 10 ps is consistent with the curves, plotted in figure 6.15, in that at this pulse duration the curves including the ultrafast dynamics of carrier heating and spectral hole burning diverge significantly from the carrier density only solution. The pulses used for most experiments reported in this thesis are ~ 700 fs and approximately Gaussian, so it is reasonable to conclude that the main contribution to the saturation energy is from these ultrafast dynamics, rather than the slowly recovering carrier density gain changes. This role of ultrafast dynamics is the reason that the saturation peak power for the pulses is so different from that required with CW light. Further experiments to measure the saturation in this SOA as a function of pulse duration would be interesting, since they could yield additional information on the relative contributions of different ultrafast processes.

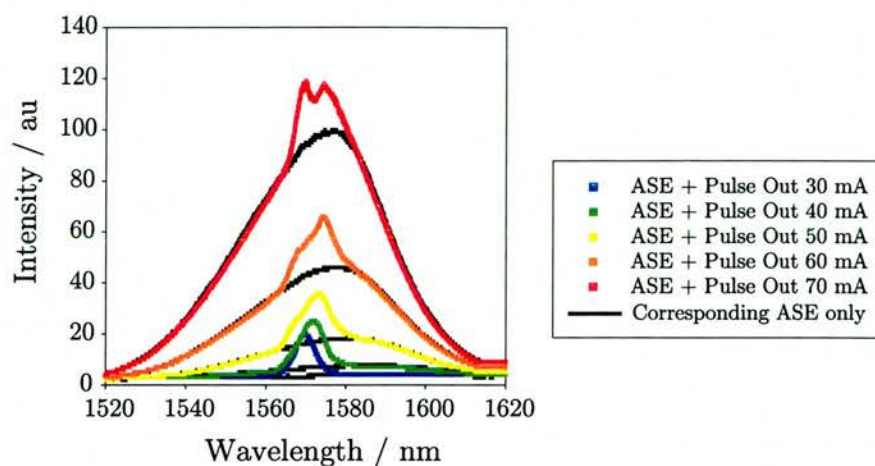


Figure 6.16: Output spectra from the SOA, with and without the presence of input pulses, for a range of electrical bias currents. The smooth curves (black) correspond to ASE only and the distorted curves (coloured) to the ASE plus a pulse.

6.5 Pulse profile experiments

Spectral measurements

In the case of measuring the output spectra the monochromator input and output slits were set much narrower, at $100\ \mu\text{m}$. It was then scanned to measure the output signal as a function of wavelength. A ‘fast scan’ mode of operation was used in order that a full spectrum was acquired and recorded in a few seconds. Also the optics were configured such that a fraction of the input beam was also coupled into the monochromator and a flip mirror was used to swap between the output and input beams. In this way, there was less than 30 seconds of delay between acquisition of input and output beams, and the continual monitoring of the source was used to confirm that the input pulse characteristics had not changed significantly during this time.

The output pulse spectra overlap the ASE occurring at these wavelengths. For example, if the input was modulated by an optical chopper the chopped pulse was observed on a background of ASE. Taking a scan wider than the pulse spectral extent, it was found that the ASE spectra, with and without input pulses, lay very nearly on top on one another, as illustrated in figure 6.16.

The output pulse spectrum was taken to be the spectrum measured with the input

pulse minus the spectrum measured without the input pulse that is

$$I_{pulse} = I_{(pulse+ASE)} - I_{ASE} + C \quad (6.8)$$

where C was a constant offset. This assumption was felt to be justified since even with the highest input energies used in these experiments the ASE change at any given wavelength was a very small fraction of the total signal at that wavelength i.e. C was very small. Note this is different from the issues encountered when attempting to measure gain of a pulse propagating through the SOA (as described earlier in this chapter), in which case the total change in ASE intensity, due to gain saturation induced by the pulse, summed over all wavelengths, may be significant. In addition, the shape of the ASE did not detectably change, so that C was taken to be a constant. This is equivalent to saying that it appears that the gain saturation is approximately homogeneous. This is expected for optical pumping with a CW beam and long pulses [3] [24] but even for the sub-picosecond pulses (350 to 900 fs) used in this experiment, any SHB which may be occurring is not time-resolved by this measurement.

Temporal measurements

Temporal changes in the pulse profile can be quantified using cross-correlation measurements [25]. This measurement is a development of the autocorrelation technique, described in detail in Chapter 3. In a cross-correlation the pulses scanned through each other are different pulses, one the input and the other the output pulse from the SOA, in contrast to the autocorrelation in which two pulses are created by splitting a single pulse. Cross-correlations can be measured even with one of the pulses being weak (in this case the output from the SOA) by increasing the intensity of the reference pulse (in this case the signal from the OPO).

Preliminary measurements indicate that the pulse profile is slightly broadened, but not dramatically distorted in the temporal domain. This is consistent with published results for other SOA structures [25] [26]. The weakness of the effect has been attributed to the combination of a relatively low level of GVD in the SOA material and the fact that the pulses are many hundreds of femtoseconds long. It is reasonable to expect that for higher pulse powers and, more importantly in the context of applications, shorter

pulse durations more significant temporal changes may be found [27][28]. These experiments are ongoing.

6.6 Results of spectral measurements

6.6.1 Under linear conditions

With the pulse energies kept well below the 3 dB saturation point, no significant spectral shifts were detected for using pulses of durations from 350 fs to 800 fs, at wavelengths from 1500 nm to 1580 nm. This is in contrast to the predictions of Zhang et al. who have demonstrated theoretically that under purely linear propagation, the combination of gain and group velocity dispersion (GVD) changing fast across the pulse, can result in large frequency shifts [29]. However the largest shifts were predicted for the input pulse wavelength centred on the rising edge of the gain, near band edge.

The ASE and transmission spectra reported in Chapter 4 demonstrate that the gain of the SOA (studied in this thesis) extends to wavelengths beyond 1580 nm. Unfortunately the pulse sources available do not extend beyond these wavelengths so it has not been possible to investigate pulse profile changes under conditions comparable to those which, according to the calculations of Zhang et al., should result in the strongest effects. It is also the case that their simulations were conducted using 150 fs pulses so the pulses sample a much wider bandwidth than the 350 fs pulses, which are the shortest used in the experiments reported in this chapter.

Consequently, it is not ruled out that significant spectral shifts could be imparted on pulses by the SOA used for the work reported in this thesis, under certain conditions. However, it is concluded that for pulse durations >350 fs centred on wavelengths in the spectral region 1510-1580 nm linear effects do not cause significant spectral changes in this SOA. Specifically, the distortions manifested in the experimental results are not attributed to the interplay between changes in gain and GVD across the pulse.

6.6.2 Under nonlinear conditions

Full spectral plots, especially contour plots, are helpful to visualise the detail of the spectral distortions. The results are presented in this form first. However it is im-

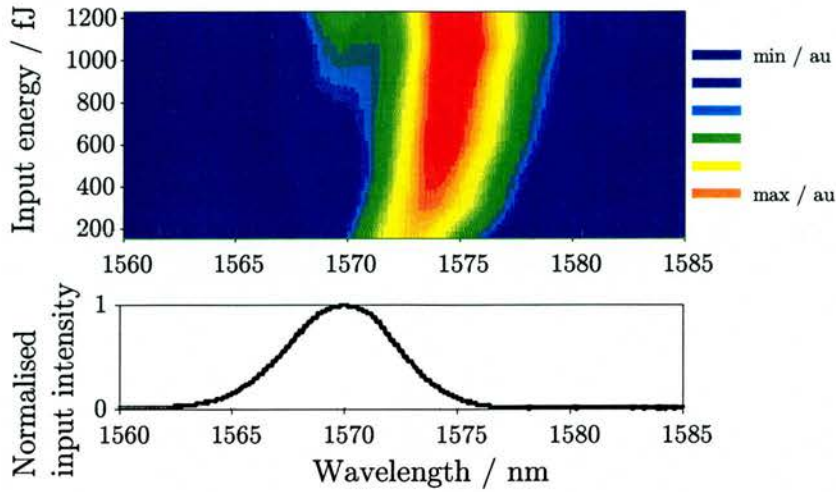


Figure 6.17: Input and output pulse spectra as a function of input energy. The electrical bias was fixed 50 mA and the pulse width was 900 fs.

portant but more difficult to quantify the degree of spectral changes; this is addressed subsequently.

Pulse energy dependence

As the energy of the input pulse was increased, the pulse was found to be first shifted and subsequently strongly distorted. Figure 6.17 illustrates the evolution of the pulse spectrum as a function of input pulse energy where red corresponds to high and blue to low intensities. The input spectral shape, which was smooth and approximately Gaussian, is shown in the lower curve.

Initially the output pulse was red-shifted with respect to the input, that is, the peak moved to longer wavelengths. Subsequently the spectral profile broadened at shorter wavelengths, on the side of the initial input. The red-shift is consistent with the carrier density decreasing as the pulse is amplified, and the pulse broadening is attributed to SPM [30].

Bias dependence

As would be expected, the magnitude of the spectral shift and appearance of distortions is also affected by the level of electrical bias, since this influences the strength of the gain. Figure 6.18, illustrates the spectral shift and pulse distortion for a high input pulse

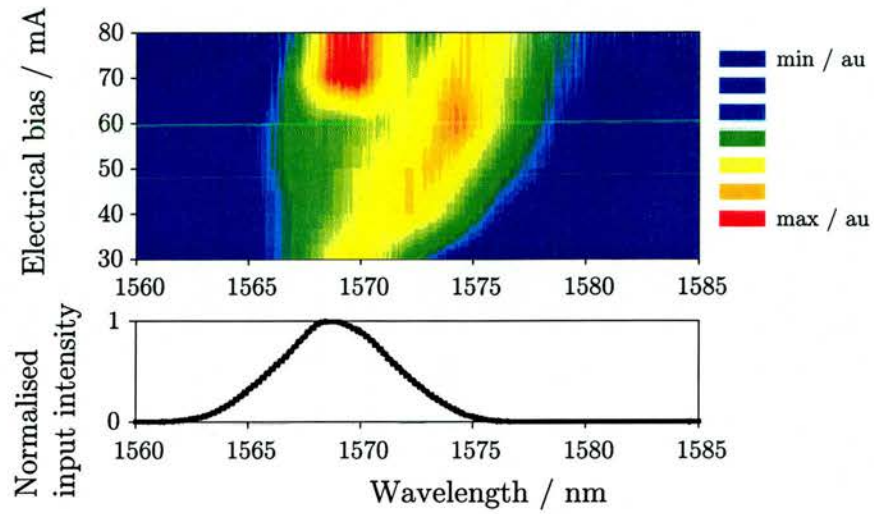


Figure 6.18: Input and output pulse spectra as a function of electrical bias. The input pulse energy was fixed at 1 pJ and pulse width was 700 fs.

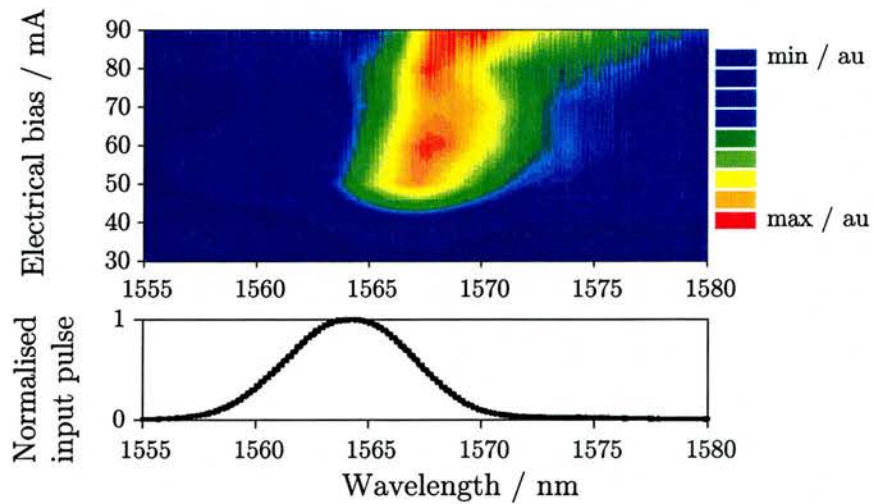


Figure 6.19: Input and output pulse spectra as a function of electrical bias. The input pulse energy was fixed at 100 fJ and pulse width of 700 fs (the same as for the data shown in figure 6.18).

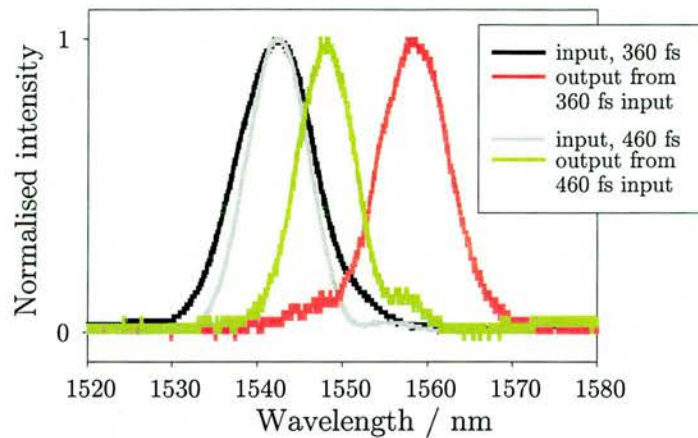


Figure 6.20: Input and output pulse spectra for two different input pulse widths of 360 and 460 fs. The input pulse energy was fixed at 450 fJ and the electrical bias was 50 mA.

energy of 1 pJ as a function of bias. The trend is qualitatively the same as that observed with increasing input pulse energy (figure 6.17): as the bias was increased, the pulse was initially shifted to longer wavelengths and subsequently a shoulder emerged at wavelengths close to the maxima of the input pulse. This shoulder grew into a new peak, and eventually at the highest biases dominated the output; the longer wavelength component having reduced in intensity.

Figure 6.19 demonstrates that for sufficiently high biases significant spectral shifts can be observed even with much lower energy input pulses. The pulse energy was 150 fJ just at the top of the experimentally determined range of 3 dB saturation energies. The central wavelength was slowly shifted as the bias was increased to 70 mA, and by 90 mA the pulse had begun to distort.

Pulse temporal width dependence

Figure 6.20 illustrates the input and output pulse spectra measured for two different input pulse widths, 360 and 460 fs. The gain conditions, as controlled by the applied electrical bias, the peak wavelength and the energy of the input pulses were set to be the same, however the magnitude of the shift is significantly different. The larger shift of the shorter, 360 fs, pulse is attributed to the stronger gain saturation observed with shorter pulses due to ultrafast processes, such as carrier heating.

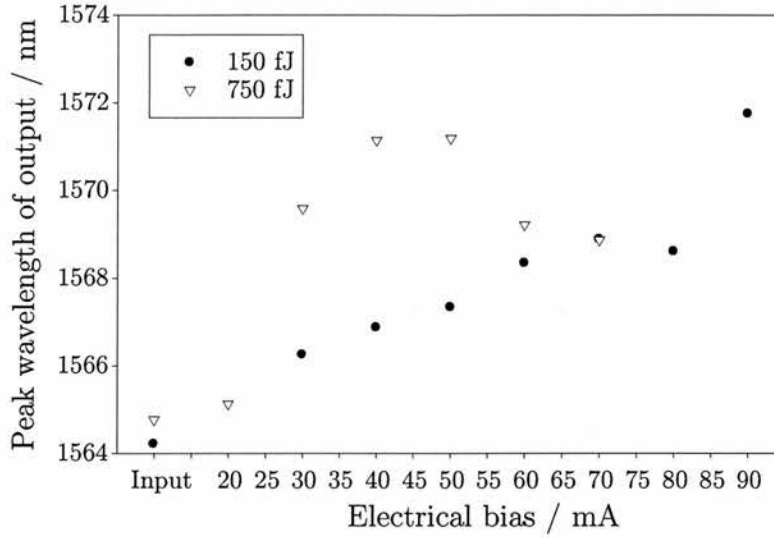


Figure 6.21: The peak wavelength of the output pulse for a range of bias currents for low (150 fJ) and higher (750 fJ) input pulse energies.

6.6.3 Analysis of spectral changes

Magnitude of wavelength shifts and SPM

A straightforward method to quantify the degree of change in the pulse profile is to fit the spectra to ascertain the peak wavelength of the output with respect to the input pulses. Figure 6.21 illustrates the change in peak wavelength with bias for two different input energies. The trend in the maxima of the pulse becomes unclear for high biases, when the pulse profile is severely distorted. Under these conditions, the pulse can not be well described by a single parameter, in particular the peak is not likely to correspond to the central wavelength. However the curve shows clearly that the initial spectral shift saturates and that it does so at a bias of approximately 60 mA.

The maximum frequency deviation expected can be estimated as a function of the maximum possible gain depletion and the pulse duration [31]. The maximum frequency deviation from the input is approximately

$$\Delta\nu = \frac{1}{2\pi} \frac{\Delta g L}{4\tau_p} \quad (6.9)$$

where τ_p is the pulse width and the single pass gain is $\exp(gL)$, which is up to ~ 20 dB in the SOA used for the experiments reported here. Note that the measured gain is the intensity gain, the maximum electric field gain is therefore half this value. Due to

the relative strengths of the real and imaginary part of the Kramers-Kronig relation i.e. $\chi_{r\max} = \chi_{i\max}/2$, the maximum phase change is another factor of 2 less. Hence the factor of 4 in the denominator of equation 6.9.

For pulse widths from 1 ps down to 350 fs expression 6.9 gives frequency deviations from 180 GHz up to over 500 GHz. At a wavelength of 1565 nm these frequency deviations correspond to maximum wavelength shifts of 1.5 nm to 4 nm. This is in reasonable agreement with the magnitude of shifts observed with this SOA under high gain conditions, for example figure 6.18. The expression, equation 6.9, is also consistent with the observed trend of larger shifts for shorter pulses but not with the size of these shifts or the degree of change with pulse duration. As illustrated by the spectra in figure 6.20, for a pulse duration of 460 fs, the shift was ~ 5 nm, and with a pulse of 360 fs this increased to ~ 15 nm.

This is perhaps not surprising since equation 6.9 takes no account of ultrafast dynamics. It is proposed that the expression can be extended in a very simplistic way by considering that the total gain change is not just due to changes in the carrier density, but to changes in the carrier distribution. Along the lines of the approach developed in the sliced-propagation model (described in section 5.6.3), the total gain change can be expressed as

$$\Delta g = \Delta g_N + \Delta g_T + \dots \quad (6.10)$$

Experiments reported in the next chapter indicate that, with the sub-picosecond pulses and other conditions equivalent to those under which the spectral measurements were taken, the magnitude of ultrafast gain changes are at least as large as or larger than those due to the slowly recovering carrier population induced gain changes. Consequently estimates of maximum spectral shifts at least double when they are based on a modified version of equation 6.9 which takes into account that there are at least two significant mechanisms for gain change (equation 6.10).

In conclusion the magnitude of the spectral shifts is too great to be due solely to gain changes from interband carrier transitions. The larger shifts are consistent with the strong ultrafast gain compression that is revealed by the pump-probe experiments reported in Chapter 7.

Self-phase modulation

The spectral shape changes are highly complex and are attributed to the combination of at least three different sources of SPM, due to carrier density changes, ultrafast gain changes of the type caused by carrier heating, and the n_2 nonlinearity [1] [32] [33] [34] [35] [36]. In general, the two peak structure in the pulse spectrum can be understood in terms of the instantaneous frequency becoming the same at two or more points within the pulse temporal profile, and, depending on the relative phase between these components, the optical fields interfere constructively or destructively.

Specifically, the shift towards longer wavelengths is consistent with the so-called slow SPM due to the long lived index change due to interband carrier transitions with the device in gain. Such an asymmetric shift towards longer wavelengths was seen in the pulse distortions calculated by the theory of Agrawal and Olsson [30] which includes only carrier depletion, but not the faster dynamic of carrier heating. The transfer of power back to shorter wavelengths is however more in line with the model of Hong et al. [37][38], which includes the SPM due to carrier heating and the instantaneous n_2 . In order to consistently fit experimental data, for both 2 ps and 460 fs input pulses, it was found by Hong et al. that it was necessary also to include two-photon absorption (TPA) in their model. In the case of the data presented in this chapter, a significant role of TPA in carrier heating is consistent with the large difference between the shifts seen for 350 fs and 450 fs, i.e. the sensitivity of the pulse output to the pulse width. Spectral shifts due to ultrafast gain changes are revisited with the analysis of the time-resolved measurements of the probe spectrum, reported at the end of Chapter 8.

6.7 Summary

In this chapter gain saturation as a function of the strength of the optical input field has been reported. Measurements were conducted using both pulses (~ 700 fs) and continuous wave (CW) light. It was found possible to saturate the gain with average powers two orders of magnitude less using the ultrashort pulses than with a CW optical input. However, given the ultrashort duration and repetition rate of the pulses, this corresponds to peak pulse powers much greater than the CW power (~ 100 mW compared

with ~ 1 mW respectively). The degree of difference has been attributed to the role of ultrafast gain compression mechanisms for pulses with durations below a critical width of ~ 10 ps. This explanation is supported by calculations from the sliced-propagation model, illustrating the pulse width dependence of the saturation energy. Calculations have demonstrated that the peak pulse powers for saturation are marginally higher than the CW power even with long pulses (> 100 ps), but that the difference diverges for progressively shorter pulses, as the pulse width approaches the time constants governing the ultrafast processes. The fact that the saturation energy changes rapidly with pulse duration for subpicosecond pulses highlights how important it is to fully characterise such a device for the pulse durations intended to be used in any application.

High levels of gain (~ 17 dB at a bias of 90 mA) were found at wavelengths which correspond to the peak of the gain. However the output power at which the gain reduced by 3 dB with respect to the small signal gain, was approximately the same for electrical biases from 50 to 90 mA. Equivalently, this corresponds to saying that the total output achieved was not readily be increased by ramping up the electrical bias. The lack of a trend with bias has been attributed to the change of gain with current not being sufficiently sublinear over this range of biases. This conclusion is backed up by calculations using the sliced-propagation model.

Also in this chapter, experiments to determine changes in the profile of pulses on propagation through the SOA have been described. Results so far suggest that in the temporal domain pulses are slightly broadened, consistent with reports in the literature. The small magnitude of the change is attributed to low GVD in the waveguide, but this would merit further investigation. Over the spectral range 1500 to 1580 nm, with pulse durations of 350 to 800 fs, no spectral changes were found in the linear regime (pulse energies low with respect to that required to cause 3 dB of gain saturation). However with higher energy pulses, wavelength shifts and severe spectral distortions, attributed to self-phase modulation, have been observed. In particular, spectral changes became very strong for the shortest pulses and this is again attributed to the influence of ultrafast dynamics. This poses a potentially serious problem with regards to using SOAs with ever shorter pulses in WDM links in optical networks since the magnitude of these unsolicited changes in the central wavelength of the pulse is inversely related

to pulse duration and could be sufficient to cause a signal to swap between adjacent wavelength channels.

Specifically in the context of interferometric switching, the energy of pulses at which large spectral shifts (>6 nm) were observed was of the same order as that which might be used for control pulses (≥ 100 fJ). In some switching configurations, the control pulse is separated from the signal with a spectral filter and care would need to be taken in order that the self-phase modulation of the control did not cause it to leak into the signal channel [39]. In Chapter 8, dynamic spectral changes in much lower energy pulses (~ 1 fJ) are reported and these are also expected to degrade interferometric switching. Note however that by contrast to the experiments presented in this chapter using high energy single pulses and for which changes are attributed to SPM, the results reported in Chapter 8 are from measurements of probe pulses, which alone propagate linearly, and the changes in their spectrum are attributed to cross-phase modulation (due to an intense pump pulse).

Overall, the results presented in this chapter demonstrate that it is not valid to make linear projections even for relatively small changes in pulse characteristics and operating conditions; the effect of the ultrafast processes on the total gain experienced by pulses and on their spectral profile has been shown to be very nonlinear indeed. Importantly the findings reported in this chapter inform the choice of pulse energies and electrical bias currents for the two and three beam pump-probe experiments reported in Chapters 7 and 8.

Bibliography for Chapter 6

- [1] N Finlayson, E M Wright, and G I Stegeman. Nonlinear optical pulse propagation in a semiconductor medium in the transient regime - i: Temporal and spectral effects. *IEEE J. Quantum Elect.*, 26(4):770–777, 1990.
- [2] T Saitoh and T Mukai. Gain saturation characteristics of traveling-wave semiconductor laser amplifiers in short optical pulse amplification. *IEEE J. Quantum Elect.*, 26(12):2086–2094, 1990.
- [3] H Ghafouri-Shiraz, P W Tan, and T Aruga. Picosecond pulse amplification in tapered-waveguide laser-diode amplifiers. *IEEE J. Sel. Top. Quant.*, 3(2):210–217, 1997.
- [4] A E Siegman. *Lasers*. University Science Books, Sausalito, CA, USA, 1986.
- [5] J M Wiesenfeld, G Eisenstein, R S Tucker, G Raybon, and P B Hansen. Distortionless picosecond pulse amplification and gain compression in a traveling-wave InGaAsP optical amplifier. *Appl. Phys. Lett.*, 53(3):1239, 1988.
- [6] T Saitoh and T Mukai. 1.5 μm GaInAsP traveling-wave semiconductor laser amplifier. *IEEE J. Quantum Elect.*, 23(6):1010–1020, 1987.
- [7] K L Hall, E R Thoen, and E P Ippen. *Semiconductors and Semimetals*, volume 59, chapter 2 Nonlinearities in Active Media. Academic Press, 1999.
- [8] K L Hall, Y Lai, E P Ippen, G Eisenstein, and U Koren. Femtosecond gain dynamics and saturation behaviour in InGaAsP multiple quantum well optical amplifiers. *Appl. Phys. Lett.*, 57(27):2888, 1990.
- [9] Y Lai, K L Hall, E P Ippen, and G Eisenstein. Short pulse gain saturation in ingaasp diode laser amplifiers. *IEEE Photonic. Tech. L.*, 2(10):711–713, 1990.
- [10] S Nakamura, Y Ueno, and K Tajima. Femtosecond switching with semiconductor-optical-amplifier based symmetric Mach-Zender-type all-optical switch. *Appl. Phys. Lett.*, 78(25):3929–3931, 2001.
- [11] P Borri, S Scaffetti, J Mork, W Langbein, J M Hvam, A Mecozzi, and F Martelli. Measurement and calculation of the critical pulse width for gain saturation in semiconductor optical amplifiers. *Opt. Commun.*, 164:51–55, 1999.
- [12] L F Tiemeijer, P J A Thijs, T van Dongen, J J M Binsma, and E J Jansen. Polarisation resolved, complete characterisation of 1310 nm fiber pigtailed multiple-quantum-well optical amplifiers. *IEEE J. Lightwave Technol.*, 14(6):1524–1533, 1996.
- [13] P Borri, W Langbein, J M Hvam, F Heinrichsdorff, M H Mao, and D Bimberg. Spectral hole-burning and carrier-heating dynamics in InGaAs quantum-dot amplifiers. *IEEE J. Sel. Top. Quant.*, 6(3):544–551, 2000.
- [14] J Stohs, D J Bossert, D J Gallant, and S R J Brueck. Gain, refractive index change, and linewidth enhancement factor in broad-area GaAs and InGaAs quantum-well lasers. *IEEE J. Quantum Elect.*, 37(11):1449–1459, 2001.

- [15] G Eisenstein, U Koren, G Raybon, J M Wiesenfeld, and M Wegener. Gain and gain saturation spectra in 1.5 μm multiple quantum well optical amplifiers. *Appl. Phys. Lett.*, 57(4):333–335, 1990.
- [16] G P Agrawal and N K Dutta. *Semiconductor lasers*. Van Nostrand Reinhold, New York, 2nd edition, 1993.
- [17] D Marcuse. Computer model of an injection laser amplifier. *IEEE J. Quantum Elect.*, 19(1):63, 1983.
- [18] M J Adams, J V Collins, and I D Henning. Analysis of semiconductor laser amplifiers. *IEE Proceedings*, 132(1):58–63, 1985.
- [19] G Eisenstein, U Koren, G Raybon, T L Koch, J M Wiesenfeld, M Wegener, R S Tucker, and B I Miller. Large- and small-signal gain characteristics of 1.5 μm multiple quantum well optical amplifiers. *Appl. Phys. Lett.*, 56(13):1201–1203, 1990.
- [20] K Dreyer, C H Joyner, J L Pleumeekers, C A Burrus, A Dentai, B I Miller, S Shunk, P Sciortino, S Chandrasekhar, L Buhl, F Storz, and M Farwell. High-gain mode-adapted semiconductor optical amplifier with 12.4 dBm saturation output power and 1550nm. *IEEE/OSA J. Lightwave Technol.*, 20(4):718–721, 2002.
- [21] A Uskov, J Mørk, and J Mark. Theory of short-pulse gain saturation in semiconductor laser amplifiers. *IEEE Photonic. Tech. L.*, 4(2):443–446, 1992.
- [22] K L Hall, G Lenz, A M Darwish, and E P Ippen. Subpicosecond gain and index nonlinearities in InGaAsP diode lasers. *Opt. Commun.*, 111:589–612, 1994.
- [23] A Mecozzi and J Mørk. Saturation effects in nondegenerate four-wave mixing between short pulses in semiconductor laser amplifiers. *IEEE J. Sel. Top. Quant.*, 13(5):1190–1207, 1997.
- [24] T Mukai, K Inoue, and T Satioh. Homogenous gain saturation in 1.5 μm InGaAsP traveling-wave semiconductor laser amplifiers. *Appl. Phys. Lett.*, 51(6):381–383, 1987.
- [25] Y-H Kao, I V Goltser, M Jiang, M N Islam, and G Raybon. Gain dispersion induced subpicosecond pulse breakup in a fibre and semiconductor laser amplifier combined system. *Appl. Phys. Lett.*, 69(27):4221–4223, 1996.
- [26] K L Hall, G Lenz, and E P Ippen. Femtosecond time domain measurement of group velocity dispersion in diode lasers at 1.5 μm . *IEEE J. Lightwave Technol.*, 10(5):616–619, 1992.
- [27] R Schreieck, M Kwakernaak, H Jckel, E Gamper, E Gini, W Vogt, and H Melchior. Ultrafast switching dynamics of Mach-Zender interferometric switches. *IEEE J. Quantum Elect.*, 37(6):603–605, 2001.
- [28] F Romstad, P Borri, W Langbein, J Mørk, and J M Hvam. Measurement of pulse amplitude and phase distortion in a semiconductor optical amplifier: from pulse compression to breakup. *IEEE Photonic. Tech. L.*, 12(12):1674–1676, 2000.
- [29] J-Z Zhang, J M Vazquez, M Mazilu, A Miller, and I Galbraith. Dispersion induced ultrafast pulse re-shaping in 1.55 μm InGaAs/InGaAsP optical amplifiers. *IEEE J. Quantum Elect.*, submitted 2003.

- [30] G P Agrawal and N A Olsson. Self-phase modulation and spectral broadening of optical pulses in semiconductor laser amplifiers. *IEEE J. Quantum Elect.*, 25(11):2297, 1989.
- [31] P J Delfyett, L T Florez, N Stoffel, T Gmitter, N C Andreadakis, Y Silberberg, J P Heritage, and G A Alphonse. High-power ultrafast laser diodes. *IEEE J. Quantum Elect.*, 28(10):2203–2219, 1992.
- [32] G I Stegeman and A Miller. *Photonics in Switching*, volume 1, chapter Physics of all-optical switching devices, page 81. Academic, London, 1993.
- [33] J-C Diels and W Rudolph. *Ultrashort laser pulse phenomena*. Academic Press, London, 1996.
- [34] E Gehrig, D Woll, M A Tremont, A Robertson, and R Wallenstein. Saturation behaviour and self-phase modulation of picosecond pulses in single-stripe and tapered semiconductor laser amplifiers. *J. Opt. Soc. B*, 17(8):1452–1456, 2000.
- [35] R Indik, A Knorr, R Binder, J V Moloney, and S W Koch. Propagation-induced adiabatic following in a semiconductor amplifier. *Opt. Lett.*, 19(13):966–968, 1994.
- [36] R A Indik, R Binder, M Mlejnek, J V Moloney, S Hughes, A Knorr, and S W Kock. Role of plasma cooling, heating and memory effects in subpicosecond pulse propagation in semiconductor amplifiers. *Phys. Rev. A*, 53(5):3614–3620, 1996.
- [37] M Y Hong, Y H Chang, A Dienes, J P Heritage, and P J Delfyett. Subpicosecond pulse amplification in semiconductor laser amplifiers: Theory and experiment. *IEEE J. Quantum Elect.*, 30(4):1122–1131, 1994.
- [38] M Y Hong, Y H Chang, A Dienes, J P Heritage, P J Delfyett, S Dijaili, and F G Patterson. Femtosecond self- and cross-phase modulation in semiconductor laser amplifiers. *IEEE J. Sel. Top. Quant.*, 2(3):523–539, 1996.
- [39] R J Runser, D Zhou, C Coldwell, B C Wang, P Toliver, K L Deng, I Glesk, and P R Prucnal. Interferometric ultrafast SOA-based optical switches: from devices to applications. *Opt. Quant. Electron.*, 33:941–874, 2001.

Chapter 7

Pump-probe transmission experiments

7.1 Introduction

This chapter reports measurements of gain dynamics in an SOA, using two-beam pump-probe experiments. In contrast to measurements reported in the previous chapter, in which the effects of separate nonlinearities are superimposed, these experiments time resolve the response of the SOA, thereby differentiating ultrafast and long-lived components of the dynamics. Characteristics of these dynamics under a wide range of optical power and electrical bias conditions are presented.

7.2 Choice of experimental technique

The investigation of the dynamic response of the SOA to optical fields is key to acquiring sufficient understanding of the behaviour of the device to be able to optimise it for applications. In particular the influence of ultrafast dynamics is critical, from their impact on fundamental device characteristics such as gain saturation, to their potential to improve or disrupt the operation of interferometric SOA-based switches. Pump-probe experiments using ultrashort optical pulses facilitate the measuring of the dynamic response of the SOA in the time domain, with a high resolution limited only by the duration of the pulses themselves.

The principle of the pump-probe technique is to induce nonlinear effects in a material using a high intensity pump pulse, and monitor these effects via changes in the transmission, through the material, of a low intensity probe pulse [1]. By varying the time delay between the pulses in a controlled manner, pump-induced changes in the

material properties can be mapped out over time. As with the autocorrelation technique used for measuring ultrashort pulse durations, pump-probe experiments convert the challenge of measuring times too short (sub-picosecond) to be ascertained using conventional electronics, into the relatively easier task of measuring distances (micrometres), which can be readily accomplished with mechanical tools (calibrated delay stages or differential screws).

In the case of bare semiconductor wafer samples this two beam pump-probe method can be used to measure absorption dynamics; with an SOA device, forward biased into gain, the regimes of gain depletion and recovery can be accessed. Refractive index dynamics are manifested by changes in the phase of the probe beam and can be measured by an interferometric pump-probe experiment, in which the two-beam pump-probe concept is extended by the addition of a third, reference beam. Three-beam pump-probe, phase measurements are the subject of Chapter 8; in the current chapter the term pump-probe is used to refer to experiments using two pulse trains to measure amplitude changes in transmission.

There are a variety of other types of experiments which yield information about the optical response of a material in the time domain. For example, photoluminescence (PL) measurements in which a sample is irradiated by an optical field, stimulating absorption, and the subsequent emission of radiation is measured over time [2]. PL spectra are often used as an initial characterisation technique for material samples [3]. The measurement provides information about optical transition energies and rates, but PL experiments are not used for the investigation of gain dynamics, there being a continual amplified spontaneous emission signal in the gain regime.

Another popular method for investigating dynamics in semiconductors is measuring four-wave mixing (FWM), in which a nonlinear $\chi^{(3)}$ interaction between pump and probe beams produces a transient signal, and this technique can be used in the gain regime [4][5]. However the pump-probe concept provides a direct way of accessing the temporal response of a sample, with the amplitude gain and refractive index dynamics being readily separable. By contrast, in FWM experiments they are intertwined in a complex way [6].

7.3 Two beam pump-probe experiments

7.3.1 The principle

In general, what is required for a pump-probe experiment is a high intensity pump and low intensity probe. In the experiments reported in this thesis, the pump and probe were degenerate pulses. These were derived from the single high intensity optical beam, from the OPO source described in Chapter 3. This beam was split into two, unequally, to give a strong pump and weaker probe. The pump and probe travel on different optical paths before reaching the sample, and one of the paths necessarily includes a variable delay. On transmission through the semiconductor the pump interacts with the material altering the gain and refractive index, and the transmission of the probe is affected accordingly.

As with the single pulse experiments reported in the Chapter 6, the period between successive input pulses was more than long enough for the SOA to fully recover between pump pulses. With this condition met it follows that, if the probe precedes the pump in time, its transmission is unchanged compared to the case of the pump signal being blocked altogether. On the other hand, when the probe follows the pump in time, the probe transmission is changed to a degree that depends on the strength of the initial interaction, between the pump and the semiconductor material, and on how much time has elapsed since the passing of the latest pump pulse, to allow the material to recover to its equilibrium state.

It is necessary to distinguish the pump and probe signals after their propagation through the sample, or at least to remove the pump. With measurements on thin samples, in which pump and probe are focused to overlap in the material but can be incident on the sample at different angles, the signals can be separated spatially [7]. However this is not possible with waveguide devices, such as SOAs, since pump and probe must propagate collinearly through the material. In the case of non-degenerate pump-probe experiments, when pump and probe are different optical frequencies, the pump can be blocked by filters. Also there is an alternative, more complex, method in which pump and probe beams are nominally at the same wavelength, but can be distinguished by heterodyne detection, pump and probe signals having been fractionally frequency

shifted (by approximately 1 MHz) with respect to one another using an acousto-optic modulator [8] [9]. However in the experiments reported in this chapter, pump and probe beams were of orthogonal linear polarisations and therefore could be separated in a straightforward manner using polarising beamsplitter cubes.

7.3.2 Operating conditions

The SOA device under investigation is primarily intended for use under conditions of gain. In the context of applications, the amplification the device can provide is desirable in that it compensates for signal loss, due for example to imperfect coupling. In addition, the cumulative amplification with propagation along the waveguide means that significant total changes in gain can be effected by moderately low energy input pulses. Moreover, as demonstrated by the results that follow, in the gain regime the behaviour of the device can be controlled by tuning the level of electrical bias. Consequently, the pump-probe experiments presented in this chapter focus on investigating dynamics under gain conditions.

The concept of the pump-probe experiment relies on the probe monitoring the dynamics initiated by the pump, whilst not itself causing significant modulation of the carrier distribution. Consequently, it was ensured that the probe pulse energy was very much lower than the pump and, moreover, that the probe was low enough that on its own it propagated linearly. The maximum level of probe pulse energy for this linear regime depended on the wavelength and bias conditions, and was ascertained with respect to the saturation measurements reported in Chapter 6. At minimum, the pump energy was ten times that of the probe; in many cases the ratio was one or two orders of magnitude higher than this.

7.3.3 Experimental configurations

Conventional collinear cross-polarised pump-probe

The experimental set-up used for the initial co-propagating pump-probe measurements is shown schematically in figure 7.1. A half-wave plate was used to rotate the linear polarisation of one of the beams, the pump (as in the figure) or equivalently the probe. The beams were then brought together collinearly with a polarising beamsplitter cube.

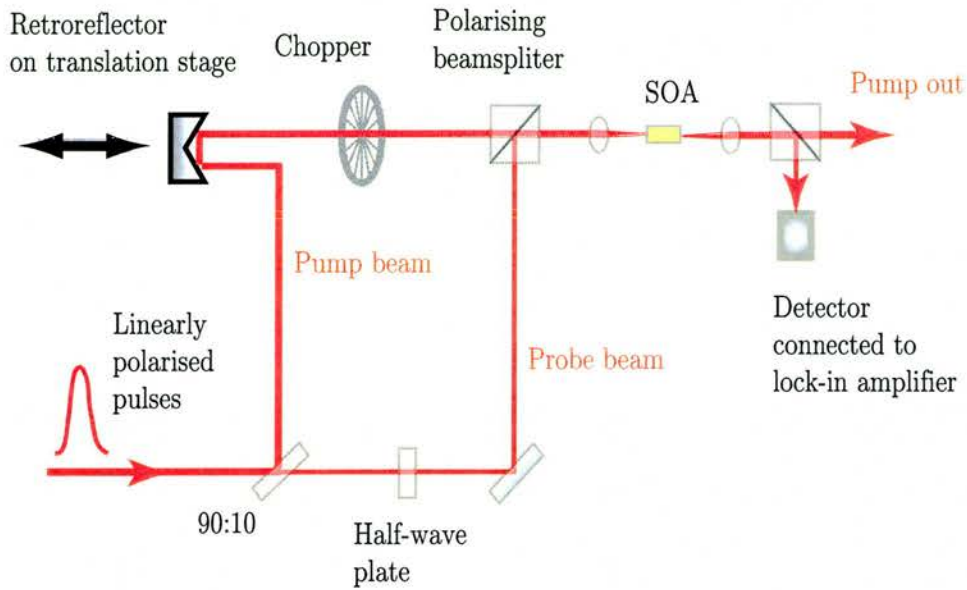


Figure 7.1: Schematic of the experimental configuration used for the co-propagating pump-probe measurements

Micro lenses were used to couple the beams into the SOA and collect the light out (as described in section 4.3). After the SOA, the signal from the pump beam was removed, again using a polarising beamsplitter cube, before the probe light reached the detector. The pump was chopped and the signal from the detector passed to a lock-in amplifier. This signal corresponded to relative changes in probe transmission due to the presence of the pump: a much more sensitive technique than measuring absolute changes in the probe transmission.

In the first experiments, the pump polarisation was chosen to be in the polarisation direction which had been measured to have higher gain i.e. the TM mode. This was due to the fact that, since the pump is amplified as it propagates and hence cumulatively depletes more gain along the length of the device, it was expected that the higher gain mode would result in a much larger gain depletion and lead to change in transmission that would be more readily detectable. Subsequently, once the set-up was optimised, the polarisations were swapped and the changes in transmission due to pump propagating in the TE mode were investigated. The input polarisations could be readily adjusted with respect to the waveguide axes using half-wave plates inserted between the polarisation cubes and the micro lenses.

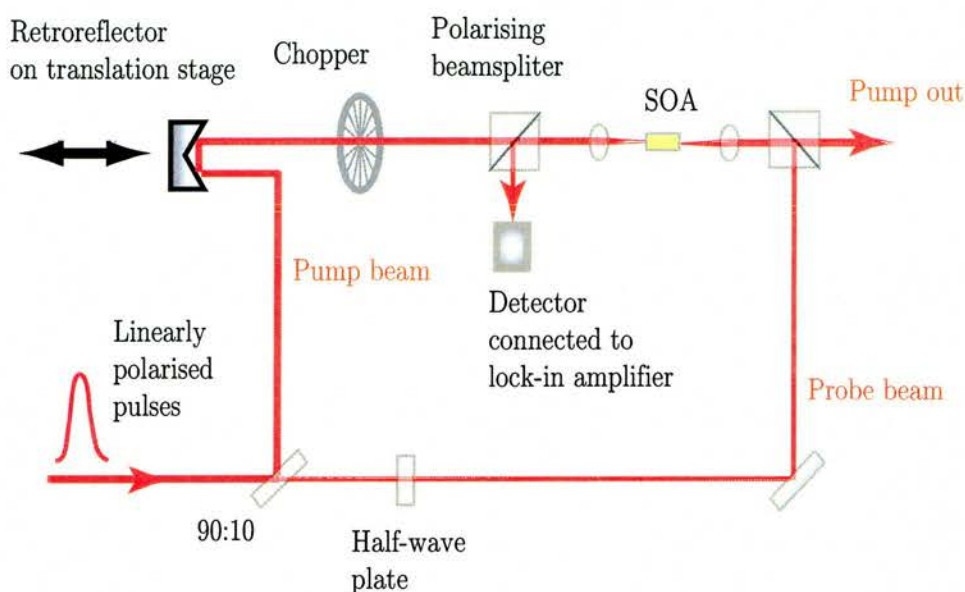


Figure 7.2: Schematic of the experimental configuration used for the counter-propagating pump-probe measurements

Counter-propagating collinear pump-probe

As a step towards the configuration used for the three-beam experiments reported in Chapter 8, a pump-probe experiment was set up with the pump and probe counter-propagating through the device, as illustrated in figure 7.2. This measures a slightly different transmission change since the concept of zero delay, a single point at which the pump and probe arrive simultaneously at device, no longer exists. With the pump and probe counter-propagating they can be made to overlap at different points along the length of the device, by adjusting the difference between their optical path lengths.

7.3.4 Data acquisition and processing

The platform on the delay stage could be moved by $1 \mu\text{m}$ steps. Each such step corresponds to a change in optical path of 7 fs, for a pulse that is reflected off a mirror mounted on the platform (and hence sees the distance change twice). By comparison, the temporal duration of the pulses was in the range 300 fs to 1.2 ps. Consequently, the limiting factor on the time resolution of the measurement was the pulse duration.

The experimental traces map out the changes in probe transmission as a function

of delay with respect to the pump pulse. These are fitted to extract the magnitudes of the transmission changes and time constants which characterise the dynamic recovery of the transmission towards its initial value (explanation of the type of fits used can be found in the Appendix).

The signal from the lock-in amplifier was recorded using a program written in *Agilent VEE*, which also controlled the movement of the delay stage and thereby the path length for the pump beam. At each step along the delay the corresponding time at which the data (the pump delay distance and corresponding lock-in signal) were acquired was also recorded in the data file. This was critical to enable changes in the probe signal to be compared with the input from the OPO, as recorded by the monitoring system. For details of this system refer to section 3.5.3, but it is worth emphasising here that the statistics describing changes in the OPO pulse characteristics proved extremely effective in identifying anomalous results, and were a means of doing so in an objective way. Rejection of data on the grounds of poor input pulse stability during an experiment had the effect of reducing the noise on an accumulated set of data considerably, and this was especially true in the case of the pump-probe scans measuring gain recovery over some hundreds of picoseconds.

Although the polarising beamsplitter rejected most of the pump intensity, some leaked through onto the detector. This is possible since although the pump and probe are nominally of orthogonal polarisations, under real experimental conditions the linear polarisations tend to contain small components of the opposite polarisation and moreover the SOA has been shown to rotate the polarisation of an optical field [10]. The presence of the leaking pump was apparent by the existence of a non-zero signal before zero delay. At this time, with the probe effectively arriving before the pump, the differential probe signal would be expected to be zero. This assertion follows from the initial condition that the pulse repetition rate is sufficiently slow to allow full recovery between successive pump pulses. The verity of this is confirmed by the rate of recovery revealed by these pump probe experiments: gain recovery occurs over a period of less than 1 ns and the period between pulses is 12.3 ns. Consequently, the data can be offset by the signal value at delays before zero delay. (To be sure of avoiding pump-induced changes in the signal, the offset needed to be determined at a time several multiples of

the pulse width before zero delay. In practice the signal used was a safe margin beyond this: an average of the signal over a period of ~ 10 ps, from delays ≥ 10 ps before the step change in the transmission signal.)

Around zero delay, the signal tended to be noisy. With higher powers it was sometimes possible to observe an interference between leaking pump and probe. The oscillating signal around zero delay can be removed from data during experiments by using a vibrating mirror such that the signal is smoothed. In the experiments reported in this thesis, an alternative approach was developed which is equivalent but reduces the possibility of losing information. After an initial rapid scan to locate zero delay, a slower scan was made for the data acquisition using a variable step size: between 1 and 5 μm around zero delay, and a longer step, 40 to 100 μm , during the period of gain recovery, where the changes in signal were smooth. Subsequently, a running average could be taken of the data around zero, which had the effect of smoothing out the oscillations. Note however that for some of the initial experiments the step sizes used were not sufficiently small to effect this averaging, hence spikes can be seen near zero delay in some data (e.g. figure 7.5), whilst they are absent from later results (e.g. figure 7.17 (b)).

On some occasions, when the alignment of the optics was not optimised, an oscillation was observed at some distance away from zero delay. This was attributed to interference from pump and probe pulses multiply reflected within the optical set-up. The envelope of these oscillations was effectively a cross-correlation measurement. The pulse widths suggested by these traces were, within reasonable experimental error, the same as the autocorrelation measurements of the source which implied that the pulses were not significantly temporally broadened on propagation through the set-up, including the 1 m length of optical fibre.

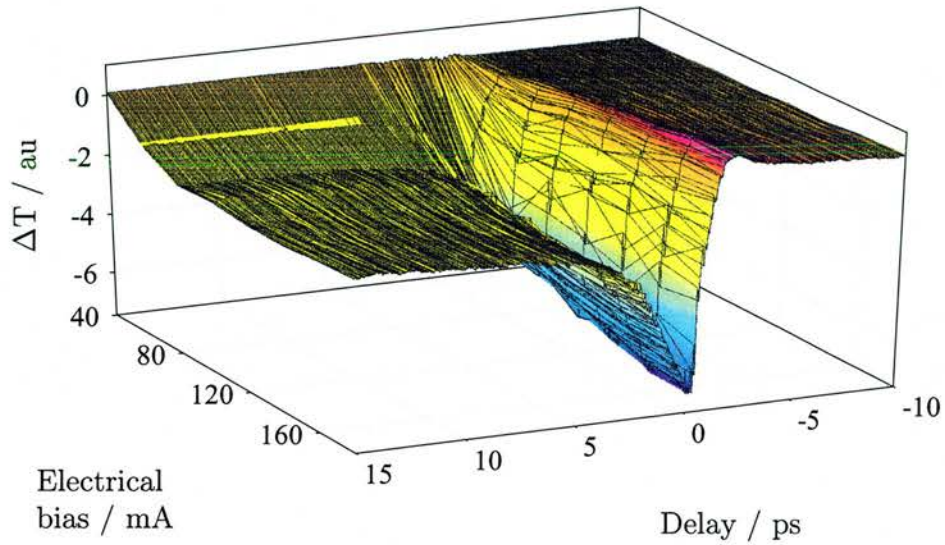


Figure 7.3: Change in transmission of the TE probe, ΔT , as a function of delay time with respect to the TM pump for a range of applied electrical biases

7.4 Transmission change results and analysis

7.4.1 Co-propagation results

Qualitative description of dynamics

Figure 7.3 shows the dynamic change of a TE probe transmission due to a TM pump over a range of electrical biases, with pulses of ~ 800 fs. As expected, there is sudden change in probe transmission due to the arrival of the pump (at $t = 0$ ps). This ‘step’ change in fact takes approximately the pulse duration to occur; the pump and probe overlap, at the so-called zero delay point, in the middle of this change. The subsequent changes in transmission observed are more complex than can be explained by just interband carrier dynamics.

The transmitted probe intensity recovers to its original equilibrium value in two stages: a fast recovery taking of the order of picoseconds or less, and a slower recovery taking several hundred picoseconds. The slow gain recovery is attributed to carrier injection that is balanced by carrier recombination. The fast dynamic does last longer than the optical pulse width, so can not be wholly explained by an instantaneous effect that follows the pulse profile, such as two-photon absorption. It is attributed to recovery

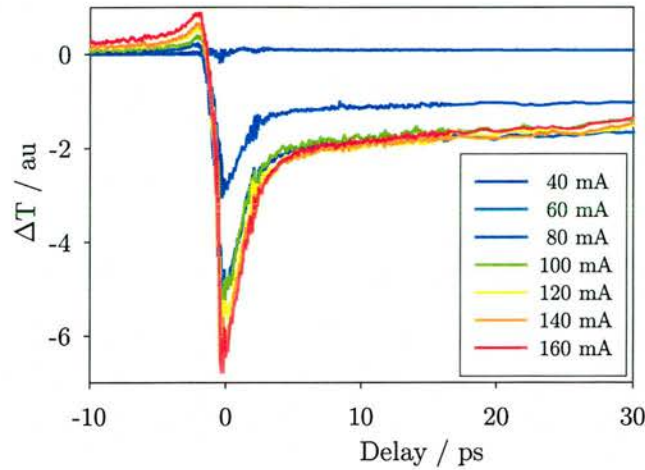


Figure 7.4: The measured changes in probe transmission as a function of delay with respect to the pump for a wide range of electrical bias currents. The central wavelength of the pulses was 1550 nm and their temporal duration ~ 700 fs.

from carrier heating which, as discussed in Chapter 2, can be caused by a variety of mechanisms including stimulated emission, free-carrier and two-photon absorption.

Another dynamical process that is expected to take place on ultrafast timescales is spectral hole burning (SHB). However, as noted previously, SHB is reported to be characterised by a time constant of the order of 100 to 250 fs. This is significantly shorter than the ultrafast gain change observed in these experiments; the pulse durations used (~ 700 fs) were too long to resolve such a fast dynamic [11] [12]. The same resolution restriction applies to the so-called spectral artifact, due to the ultrafast dynamic coupling of the gain and refractive index and, moreover, it is expected that the spectral artifact in these experiments would be small since the gain does not change very steeply across the spectral width of the pulse profile [13][14][15].

Dynamics as a function of applied electrical bias

For a fixed pump pulse input energy, the change in probe transmission increases with bias, as illustrated by the data in figure 7.4. The step change at zero delay grows with bias and the remaining change, after the ultrafast dynamic, is also larger.

These trends with bias can be explained via the action of a stronger pump pulse: the increase in magnitude of the long-lived gain change being due to the pump having been more amplified under conditions of increased bias. The pump is therefore able to

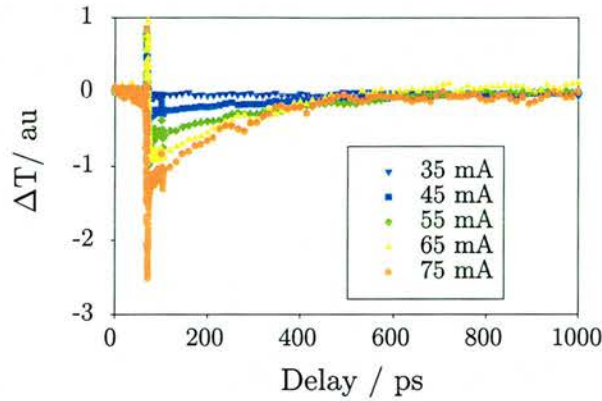


Figure 7.5: The measured changes in probe transmission as a function of delay with respect to the pump for a range of electrical bias currents. The central wavelength of the pulses was 1560 nm and their temporal duration ~ 700 fs.

extract more gain, from interband carrier transitions, and the probe is less amplified. Stronger stimulated emission results directly in a larger change in the average temperature of the carriers. It follows that with an increase in the magnitude of the long-lived gain change there is a concomitant increase in the magnitude of the short-lived change due to carrier heating. On top of this, the increased intensity of the optical field will tend to increase the two photon absorption and its contribution to the heating of the carrier distribution.

The large magnitude of the short-lived gain change is consistent with published measurements of carrier heating and suggestions that that it may be especially strong in strained devices [16][17][18]. Both short and long-lived contributions to the magnitude of the transmission change appear to increase less fast for the highest biases: this signature of saturation is discussed further in section 7.4.1.

Another change in the pump-probe traces with increasing bias is that the slow gain recovery occurs much faster with higher biases. This can be seen in figure 7.5, which shows the evolution of the transmission changes over a much longer time than figure 7.5. The pump-probe traces converge at longer delays, despite the fact that the initial step change in transmission is larger for the higher biases. The ‘slow’ recovery time (as opposed that of the ultrafast dynamic) is plotted against applied electrical bias in figure 7.6. The more rapid recovery of the probe transmission with higher biases is intuitively understandable in that this slow recovery of the gain is due to the increase

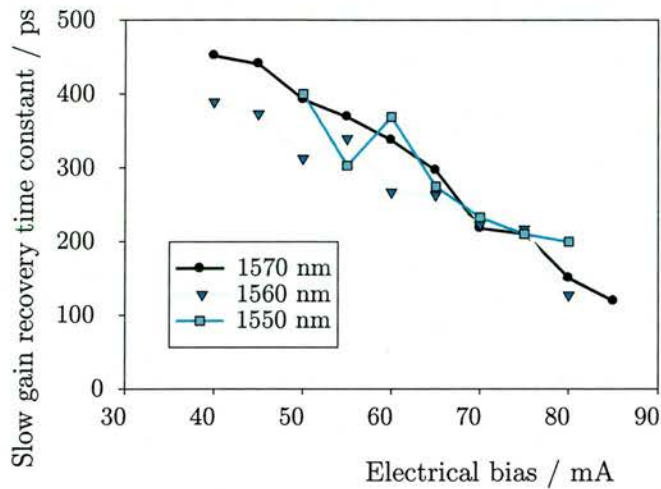


Figure 7.6: The fitted slow gain recovery times as a function of electrical bias current for several input wavelengths.

of the carrier density towards its equilibrium value which is directly related to the rate of electrical carrier injection.

For conditions under which Auger recombination dominates the slow gain recovery in the SOA, it is expected that the slow time constant, τ_N is proportional to $J^{-2/3}$. For derivation of this relation refer to the Appendix. This proportionality suggests a log plot of the time constant as a function of current, J , should have a slope of $-2/3$ if the key process governing gain recovery is Auger. Plotting the experimental results in this way, for example as shown in figure 7.7, was found to yield gradients steeper than $-2/3$ (-1.32 and -1.72 respectively from graphs (a) and (c)). This corresponds to saying that the measured time constant falls faster with applied bias than predicted for the case of Auger dominated recombination. Note also that a straight line did not give a good fit to the experimental data, in particular in figure 7.7 (c), even by eye the trend of the data points is not convincingly linear.

Recombination in SOAs that is faster than that predicted by an Auger dominated regime has been attributed to rapid carrier diffusion from reservoirs of carriers adjacent to the active region [19]. However that rapid recovery was due to device design and was bias independent. In the case of the SOAs investigated in this thesis, it is believed that the faster recovery occurs due to fact that it is a long waveguide in which gain is therefore significantly affected by the level of ASE [20][21]. In effect the ASE provides

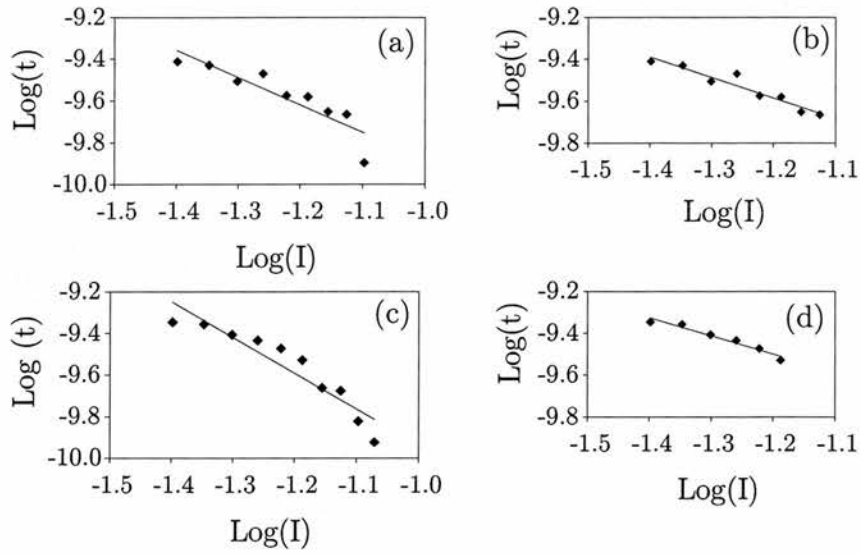


Figure 7.7: The log of slow gain recovery times as a function of the log of the electrical bias current. For Auger dominated recombination, the relationship would be inversely proportional with a slope of $-2/3$. Graphs (a) and (c) include the data from the full range of bias currents, and yield slopes of -1.32 and -1.72 respectively. Graphs (b) and (d) are a subset of the same data but with one and four data points respectively removed from the higher range of electrical biases. Fits to these subsets of the data yield slopes of -0.97 and -0.86 respectively. The data in (a) and (b) is for measurements taken at 1560 and that in (c) and (d) from 1570 nm.

a gain loss mechanism, which speeds up device recovery in a similar fashion to the demonstrated effects of holding or assist beams [22][23][24]. It can be thought of in the following manner: in the hypothetical case that there were no ASE the carrier density to which the device would recover would be greater; in other words the recovery in the presence of ASE reaches its limit sooner than it would otherwise and hence the rate of recovery appears faster.

This reasoning is backed up by the fact that taking only a subset of the data, that from lower biases where the ASE intensity is less strong, the experimentally determined relationship between slow gain recovery and bias is closer to that predicted for Auger, as illustrated in figure 7.7 (b) and (d). Also, the subset of data gives a better linear fit (than when using all the data points, as in 7.7 (a) and (c)). It is concluded that at moderate biases, up to about 60 mA, the device behaviour is consistent with the Auger mechanism. However at higher biases the relationship between current and device recovery is different: the gain recovers more rapidly and this is attributed to the

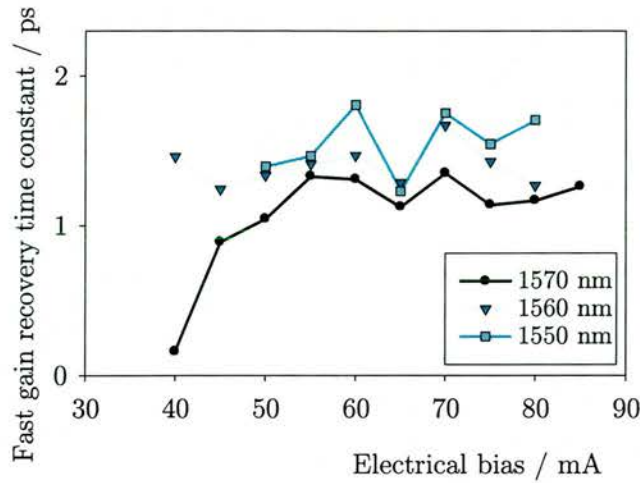


Figure 7.8: The fitted fast gain recovery times as a function of electrical bias current for several input wavelengths.

influence on the dynamics of ASE.

The characteristic decrease in recombination time with increased injection current can be used to optimise SOAs for high repetition rate applications. By contrast, the fast recovery appears to slow down as the applied bias is increased, as illustrated in figure 7.8. This has also been reported by Occhi et al. [11]: they note that the curve for the recovery time and the total gain compression follow the same trend, but do not advance any further explanation. Changes in the ultrafast rate of the SOA recovery as a function of applied bias merit further investigation and, to achieve higher resolution, it would be desirable to use pulses with durations shorter than the ~ 700 fs pulses with which the data in figure 7.8 was obtained.

Dynamics for different polarisations

The measurements reported in Chapters 4 and 6 revealed that the gain available to the TM polarisation was significantly more than that available to the TE polarisation at biases (≥ 60 mA). Figure 7.9 shows pump-probe traces for identical bias conditions and pulse energies, but with the pump and probe polarisation directions reversed. It can be seen that the step change in transmission is significantly larger for TM pump and TE probe than vice versa. This is expected, and has a parallel explanation to that given for the larger transmission changes observed at higher bias levels: with the pump

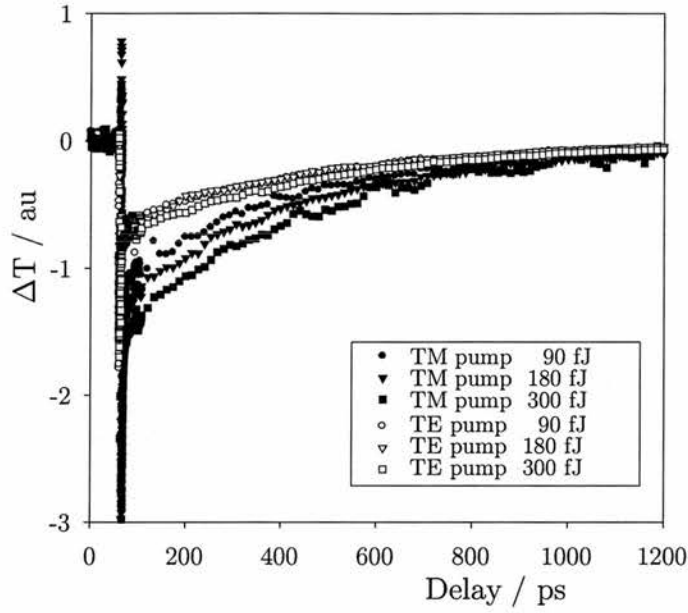


Figure 7.9: Probe transmission as a function of pump delay for pump in the TM and probe in TE mode and vice versa, for a range of pump pulse powers. All pulses were at a wavelength of 1565 nm and the electrical bias current was 60 mA.

in the TM direction it is more amplified, hence extracts more gain, leaving less for the probe, and there is correspondingly larger change in probe transmission compared with the case of the pump being in the TE mode.

Another feature of the pump-probe traces for the two polarisations, seen in figure 7.9, is that the curves converge, which appears to suggest that the rate of gain recovery is different for the case of pump in TM and TE modes. Any polarisation of the carriers due to the polarisation of the optical field would be expected to vanish very rapidly (~ 50 fs) so this apparent difference between the time dynamics of the gain observed with the exchange of polarisations was not expected. This issue is revisited, in the next section, with the analysis of results obtained with different pump pulse energies.

Dynamics as a function of pump pulse energy

Figure 7.10 (a) and a zoom on the same data in (b), show typical pump-probe traces from an experiment with pump and probe wavelengths in the central part of the gain spectrum of the SOA, in this case 1565 nm, and the device sufficiently biased to be in gain in this spectral region. For the data shown in figure 7.10 the pump was set to the mode that gave the greatest gain, that is, with its polarisation in the TM direction; the

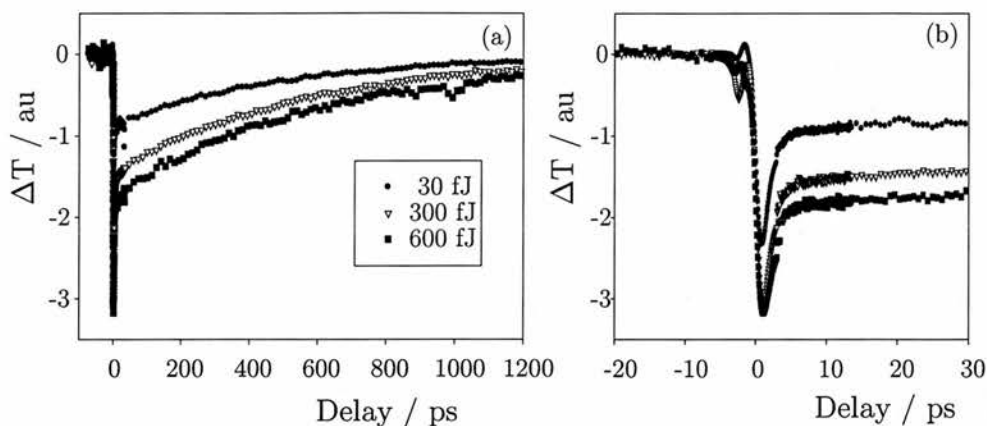


Figure 7.10: Probe transmission as a function of pump delay for three different pump pulse energies (a) and close up on times around zero delay (b). All pulses were at a wavelength of 1565nm and the electrical bias current was 45 mA. Note that the oscillation visible in figure (b) as the signal first starts to change, is thought to be due to a stray reflected signal and the step size was not short enough for the signal to be smoothed by the taking of a running average.

probe was cross-polarised, that is in the TE mode.

Under the conditions of constant electrical bias, the magnitude of the change in probe transmission is found to increase as a function of pump pulse energy. This trend holds both for maximum initial change in transmission, after zero delay, and the remaining difference in transmission (with respect to the case of no pump) after the initial rapid gain recovery. These increased transmission changes with pump energy can again be understood with a similar logic to that applied to the larger step changes under conditions of higher bias; essentially a stronger pump causes more gain depletion. Again, discussion of the limits on the amplitude of these observed gain changes is deferred to section 7.4.1.

Figure 7.11 illustrates the time constants from curve fitting pump-probe traces for different pump pulse energies: firstly from a direct exponential fit to the transmission change, and secondly from an exponential fit to the natural log of the transmission change. The former yields time constants that increase significantly with pump pulse energy (black diamonds). Such a link between the SOA time dynamics and the strength of optical pumping is not intuitive (contrast bias dependent changes in the rate of gain recovery which are expected since the bias controls the carrier density). The latter form

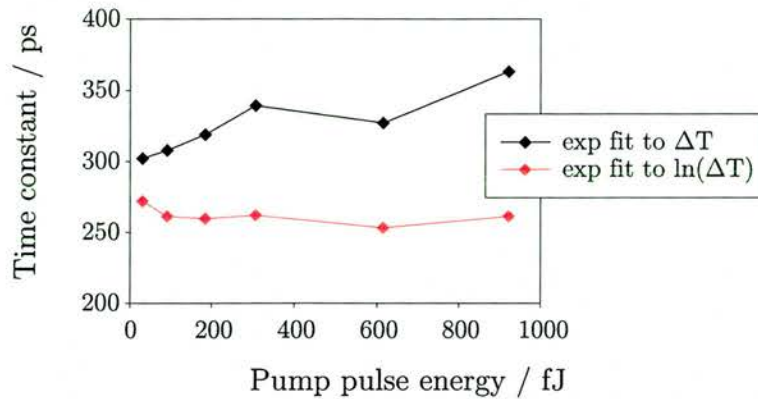


Figure 7.11: The time constant obtained from fits to pump-probe traces. When a simple exponential increase in transmission is assumed longer time constants are found for larger magnitudes of gain depletion (black); when fits were made to the natural log of the transmission change there was no significant trend in time constant as a function of pump pulse energy (red).

of fit is found to yield a time constant that does not change significantly with pump pulse energy (red diamonds). This fit, to the log of the transmission change, allows for the fact that the transmission change is dependent on a gain change which is itself related to the characteristic time constant through two exponentials, i.e. the carrier density recovery is exponential in time, but also the measured gain is exponential with propagation distance through the waveguide. (This double exponential relationship between the time constant and experimentally measured gain recovery is detailed in the Appendix.)

Similarly, the differences between the recovery from gain depletion with pump in TE and TM polarisations is attributed to the relative magnitudes of change in transmission, rather than to any change in the underlying characteristic time constant of the recovery. There is no physical mechanism by which either changes in energy, or polarisation of the gain-depleting optical field, influence the subsequent rate of gain recovery, over hundreds of picoseconds. It is nevertheless true that the gain (both amplitude and phase) takes longer to recover by a set amount (e.g. a change of phase of π) when the active material is more saturated. This imposes a limit on the rate of operation of interferometric switches, since recovery of pump-induced differential changes between data pulses is critical. Therefore it can be concluded that for ultrafast optical

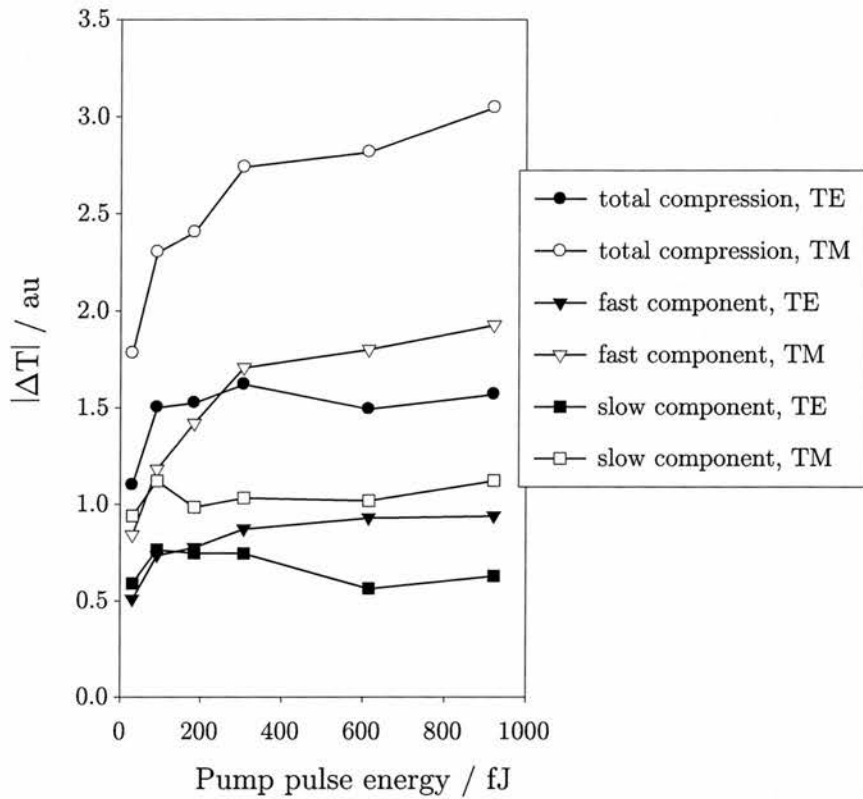


Figure 7.12: The magnitude of the total change in transmission (total gain compression), and separately the two components of this change corresponding to the slow and fast dynamics, as a function of pump pulse energy. Data is shown for both pump in TM (black) and pump in TE (white), with probe in the orthogonal polarisation in each case.

switching applications, it is desirable not to operate the SOA with very high energy control (pump) pulses which cause severe saturation of the gain.

Gain saturation

The phenomenon of gain saturation has been discussed in Chapter 6. Essentially as the intensity of an input optical field is increased the available gain is exhausted. In the context of the pump-probe experiment this is manifested by successive increases in the pump pulse energy causing progressively smaller changes to the amount by which the probe transmission is reduced.

Results presented so far, in this chapter, demonstrate that the magnitude of the observed changes in transmission tends to increase with pump pulse energy and applied electrical bias. Saturation is manifested when these parameters continue to be

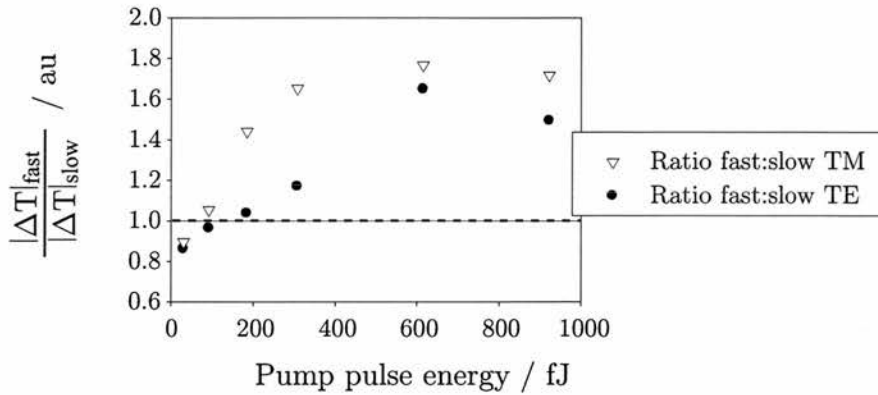


Figure 7.13: The ratio of the short-lived and long-lived components which make up the total transmission change. Data is shown for both pump in TM and TE modes, with probe in the orthogonal polarisation in each case.

increased. It is useful to consider the magnitude of the total step change and to define its fast and slow components. These correspond to the short-lived change in transmission, from the minimum (just after zero delay) to the crossover point between the fast and slow dynamics, and the remaining difference, after this initial fast recovery, respectively. The point in mid recovery that was taken as this crossover between the fast and slow dynamics was defined graphically: the logarithm of the transmission change was plotted and the crossover delay corresponded to the time at which lines fitted separately through the two recovery regimes intersected.

In figure 7.12 the total, fast and slow step changes in transmission are plotted as a function of pump pulse energy, for both TE and TM polarisations. It can be seen clearly that with successive increases of pump pulse energy, the step changes in transmission slow down and saturate. The TE polarisation seems to saturate at slightly lower pump powers than the TM, for which the gain is higher.

Over most of the range of input energies, and for both TE and TM pump, the fast component gives a larger contribution to the total gain compression than the slow. This is shown clearly in figure 7.13 in which the ratio of fast to slow gain compression is plotted as a function of bias. Note however that at the lowest input energies, the long-lived compression was the larger component; only by a small fraction but in both TE and TM data. The fact that the strength of the fast dynamic overtook the growth in the magnitude of the long-lived gain change as the pump pulse energy was increased

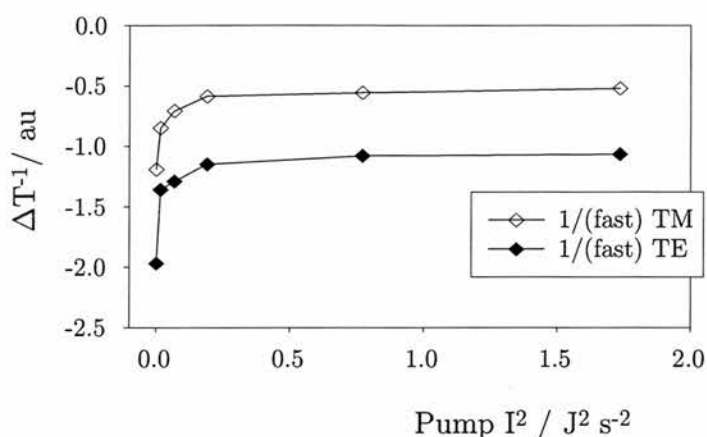


Figure 7.14: The reciprocal of the magnitude of the short-lived transmission change as a function of the square of the pump intensity. Data is shown for both pump in TM and TE modes, with probe in the orthogonal polarisation in each case.

suggests that two-photon absorption (TPA) was making a significant contribution to the ultrafast dynamic. This suggestion is supported by the reciprocal of the ultrafast transmission change becoming linear as a function of the pump intensity squared, a signature of TPA, for the higher pump intensities as shown in figure 7.14 [25]. The trend would merit investigation over a wider range of pump intensities and wavelengths. It is however concluded that it is likely that TPA is making a significant contribution to the ultrafast response of this SOA, at photon energies in the region of peak gain.

Saturation of the step changes in transmission is also clearly manifested as a function of bias, as illustrated in figure 7.15 which shows the total, fast and slow step changes as a function of bias. The increment by which the step changes grow with linear steps in bias becomes smaller at higher biases. This is a manifestation of the maximum level of population inversion being reached - eventually no more carriers can be injected because there are no more states to fill, and as this point is approached, despite the higher levels of bias being applied, the amount by which the gain and hence the transmission can be changed is limited. Note that at a bias of 40 mA the magnitude of the step change is only just greater than zero, suggesting that the amount of gain depletion by the pump was minimal and therefore corresponds to the device being close to transparency. This agrees with the transparency indicated by the trend of small signal gain measurements, and the difference with respect to the dV measurements of

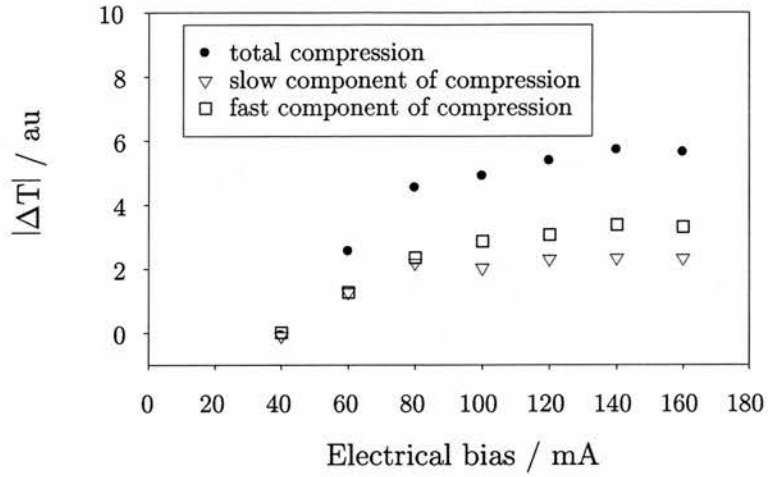


Figure 7.15: The magnitude of the total change in transmission (total gain compression), and separately the two components of this change corresponding to the slow and fast dynamics, as a function of electrical bias current. Data is for TM pump and TE probe, at 1550 nm and pump pulse energy of 150 fJ.

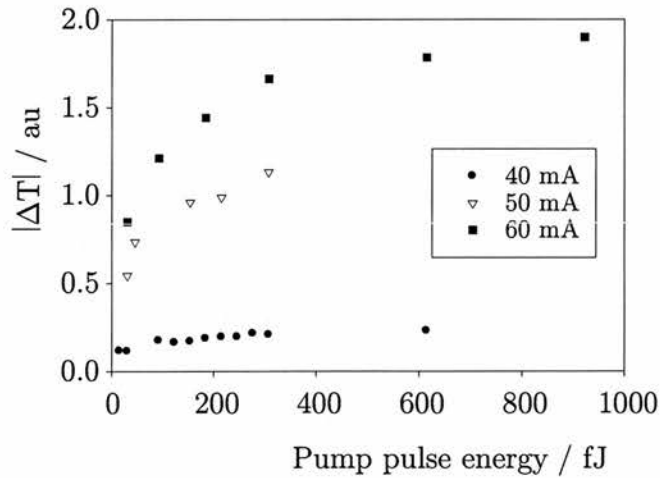


Figure 7.16: The magnitude of the total change in the transmission (total gain compression) as a function of pump pulse energy for a range of applied electrical biases. The pump is in the TM polarisation direction and the wavelength was 1560 nm.

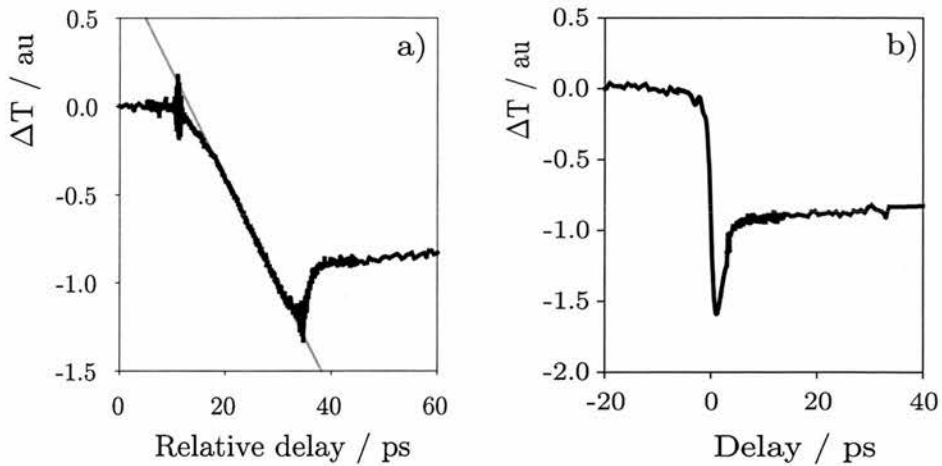


Figure 7.17: Change in probe transmission as a function of delay with respect to change in pump path length for the pulses counter-propagating (a). The electrical bias was 60 mA, pulses were at a wavelength of 1565 nm, pump pulse energy was 180 fJ and the probe 3 fJ. For comparison, the trace for the pump and probe co-propagating through the SOA is shown in (b).

material transparency is attributed to the former two including waveguide losses (see section 5.7.2).

Also note that with these pump-probe measurements, no strong trend as a function of bias was found in the energy at which the pump-induced gain compression saturates. For example, in figure 7.16, the curves do not flatten at distinctly different energies for the three biases. This is consistent with the results reported in Chapter 6, in which no clear trend in saturation energy with bias was observed and, likewise, is attributed to the saturation energy being almost flat over biases from 40 to 90 mA (as illustrated by figure 6.9).

7.4.2 Counter-propagation results

Counter-propagation transmission change

The nature of the transmission change measured with the pump and probe counter-propagating through the device was observed to be significantly different to the co-propagating case. Figure 7.17(a) illustrates the evolution of probe transmission as a function of changes in the pump delay for the the pump and probe counter-propagating through the device. For comparison, a trace for the co-propagating geometry over the

same length of time is shown in (b).

The counter-propagating probe experiences pump-induced gain changes from only the fraction of the device through which the pump has already travelled by the point that they cross in the loop. This results in the transmission reaching its minimum value much more slowly than in the co-propagating case. From the onset of reduced transmission, the full time taken to reach the point of minimum transmission is expected to be twice the propagation time through the active region. This is $2nL/c$ where n is the effective refractive index and L the length of the active region. The measured value of 22 ps is consistent with the 1 mm device length and an effective refractive index of approximately 3.4.

By comparison to the trace from the co-propagating geometry, figure 7.17 (b), the ultrafast component in (a), is a very much smaller fraction of the total reduction in transmission. This is consistent with the recovery time for this feature being ~ 1.2 ps, which is much less than the propagation time through the device (22 ps). Consider that the reduction in the counter-propagating trace occurs as the point where the pump and probe overlap moves closer to the facet where the probe enters and the pump exits the device. The minimum probe transmission is observed for the delay at which pump and probe meet at this facet, since under this condition the pump has been allowed to induce gain depletion along the full length of the device before the probe passes. However, since ultrafast recovery occurs continually as the probe propagates through the device, the ultrafast pump-induced gain changes at the opposite end of the waveguide, the exit facet for the probe, have recovered before the probe arrives there.

The only region of the device in which the probe experiences the total effect of the pump-induced gain depletion is that portion close to the point where it entered the waveguide, since there it was propagating through the material immediately after the pump. By contrast with the pump and probe co-propagating the probe can be arranged to follow immediately behind the pump experiencing the maximum effect of the ultrafast pump-induced gain compression all along the length of the waveguide: the transmission change is cumulative with propagation and therefore large.

As expected the recovery of the device on longer timescales, subsequent to the fast dynamic, is found to be the same as that measured using the co-propagating geome-

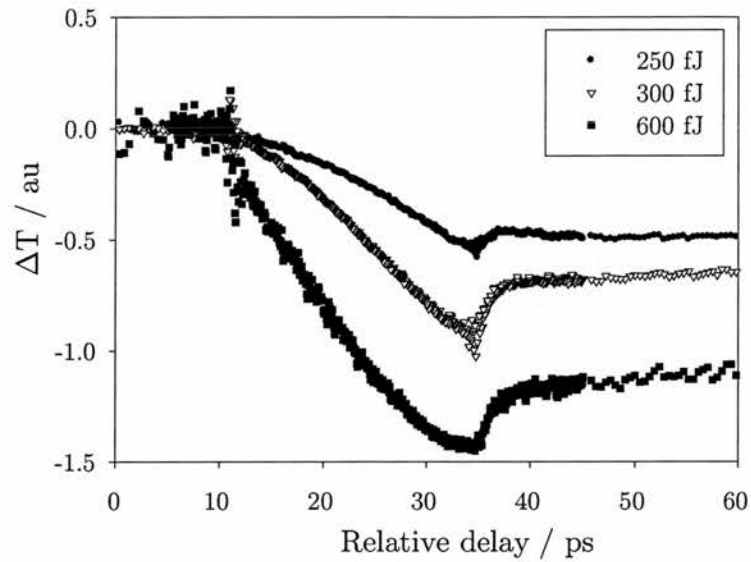


Figure 7.18: Change in probe transmission with delay (i.e. with respect to change in pump path length) for the pulses counter propagating for a range of pump pulse energies. The probe pulse energy was constant at 10 fJ, the electrical bias was 60 mA and pulses were at a wavelength of 1565 nm.

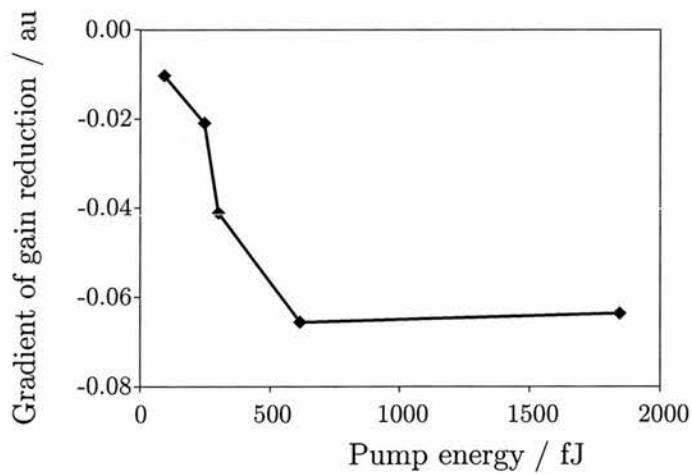


Figure 7.19: The slope of probe transmission change, over the section it was linear, as a function of pump pulse energy. The experimental conditions were the same as those listed in figure 7.18.

try. All these characteristics of the counter-propagating pump-probe trace have been successfully reproduced by the sliced propagation model (illustrated in figure 5.11 and plots shown later in this chapter). Note the oscillation seen in the data at the beginning of the transmission change is attributed to interference between the probe and a small part of the fraction of the pump that is co-polarised with the probe being reflected at the device facet.

Longitudinal dynamics

In the counter-propagating pump-probes, the change of probe transmission is not linear through out the period over which it is reduced to its minimum value. This is visible in figure 7.17(a) as the probe transmission deviating from the constant gradient (red line). The initially slow and then accelerated rate of change of transmission occurs over too long a time period to be due just to the pulse profile. The change of curvature is attributed to the amplification of the pump as it propagates through the SOA; the further through the device the pump has travelled by the point the probe passes it, the more the pump has been amplified, extracted gain and hence compressed the probe transmission. However in figure 7.17(a) the change of transmission rapidly tends towards a linear function of delay.

The counter-propagating pump-probe trace was found to change with different pump pulse input energies, as illustrated in figure 7.18. In particular, the gradient of the linear fall in transmission was found to increase as a function of pump pulse energy, as shown in figure 7.19. The change in slope appears to saturate with higher pulse energies. The smaller magnitude of transmission change for a given change in delay suggests that the amplified pump pulse is so intense that it is saturating the gain available (as limited by the carrier population inversion due to the fixed level of applied bias).

Figure 7.20 shows the data from 7.19 re-plotted with data from the single pulse measurements of gain saturation reported in Chapter 6 and illustrates the consistency of the saturation behaviour of the device as determined by the two techniques. Indeed the the longitudinal gain saturation revealed by the counter-propagating pump-probe experiments adds to the understanding of the characteristic saturation of the total de-

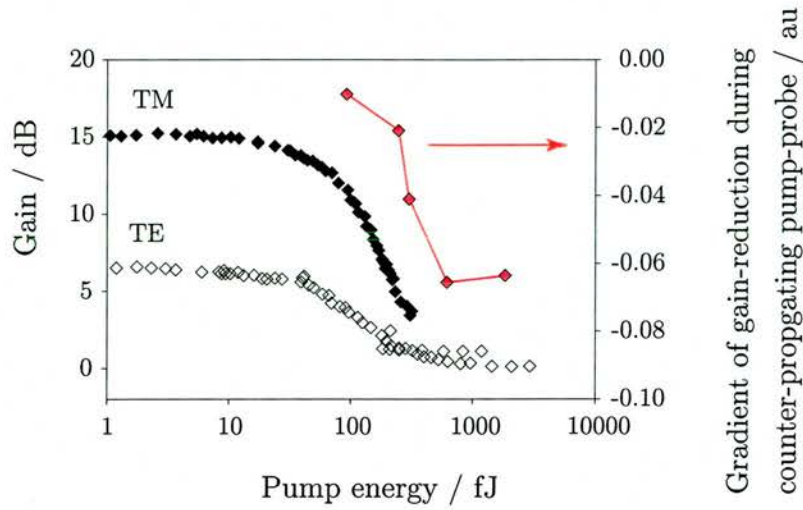


Figure 7.20: Data from figure 7.19 re-plotted with single pulse saturation results from the experiments reported in Chapter 6, where experiments were conducted at wavelengths of 1565 nm and 1570 nm, respectively.

vice gain as obtained by measuring input and output powers. It would be very interesting to apply this technique to devices in which the nonlinear material (providing gain or absorption) was localised or patterned within a waveguide e.g. an SOA with different electrical contact regions or quantum dot embedded within a photonic band gap material [26].

These conditions have been explored using the slice propagation model. Figure 7.21 shows a series of probe transmission curves, calculated for a range of pump input energies. The curves in (a) reproduce the trend seen in the experimental curves in figure 7.18. The corresponding curves for the counter-propagating probe are plotted in (b), for comparison.

With the model it is possible to investigate the gain along the length of the SOA corresponding to each of the pump input energies. The calculated amplification available per unit length (i.e. per $25 \mu\text{m}$ slice) along the device is plotted in figure 7.22. These curves reveal that for the lowest level of input (blue) the level of amplification does not change steeply at the beginning and is only significantly reduced from its initial value in the second half of the device. By contrast, in the case of the highest energy pump (red), $10 E_{sat}$, the gain is strongly depleted from the beginning of the device; by the end of the device the rate of reduction of gain slows and the amplification

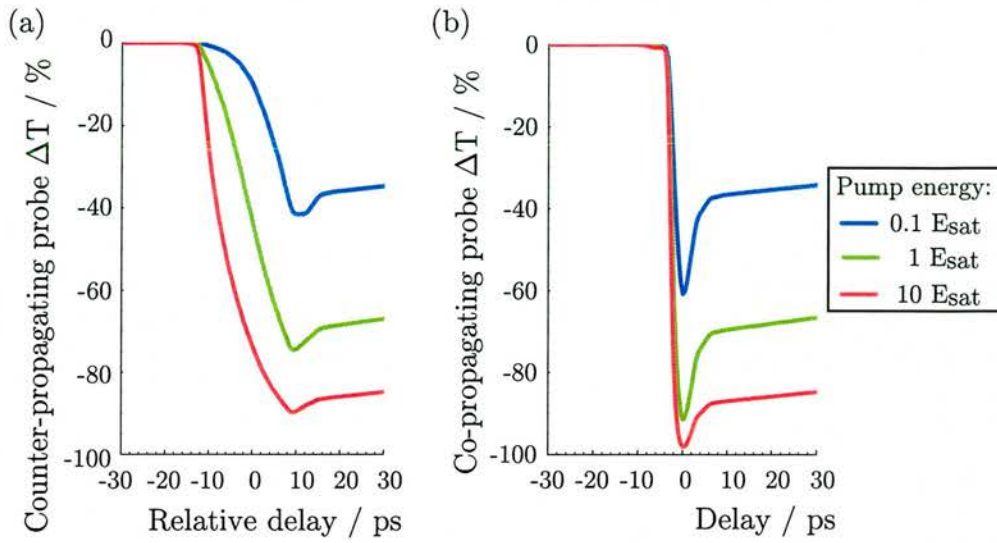


Figure 7.21: Calculated fractional change in probe transmission with delay for the pulses (a) counter- and (b) co-propagating with the pump for three pump pulse energies with respect to the 3 dB saturation energy.

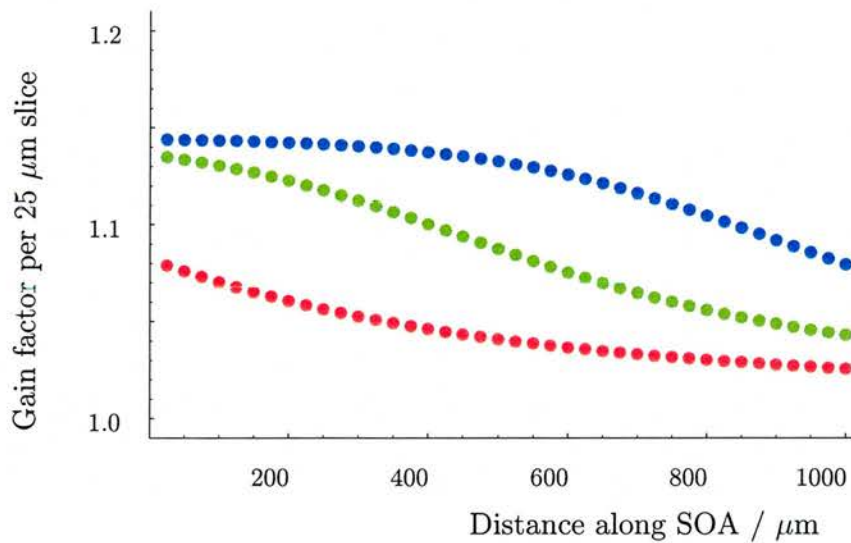


Figure 7.22: Calculated amplification (gain factor) per unit length travelled by the pump pulse along the length of the device, for the same three pump energies as used for the plots in figure 7.21.

(gain factor) approaches $\times 1$ indicating that the material in this part of the waveguide is being bleached towards transparency. Under the intermediate conditions (green), the amplification per slice is reduced almost linearly through much of the device. These curves mirror the characteristics of the counter-propagating pump probe traces from calculations (figure 7.21) and experiments (figure 7.18).

7.5 Summary

In this chapter two beam pump-probe experiments have been reported. They have revealed a two stage gain recovery. The slow, carrier density dependent gain recovery in the SOA is characterised by time constants of hundreds of picoseconds for low biases ($\tau_N \sim 350$ ps at 50 mA). However this ‘slow’ time constant falls rapidly with bias (to ~ 100 ps at 85 mA). At low to moderate biases (40 mA to 60 mA) the trend with bias is consistent with Auger being the dominant mechanism of carrier recombination. For higher biases, the rate of recovery increases and it is concluded that this is due to the strong ASE in this long (1 mm) waveguide; an effect similar to that of a holding beam.

In addition to the slowly recovering gain change, a strong ultrafast dynamic is observed, and this is attributed to carrier heating and two-photon absorption. In contrast to the increased rate of recovery of the carrier density dependent gain with bias, the ultrafast recovery seems fastest for low biases (< 1 ps) with the change saturating for higher biases (~ 1.5 ps). The trend in this ultrafast recovery time appears to be correlated with the saturation of the magnitude of the ultrafast gain compression. However the governing mechanism has not yet been identified; this trend merits further investigation.

Saturation of the transmission change with increasing pump input pulse energy and applied bias have been found to back up the single pulse results reported in Chapter 6. As with the single pulse data, there is no strong trend as a function of bias in the energy at which the SOA saturates.

In addition to the classic co-propagating pump and probe transmission measurements, dynamics measured with counter-propagating pulses have been presented. The counter-propagating probe has been shown to experience a slow fall in transmission,

corresponding to twice the transit time through the SOA (22 ps), which compares with the rapid transmission change following the pulse profile (~ 1 ps) observed with the conventional co-propagating configuration. The implications of this difference for switching configurations such as the TOAD in which pulses counter-propagate, are explored in the next chapter. What has been focused on in this chapter is the use of counter-propagating beams to explore dynamics within the SOA. In particular longitudinal gain saturation was identified. By contrast, there is no way by which the spatial dynamics inside a processed waveguide can be monitored using co-propagating beams. This additional information about longitudinal gain saturation, builds on the measurements of the saturation characteristics of total device gain reported in Chapter 4.

Bibliography for Chapter 7

- [1] R R Alfano, editor. *Semiconductors probed by ultrafast laser spectroscopy*, volume I and II. Academic, Orlando, 1984.
- [2] A J Taylor and J M Weisenfeld. Time-resolved photoluminescence of dense electron-hole plasmas in InGaAsP films. *Phys. Rev. B*, 35(5):2321–2329, 1987.
- [3] C Monier, M F Vilela, I Serdiukova, and A Freundlich. Band discontinuity in strained In(As,P)/InP heterostructures. *Appl. Phys. Lett.*, 72(13):1587–1589, 1998.
- [4] N K Das, Y Yamayoshi, and H Kawaguchi. Analysis of basic four-wave mixing characteristics in semiconductor optical amplifier by the finite-difference beam propagation method. *IEEE J. Quantum Elect.*, 36(10):1184–1191, 2000.
- [5] K E Stubkjaer. Semiconductor optical amplifier-based all-optical gates for high-speed optical processing. *IEEE J. Sel. Top. Quant.*, 6(6):1428–1435, 2000.
- [6] K L Hall, G Lenz, A M Darwish, and E P Ippen. Subpicosecond gain and index nonlinearities in InGaAsP diode lasers. *Opt. Commun.*, 111:589–612, 1994.
- [7] A M Fox, R J Manning, and A Miller. Picosecond relaxation mechanisms in highly excited GaInAsP. *J. Appl. Phys.*, 65(11):4287–4289, 1989.
- [8] K L Hall, G Lenz, E P Ippen, U Koren, and G Raybon. Carrier heating and spectral hole burning in strained-layer quantum-well laser amplifiers at 1.5 μm . *Appl. Phys. Lett.*, 61(21):2512, 1992.
- [9] P Borri, W Langbein, J Mork, and J M Hvam. Heterodyne pump-probe and four-wave mixing in semiconductor optical amplifiers using balanced lock-in detection. *Opt. Commun.*, 169:317–324, 1999.
- [10] R J Manning, A Antonopolous, R Le Roux, and A E Kelly. Experimental measurement of non-linear polarisation rotation in semiconductor optical amplifiers. *Electron. Lett.*, 37(4):229–231, 2001.
- [11] L Occhi, Y Ito, H Kawaguchi, L Schares, J Eckner, and G Guekos. Intraband gain dynamics in bulk semiconductor optical amplifiers: measurements and simulations. *IEEE J. Quantum Elect.*, 38(1):54–60, 2002.
- [12] R A Indik, R Binder, M Mlejnek, J V Moloney, S Hughes, A Knorr, and S W Kock. Role of plasma cooling, heating and memory effects in subpicosecond pulse propagation in semiconductor amplifiers. *Phys. Rev. A*, 53(5):3614–3620, 1996.
- [13] M Y Hong, Y H Chang, A Dienes, J P Heritage, P J Delfyett, S Dijaili, and F G Patterson. Femtosecond self- and cross-phase modulation in semiconductor laser amplifiers. *IEEE J. Sel. Top. Quant.*, 2(3):523–539, 1996.
- [14] K L Hall, E R Thoen, and E P Ippen. *Semiconductors and Semimetals*, volume 59, chapter 2 Nonlinearities in Active Media. Academic Press, 1999.
- [15] T Hessler, J L Pleumeekers, P E Selbmann, M-A Dupertuis, B Deveaud, R Schrieck, B Dagens, and J-Y Emery. Propagation effects on sub-picosecond gain dynamics in semiconductor optical amplifiers. In *Proceedings of IEEE Conference on Lasers and Electro-Optics*, 1999.

- [16] M Willatzen, T Takahashi, and Y Arakawa. Nonlinear gain effects due to carrier holeburning in strained-quantum- quantum-well lasers. *IEEE Photonic. Tech. L.*, 4(7):682–685, 1992.
- [17] C-K Sun, H K Choi, C A Wang, and J G Fujimoto. Studies of carrier heating in InGaAs/AlGaAs strained-layer quantum well diode lasers using a multiple wavelength pump probe technique. *Appl. Phys. Lett.*, 62(7):747, 1993.
- [18] J Mork, J Mark, and C P Seltzer. Carrier heating in InGaAsP laser amplifiers due to two-photon absorption. *Appl. Phys. Lett.*, 64(17):2206, 1994.
- [19] G Eisenstein, R S Tucker, J M Wiesenfeld, P B Hansen, G Raybon, B C Johnson, T J Bridges, F G Storz, and C A Burrus. Gain recovery of travelling-wave semiconductor optical amplifiers. *Appl. Phys. Lett.*, 54(5):454–456, 1989.
- [20] F Girardin, G Guekos, and A Houbavlis. Gain recovery of bulk semiconductor optical amplifiers. *IEEE Photonic. Tech. L.*, 10(6):784–786, 1998.
- [21] S Bischoff, A Buxens, St Fisher, M Dülk, A T Clausen, H N Poulsen, and J Mørk. Comparison of all-optical co- and counter-propagating high-speed signal processing in SOA-based Mach-Zender interferometers. *Opt. Quant. Electron.*, 33:907–926, 2001.
- [22] R J Manning and D A O Davies. Three-wavelength device for all-optical signal processing. *Opt. Lett.*, 19(12):889, 1994.
- [23] R J Manning, D A O Davies, D Cotter, and J K Lucek. Enhanced recovery rates in semiconductor laser amplifiers using optical pumping. *Electron. Lett.*, 30(10):787–788, 1994.
- [24] M A Dupertuis, J L Pleumeekers, T P Hessler, P E Selbmann, B Deveaud, B Dagens, and J Y Emery. Extremely fast high-gain and low-current SOA by optical speed-up at transparency. *IEEE Photonic. Tech. L.*, 12(11):1453–1455, 2000.
- [25] J Mark and J Mork. Subpicosecond gain dynamics in InGaAsP optical amplifiers: Experiment and theory. *Appl. Phys. Lett.*, 61(19):2281, 1992.
- [26] H Nakamura, H Kanamoto, Y Nakamura, S Ohkouchi, Y Tanaka, Sugimoto, H Ishikawa, and K Asakawa. Large enhancement of optical nonlinearity using quantum dots embedded in a photonic crystal structure for all-optical switch applications. In *IEEE/LEOS Annual meeting conference proceedings*, volume 2, pages 764–765, November 2002.

Chapter 8

Phase changes and refractive index dynamics

8.1 Introduction

Building on the two beam pump-probe experiments reported in the previous chapter, this chapter reports experiments in which an additional third beam is introduced as a reference probe. The interference signal between the two probes enables their relative changes in phase, due to pump-induced refractive index changes, to be detected.

The three beam pump-probe set-up described in this chapter is equivalent to the TOAD optical switching configuration. Experiments investigating the characteristics of the interferometric optical switching achieved using this SOA are reported. Results include contrast ratios and minimum switching energies ascertained as a function of electrical bias and operating wavelength. The shape of the switching window obtained under different operating conditions is also discussed.

Finally, in this chapter, measurements of probe spectra during a pump-probe experiment are reported. Dynamic changes in the probe wavelength are also a manifestation of pump-induced refractive index changes.

8.2 Three beam pump-probe experiments

8.2.1 Experimental configuration

The set-up used for the interferometric measurements involved the simultaneous coupling into the SOA of the pump, and both the co- and counter-propagating probe beams, used in pump-probe experiments described in Chapter 7. This combined con-

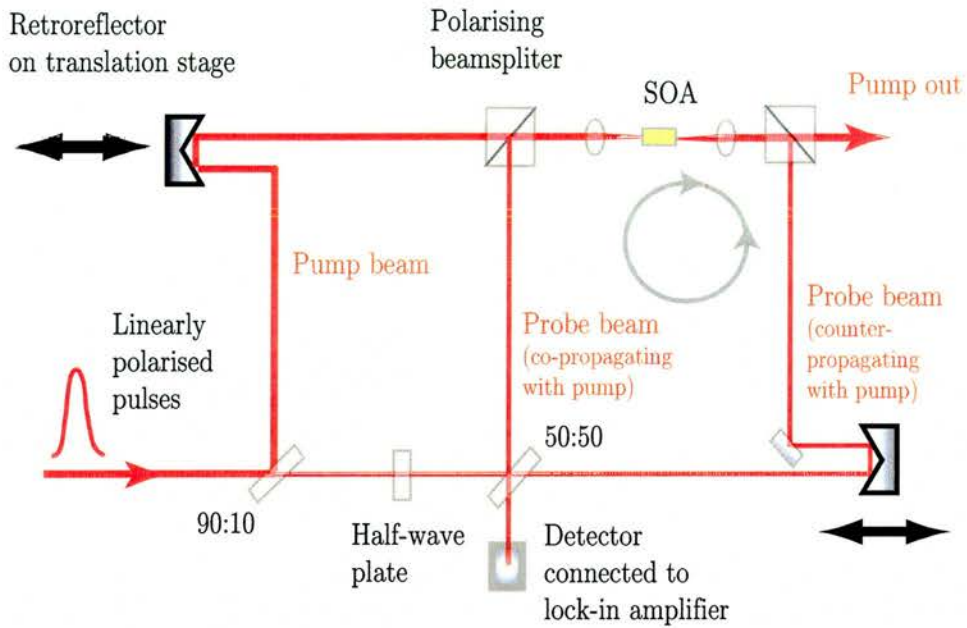


Figure 8.1: Schematic of the experimental configuration used for the interferometric measurements to determine changes in the probe phase at different delays with respect to the pump pulse

figuration, illustrated schematically in figure 8.1, essentially corresponds to a TOAD interferometric switch (introduced in Chapter 1) constructed from bulk optics.

The location of the SOA in the loop determines the optical path lengths and hence the relative arrival times at the device of the two probes. For any asymmetric placement of the SOA (i.e. such that it is not exactly half way round the loop, opposite the 50:50 beamsplitter), the probes necessarily arrive at different times with different delays with respect to the pump. Consequently for a given pump path length, if one or both probes arrives after the pump, each experiences the active material in a different state.

The state of SOA at the time they propagate through it determines the amount each probe is amplified and also the degree by which the phase of each is altered. The changes in phase being due to the fact that in addition to changing the available gain (as measured in Chapter 7), the pump interaction with the carriers causes a concomitant modulation of the refractive index of the material.

As shown in figure 8.1, after passing through the SOA the probes return to the 50:50 power beamsplitter and interfere. Note, the interference signal measured in these experiments is that which passes through the loop, not the signal that appears

reflected back along the direction of the original probe signal input. The reflection and transmission through the beamsplitter is such that the null state of this interference is destructive. (The mathematical expressions for this are detailed in section 5.8.4.) Hence when there is no pump or the pump pulse energy is so low that the refractive index is not significantly modified, the interference signal that reaches the detector from the recombined probes is low. Changes in the relative phase of the probes will initially result in increase of the strength of this signal.

Advantages of the TOAD-like set-up for experiments

It is the relative difference in phase that is critical for the use of SOAs interferometric switching applications. For measuring the differential changes in phase due to the pump pulse, the set-up used in the experiments reported in this thesis has several advantages. In particular parasitic changes in the index of refraction do not contribute to the signal since all three pulses pass through the waveguide [1]. Secondly, path length changes due to thermal fluctuations between the probe and reference are negligible since, although they propagate in different directions (clockwise and counter-clockwise), both follow the same path. Consequently active stabilisation of the interferometer is not required.

8.2.2 Difference frequency lock-in detection

In practice it was found that there were reflections from some optical elements within the loop and these enabled light to return to the beamsplitter without having passed through the SOA. The background signal due to such reflections is minimised in an integrated switching set-up. However, in these experiments, to distinguish the components of probe signal which had travelled completely around the loop lock-in detection using a double optical chopper was implemented.

The chopper had different period patterns on the inner and outer halves of its disc. This meant that the frequency of modulation of an optical beam depended on the radial distance from the centre of the disc at which the beam was incident. The disc was aligned on the optical bench, just after the 50:50 beamsplitter, such that the transmitted and reflected probe beams both passed through the chopper; one through the inner

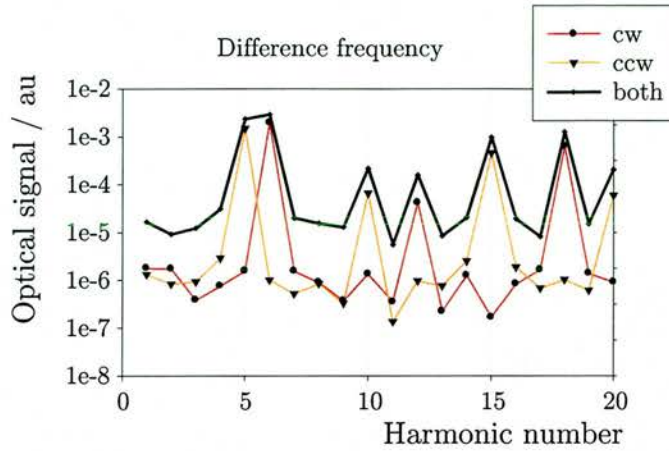


Figure 8.2: The strength of signal when the difference frequency is used as the reference frequency for the lock-in.

and one the outer pattern. The signal due to the interference of the co- and counter propagating beams that had passed through the SOA, and thence around the whole loop, had therefore been modulated at both frequencies.

The interference signal was measured using a large area Germanium detector and a lock-in amplifier. The driving electronics of the double chopper could give a reference frequency at either of the two frequencies or at the sum or difference frequency. To check for the strongest detection of the interference the lock-in was programmed to scan through the harmonics at each of these signals. As illustrated in figure 8.2, it was discovered that a reference signal for which both clockwise and counter-clockwise probes were independently detectable and balanced in strength, and where their combined interference signal was reasonably strong, was the first harmonic of the difference frequency.

8.2.3 Interferometric experiments

As shown schematically in figure 8.3, the variable delay on the pump arm allowed the pump to be scanned from before the short path probe pulse (time position 1) to arriving after both of the probes (time position 3).

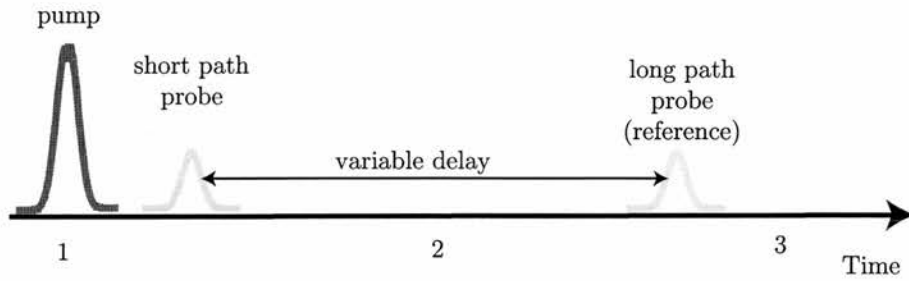


Figure 8.3: Schematic of the relative delays of the pump and the two probes. The pump can be scanned to arrive at times 1, 2 and 3 with respect to the two probes. The delay between the two probes can also be varied, though over a smaller range.

Phase measurements

For the first type of measurement presented in this chapter (see figure 8.4), the short path probe was taken to be the reference and the long path probe the signal. The slow recovery time of the gain of the SOA has been measured to be hundreds of picoseconds and the period between pulses from the OPO was more than 12 ns. Given these timescales, the optical path lengths of the two probe pulses were adjusted in order that the difference between their arrival times at the SOA was a few nanoseconds. This ensured that if the pump was at zero delay with respect to the second (long path) probe, the first (short path) probe would arrive before the pump and find the device in equilibrium, unperturbed by the pump-induced gain changes.

The strength of pulse interference was measured as the pump was scanned from arriving just before the long path probe to many hundreds of picoseconds after it. For long delays it was not important whether the signal probe was co- or counter-propagating with the pump. However, in order to investigate the full magnitude of the phase changes due to fast gain dynamics it is clear from the direction dependent transmission dynamics reported in Chapter 7 that it was necessary to ensure that the long path probe was the one co-propagating with the pump.

Switching window measurements

With the pump delay reduced to the point at which it precedes both probes (time position 1 in figure 8.3) and then scanned to the point where it follows both (time position 3), the interference signal can be viewed in a different context: essentially it maps out

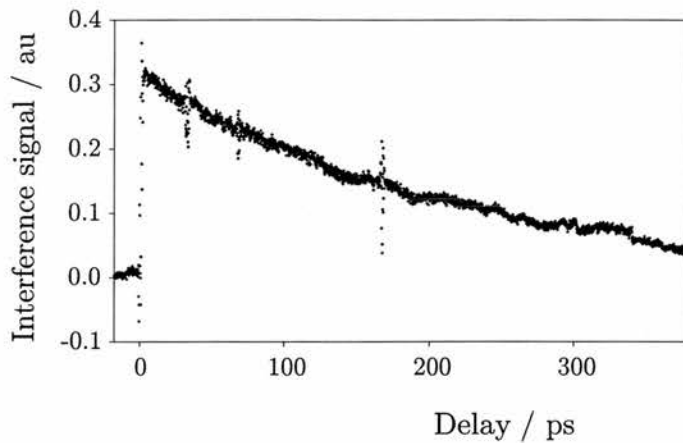


Figure 8.4: Interference signal between the two probes as a function of pump delay using probe energies of approximately 15 fJ and a pump pulse energy of 250 fJ. All pulses are degenerate at 1572 nm

the shape of the switching window for this interferometric configuration. The later measurements presented in this chapter correspond to this type of scan.

The variable delay within the loop, shown in figure 8.1, allowed the difference between the arrival times at the SOA of the two probes to be changed. This enabled the temporal width of the switching window to be varied. In addition, the strength of the interference signal within the window was investigated for a variety of electrical bias currents, pump pulse energies and at different wavelengths.

8.3 Interferometric results and analysis

8.3.1 Dynamics as function of pump delay

Figure 8.4 shows the interference signal, measured after the beamsplitter where the two probes meet, as a function of pump delay. The step increase in the signal is rapid, following the pump pulse profile, as seen in the co-propagating pump-probe transmission measurements. The strength of signal reduces back to the pre-zero delay level over a period of hundreds of picoseconds. Fits to this recovery yielded time constants equivalent, within the limit of experimental error, to those found for amplitude gain recovery under similar conditions.

The strength of the interference signal between the probe pulses must reflect the

change in relative phase of the probes, caused by the pump. However, regardless of the relative phase, their relative amplitudes impose limits on the minimum and maximum strength of the interference signal. In effect this interference signal is an indirect measure of relative amplitude changes of the probes.

Consider that the reference precedes the pump through the SOA so it encounters the active medium totally unperturbed by the pump and experiences the maximum level of gain. By contrast when the signal pulse arrives just after the pump, it experiences significantly lower gain, with respect to that experienced by the reference. Therefore at the point the probes interfere, when both have been through the SOA, the signal pulse is much smaller in amplitude than the reference pulse. It follows that although when $\Delta\phi = \pi$ the interference signal will indeed increase from its minimum level, it is also the case that even for small $\Delta\phi$ the interference signal will tend to increase due to the destructive interference being degraded by the difference in amplitude between the probes. For this reason, it is concluded that in measurements such as that illustrated in figure 8.4 any modulations due to differential changes in probe phases, as the SOA recovers, are dominated by the amplitude modulation of the signal probe with respect to the reference probe. To quantify the magnitude of the phase change, it was necessary to identify turning points in the magnitude of the interference signal as the experimental conditions controlling the magnitude of the gain change were varied. This concept was pursued in the experiments reported in the next section.

Importantly, the fast dynamic that is found to be strong in two beam pump-probes, was not manifested in these three beam interferometric measurements. Since the scan of interference as a function of delay is thought to be dominated by the probe to probe amplitude modulation it is surprising that there is not a spike corresponding to the strong gain compression near zero delay. It is concluded that under the conditions explored with these experiments and with this particular SOA, the coupling between refractive index and carrier population distribution changes is weak. This issue is returned to with discussion of the switching window shapes in section 8.3.6.

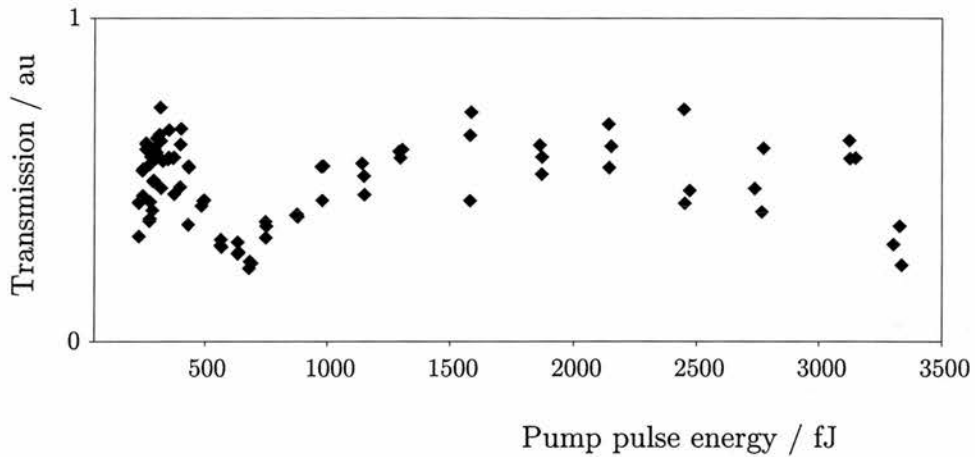


Figure 8.5: Change in the interference signal as a function of pump pulse energy. The null (no pump) interference is destructive giving a low signal. Each peak in the signal corresponds to the pump having induced an odd multiple of π phase difference between the two probes.

8.3.2 Interference strength as a function of pump pulse energy

By measuring the interferometric signal as a function of pump pulse energy, at a fixed delay, the evolution of the phase change can be observed. Figure 8.5 shows this signal as a function of pump pulse energy. The interference signal increases to a maximum, decreases and increases again. Maxima in the signal correspond to $\Delta\phi = n\pi$ where n is odd; minima to $\Delta\phi = m\pi$ where m is 0 or an even integer (as outlined in section 5.8.4).

Far from the change in phase increasing linearly with the strength of the optical pumping, it actually takes exponentially larger increases in the pump energy to achieve the similar incremental phase changes. To see the phase change of more than 3π , shown in figure 8.5, it was necessary to move to delay close to zero delay ($\sim 2ps$) and use the maximum optical energy that the pulsed source could provide. This data was noisy, which is attributed to timing and wavelength jitter in the optical pulse source. However the curve illustrates the cycle of maxima and minima produced by changing the pump pulse energy and corresponds well, qualitatively, to the change in the strength of the interference as a function of pump pulse energy calculated for the ideal case with the sliced-propagation model (illustrated in figure 5.14).

This interference measures the signal transmitted out of the loop after the beam-

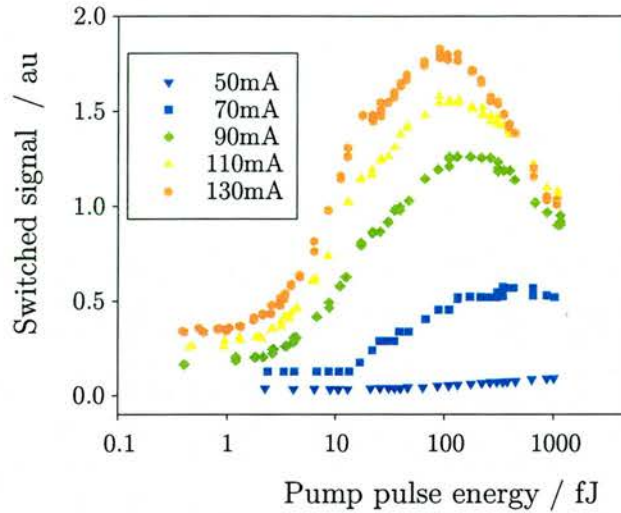


Figure 8.6: The interference signal, corresponding to the signal that is switched out of the loop (transmitted) as a function of pump pulse energy for a range of electrical bias currents. The input wavelengths of all pulses is 1567 nm

splitter, and corresponds to the transfer function of the switching configuration. Moving from the signal minima to maxima and vice versa, by controlling the pump energy, corresponds to turning the switching on and off. By comparison to the data shown in figure 8.5, the noise was reduced when the maximum pump pulse energies required were low enough that the pulse source did not have to be operated at the edge of its stability. Also the contrast ratio between maxima and minima was improved by adjusting the experimental conditions. These improvements are shown in the subsequent results presented in this chapter.

8.3.3 The effect of changing the bias

Figure 8.6 shows the evolution of the interference of the probes (switched signal) as the pump (control) pulse energy is increased for a range of electrical biases. The minimum pump energy necessary for switching is defined to be that which causes a phase change, $\Delta\phi = \pi$, and hence a maxima in probe interference. The energies for the first maxima, taken from the data in figure 8.6, are plotted as a function of bias in figure 8.7.

It can be seen that the required switching energy can be reduced by increasing the bias. This is consistent with the pump being more amplified under higher bias condi-

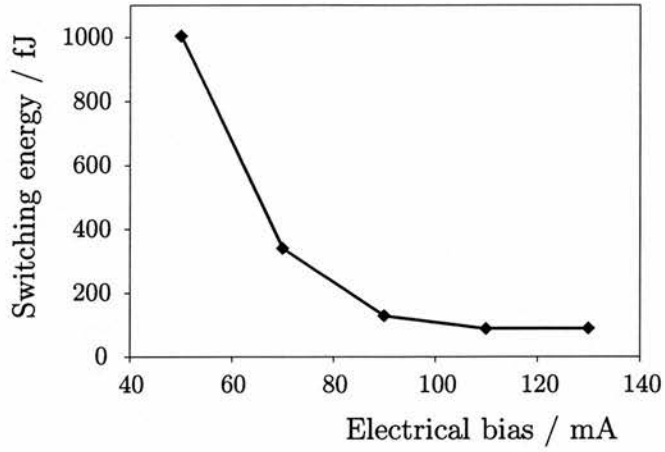


Figure 8.7: The pump pulse energy necessary to induce π phase difference between the probes and hence achieve maximum switched signal as a function of electrical bias. These values are taken from the data shown in figure 8.6

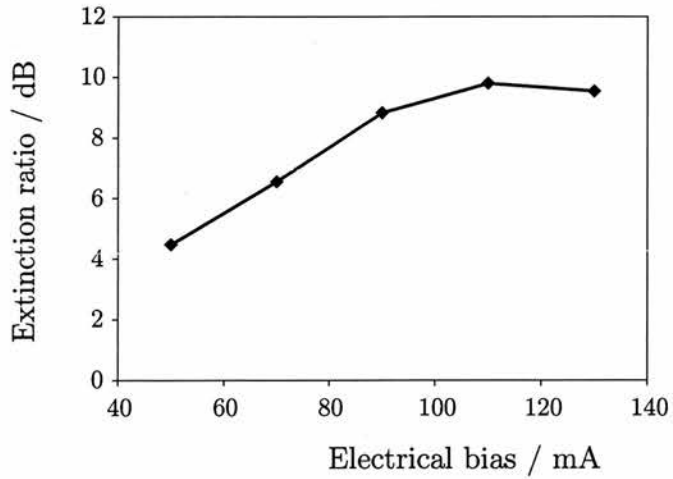


Figure 8.8: The extinction ratio between the null (no pump) probe interference signal and the maximum switched signal as a function of electrical bias. These values are taken from the data shown in figure 8.6

tions, therefore extracting more gain as it propagates through the SOA and causing a larger refractive index change in the material.

The extinction ratio between the on and off states of interferometric set-up is defined by

$$R = \frac{max}{min} \quad (8.1)$$

Figure 8.8 shows the extinction ratio as a function of bias; the maximum extinction ratio is achieved at approximately 110 mA, for these operating conditions i.e. in the middle of the gain. Thereafter, the improvement in extinction ratio appears to saturate. This can be explained by the fact that the increase in gain with each step in bias has become very small (as illustrated by figure 4.9). However, the improvement of the extinction ratio with bias does not just slow, the curve in figure 8.8 becomes totally flat and at the highest bias used in the experiment the measured extinction ratio gave a slightly lower value. The significance of this last point is marginal, it appears to be counter intuitive that there is no improvement in the contrast ratio when the gain is still increasing, albeit by progressively smaller amounts, with each step up in bias. As the ASE measurements warn, the high power of ASE at higher biases will tend to degrade the signal-to-noise of the signal which passes through the SOA, and it is also possible that the behaviour of the device is changed due to the emergence of cavity modes en route to lasing. However measurements of the probe spectra point to another possible contributory factor, namely degradation of the constructive interference by significant cross-phase modulation between the pump and signal probe, and this is discussed in the final section of this chapter.

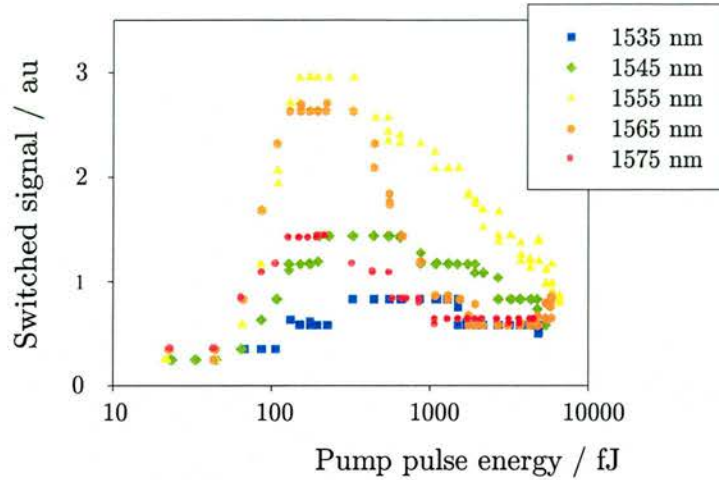


Figure 8.9: The interference signal, corresponding to the signal that is switched out of the loop (transmitted) as a function of pump pulse energy for a range of input wavelengths. The electrical bias used in all cases is 100 mA

8.3.4 Different operating wavelengths

The evolution of the interference with pump pulse energy was also investigated in different parts of the gain spectrum. Figure 8.9 shows the interference signal up to the first maxima as a function of pump pulse energy at five different wavelengths. Corresponding to the first maxima of the curves in figure 8.9, the energy required to achieve a π phase change was lowest for wavelengths in the middle of the gain spectrum (minimum measured for 1565 nm), as shown in figure 8.10. The contrast ratio was also found to vary with wavelength as illustrated in figure 8.11. The best (highest) values of extinction ratios were found for wavelengths where there is high gain, in the same range as the lowest switching energies.

It appears that the occurrence of the highest contrast ratios is marginally weighted towards the long wavelength side of the maximum gain. An increase in contrast ratio as the wavelength is tuned towards band edge is consistent with results reported in the literature [2]. This is attributed to the slightly lower amplitude gain at these wavelengths leading to a reduction in the amplitude modulation between the co- and counter-propagating components of the signal pulse, whilst there remains a signifi-

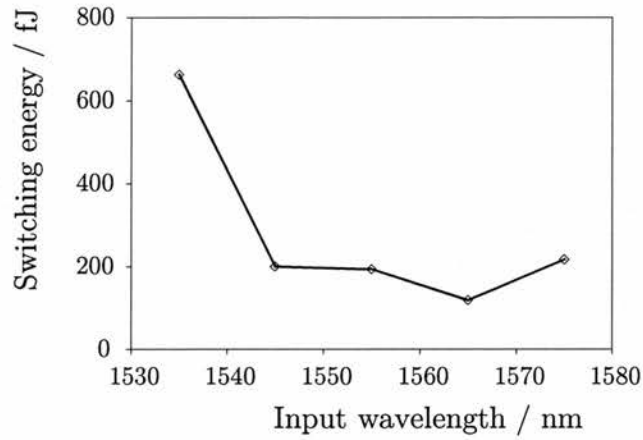


Figure 8.10: The pump pulse energy necessary to induce π phase difference between the probes and hence achieve maximum switched signal as a function of input wavelength. These values are taken from the data shown in figure 8.9

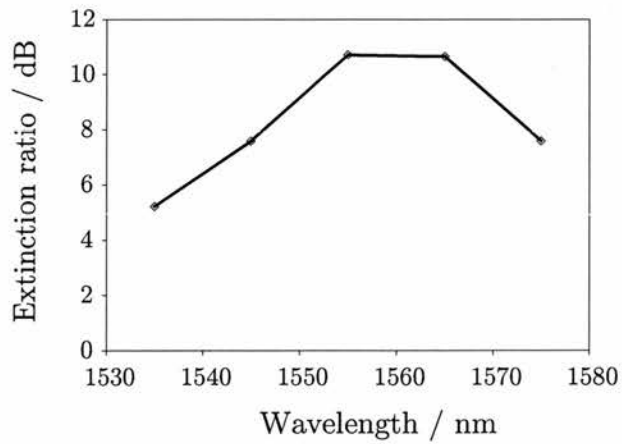


Figure 8.11: The extinction ratio between the null (no pump) probe interference signal and the maximum switched signal as a function of wavelength. These values are taken from the data shown in figure 8.9

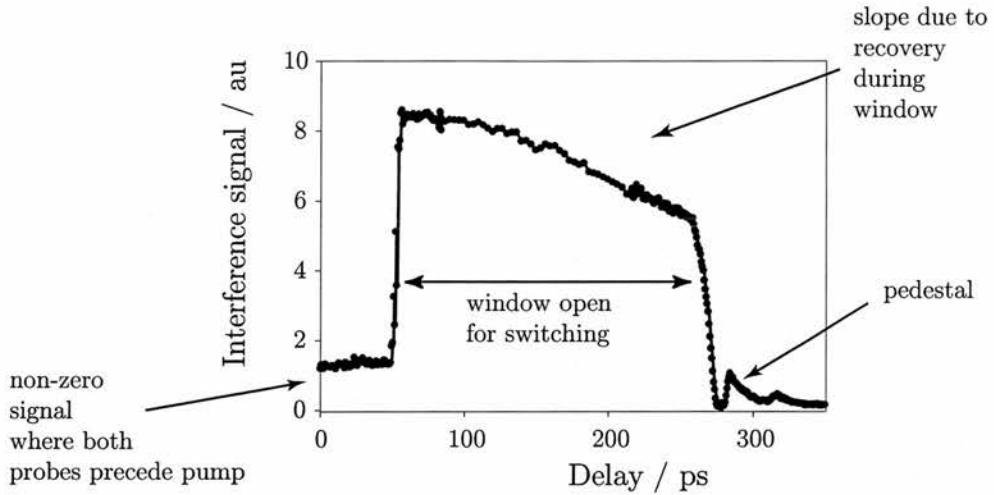


Figure 8.12: The interference signal as the pump path length to the SOA is scanned from shorter than the shortest probe path to longer than the longest probe path. This corresponds to the time during which the probe signal is transmitted through the loop i.e. the switching window. Note that the delay between the probes, fixed during this experiment, is so long that the signal changes due to the slow recovery of the SOA.

cant refractive index change. These factors can result in better contrast between the constructive maximum and destructive minimum of the interference.

8.3.5 Switching window

Wide and narrow windows

With the pump energy set such that it induces $\Delta\phi \approx \pi$, there is strong constructive interference between the probes over the range of delays for which the pump arrives at the device between the two probes (i.e. the central time period, 2 in figure 8.3). Figure 8.12 shows the interference signal as a function of pump delay for the pump scanning past the points at which its arrival at the SOA is coincident with each of the probes (i.e. from position 1 to position 3 in figure 8.3). The central increase in the interference signal is the switching window. For this relatively long probe separation, it is possible to see the recovery of the SOA during the window.

Also in figure 8.12, outside the window the signal is non-zero for short delays (position 1 - both probes before the pump) and there is a pedestal at long delays (position 3 - both probes after the pump). Both are due to imperfect destructive interference at these points. The peak of the pedestal occurs at a time which corresponds to the second

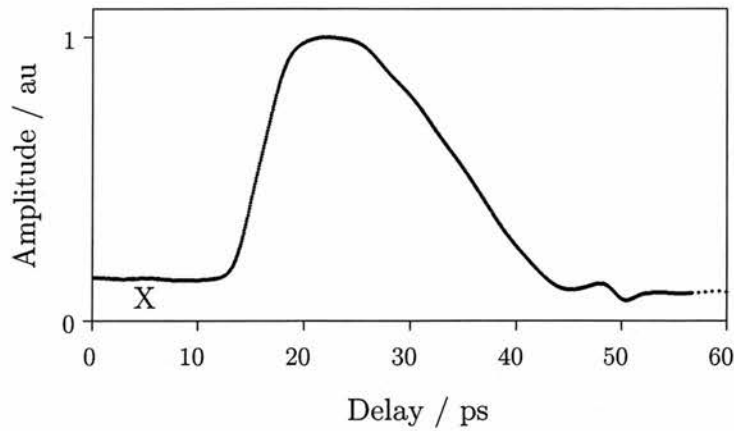


Figure 8.13: Switching window showing the asymmetric shape of the switching window due to the difference in dynamics for the co- and counter-propagating probes.

probe experiencing its maximum pump-induced change, whilst the first probe experiences significantly recovered gain and index. Minimisation of these signals, which tend to degrade the quality of switching, is discussed in the next section.

The experimentally measured window for a much shorter probe-probe path difference, of approximately 15 ps, is shown in figure 8.13. In this case the top of the window is essentially flat, since there is insufficient time for significant recovery of the device. The pedestal is reduced to a small oscillation (on the right hand side of the window, at a delay of ~ 50 ps). With the plot extending over a relatively small range of delays (with respect to figure 8.12), it can be seen clearly how the different nature of the dynamics for the co- and counter-propagating pulses defines the shape of the switching window: the switch on is fast and the switch off is slow, corresponding to the probes co- and counter-propagating with the pump, respectively. The time for the counter-propagating switch off is 22 ps, which corresponds to twice the transit time through the device, as discussed in Chapter 7.

Optimising the switching window

A criteria for high quality switching is the achievement of a high contrast ratio, between the on and off states of the switch. To achieve a high contrast ratio, with this interferometric configuration, it is critical to minimise the signal at delays outside the switching window. Non-zero background level outside the window is attributed to

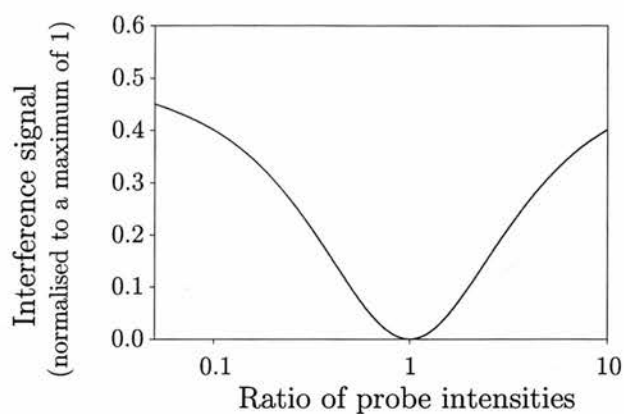


Figure 8.14: The calculated interference signal as a function of the ratio of probe input powers, at negative delays with respect to the pump i.e. a point where both probes precede the pump (e.g. X in figure 8.13). This corresponds to the background offset signal outside the switching window.

- an offset occurring when both probes precede the pump through the SOA: the magnitude depends on the relative difference between the input intensities of the two probes
- a pedestal occurring when both probes propagate through the SOA after the pump but they still do so at different times: the magnitude depends on inter-probe delay, and also the pump pulse energy.

To address the first issue, the need to minimise the offset at short delays (where both probes precede the pump through the device), it is necessary to adjust the splitting ratio of the signal into two components to closely balance them. In the experiment this was determined by the quality and alignment of the beamsplitter. Ideally the ratio is 1:1; the interference signal at the output at delays when both probes precede the pump is then zero [3]. The effect of their ratio straying from this ideal is demonstrated by the calculations from the sliced-propagation model, shown in figure 8.14. As the ratio becomes larger or smaller than 1:1, the background signal rapidly rises, thereby degrading the contrast ratio. In the experiments, the beamsplitter was adjusted to minimise the pre-pump interference signal between the probes. However complete elimination of the background signal was not achieved; rather than the splitting ratio not being balanced, this may be due to directionally dependent losses within the loop

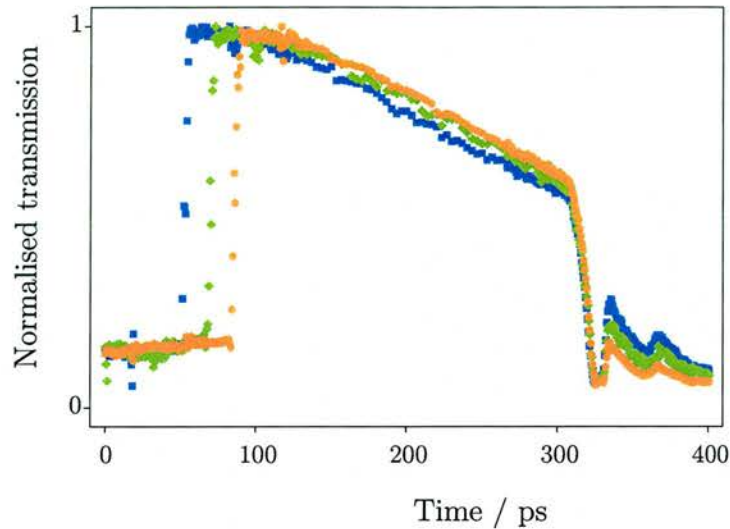


Figure 8.15: Experimentally measured switching window for three different delays between the probes.

(e.g. non-symmetrical coupling). This highlights the degree to which optimisation of alignment and the characteristics of each optical element in the switch is critical to the quality of the interferometric switching.

The second issue raises an intrinsic problem which necessitates a trade off: some degree of delay between the probes is necessary in order that the switching window opens at all; too much delay results in the magnitude of the probes being significantly different and the differential phase straying from π at the closing side of the switching window. Experimental data in figure 8.15 illustrate the change in the height of the pedestal as the delay between the arrival of the probes at the SOA. The largest pedestal occurred for the longest inter-probe delay, for which the greater degree of recovery of the device between the probes is revealed by the curve (blue) being the lowest (of the three curves) on the right hand side of the window. Correspondingly, the smallest pedestal occurred for the shortest inter-probe delay, for which SOA (as experienced by the first probe) had had the least time to recover by the time of arrival of the second probe (orange curve).

To quantify this trend the pedestal was investigated with the sliced-propagation model. Figure 8.16 shows the calculated shape of the window, taking into account only the carrier density dependent gain changes, and this reproduces the characteristics

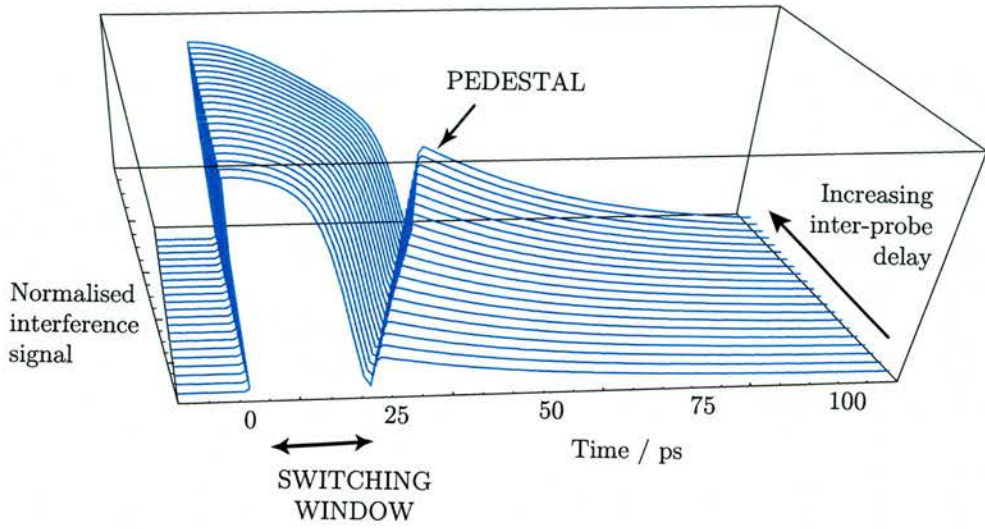


Figure 8.16: Calculated switching window for different delays between the probes, considering only carrier density dependent gain changes i.e. $g = g_N$.

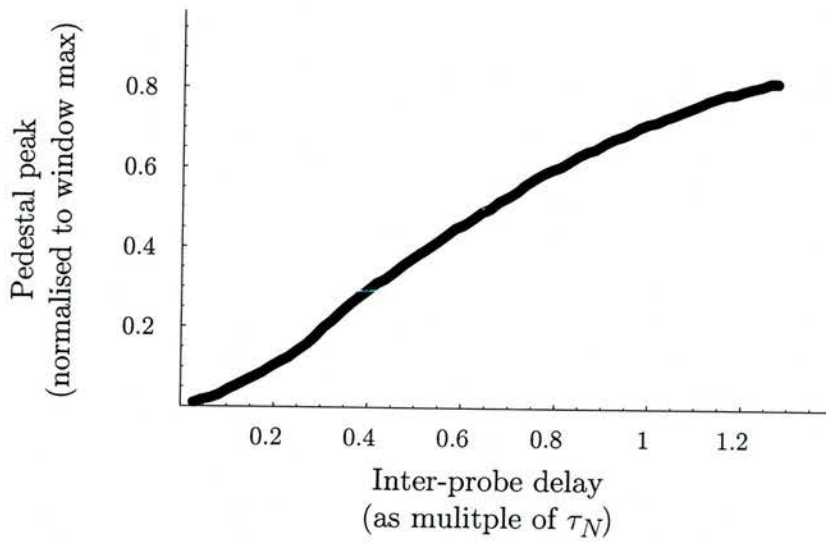


Figure 8.17: The pedestal as a function of the inter-probe delay, expressed as a fraction of the device slow recovery time constant, τ_N . The input parameters were the same as those used for the curves in figure 8.16.

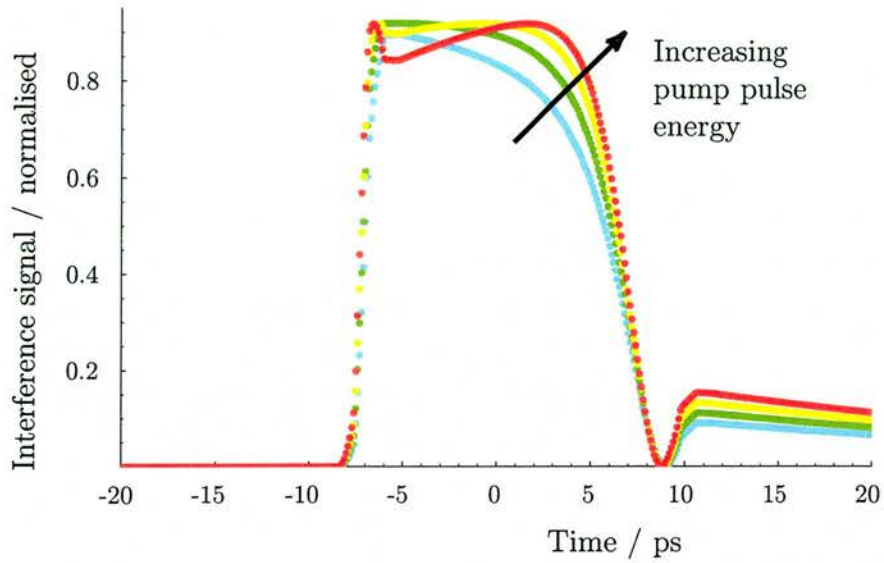


Figure 8.18: The calculated window shape for different pump energies (corresponding to 13, 16, 19 and 22 % of the saturation energy, respectively for the curves from blue to red along the arrow). The other parameters were the same as those used for the curves in figure 8.16.

of the experimental traces. The peak magnitude of the pedestal from this calculated window is shown in figure 8.17 as a function of delay between probes. This delay is expressed as a function of the slow gain recovery time; it can be seen that as the inter-probe delay approaches the recovery time, the pedestal grows towards an equivalent strength to the maximum interference signal inside the window, and the contrast ratio becomes totally eliminated.

The conditions for these calculations were an extreme case of wide windows, high bias (100 mA) and rapid gain recovery; the pedestal is correspondingly worse than manifested in the experimental data. However this analysis serves to demonstrate that to minimise the pedestal it is necessary to reduce the width of the switching window. The calculations suggest that to maintain the peak of the pedestal at less than 10% of maximum interference signal, the switching window width needs to be $\leq 10\%$ of the gain recovery time. Alternatively, for a fixed inter-probe delay, electrical bias and other operating conditions, the difference between the probes should be compensated for by the introduction of a non-reciprocal phase shift the loop (i.e. phase dependent on direction of propagation), for example, using a birefringent material [3].

Optimisation of the contrast ratio of the switch also requires identifying the optimal control pulse energy. It tends to be loosely said that for an interferometric switch it is necessary ‘to achieve a π phase change’. To optimise the switching it is arguably best that the differential phase of π between the probes occurs at delays corresponding to the centre of the switching window, rather than the maximum phase change induced by the control pulse being π . This can be achieved by causing the maximum pump-induced phase change to be greater than π , i.e. using a marginally higher energy pump pulse energy, as illustrated in figure 8.18.

For the lowest pump pulse energy (blue curve) the maximum change experienced by the first probe is π ; for the higher pump pulse energies, $\Delta\phi_{max} > \pi$ (green, yellow and red curves). Too high a pump energy causes an overshoot which results in oscillations within the switching window, however increasing the pump pulse energy by 19% above the energy needed to achieve a maximum phase change of π , yields a more symmetrical window with a flatter top. This is desirable since a flat topped window makes the switching less sensitive to jitter in the arrival time of the pulses, but the benefit has to be balanced against a slightly increased pedestal.

For ultrafast switching a narrow window is required. Successive reductions in the width of the window is limited in switching configurations such as the TOAD by the slow gain change experienced by counter-propagating probes. In turn, this is determined by the length of the SOA. A shorter device may be used, but will tend to require higher electrical biases to achieve the necessary magnitude of gain changes. Alternatively the counter-propagating pump-probe results as a function of pump pulse energy (e.g. figure 7.18) indicate that for a given device length the counter-propagating window edge can be made to appear more steep, and thereby a narrower window made possible, by operating the SOA in a highly saturated regime.

Overall the investigation of the optimisation of the interferometric switching window, presented in this section, highlights the degree to which levels of electrical bias current and the pump pulse energy are critical, and the way in which they need to be tuned for different switching window widths.

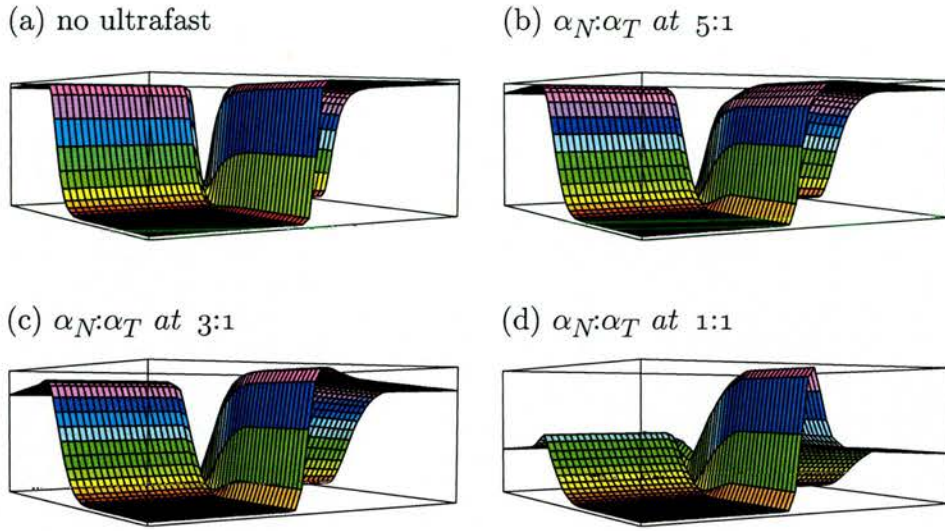


Figure 8.19: The calculated interference signal as a function of the relative delays of the two probes and the pump, where in (b), (c) and (d) changes in gain and phase are due to changes in carrier density and temperature ($g = g_N + g_T$) for different α -parameter ratios ($\alpha_N : \alpha_T$). For comparison, in (a) $g = g_N$ as in figure 5.15

8.3.6 Amplitude gain to refractive index coupling

In none of the interference experiments have ultrafast changes in the signal, of the sort that might be expected as the signature of ultrafast dynamics, been observed. This was in strong contrast to the amplitude transmission measurements, reported in Chapter 7, which revealed strong ultrafast amplitude gain changes. The nature of the probe-probe interference signal, under conditions where ultrafast gain was strong, was explored using the sliced-propagation model.

In figure 8.19 (b), (c) and (d) the surface and curves were calculated assuming that $g = g_N + g_T$; for comparison (a) was calculated with $g = g_N$ i.e. the case of no ultrafast dynamics. The difference between (b), (c) and (d) is due changes in the ratio between the carrier density gain to index and carrier heating to index coupling, as quantified by α_N and α_T , respectively. Specifically, $\alpha_T = 2$ is fixed, and in α_N is 10, 5 and 2 in (b), (c) and (d) respectively. The saturation energies E_{satN} and E_{satT} which determine the relative strength of the slow and ultrafast contributions to the gain compression were fixed (at 2 pJ and 0.5 pJ, respectively). The pump input energy was altered, between the plots, to achieve constructive interference during the windows.

These plots serve to illustrate that even where ultrafast gain changes are occurring,

the switching window is not necessarily qualitatively changed. In the case of the device studied, despite the observation that its gain saturation and transmission pump-probe characteristics are strongly influenced by ultrafast processes, ultrafast dynamics are not seen in the interference measurements. The degree of influence on the switching window shape of different gain change mechanisms is determined by the strength of the coupling between the amplitude gain and the refractive index, as quantified by the relevant α -parameters. Strong coupling between ultrafast gain and index changes has been found to degrade the switching [4] [5]. Correspondingly, the lack of ultrafast changes in the interferometric measurements reported in this chapter, leads to the conclusion that in the SOA device studied, the gain change to index coupling is weak for ultrafast carrier heating and two-photon absorption processes, to which the ultrafast amplitude transmission changes have been attributed.

Correspondingly, the lack of ultrafast changes in the interferometric measurements reported in this chapter, leads to the conclusion that in the SOA device studied, the ultrafast amplitude gain to index coupling is weak. In particular, it is concluded that the α -parameters for ultrafast processes of carrier heating, α_T and two-photon absorption, α_{TPA} , to which the ultrafast amplitude transmission changes have been attributed are small, compared with α_N , for the slow carrier density dependent gain changes. In addition, given the low levels of pulse energy required to achieve the first π phase change, it is estimated that α_N for this SOA is large, in the range of 6 to 10, which published results indicate is reasonable. For example, Tiemeijer et al. [6] obtain values from 1.5 to 11 for strained InGaAs/InP devices where the value depends on factors including the strain in the material and the wavelength of operation.

8.4 Dynamic spectral shifts

8.4.1 Measurement of probe spectra

The wavelength of a probe after propagation through the SOA at different delays with respect to the pump was measured. Note that this was a two beam experiment; probe spectra were measured directly without reference to a second probe.

Results presented in Chapter 6 demonstrate the magnitude of wavelength shifts

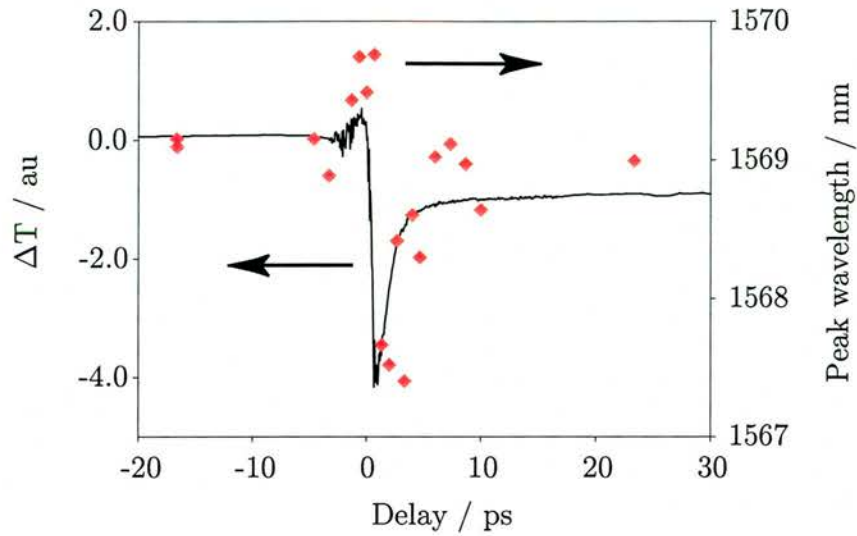


Figure 8.20: The peak wavelength of the probe output from the SOA (black diamonds) as a function of delay with respect to the pump. The underlying curve (solid black line) is the corresponding measured transmission changes.

observed with a single pulse propagating through an SOA due to carrier changes it, itself, causes. This is so-called self phase modulation (SPM). The SPM resulted in severe pulse distortion for high pulse energies (~ 1 pJ). By contrast in the experiment reported in this section, the answer was sought as to whether spectral changes on a weak probe pulse (~ 1 fJ) were observable due to the carrier dynamics caused by a strong pump pulse: this would be cross-phase modulation.

8.4.2 Results of spectral measurements during pump-probe

Figure 8.20 shows the peak wavelength of a probe pulse (red diamonds) at different stages during a pump-probe experiment. Quantifying of the change in the probe spectrum by its peak wavelength was reasonable given that the pulse did not break up. The probe was first blue-shifted, that is to shorter wavelengths, and then rapidly red-shifted. From the curve of the concomitant transmission changes (black line) it can be seen that the underlying rapid carrier dynamics are coincident with these spectral dynamics and the spectral changes are attributed to these dynamics.

The degree of this cross-phase modulation imposed on the probe by the pump-induced gain changes is significant: the probe wavelength is changed by $> \pm 1$ nm. A reduction in spectral overlap of the probes may explain the observation (reported

in section 8.3.3) that, beyond a certain point, contrast ratio and minimum switching energies can not be further improved by continuing to ramp up the bias current.

Sutkus et al. [7] and more recently Schrieck et al. [8] report such spectral shifts under pump-probe conditions. Sutkus et al. proposed a qualitative explanation for the spectral shifts based on the time dynamics revealed in the pump-probe: in general the blue shift is attributed to the rapid carrier heating dynamic and the red shift to the longer-lived carrier population changes due to interband transitions.

The fact that ultrafast index dynamics are manifested in these spectral measurements, but not detected in the interferometric time resolved measurements, merits further investigation. It would be interesting to conduct more experiments measuring the probe spectrum over a wide range of conditions. To more precisely correlate spectral changes with the gain dynamics, it is necessary to use the full spectrum [9] (as opposed to the peak wavelength). Further experiments would then need to be complemented by the extension of the model to include a description of the spectral characteristics of the pulse. Such a model would facilitate exploration of the influence of probe wavelength changes on the quality of interferometric switching.

8.5 Summary

The aim of experiments described in this chapter experiments was to measure phase changes and to characterise switching with the SOA. In particular, the device has been used to demonstrate interferometric switching, in a TOAD-like configuration, with control pulse energies as low as 100 fJ.

A range of approaches to optimising the switching window with the aim of realising narrow flat-topped steep-sided switching windows have been investigated, experimentally and using the sliced-propagation model. The analysis has focused on the window obtained with the TOAD switching configuration, however most of the results are more generally applicable.

Calculations confirm the experimental observation that minimisation of the background signal outside the intended switching window is critically dependent on achieving a splitting ratio, for the two probes that later interfere, close to 1:1. It has been

proposed that the use of a control pulse energy which effects a maximum differential phase slightly higher than π be used to achieve a flatter top to the switching window. Also the growth of a pedestal outside the switching window has been shown to be correlated with the width of window with respect to the gain recovery of the device. The switching energy was reduced to a minimum by increasing the bias current to 110 mA and the contrast ratio improved to 10 dB. This contrast ratio, though less than the best reported, is comparable to values reported in the literature [10] [11]. It is possible that the extinction ratio was deteriorated by unguided light i.e. any component of the probes which did travel completely round the loop and reach the detector after the beamsplitter, but which had not been coupled through the active region of the SOA [12].

The asymmetric nature of the switching window of the TOAD, distinct from other interferometric configurations, has been experimentally measured and reproduced with the sliced-propagation model. For slow bit rate applications with pulse durations that are long, with respect to the transit time through the SOA (22 ps), the difference between co- and counter-propagating dynamics is not problematic. Further, switching configurations using SOAs in which the control pulse counter-propagates with respect to both signal components (such as the colliding pulse Mach-Zender interferometer) may be desirable since the leak of control bits into the output signal stream is easily avoided, without the need for a spectral filter [13] [14]. However, in the drive for high bit rate switching narrow switching windows are required. In this context, the fact that, with counter-propagating geometries, the time for changes in transmission (switch on/off) has a lower limit determined by the propagation through the device becomes problematic. It has been shown that higher input pump pulse energies steepen the slow (counter-propagating probe) transmission change. Alternatively, the limit can be reduced by the use of shorter devices [15]. However neither strategy avoids the fact that for the minimum π phase changes required for high quality interferometric switching, the bias and/or optical input power requirements tend increase with narrow switching windows.

It is necessary to conclude that whilst the TOAD-like switch has the advantage of being inherently stable, it also has inherent disadvantages. Interferometric switches

in which both probes co-propagate with the control pulse (e.g. the SMZ or DISC, introduced in section 1.2.3) avoid the device length limitation on the switching window. On the other hand, these configurations have other disadvantages, in particular unlike the TOAD loop with its single SOA, they are not intrinsically balanced. An alternative strategy, to counter the problem of the asymmetry in the TOAD switching window, would be to utilise a configuration employing two TOADs that succeeds in combining from each TOAD just the steep side of their switching window. Overall this configuration yields a transmission change which switches rapidly both on and off [16]. Whilst further complication of the switching configuration would appear undesirable, recent reports of extremely high quality integrated fabrication of single TOADs render the proposal of a double TOAD configuration a plausible solution [17]. To keep the total power demands of the system low, with ever shorter windows and higher repetition rates, it may be necessary to return to fundamental device properties e.g. changing composition to maximise material response.

Finally, it has been demonstrated that the peak wavelength of a co-propagating probe varies over a range of 2 nm during the ultrafast pump-induced dynamics. Such spectral shifts are expected to be a contributing factor to the degradation of the contrast ratio as the switching window is reduced for all SOA-based switching configurations. Indeed it has been suggested that changes in the probe pulse profile in the spectral and temporal domains are the key factors in determining the ultimate upper limit on the speed of operation of interferometric switches [18]. This is a concern for the future. However the coupling between the amplitude gain and refractive index dynamics with the SOA studied is weak, and switching that is not disrupted by ultrafast dynamics has been demonstrated with pulses as short as 600 fs.

Bibliography for Chapter 8

- [1] M J LaGasse, K K Anderson, C A Wang, H A Haus, and J G Fujimoto. Femtosecond measurements of the nonresonant nonlinear index in AlGaAs. *Appl. Phys. Lett.*, 56(5):417–419, 1990.
- [2] R J Manning, A E Kelly, A J Poustie, and K J Blow. Wavelength dependence of switching contrast ratio of semiconductor optical amplifier-based nonlinear loop mirror. *Electron. Lett.*, 34(9):916, 1998.
- [3] G Toptchiyski, S Randel, K Petermann, S Diez, E Hilliger, C Schmidt, C Schubert, R Ludwig, and H G Weber. Analysis of switching windows in a gain-transparent-SLALOM configuration. *IEEE/OSA J. Lightwave Technol.*, 18(12):2188–2195, 2000.
- [4] G Toptchiyski, S Kindt, K Petermann, E Hilliger, S Diez, and H G Weber. Time-domain modeling of semiconductor optical amplifiers for OTDM applications. *IEEE/OSA J. Lightwave Technol.*, 17(12):2577, 2000.
- [5] R P Schrieck, M H Kwakernaak, H Jäckel, and H Melchior. All-optical switching at multi-100-Gb/s data rates with Mach-Zender interferometer switches. *IEEE J. Quantum Elect.*, 38(8):1053–1061, 2002.
- [6] L F Tiemeijer, P J A Thijs, P J de Waard, J J M Binsma, and T B Dongen. Dependence of polarisation, gain, linewidth enhancement factor, and K factor on the sign of the strain of InGaAsP/InP strained-layer multiquantum well lasers. *Appl. Phys. Lett.*, 58(24):2738–2740, 1991.
- [7] K Sutkus, K Shum, R R Alfano, and P J Delfyett. Effect of carrier heating on the wavelength chirp of ultrashort laser pulses in semiconductor travelling wave amplifiers. *IEEE Photonic. Tech. L.*, 6(3):372–375, 1994.
- [8] R Schrieck, M Kwakernaak, H Jckel, E Gamper, E Gini, W Vogt, and H Melchior. Ultrafast switching dynamics of Mach-Zender interferometric switches. *IEEE J. Quantum Elect.*, 37(6):603–605, 2001.
- [9] M Y Hong, Y H Chang, A Dienes, J P Heritage, P J Delfyett, S Dijaili, and F G Patterson. Femtosecond self- and cross-phase modulation in semiconductor laser amplifiers. *IEEE J. Sel. Top. Quant.*, 2(3):523–539, 1996.
- [10] S Adachi. Material parameters of $In_{1-x}Ga_xAs_{1-y}P$ and related binaries. *J. Appl. Phys.*, 53(12):8775–8792, 1982.
- [11] C Schubert, J Berger, S Diez, H J Ehrke, R Ludwig, U Feiste, C Schmidt, H G Weber, G Toptchiyski and S Randel, and K Petermann. Comparison of interferometric all-optical switches for demultiplexing applications in high-speed OTDM systems. *IEEE/OSA J. Lightwave Technol.*, 20(4):618–624, 2002.
- [12] S Kitamura, H Hatakeyama, T Tamamuki, T Sasaki, K Komatsu, and M Yamaguchi. Angle-facet S-bend semiconductor optical amplifiers for high-gain and large-extinction ratio. *IEEE Photonic. Tech. L.*, 11(7):788–790, 1999.
- [13] R J Runser, D Zhou, C Coldwell, B C Wang, P Toliver, K L Deng, I Glesk, and P R Prucnal. Interferometric ultrafast SOA-based optical switches: from devices to applications. *Opt. Quant. Electron.*, 33:941–874, 2001.

- [14] R. Hess, M. Caraccia, W. Vogt, E. Gamper, P. A. Besse, M. Duell, E. Gini, H. Melchior, B. Mikkelsen, M. Vaa, K. S. Jepsen, K. E. Stubkjaer, and S. Bouchoule. All-optical demultiplexing of 80 to 10 gb/s signals with monolithic integrated high-performance mach-zehnder interferometer. *IEEE Photonic. Tech. L.*, 10(1):165, 1998.
- [15] S Bischoff, A Buxens, St Fisher, M Dülk, A T Clausen, H N Poulsen, and J Mørk. Comparison of all-optical co- and counter-propagating high-speed signal processing in SOA-based Mach-Zender interferometers. *Opt. Quant. Electron.*, 33:907–926, 2001.
- [16] B C Wang, V Baby, W Tong, L Xu, M Friedman, R J Runser, I Glesk, and P R Prucnal. A novel fast optical switch based on two cascaded terahertz optical asymmetric demultiplexers (TOAD). *Opt. Express*, 10(1):15–23, 2002.
- [17] V M Menon, W Tong, C Li, F Xia, I Glesk, P R Prucnal, and S F Forrest. All optical wavelength conversion using a regrowth free monolithically integrated Sagnac interferometer. *IEEE Photonic. Tech. L.*, 15(2):254–256, 2003.
- [18] S Nakamura and K Tajima. Analysis of subpicosecond full-switching with a symmetric Mach-Zender all-optical switch. *Jpn. J. Appl. Phys.*, 35(11A):1426–1429, 1996.

Chapter 9

Summary and Conclusions

9.1 Overall Summary

Research into the behaviour of SOAs and their applications is reviewed in Chapter 1. Theory describing the material and its variations in gain and refractive index, on which these applications depend, is described in Chapter 2. The design and monitoring of the optical parametric oscillator, which provided the sub-picosecond pulses used in subsequent experiments, is detailed in Chapter 3. Chapter 4 reports characterisation of the SOA, in particular the relative gain at different wavelengths and as a function of the electrical bias applied to the device. The development of a phenomenological rate-equation based model of the SOA dynamics to complement understanding of the experimentally observed device behaviour, is detailed in Chapter 5. The device small signal gain is quantified by experiments in which a single pulse train is propagated through the SOA. This measurement and observed changes in the spectral profile of pulses, on propagation through the device, are presented in Chapter 6. Chapter 7 reports time-resolved measurements of gain changes using pump-probe transmission experiments, and Chapter 8 describes the investigation of the corresponding refractive index changes, through interferometric phase measurements and changes in the probe spectra as a function of pump delay. In particular, the interferometric experiments allow for the investigation of interferometric switching using the SOA.

9.2 Discussion and conclusions

The notion of exploiting the ultrafast carrier dynamics in SOAs for switching applications has great appeal: whilst they are short-lived, the magnitude of the associated ultrafast complex gain changes may be large. Depending on the value of the α -parameters, which quantify the relative magnitude of refractive index to amplitude gain changes, carrier density changes induced by an intense pulse may translate to large phase changes in a trailing weak pulse. The implication is that by taking advantage of ultrafast dynamics the necessary minimum phase change of π for interferometric switching may be achieved with lower energy pulses. Moreover since the dynamic is short-lived, the same large phase change could be accessed repeatedly at short intervals.

Most existing optical networks use pulses of tens of picoseconds or longer, and transition to the use of femtosecond pulses may not be implemented directly since it would require technological leaps in pulse sources and dispersion control in optical fibres. However the demands of telecommunications for faster signal processing mean optical signal processing is already being introduced to real world systems, with progressively shorter pulses being used. It is therefore important to ascertain which of the ultrafast semiconductor nonlinearities that have been identified using ultrashort pulses of ~ 150 fs duration (see for example [1] and references therein), are manifested with pulses of durations from several hundred femtoseconds up to 1 ps, and how strongly. Do these ultrafast processes modify the device behaviour as observed with pulses of durations several times the characteristic time constants of the process? The results presented in this thesis contribute to an understanding of these questions.

The role of ultrafast dynamics was found to be significant in several experiments. For example, the saturation of the SOA with the 700 fs pulses occurred at optical intensities two orders of magnitude different from the case of CW light (as reported in Chapter 6). This is attributed to the contribution to the saturation from ultrafast gain dynamics, and calculations suggest that the saturation energy is dominated by ultrafast processes, and changes rapidly for small changes in pulse duration, with pulses of less than 10 ps. Moreover, strong ultrafast gain compression, attributed to carrier heating

and two photon absorption, was measured in the amplitude pump-probe measurements (in Chapter 7).

By contrast, ultrafast dynamics were not manifested strongly in time-resolved interferometric measurements. In particular, in the experimental measurements of the switching window (Chapter 8) ultrafast phase changes were not apparent. In particular the window had the following features:

- the top of the switching window was not flat
- there was a pedestal outside the window at delays where the pump precedes both probes through the device

Slow gain recovery during the window is sufficient to explain both of these distortions to the window. It is not asserted that there is no influence from the ultrafast dynamics, but simulations (presented in Chapter 8, using the sliced-propagation model detailed in Chapter 5) illustrate that slow dynamics alone can produce switching windows with the same qualitative features as the experimental data.

Evidence of refractive index dynamics in the SOA came from spectral measurements. Firstly, with single pulse experiments it was demonstrated that there was strong self-phase modulation with pulse energies close to the saturation energy and above, especially at high biases (Chapter 6). This strong SPM is consistent with reports in the literature and was expected [2][3]. Secondly however, it was also found that the spectrum of the probe pulse, which was four orders of magnitude below the saturation energy, was dynamically shifted, during the first few picoseconds after the intense pump (Chapter 8). This suggests that despite the influence of ultrafast gain changes not being strongly manifested in the interferometric measurements, there were significant underlying refractive index changes. Are these spectral shifts strong enough to degrade switching? The experiments conducted so far do not yield a definitive answer, but it is suggested that this was a contributory factor to the limit on improvement of the contrast ratio when ramping up the electrical bias (as discussed in Chapter 8).

It was noted in Chapter 1 that SOA-based interferometric switching configurations, such as the TOAD, could be used for the key processing function of demultiplexing. To achieve high quality demultiplexing it is necessary that

- the gain depletion effected by each control pulse must cause there to be an odd multiple of π differential phase between the clockwise and anticlockwise propagating components of the signal pulses
- either the control pulse repetition rate must be slow enough to allow the device to fully recover between control pulses or the device must be operated in a quasi-equilibrium regime

To effectively annul the switched pulses from the input train and to minimise amplitude modulation in the switched pulse train both of these criteria need to be adhered to as closely as possible.

Firstly, as demonstrated by the experimental results in Chapter 8, when biased to only 70 mA, the 1 mm long SOA could effect a phase change of greater than 3π . Moreover at a bias of 100 mA the first π change can be realised with a control pulse input energy as low as 100 fJ.

Secondly, as shown by results in Chapter 7, the rate of recovery of the SOA can be increased by applying a higher bias. For wide switching windows this tends to eliminate the flat region within the window and result in there being a significant pedestal outside the window. Fortunately, though still a factor, these effects are less severe for narrow windows. An alternative method of speeding up the device recovery, that has been suggested in the literature [4][5], is the use of a holding beam; however the engineering complication entailed by the requirement for an extra input is undesirable. At least for the demultiplexing function, the most attractive option is to operate SOA-based interferometric switches in a quasi-equilibrium regime, in which full device recovery between switching events is not required. Evolution of this regime has been demonstrated with a simple rate equation model (Chapter 5).

All the modelling was phenomenological, based on rate-equations (detailed in Chapter 5). The development of a sliced-propagation model, implemented by iterative calculations of propagation through thin slices of the SOA, facilitated the evaluation of dynamics of a probe which counter-propagates with respect to a pump pulse (in addition to the evolution of co-propagating pulses). Using this model dynamic changes inside the SOA were explored. For example, the counter-propagating pump-probe

traces (presented in Chapter 7) suggested longitudinal gain saturation occurring at different positions along the device depending on experimental conditions. Successfully reproducing the features of these pump-probe traces with the model and subsequently calculating the gain at different positions along the device, supported the attribution of the changing characteristics of the experimental curves to longitudinal saturation. To bring this process full circle it would be interesting to investigate a set of different length devices (that were otherwise identical) such that a series of experiments could be conducted and trends as a function of length compared with the model results. This would give full confidence in the use of the model to assist with the analysis of future experiments.

Throughout the interpretation of experimental data the modelling has proved a useful tool. In the light of experimental results in the spectral domain, and possible further measurements, the inclusion of spectral effects would be a useful extension of this model for future work. A further extension would be to include ASE since it can have a significant influence on device performance as noted in the literature (see for example [6]) and it has already been implicated as the process behind experimentally measured characteristics of the device studied (e.g. the speed up in gain recovery at high biases discussed in Chapter 7).

The careful study of the InGaAs strained superlattice SOA focused on in this project has given a detailed understanding of the device with pulses of $\sim 700 \pm 300$ fs. Unfortunately duration of output pulses from the OPO source was not readily tunable, and a key future experiment would be to implement tunable pulse stretching/compression (for example, using a set of four prisms) to facilitate investigation of trends in the SOA behaviour as a function of pulse width. Beyond this, two directions to be pursued in future experiments with this device could be firstly to subject the SOA-based switch to full systems testing and secondly to extend the detailed laboratory experiments to measurements with shorter pulses, with full pulse characterisation. The former would be interesting to compare how the operating conditions for optimum switching, as assessed by parameters from systems measurements such as Bit Error Rate, compare with the optimum operating conditions identified in the study so far [7][8]. The latter would be aimed at the identification of the role of different ultra-

fast dynamics (carrier heating, spectral hole burning and two photon absorption). With even shorter pulses, the spectral and temporal changes in pulse profile on propagation through the SOA are expected to be even more complex, and it would therefore be interesting to carry out full characterisation of the output pulses using a technique such as Frequency Resolved Optical Gating (FROG) [9][10].

Given the lack of ultrafast changes in interferometric measurements, it can be concluded that for the SOA device studied, the ultrafast gain change to index coupling is relatively weak, for all the ultrafast processes under the conditions investigated. However pump-induced changes in the probe spectra are evidence that ultrafast index changes are occurring. To time resolve these index dynamics and to separately identify α_T , α_{SHB} and α_{TPA} significantly shorter pulses (<300 fs) and possibly higher pulse energies would be necessary. On the other hand, the interferometric experiments already undertaken are a positive result in that they have demonstrated that the SOA can be used for switching without severe disruption of the operation by ultrafast dynamics with pulses as short as 600 fs.

In addition to further experiments with the same type of device, it would be interesting to subject different SOAs to the same range of experiments. Whilst the SOA already studied has strengths, e.g. the high gain in the material and length of the waveguide enable the achievement of low energy switching, it also has weaknesses e.g. the difference in the gain between TE and TM modes. More recently devices with much lower polarisation sensitivity have been produced [11]. It would also be interesting to look at SOAs based on new types of material whose dynamic properties have not yet been thoroughly investigated. These include quantum dot structures and different material compositions, such as a plethora of new nitride materials [12][13]. Devices with quantum dots in the active region have so far demonstrated dynamics with different characteristic time constants (compared to quantum well and bulk materials) and offer the possibility of ultrafast gain recovery [14][15][16]. An example of new Nitride materials are the dilute Nitrides: GaInNAs on GaAs, which have unusual band structures and hence material properties [17][18]. A key question would be the degree to which these manifest ultrafast refractive index changes. The discovery of strong ultrafast index dynamics presents new challenges, but also new opportunities; with ultra

narrow switching windows, the interferometric switching would tend to be more jitter sensitive, but operation at higher bit rates could be realised.

The measurements taken in this research, and modelling necessary to interpret them, are intrinsically valuable to improve our understanding of the physical processes that govern the material recovery, and are important to investigate SOAs potential as processing devices for communications systems in the very near future [19][20]. It is impossible at this stage to predict even which switching technologies emerging from research laboratories will make it onto the world market place, let alone the precise device design adopted. However it is only armed with the experimental data of the type reported here that SOAs can be assessed for the contribution that they could make to the development of all-optical networks.

Bibliography for Chapter 9

- [1] K L Hall, E R Thoen, and E P Ippen. *Semiconductors and Semimetals*, volume 59, chapter 2 Nonlinearities in Active Media. Academic Press, 1999.
- [2] G P Agrawal and N A Olsson. Self-phase modulation and spectral broadening of optical pulses in semiconductor laser amplifiers. *IEEE J. Quantum Elect.*, 25(11):2297, 1989.
- [3] N Finlayson, E M Wright, and G I Stegeman. Nonlinear optical pulse propagation in a semiconductor medium in the transient regime - i: Temporal and spectral effects. *IEEE J. Quantum Elect.*, 26(4):770–777, 1990.
- [4] R J Manning, D A O Davies, D Cotter, and J K Lucek. Enhanced recovery rates in semiconductor laser amplifiers using optical pumping. *Electron. Lett.*, 30(10):787–788, 1994.
- [5] M A Dupertuis, J L Pleumeekers, T P Hessler, P E Selbmann, B Deveaud, B Dagens, and J Y Emery. Extremely fast high-gain and low-current SOA by optical speed-up at transparency. *IEEE Photonic. Tech. L.*, 12(11):1453–1455, 2000.
- [6] H Shi. Performance analysis on semiconductor laser amplifier loop mirrors. *IEEE/OSA J. Light-wave Technol.*, 20(4):682–688, 2002.
- [7] R J Runser, D Zhou, C Coldwell, B C Wang, P Toliver, K L Deng, I Glesk, and P R Prucnal. Interferometric ultrafast SOA-based optical switches: from devices to applications. *Opt. Quant. Electron.*, 33:941–874, 2001.
- [8] M Dülk, St. Fisher, M Bitter, M Caraccia, W Vogt, E Gini, H Melchior, W Hunziker, A Buxens, H N Poulsen, and A T Clausen. Ultrafast all-optical demultiplexer based on monolithic Mach-Zender interferometer with integrated semiconductor optical amplifiers. *Opt. Quant. Electron.*, 33:899–906, 2001.
- [9] F Romstad, P Borri, W Langbein, J Mørk, and J M Hvam. Measurement of pulse amplitude and phase distortion in a semiconductor optical amplifier: from pulse compression to breakup. *IEEE Photonic. Tech. L.*, 12(12):1674–1676, 2000.
- [10] D N Fittinghoff, J L Bowie, J N Sweetser, R T Jennings, M A Krumbügel, K W DeLong, R Trebino, and I Walmsey. Measurement of the intensity and phase of ultraweak, ultrashort laser pulses. *Opt. Lett.*, 21(12):884–886, 1996.
- [11] M Itoh, Y Shibata, T Kakitsuka, Y Kadota, and Y Tohmori. Polarisation-insensitive SOA with strained bulk active layer for network device application. *IEEE Photonic. Tech. L.*, 14(6):765–767, 2002.
- [12] S Makino, T Miyamoto, T Kageyama, Y Ikenaga, F Kyoama, and K Iga. Formation of GaInNAs/GaAs densely packed quantum dots by chemical beam epitaxy. In *IEEE International conference on Indium Phosphide and related materials*, pages 91–94, 2001.
- [13] A Fiore, A Markus, J X Chen, C Parathoen, and M Ilegems. 1300 nm on gallium arsenide: Quantum dots vs. GaInNAs. In *IEEE/LEOS Annual meeting conference proceedings*, volume 2, pages 612–613, November 2002.

- [14] P Borri, W Langbein, J M Hvam, F Heinrichsdorff, M H Mao, and D Bimberg. Spectral holeburning and carrier-heating dynamics in quantum-dot amplifiers: comparison with bulk amplifiers. *Phys. Stat. Sol. B*, 224(2):419–423, 2001.
- [15] T Akiyama, H Kuwatsuka, T Simoyama, Y Nakata, K Mukai, and H Ishikawa. Ultrafast nonlinear processes in quantum-dot amplifiers. *Opt. Quant. Electron.*, 33:927–938, 2001.
- [16] T W Berg, S Bischoff, I Magnusdottir, and J Mrk. Ultrafast gain recovery and modulation limitations in self-assembled quantum dot devices. *IEEE Photonic. Tech. L.*, 13(6):541–543, 2001.
- [17] S Calvez, A H Clark, J-M Hopkins, R Macaluso, P Merlin, H D Sun, M D Dawson, T Jouhti, and M Pessa. 1.3 μm GaInNAs optically-pumped vertical cavity semiconductor optical amplifier. *Electron. Lett.*, 39(1):100–102, 2003.
- [18] W Ha, V Gambin, M Wistey, S Bank, K Seongsin, and J S Harris JR. Multiple-quantum-well GaInNAs-GaNAs ridge-waveguide laser diodes operating out to 1.4 μm . *IEEE Photonic. Tech. L.*, 14(5):1041–1135, 2002.
- [19] M Willatzen, J Mark, and J Mork. Carrier temperature and spectral holeburning dynamics in InGaAsP quantum well laser amplifiers. *Appl. Phys. Lett.*, 64(2):143–145, 1994.
- [20] D Cotter, R J Manning, K J Blow, A D Ellis, A E Kelly, D Nasset, I D Phillips, A J Poustie, and D C Rogers. Nonlinear optics for high-speed digital information processing. *Science*, 286(5444):1523–1528, 1999.

Appendix

Relationship between carrier recombination and gain

Transmission pump-probe experiments measure the compression and subsequent recovery of the gain in the SOA. The changes in transmission are commonly described by characteristic gain recovery times. However there is an important difference between quoting the time required for the gain of an SOA to recover (e.g. time for recovery from 10 to 90% of the equilibrium gain, or for phase to recover by π [1]) and the value of the underlying carrier recombination time; a distinction sometimes not made clear in the literature. To fully understand the experimental data it is useful to consider the complexity of the relationship between carrier recombination and the observed rate of gain recovery.

Carrier density as a function of time

After gain depletion, the slow recovery of the gain is driven by carrier injection balanced by carrier recombination. On shorter timescales faster processes are also significant. However if at this stage only the slow recovery, remaining after pulse has passed and not including the fast dynamics, is considered, the change in carrier density, N , can be described by a simple rate equation of the form

$$\frac{\partial N}{\partial t} = \frac{J}{eV} - R(N) \quad (10.1)$$

where J is the applied electrical bias, q is the carrier charge, V the active volume of the device and $R(N)$ is the carrier recombination of the device. To a first approximation it is assumed that $R(N) = N/\tau_N$ where τ_N is the characteristic carrier recovery time.

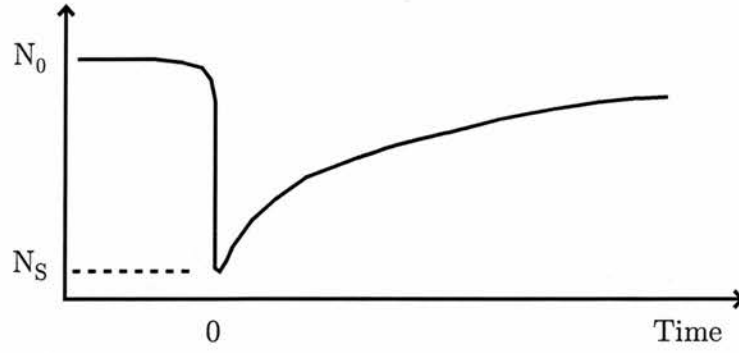


Figure 10.1: Schematic of the change of carrier density and exponential recovery. At time zero, the carrier density is reduced from its equilibrium value, N_0 , to the value N_s

From this and the rate equation the equilibrium carrier density, N_0 , can be expressed as

$$N_0 = \frac{J\tau_N}{eV} \quad (10.2)$$

Note that equation 10.1 is equivalent to equation 5.1, defined at the outset in the modelling described in Chapter 5, under the assumption that there is no optical field. Also note that the recombination rate is not in practice well described by a fixed time constant; the variation of τ_N as a function of current is discussed in the last section of this Appendix.

To describe the evolution of carrier density as the material recovers from gain depletion, consider that the carrier density is reduced from its initial equilibrium value, N_0 , to some saturated value, N_s , as illustrated schematically in figure 10.1. By separating the variables in equation 10.1 and integrating carrier density, from N_s the initial carrier density to N_t after some time t , and time, from 0 to t , one obtains (after some rearrangement) the expression

$$N(t) = (N_0 - N_s)(1 - \exp^{-t/\tau_N}) + N_s \quad (10.3)$$

Equation 10.3 behaves as expected: in the limit $t \rightarrow 0$ the carrier density, $N(t)$, tends to the initial value of N_s ; and as $t \rightarrow \infty$ the carrier density returns to its equilibrium value, N_0 .

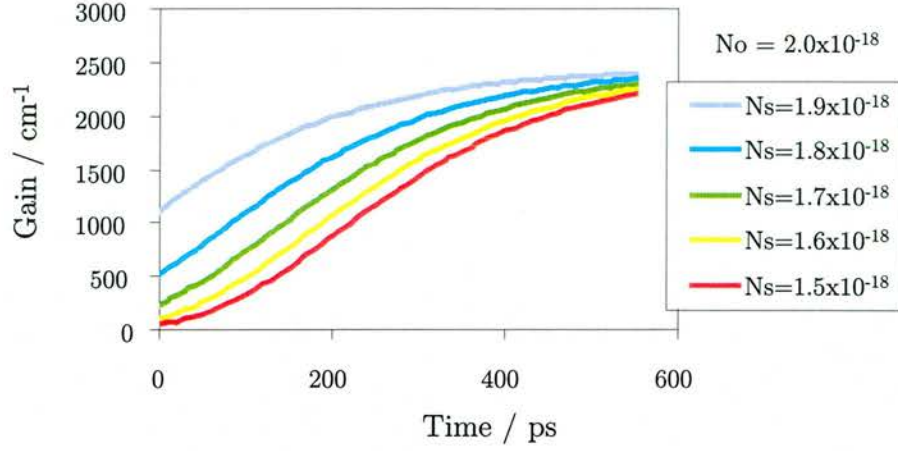


Figure 10.2: The calculated gain recovery from a depleted carrier density level, N_s , to equilibrium carrier density, N_0 , for five values of N_s , using equation 10.6.

Device gain as a function of carrier density

The gain experienced on propagation through the SOA can be described simply by an equation of the form

$$G = \exp^{\Gamma L \left. \frac{\partial g}{\partial N} \right|_{N_{tr}} (N - N_{tr})} \quad (10.4)$$

where Γ is the optical mode confinement factor, L is the length of the device, $\left. \frac{\partial g}{\partial N} \right|_{N_{tr}}$ is the differential gain and $(N - N_{tr})$ is the excess carrier density, with respect to transparency. However N is not constant. After gain depletion $N(t)$ is given approximately by equation 10.3. With this substitution into equation 10.4, the gain at $t = 0$, directly after depletion, is given by

$$G_0 = \exp^{\Gamma \left. \frac{\partial g}{\partial N} \right|_{N_{tr}} L (N_s - N_{tr})} \quad (10.5)$$

since $N(0) = N_s$.

Hence finally, by substituting equation 10.5 into equation 10.4 and simplifying, an expression for the evolution of the gain after depletion as a function of the carrier recovery time is obtained

$$G(t) = G_0 \exp^{\Gamma \left. \frac{\partial g}{\partial N} \right|_{N_{tr}} L [(N_0 - N_s)(1 - \exp^{-t/\tau_N})]} \quad (10.6)$$

Figure 10.2 shows the calculated gain recovery from five different levels of gain depletion. The equilibrium carrier density, N_0 is set at $2.0 \times 10^{18} \text{ cm}^{-3}$ and the time

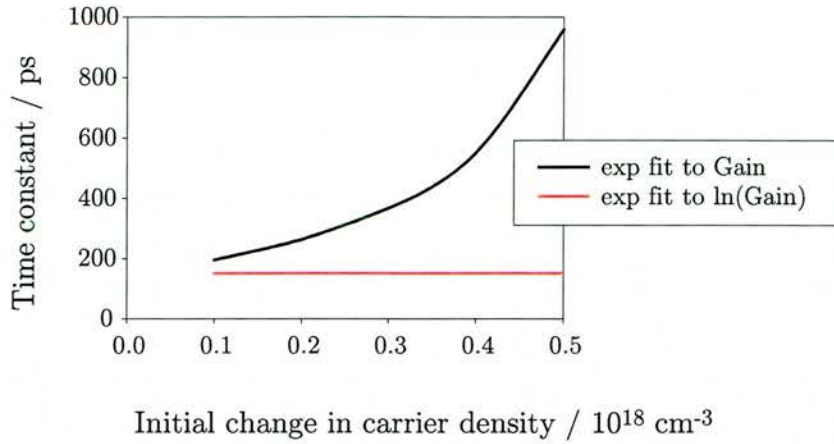


Figure 10.3: The time constant obtained from fits to gain dynamics of the form illustrated in figure 10.2. When a simple exponential is assumed longer time constants are found for larger magnitudes of gain depletion; when the form of gain expressed in equation 10.6 is considered the constant input parameter time constant (150 ps) is retrieved.

constant, τ_N is given the same value, 150 ps, for all five curves. This corresponds experimentally to fixing the applied bias and changing the pump pulse energy. Note that the curvature of the gain recovery changes from the least to the most depleted cases.

The expression in equation 10.6 is an approximation, in two major respects. Firstly, the gain accumulation would be properly described by integration over the length of the device, not simply by a linear multiplication by the length, L (as assumed in equation 10.4). Secondly, the gain is influenced not just by the evolution of the magnitude of the carrier population, $N(t)$ as described by τ_N , but also by the distribution of that population. It can be shown that including ultrafast gain processes equation 10.6 is extended with additional term inside the square brackets [2][3]). For a single ultrafast gain process with the characteristics of carrier heating the necessary term is of the form $-exp^{-t/\tau_T}$, where τ_T is time constant governing the rate of recovery from carrier heating [4].

Essentially the expression in equation 10.6 serves to demonstrate that, even without the complexity of the ultrafast dynamics, a fit of the SOA gain recovery with a single exponential does not yield the underlying time constant. Experimentally, both increasing pump pulse energy and changing the pump from TE to TM mode, the observed

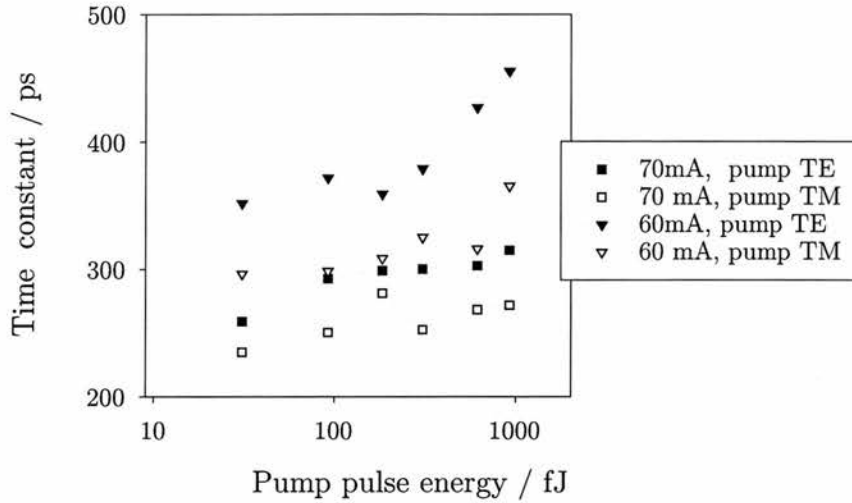


Figure 10.4: Time constants from fits to pump-probe traces from experiments with different energy pump pulses, electrical biases of 60 and 70 mA and both polarisations. The fit used to obtain these time constants was a simple exponential of the form $y = y_0 + a \exp(-t/\tau)$. These fits found time constants that changed significantly as a function of both pump pulse energy and polarisation, as well as electrical bias; only the later was expected and has a clear physical explanation.

effect was an increase in the magnitude of transmission change seen by a probe. Such a change corresponds to increasing the value of $|N_0 - N_s|$ in equation 10.6 and thereby the nature of the dynamic gain recovery is altered despite the fact that the underlying time constant is fixed, as illustrated by the curves in figure 10.2. To illustrate this, fits to generated curves like those in figure 10.2, are plotted in figure 10.3. A simple exponential fit to the gain obtains a time constant that changes as a function of the magnitude of the initial gain depletion (black curve). This compares with a fit to the natural log of the gain dynamic which, as expected, recovers the input value of time constant (150 ps) used to generate the curves, independent of degree of gain depletion (red line).

Figure 10.4 is included as a caveat: it illustrates the results of a direct exponential fits to experimentally measured transmission changes (rather than the logarithm of the transmission change) which yield time constants dependent not only on bias, but also on the pump pulse energy and polarisation. Since any polarisation of carriers is expected to randomise after less than 100 fs, the later two parameters would only be expected to influence the number of interband transitions and hence the magnitude of

the transmission change: there is no clear mechanism for either to affect the subsequent recovery.

Carrier lifetime as a function of applied bias

To understand the change in the rate of the SOA gain recovery with changes in the level of electrical bias it is necessary to consider the relationship between static and dynamic carrier lifetimes, carrier density and electrical bias current (see for example [5]).

As outlined in Chapter 2, carrier recombination can occur by a range of processes which occur with different characteristic rates. However it is reasonable to assume that Auger is the dominant process at the high carrier densities in a biased SOA device and so the full expression for the rate of recombination, equation 2.27, can be reduced to

$$R(N) \approx CN^3 \quad (10.7)$$

where C is the Auger coefficient. Under these conditions the equilibrium carrier density, found from the carrier density rate equation (equation 10.1), can be expressed as

$$N_0 = \sqrt[3]{\frac{J}{CeV}} \quad (10.8)$$

In experimental measurements what is actually measured is the dynamic differential lifetime, that is

$$\tau_N = \left[\frac{dR(N)}{dN} \right]^{-1} \quad (10.9)$$

For moderate gain compression the carrier density deviates only slightly from the equilibrium value and therefore, combining equations 10.7, 10.8 and 10.9, the time constant can be related to applied bias current as follows

$$\tau_N = \frac{1}{3} \left(\frac{eV}{\sqrt{C}} \right)^{\frac{2}{3}} J^{-\frac{2}{3}} \quad (10.10)$$

In conclusion, if Auger is the dominant process in the slow gain recovery of the SOA, the slow gain recovery time constant is proportional to $J^{-\frac{2}{3}}$.

Bibliography for Chapter 10

- [1] R Gutiérrez-Castrejón, L Occhi, L Schares, and G Guekos. Recovery dynamics of cross-modulated beam phase in semiconductor amplifiers and applications to all-optical signal processing. *Opt. Commun.*, 195:167–177, 2001.
- [2] K L Hall, E R Thoen, and E P Ippen. *Semiconductors and Semimetals*, volume 59, chapter 2 Nonlinearities in Active Media. Academic Press, 1999.
- [3] A Mecozzi and J Mørk. Saturation effects in nondegenerate four-wave mixing between short pulses in semiconductor laser amplifiers. *IEEE J. Sel. Top. Quant.*, 13(5):1190–1207, 1997.
- [4] L Occhi, Y Ito, H Kawaguchi, L Schares, J Eckner, and G Guekos. Intraband gain dynamics in bulk semiconductor optical amplifiers: measurements and simulations. *IEEE J. Quantum Elect.*, 38(1):54–60, 2002.
- [5] G Eisenstein, R S Tucker, J M Wiesenfeld, P B Hansen, G Raybon, B C Johnson, T J Bridges, F G Storz, and C A Burrus. Gain recovery of travelling-wave semiconductor optical amplifiers. *Appl. Phys. Lett.*, 54(5):454–456, 1989.

Conference publications

Ultrafast dynamics in semiconductor optical amplifiers with implications for interferometric switching, J G Fenn, M Mazilu, A Gomez Iglesias and A Miller, IEEE/LEOS Annual meeting conference proceedings, volume 2, pages 401-402, November 2002.

Ultrafast gain dynamics in semiconductor optical amplifiers, J G Fenn, The Rank Prize Funds Symposium on Optical Gain and Recombination in Semiconductors, Cumbria, UK, October 1999.

Acknowledgements

I am indebted to many friends and colleagues for their support throughout my years in St Andrews. Thanks especially to:

All the A-team, past and present -

Alan for your patience in lengthy discussions of results and your enthusiasm;

David for steady encouragement in my work and keeping me dancing;

Dawn and Jonathan for getting me started;

John-Mark for building my confidence in the lab and staying in touch from the West coast;

Steve for being a source of sound advice with regards to theory and lab practice, and a sympathetic listener;

Mike for vital support with maths and friendship;

Andy for making me laugh (and your hours on the computers);

Alvaro and Matt for cheerful company and fresh ideas, and patience in the lab;

Jean-François for that late night music... and coffee;

Charis for reminding me why I loved being in Scotland!

Lots of people from the mechanical workshop and electronics for skilled technical help, that I so needed;

Bob for the devices, and very useful discussions;

Ian, Jian Zhong, Javier et al. (from Heriot Watt) for insightful meetings over many cups of tea;

Tim, Rab, Chris, Alex (St Andrews) and Marc (in Glasgow) for putting up with me cluttering your work space (and trusting me to use your lasers);

The W-Squad - for sharing experimental experience and Cafe-in-the-Park socialising, and Iain for steadying me through the last minute crises;

Vene, for coping with an unpredictable flatmate, whilst I was in the midst of writing up;

Paul for being a friendly face and sounding board throughout the roller-coaster ride.

Mum, Dad, Rob, Chas and other family - near and far - for staying in touch and accepting the adage "no news is good news".

And Berni... for being there and believing in me.